Investigating Superconductivity by Tunneling Spectroscopy Using Oxide Heterostructures

Evangelos Fillis-Tsirakis

Dissertation at the **University of Stuttgart**

Max-Planck-Institute for Solid State Research, 2017

Investigating Superconductivity by Tunneling Spectroscopy Using Oxide Heterostructures

Von der Fakultät Mathematik und Physik der Universität Stuttgart
zur Erlangung der Würde eines Doktors
der Naturwissenschaften (Dr. rer. nat.) genehmigte Abhandlung

vorgelegt von
Evangelos Fillis-Tsirakis
aus Athen, Griechenland

Hauptberichter:	Prof. Dr. Jochen Mannhart
Mitberichter:	Prof. Dr. Martin Dressel

Tag der mündlichen Prüfung: 19. Juni 2017

Max-Planck-Institut für Festkörperforschung
Stuttgart, 2017

Contents

Zusammenfassung

Der rapide Fortschritt der Festkörperphysik während des letzten Jahrhunderts bis heute wird angetrieben durch die Vielzahl wissenschaftlicher und technischer Fortschritte. Oxidische Materialien und künstlich erzeugte, auf oxidischen Materialien bestehende Heterostrukturen stehen im Fokus der Aufmerksamkeit, sowohl als Modellsysteme für das Verständnis einer Vielzahl physikalischer Phänomene als auch aufgrund ihrer weitreichenden Anwendungsmöglichkeiten [1]. Das Elektronensystem an der $LaAlO_3/SrTiO_3$ Grenzfläche ist ein hervorragendes Beispiel für diese Vielseitigkeit, denn das dort erzeugte 2-dimensionale Elektronensystem (2DES) zeigt Ferromagnetismus, Ferroelektrizität, Piezoelektrizität, Rashba Spin-Orbit Kopplung, Supraleitung und starke elektronische Korrelationen; Eigenschaften die auch untereinander koexistieren. Die Ähnlichkeit zwischen dem $LaAlO_3/SrTiO_3$ 2DES und den Hochtemperatur-Supraleitern macht die Erkenntnisse über das $LaAlO_3/SrTiO_3$ Modellsystem zweifellos noch wertvoller. Die Möglichkeit, das 2DES mittels externer Parameter wie Gate-Spannung, Temperatur, Druck und Magnetfeld zu steuern macht es vielseitig nutzbar. Diese Funktionalität wurde in der vorliegenden Arbeit ausgenutzt um den supraleitenden Grundzustand der $LaAlO_3/SrTiO_3$ Grenzfläche im Bereich starker Entvölkerung und unter dem Einfluss externer Magnetfelder zu untersuchen. Zu diesem Zweck untersuchte ich mittels Pulsed Laser Deposition (PLD) gewachsenen Proben mit planaren Tunnelkontakten.

Eine Phase ähnlich der Pseudogap in Kuprat-Supraleitern wurde im unter-dotierten Regime des supraleitenden $LaAlO_3/SrTiO_3$ 2DES beobachtet [2]. Kombinierte Transport- und Tunnelspektroskopie-Messungen in planaren Tunnelkontakten haben gezeigt, dass eine supraleitende Bandlücke in der Zustandsdichte auch in den in Transportmessungen nicht supraleitenden unterdotierten Bereichen des Phasendiagramms gemessen werden kann. Der Temperaturverlauf der Bandlücke ähnelt dem der Temperatur T^* im Pseudogap-Regime der Kuprate. Diese Erkenntnis führte zu der Vermutung, dass eine solche Pseudogap-Phase eine intrinsische Eigenschaft zweidimensionaler Supraleiter sein könnte, sowohl des 10 nm dicken $LaAlO_3/SrTiO_3$ 2DES als auch der CuO_2-Ebenen in der Kupratstruktur. Des Weiteren wurden in diesen Messungen Werte für die supraleitende Bandlücke Δ, den Quasipartikel Lebensdauerparameter Γ sowie die kritische Temperatur T_c bestimmt. Weitere Untersuchungen enthüllten, dass durch Entvölkern des Elektronensystems die Elektron-Phonon-Kopplung verstärkt wird und so das Pseudogap-

ähnliche Verhalten erklärt wird (H. Boschker et al. [3]).

Widerstandsmessungen bei T = 50 mK wurden bei verschiedenen Gate-Spannungen und Magnetfeldern senkrecht zur Grenzfläche durchgeführt, um den Supraleiter-Isolator-Übergang durch Ladungsträger Entvölkerung zu untersuchen. Es zeigte sich, dass ein endlicher Widerstand bei Gate-Spannungen von -130 V bis -140 V einsetzte, jedoch sättigte der Widerstand $R_{H=0}$ erst bei V_g = -250 V im MΩ-Bereich. Dieses graduelle Ausschalten der Supraleitung durch Entvölkerung stimmt mit früheren $R(T)$-Messungen überein [2] und unterstreicht die Existenz einer metallischen Phase zwischen der supraleitenden und der isolierenden Phase. Dieser Phasenübergang in $LaAlO_3/SrTiO_3$ wurde daher als Supraleiter-Metall-Isolator-Übergang (SMIT) charakterisiert. Ein Ziel dieser Messungen war die mögliche Existenz einer Superisolator-Phase zu untersuchen, die von verschiedenen Autoren in dünnen metallischen Schichten vorhergesagt wurde. Eine solche Phase wurde in meinen Messungen im $LaAlO_3/SrTiO_3$ 2DES nicht gefunden.

Die Form der Supraleitung im gesamten Phasendiagramm und insbesondere über den Verlauf der SMIT wurde durch Tunnelspektroskopie bei verschiedenen Magnetfeldern gemessen. Die Entwicklung der Tunnel-Spektren im Magnetfeld senkrecht zur Grenzfläche wurde detailliert analysiert, bei Ladungsträgerdichten die den überdotierten, optimal dotierten, unterdotierten und metallischen bzw. isolierenden Bereichen des Phasendiagramms entsprechen. In allen Bereichen ist die Entwicklung graduell und das experimentell bestimmte kritische Feld H_c variiert kontinuierlich im gesamten Phasendiagramm, insbesondere auch in der SMIT-Region [4]. Dieses Ergebnis unterstützt das Szenario, dass der supraleitende Grundzustand bei wachsendem Magnetfeld durch Vortex-Penetration bestimmt wird und somit die Phasenkohärenz bis weit in das metallische Regime bestehen bleibt. Diese Hypothese wird weiterhin durch das Vorhandensein von Quasipartikel-Peaks im entvölkerten Bereich des Phasendiagramms gestützt. Zudem erlauben meine Messungen eine präzise Bestimmung des H_c, der Kohärenzlänge ξ und der Fermi-Geschwindigkeit v_F des $LaAlO_3/SrTiO_3$ Supraleiters als Funktion von V_g.

Die Temperaturabhängigkeit von H_c, von 50 mK bis T_c, wurde in den überdotierten, optimal dotierten, unterdotierten und metallischen bzw. isolierenden Bereichen des Phasendiagramms gemessen. Ein linearer Zusammenhang von H_c und T bis zu den tiefsten Temperaturen wurde in allen Bereichen des Phasendiagramms gefunden, was bedeutet, dass es sich um einen reinen Supraleiter handelt. Das lineare Verhalten kann aber auch auf die Anisotropie durch verringerten Dimensionalität oder auf dem einsetzenden Multiband-Charakter des $LaAlO_3/SrTiO_3$ Supraleiters zurückgeführt werden. Meine Daten reichen nicht aus, um das letztere Szenario abschließend zu beurteilen, daher sind weitere Messungen mit anderen Proben notwendig um diese Frage zu entscheiden.

Zusätzlich zur Supraleitung an der $LaAlO_3/SrTiO_3$ Grenzfläche untersuchte ich auch Supraleitung in dotiertem $SrTiO_3$, dem ersten oxidischen Halbleiter in dem Supraleitung gefunden wurde. Seine fundamentale Bedeutung liegt darin, dass Supraleitung bei ultra-niedrigen Ladungsträgerdichten auftritt und dass es ein Wegbereiter für die Entdeckung der Kupfer-basierten Verbindungen war. Eine kombinierte Untersuchung dieses Systems und des $LaAlO_3/SrTiO_3$ 2DES mittels Tunnelspektroskopie kann neue Aspekte der hier beobachteten Supraleitung aufzeigen. Es ist faszinierend, dass Zwei-Band-Supraleitung in dotiertem $SrTiO_3$ gefunden wurde [5,6], jedoch nicht an der $LaAlO_3/SrTiO_3$ Grenzfläche, obwohl die Energie-Bandstruktur und die Hierarchie am Fermi-Level in beiden Materialien ähnlich sind.

In dieser Arbeit wurden planare Tunnelkontakte zwischen Indium und 0.5 wt% Nb-dotiertem $SrTiO_3$ hergestellt. Tunnelspektroskopische Messungen werden zwischen dem In-film und dem $SrTiO_3$-Kristall durchgeführt, wobei die Schottky-Barriere an der Grenzfläche als Tunnel-Barriere fungiert. Messungen über weite Energiebereiche (ca. 100 meV) lösten die zwei höchsten longitudinal optischen Phononen-Moden (LO3 und LO4) auf, in Übereinstimmung mit den Literatur-Berichten. Diese Ergebnisse zeigen, dass das Tunneln durch diesen Kontakt eine einfache und verlässliche Methode zur Untersuchung der spektralen Zustandsdichte in der Nähe der Fermi-Energie ist. Jedoch bildet die Instabilität während der Messung welche durch die Schottky-Konfiguration einer dünnen Isolator-Schicht zwischen $SrTiO_3$ und In erzeugt wird, einen Nachteil. Die Transmittivität der Barriere ändert sich in Abhängigkeit der angelegten Spannung und ist oft für ein Hintergrundrauschen in den Tunnelspektren verantwortlich. Dies wurde während meiner Arbeit demonstriert und kann für darauf aufbauende Arbeiten eine nützliche Information sein.

Das Hauptziel meiner Forschung an Nb-dotiertem $SrTiO_3$ im überdotierten Regime war die Untersuchung der supraleitenden Eigenschaften des Grundzustands. Die supraleitende Bandlücke Δ und das kritische Feld H_c wurden gemessen und ihre Temperaturabhängigkeit wurde untersucht. Eine supraleitende Bandlücke von ca. 75 meV wurde bei der Grundtemperatur des Kryostaten gemessen. Diese Bandlücke ist geringfügig höher als diejenige der $LaAlO_3/SrTiO_3$ Grenzfläche. Die Temperaturabhängigkeit der Bandlücke ergibt eine BCS-Verhaltnis von mehr als 4, was nur in stark gekoppelten Supraleitern beobachtet wird. Die Änderung des kritischen Magnetfelds mit zunehmender Temperatur zeigt Anzeichen eines zwei-Band-Verhaltens mit einer positiven Krümmung bei $T = 0.5\,T_c$, wie von der Theorie vorhergesagt [7]. Unter Annahme eines Modells, das für den zwei-Band-Supraleiter MgB_2 [8] entwickelt wurde und unter Verwendung von Literaturwerten für die Kopplungskonstanten von $SrTiO_3$ [9] wurde für das Szenario, dass zwei Bänder mit einem Diffusivitätsverhältnis von 5:1 an der Supraleitung beteiligt sind, eine gute Annährung meiner Daten erzielt. Zur Unterstützung dieses Ergebnisses sind in Zukunft weitere Messungen an $SrTiO_3$ Substraten mit verschiedenen Nb-Dotierungen notwendig.

Zusammenfassend beschrieben hat meine Arbeit zum Verständnis der Supraleitung im dotierten $SrTiO_3$ Kristall und an der $LaAlO_3/SrTiO_3$ Grenzfläche beigetragen. Sie baut auf den vergangenen Arbeiten aus meiner Gruppe auf und hat einige neue Eigenschaften der Supraleiter mit den geringsten bekannten Ladungsträgerkonzentrationen aufgezeigt. Die Verwendung von Tunnelspektroskopie in planaren Kontakten erwies sich als entscheidendes Werkzeug zur Darstellung der Zustandsdichte und die Verbindung mit Transportmessungen ist eine wirkungsvolle Methode um neue physikalische Phänomene in Supraleitern aufzudecken. Als direkte Fortführung meiner Arbeit schlage ich die Untersuchung der supraleitenden Eigenschaften von dotiertem $SrTiO_3$ im gesamten Phasendiagramm vor, sowie die Untersuchung von $LaAlO_3/SrTiO_3$ Grenzflächen mit amorphem $LaAlO_3$ [10] oder mit $SrTiO_3$ Substraten mit in [110]- oder [111]–Kristallrichtung orientierten Oberflächen [11, 12]. Obwohl es eine große technische Herausforderung darstellt, könnte die Fabrikation von Kontakten, in denen Elektronen von der Seite in das $LaAlO_3/SrTiO_3$ 2DES tunneln (wie in der in Ref. [13] beschriebenen DC-SQUID Konfiguration für YBCO) eine alternative Sichtweise auf die faszinierenden Eigenschaften dieses empfindlichen Systems eröffnen. Im größeren Puzzle der Hochtemperatur-Supraleitung fehlen noch immer einige Teile. Vielleicht wird durch diese endlosen Stunden der Optimierung, Messung und Auswertung eines der sehr vielen neuartigen supraleitenden Verbindungen der Fortschritt der wissenschaftlichen Gemeinschaft vorangetrieben und die Mysterien von heute werden zum Wissen von morgen.

References

[1] M. Lorenz et al., J. Phys. D: Appl. Phys. **49**, 433001 (2016).

[2] C. Richter, H. Boschker, W. Dietsche, E. Fillis-Tsirakis, R. Jany, F. Loder, L. F. Kourkoutis, D. A. Muller, J. R. Kirtley C. W. Schneider and J. Mannhart, Nature **502**, 528 (2013).

[3] H. Boschker, C. Richter, E. Fillis-Tsirakis, C. W. Schneider and J. Mannhart, Sci. Rep. **5**, 12309 (2015).

[4] E. Fillis-Tsirakis, C. Richter, J. Mannhart and H. Boschker, New J. Phys. **18**, 013046 (2016).

[5] G. Binnig, A. Baratoff, H. E. Hoenig and J. G. Bednorz, Phys. Rev. Lett. **45**, 1352 (1980).

[6] X. Lin, A. Gourgout, G. Bridoux, F. Jomard, A. Pourret, B. Fauque, D. Aoki and K. Behnia, Phys. Rev. B **90**, 140508(R) (2014).

[7] J. M. Edge and A. V. Balatsky, J. Supercon. Nov. Magn. **28**, 2373 (2015).

[8] A. Gurevich, Phys. Rev. B **67**, 184515 (2003).

[9] R. M. Fernandes, J. T. Haraldsen, P. Wölfle and A. V. Balatsky, Phys. Rev. B **87**, 014510 (2013).

[10] G. E. D. K. Prawiroatmodjo, F. Trier, D. V. Christensen, Y. Chen, N. Pryds and T. S. Jespersen, Phys. Rev. B **93**, 184504 (2016).

[11] G. Herranz, G. Singh, N. Bergeal, A. Jouan, J. Lesqueur, J. Gasquez, M. Varela, M. Scigaj, N. Dix, F. Sanchez and J. Fontcuberta, Nature Commun. **6**, 6028 (2015).

[12] G. Herranz, F. Sanchez, N. Dix and J. Fontcuberta, Sci. Rep. **2**, 758 (2012).

[13] D. A. Wollman, D. J. van Harlingen, J. Giapintzakis and D. M. Ginsberg, Phys. Rev. Lett. **74**, 797 (1995).

Chapter 1

Introduction

In the beginning of the 20^{th} century, physics featured major breakthroughs in theory and experiment, with revolutionary ideas that inevitably dismantled the older scientific dogma of physical laws of the universe. With technology rapidly advancing, conditions were set for scrutinizing physical concepts by experiment and the conviction that classical physics is valid in the micro-world was revoked. Within Albert Einstein's theory of special relativity in 1905, the speed of light in vacuum is established as a universal constant while energy and mass are interchangeable quantities. In parallel, the birth of quantum theory by Max Planck in the early 1900's has guided the explanation of the photoelectric effect and also paved the way for the introduction of the Bohr-model in 1913. A longstanding paradox, the discrepancy between expectation from classical theory and measurement of the energy distribution of radiation from a "blackbody" was settled in the years to come, with the evolution of quantum theory into the modern quantum mechanics. The latter bolstered the field of solid-state physics, as it provided the basis in the understanding of materials' macroscopic properties by looking at their behavior in the sub-atomic scale. Consequently, quantum mechanics enabled the investigation of materials with unique large-scale properties and the research within solid-state physics has been further subdivided into specialized branches, e.g. electromagnetism, highly-correlated materials and superconductivity.

Superconductivity, or "supra-conductivity" as was initially referred to, began in 1911 through the study of resistance-reduction in metals at extremely low temperatures, by Heike Kamerlingh Onnes. Within solid-state physics, it is still highly active and has, at certain periods, drawn exceptionally high scientific attention. The vanishing resistivity of conducting materials below a critical temperature offers enormous potential for application, a part of which is realized today. Important representative examples are highly efficient power cables with capability of dissipationless transport, ultrafast digital circuits and magnetic resonance imaging (MRI) and nuclear magnetic resonance (NMR) machines. The pioneering theory of John Bardeen, Leon Cooper and Robert Schrieffer in 1957 (BCS-theory) established a consen-

sus on the understanding of conventional superconductivity within a rigorous, microscopic description that applied to all known superconducting materials until the 80's [1]. Yet, practical utilization of this brand new physics was rather challenging at the time. Fundamental difficulties arose from the simple fact that superconductivity manifested itself at $T \rightarrow 0$, a temperature range unaffordable for large-scale application. This also explains the enormous hype created in the mid 80's with the invention of high-temperature superconductors (HTS) by Karl Alex Müller and Georg Bednorz, the copper-oxide based superconducting compounds or cuprates [2].

1.1 What motivates my study

High-temperature superconductivity has been on the forefront of solid-state research for the last three decades. A hypothetical compound that is well-superconducting at room temperature would undoubtedly revolutionize today's world, at least on a technological level. At present, as such a revolution is still visionary, the pursuit of finding new superconductors with higher critical temperatures is ongoing. Research has already exhausted non-complex material candidates and this pursuit requires tailoring entirely new families of compounds through state-of-the-art fabrication procedures. The guiding recipe for fabrication demands a new, fundamental theory of what is today referred to as "unconventional superconductivity", which is seen in the currently known HTS-compounds (and also in other families of complex superconducting materials). A significant number of studies have underlined the inadequacy of the BCS-framework for explaining superconductivity in the HTS-compounds and their extremely high critical temperatures (T_c) [3]. Despite indications that spin-mediated electronic pairing drives superconductivity therein, a concrete and widely accepted explanation is pending. The copper-oxide HTS are characterized by complex phase diagrams [4], with abnormal metallic behavior in the normal state, showing exceptionally high resistivity at high temperatures (bad metals). Their layered structure hosts superconductivity within the CuO_2-planes at low temperatures. The doping dependence of T_c is non-monotonic (dome-shaped) and the superconducting phase resides in the vicinity of a magnetically-ordered regime, a feature also seen in the Fe-based superconductors [5]. The enigmatic nature of the pseudogap phase [6], a precursor to the superconducting with decreasing temperature, is believed to hold pieces of the puzzle of HTS. To explore the 2D-nature of superconductivity in these compounds, it is crucial to extend the investigation in artificially constructed superconducting materials that resemble their properties in confined dimensions. Oxide systems are good candidates as they are similar to the HTS-compounds in structure, provide templates where electrons are highly correlated and also frequently host two-dimensional electron gases (2DEGs).

In this thesis I investigate superconductivity at the interface of two perovskite oxides, lanthanum aluminate ($LaAlO_3$) and strontium titanate ($SrTiO_3$) [7]. A heterostructure with the two as building blocks is grown by pulsed-laser deposition (PLD) and, under certain conditions, the interface hosts a conducting 2D electron system (2DES). This oxide heterostructure, initially fabricated in 2004 by Akira Ohtomo and Harold Hwang, is unique in that the emergent 2DES resides at the interface of two band insulators, is highly correlated and is also superconducting at low temperatures [8, 9]. Owing to the coexistence of fascinating electronic properties such as ferromagnetism, incipient ferroelectricity and Rashba spin-orbit coupling, the $LaAlO_3/SrTiO_3$ interface offers a functional physical template that is valuable not only for basic research but also for the oxide-electronics based technology [10]. The emergent superconductivity in this system is particularly interesting as it appears at extremely low charge carrier densities n_s, unlike in any other compound known to-date. The non-monotonic dependence of T_c on n_s defines a dome-shaped superconducting phase that is qualitatively reminiscent of the high-temperature superconductors. The electric field effect [11] enables the reversible tuning of n_s at the interface and the system can be driven through a superconductor-to-insulator transition (SIT) with a quantum critical point (QCP) at low doping [8, 12]. These transitions are generally induced either by tuning the level of disorder or by applying external magnetic fields and provide information about the long-range phase coherence of the superconducting ground state [13]. Several superconductors have been studied in this regard, with the majority featuring studies of thin metallic films (Ge, Bi, Ta, InOx, MoGe). The characteristics of an SIT at the $LaAlO_3/SrTiO_3$ 2DES, a dilute oxide superconductor, can provide input for the general understanding of such transitions and consequently of superconductivity.

In parallel, I study the 3D counterpart of the $LaAlO_3/SrTiO_3$ 2DES, the bulk $SrTiO_3$ crystal, which upon doping can be rendered superconducting at record-low carrier densities of the order of 10^{17} cm^{-3} [14]. Whether the $LaAlO_3/SrTiO_3$ and semiconducting $SrTiO_3$ superconductors are intrinsically alike is not directly addressed in literature. In the latter case, the superconducting phase extends over a larger doping range (several orders of magnitude wide), while in both cases the rise (underdoped region) and destruction (overdoped region) of superconductivity are not entirely understood. My experiments will also try to identify potential competing orders and investigate whether electron-phonon coupling can account for the observed superconductivity. Furthermore, effort will be put in investigating the hypothesis of multiband superconductivity in semiconducting $SrTiO_3$ through a systematic study, as so far there exists scarce experimental evidence [15, 16].

The main experimental technique this thesis relies on is tunneling spectroscopy using planar junctions. Owing to its high energy resolution and capability to probe the spectral density-of-states (DOS) very close to the Fermi energy, this technique is a valuable tool for studying superconductivity while

tuning external parameters such as carrier concentration, temperature and magnetic field. By combining tunneling spectroscopy with transport measurements, different perspectives of the system's superconducting ground state are obtained and compared. As tunneling spectroscopy is a widely used technique in experimental solid-state physics, it is possible to compare results with studies of similar systems or even motivate the future study of other systems based on this approach. For the former case, interesting systems are the superconducting monolayer of FeSe on $SrTiO_3$ [17] and the multiband, BCS-superconductor MgB_2 [18,19]. The overall output of this work will hopefully aid the understanding of superconductivity in the $LaAlO_3/SrTiO_3$ 2DES and its pairing mechanism, and also highlight the link between 3D (doped $SrTiO_3$) and 2D ($LaAlO_3/SrTiO_3$ interface). From the resemblance of the copper-oxide based HTS to $LaAlO_3/SrTiO_3$, in terms of their quasi-2D nature, all novel aspects discovered in the dilute-limit carry potential implications about the nature of high-temperature superconductivity.

1.2 Outlook

The second chapter elaborates on the physical background required to carry-out measurements and analyze the results. This includes aspects of superconductivity and the BCS-theory, basic principles of the tunneling-effect and its applicability in the study of physical systems as well as the oxide-systems I have focused on: the $LaAlO_3/SrTiO_3$ 2DES and semiconducting $SrTiO_3$.

Chapter 3 briefly describes important steps of the sample fabrication procedure. Laboratory equipment used for fabricating Schottky junctions with Nb-doped $SrTiO_3$ are also presented. A brief description of our key measurement set-up, the dilution refrigerator unit and principles of its operation in the mK-regime conclude this chapter.

Chapter 4 discusses all experimental results obtained by transport and tunneling spectroscopy measurements at the interface of $LaAlO_3/SrTiO_3$. This chapter contains three main parts. In the first, combined transport and tunneling measurements identify a pseudogap-like regime at the underdoped superconducting region, in terms of the measured critical temperatures by the two methods. Analysis of the tunnel spectra with the Dynes-model follows [20]. The second part elaborates on transport measurements while tuning the carrier density and in the presence of magnetic fields, revealing a smooth transition from the superconducting to the insulating side. The last part contains results from magnetic-field dependent tunneling spectroscopy. The obtained evidence of persisting superconducting phase-coherence at the extremely depleted regime in the $LaAlO_3/SrTiO_3$ phase diagram are discussed. In addition, the temperature dependence of the critical field is measured in-and-out of the superconducting dome.

Chapter 5 analyzes tunneling spectroscopy measurements on semiconducting $SrTiO_3$ Schottky junctions. The first part elaborates on measurements of the $I-V$ characteristics at 4.3 K, with the aim to characterize the junctions, identify intrinsic properties of the $SrTiO_3$ substrate and compare with literature. The second part presents measurements in the mK-regime, with and without the presence of magnetic fields, where superconducting features are resolved in the tunnel spectra. The results carry possible signatures of multiband superconductivity in the temperature dependence of the critical field, for a slightly overdoped sample. Such signatures do not appear in the temperature dependent tunnel spectra.

The last chapter summarizes the main experimental output of this thesis. Implications are discussed in the context of superconductivity, respectively for each system, along with a generic perspective from literature. As a conclusion, potential for short-term future research is suggested as a follow-up on my work.

References

[1] J. Bardeen, L. N. Cooper and J. R. Schrieffer, Phys. Rev. **108**, 1175 (1957).

[2] J. G. Bednorz and K. A. Müller, Z. Phys. B: Cond. Matter **64**, 189 (1986).

[3] A. Bussmann-Holder and H. Keller: *High-T_c Superconductors and Related Transition Metal Oxides*, © Springer-Verlag, Berlin Heidelberg (2007).

[4] L. Taillefer, Annu. Rev. Cond. Matt. Phys. **1**, 51 (2010).

[5] Y. Kamihara, H. Hiramatsu, M. Hirano, R. Kawamura, H. Yanagi, T. Kamiya and H. Hosono, J. Am. Chem. Soc. **128**, 10012 (2006).

[6] H. Ding, T. Yokoya, J. C. Campuzano, T. Takahashi, M. Randeria, M. R. Norman, T. Mochiku, K. Kadowaki and J. Giapintzakis, Nature **382**, 51 (1996).

[7] A. Ohtomo and H. Y. Hwang, Nature **427**, 423 (2004).

[8] A. D. Caviglia, S. Gariglio, N. Reyren, D. Jaccard, T. Schneider, M. Gabay, S. Thiel, G. Hammerl, J. Mannhart and J.-M. Triscone, Nature **456**, 624 (2008).

[9] S. Gariglio, N. Reyren, A. D. Caviglia and J.-M. Triscone, J. Phys. Condens. Matter **21**, 164213 (2009).

[10] S. Gariglio, M. Gabay and J.-M. Triscone, APL Mater. **4**, 060701 (2016).

[11] J. Mannhart, J. G. Bednorz, K. A. Mueller and D. G. Schlom, Z. Phys. B **83**, 307 (1991).

[12] N. Reyren, S. Thiel, A. D. Caviglia, L. F. Kourkoutis, G. Hammerl, C. Richter, C. W. Schneider, T. Kopp, A.-S. Ruetschi, D. Jaccard, M. Gabay, D. A. Muller, J.-M. Triscone and J. Mannhart, Science **317**, 1196 (2007).

[13] A. M. Goldman and N. Markovic, Phys. Today **51**, 39 (1998).

[14] X. Lin, Z. Zhu, B. Fauque and K. Behnia, Phys. Rev. X **3**, 021002 (2013).

[15] G. Binnig, A. Baratoff, H. E. Hoenig and J. G. Bednorz, Phys. Rev. Lett. **45**, 1352 (1980).

[16] X. Lin, A. Gourgout, G. Bridoux, F. Jomard, A. Pourret, B. Fauque, D. Aoki and K. Behnia, Phys. Rev. B **90**, 140508(R) (2014).

[17] Q.-Y. Wang, Z. Li, W.-H. Zhang, Z.-C. Zhang, J.-S. Zhang, W. Li, H. Ding, Y.-B. Ou, P. Deng, K. Chang, J. Wen, C.-L. Song, K. He, J.-F. Jia, S.-H. Ji, Y.-Y. Wang, L.-L. Wang, X. Chen, X.-C. Ma and Q.-K. Xue, Chin. Phys. Lett. **29**, 037402 (2012).

[18] A. Bianconi, D. Di Castro, S. Agrestini, G. Campi, N. L. Saini, A. Saccone, S. De Negri and M. Giovannini, J. Phys. Cond. Matt. **13**, 7383 (2001).

[19] J. P. C. Canfield, S. L. Bud'ko and D. K. Finnemore, Physica C, **385**, 1 (2003).

[20] R. C. Dynes, V. Narayanamurti and J. P. Garno, Phys. Rev. Lett. **41**, 1509 (1978).

Chapter 2

Background Knowledge

This chapter contains the background necessary for the discussion of the results presented in chapters 4 and 5. Each section elaborates on independent physical aspects that surround the direction of this thesis, have guided the experimental work and are referred to when interpreting the obtained results. Aspects of superconductivity are discussed on the first section, where topics relevant to this work are highlighted in subsections. In the second, the main experimental tool, tunneling spectroscopy, is introduced along with paradigms of physical systems where net electron-tunneling can occur. Two more sections elaborate on the systems I have worked with, the interface between the oxides lanthanum aluminate ($LaAlO_3$) and strontium titanate ($SrTiO_3$), and Schottky junctions between Nb-doped $SrTiO_3$ and metallic films. These last sections also include the status-quo of the respective system as of 2016.

2.1 Superconductivity

Condensed-matter physicists of the 19th century were particularly curious about how materials behave at extremely low temperatures. A common experimental tool for reducing temperature close to zero was the liquefaction of gases, with ammonia [1] and chlorine [2] being the mainstream choice of the time. Gas liquefaction was achieved solely by compression, while many debated that light gases are "permanent" and cannot be liquefied even at $T \to 0$ [3]. This debate ended in 1877, when two independent researchers, L. P. Cailletet [4] and R. P. Pictet [5] liquefied the first permanent gas, oxygen, using different techniques. In 1906 [6], H. Kammerlingh-Onnes and Sir J. Dewar liquefied hydrogen [3], reaching temperatures below 20 K through cooling cycles with several cryo-liquids.

In 1868, helium-gas was discovered through a spectroscopic study of the chromosphere during a solar eclipse [7]. After forty years and following several failed attempts from a number of groups, H. Kammerlingh-Onnes and his chief technician G. J. Flim were able to liquefy He for the first time in their lab in Leiden, the Netherlands [8]. This was achieved in a system where He was cycled five times in a cascade process that involved four other cryo-liquids, with O_2 and H_2 among them. The liquefaction point of He was determined to be 4.25 K. By 1922, a minimum temperature of 0.83 K was reached by additional pumping on the liquid-He bath.

Three years after their milestone of liquefying He, H. Kammerlingh-Onnes et al. observed the vanishing of electrical resistance with decreasing temperature in samples of purified Hg. Prior to this experiment, it was believed that at $T \to 0$ resistivity saturates at low but finite values which are purity dependent for all metals. Others believed that at this regime, the conductivity essentially vanishes and the electrical resistance diverges. This was the first experimental manifestation of superconductivity. In the years that followed, more fascinating experiments focused on the superconductivity of metallic compounds. To eliminate the problem of measuring extremely low resistances, the decay of current flowing through a superconducting ring was monitored as a function of time [9]. In metallic rings that could be turned superconducting, current-decay was not observed in years. In 1933, W. Meissner and R. Ochsenfeld demonstrated that superconductors expel magnetic field lines completely and were characterized as perfect diamagnets [10]. The field expulsion was strong enough for a permanent magnet to levitate above a superconducting surface (Meissner effect).

In parallel, attempts on establishing a theoretical framework for superconductivity were pursued. The "two-fluid model" was the first attempt to quantitatively describe superconducting phenomena [11–13]. This model assumes that the total charge carrier density is the sum of two components: the normal conducting and the superfluid density. F. and H. London proposed a phenomenological theory according to which superconducting electrons move without dissipation [14,15]. They were also the first to predict the quantization of magnetic flux through a superconducting ring. A. Pippard generalized the London-theory

and was the first to discuss coherence of the superconducting wavefunction, in addition to introducing the notion of a coherence length [16, 17]. A more complete theory was introduced in 1950 by V. Ginzburg and L. Landau, who studied the transition to the superconducting state from a thermodynamic perspective, also based on the London-theory [18]. They also discussed the existence of two different types of superconductors, yet all experimental evidence of the time pointed only to type-I. The discrimination between type-I and type-II superconductivity was bolstered by A. Abrikosov two years later, following his theoretical establishment of the type-II superconductor [19, 20], which was triggered by an effort to experimentally verify the GL-theory. The latter is itself a limiting case of conventional superconductivity (type I with $\kappa < 1/\sqrt{2}$), as shown by Abrikosov.

Elaborate information on the content of Ginzburg-Landau, Abrikosov and London theories, as well as on the history of superconductivity, can be found here [9, 21–23].

2.1.1 The Bardeen-Cooper-Schrieffer Microscopic Theory

J. Bardeen, L. Cooper and R. Schrieffer published the currently accepted theory for explaining superconductivity in 1957, commonly known as the BCS-theory [24]. They described a lattice mediated electron-electron interaction on a microscopic level, through which a coherent-state, many-body wave function could be constructed.

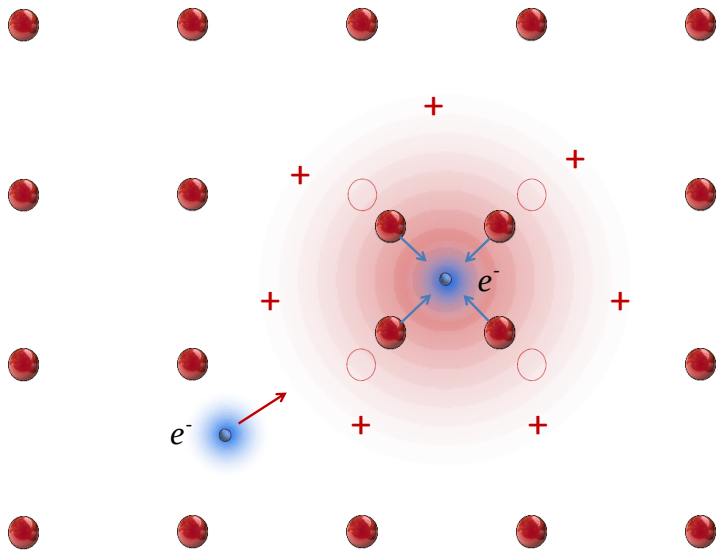

Figure 2.1: *A schematic of the lattice mediated electronic attraction, described in the BCS theory. Negative electronic charge can attract the positive ions (red spheres) of the lattice, which oscillates. Overcompensation of the electronic charge results in positive charge accumulation at the electron's vicinity. Consequently a second electron is attracted, whose potential energy is reduced, indirectly due to the presence of the first.*

Figure 2.1 illustrates the BCS pairing mechanism in a simplistic schematic. The lattice's positive ions are attracted by the Coulomb potential of a propagating electron and oscillate, in an effort to compensate for the negative charge. This trace of polarization induced by the first electron can reduce the potential energy of a second electron. This is the lattice-mediated pairing of two electrons described in the BCS theory. The ionic oscillation has an upper limit that is set by the Debye frequency ω_D and is material dependent. If the electronic density oscillation ω is small, ions can oscillate in phase, but with small displacement due to lattice stiffness. Above a threshold frequency ω_T but below ω_D, so that $\omega_T < \omega < \omega_D$, the lattice ions overcompensate the electronic charge and therefore more electrons are attracted in the region. This is the frequency-window where lattice mediated electronic attraction arises and superconductivity occurs. The above involve the assumption that all lattice ions can oscillate in resonance and thus can be driven by the electronic stimulus.

Looking at the pairing interaction from a momentum perspective, an itinerant electron creates a lattice vibration, i.e. a phonon, that is absorbed by a second electron. If the participating phonon has momentum q, it is required that the first electron with initial momentum k_1 transitions into a momentum state k_1', with $k_1 = q + k_1'$. Accordingly, the second electron from an initial state k_2 reaches k_2' upon phonon absorption, with $k_2 = k_2' - q$. Momentum conservation requires that $k_1 + k_2 = k_1' + k_2'$. In addition, for the pairing interaction to take place the initial states k_1 and k_2 must be occupied by electrons and the k_1' and k_2' states must be unoccupied. BCS-theory has shown that the maximum energy gain obtained by superconductivity is when the number of electron-pairs, i.e. the Cooper pairs, is maximal. This requires that any two electrons participating in phonon exchange have opposite momentum and therefore $k_1 + k_2 = k_1' + k_2' = 0$. In addition, paired-electrons have opposite spins due to the Pauli principle and thus a Cooper-pair has zero momentum and spin. These conditions characterize the conventional, BCS-superconductivity in the absence of external magnetic fields.

The calculated energy difference W_0 between normal and superconducting state, in the weak-coupling limit and at $T \to 0$, is given by the expression [24]:

$$W_0 = E_s - E_n = -2N_0(\hbar\omega)^2 exp\left[-\frac{2}{N_0 \cdot V}\right] \tag{2.1}$$

Here, ω is the average phonon frequency and N_0 is the density of states at the Fermi energy E_F. V is the average of the matrix element $V_{kk'}$ of the pairing interaction operator. It varies continuously in the interval $[k, k']$ and is non-zero for energies $-\hbar\omega < E - E_F < \hbar\omega$. Neglecting anisotropic effects, one can consider V instead of $V_{kk'}$, which is regarded as the strength of the electron-phonon coupling. The phonon energy has an upper limit set by the Debye frequency ($E_{ph} \leq \hbar\omega_D$), with $\hbar\omega_D << E_F$. The reduction of the total energy in the system comes from superconducting electrons at states E_e very close

to E_F, i.e.: $\hbar\omega_D \geq |E_F - E_e|$.

An expression for the minimum excitation energy Δ from the superconducting ground state can be inferred from the above [21]:

$$\Delta \propto 2\hbar\omega_D \cdot exp\left[-\frac{1}{N_0 \cdot V}\right] \tag{2.2}$$

Δ is also referred to as the superconducting order parameter, the amplitude of which can be measured in experiment. From now on, Δ will denote this amplitude. The splitting of the density of states around the Fermi energy of a superconductor equals 2Δ and is typically determined by tunneling spectroscopy.

BCS-superconductors exhibit a characteristic temperature dependence of their superconducting energy gap Δ, which is constant at $T \ll T_c$ and, as $T \to T_c$, $\Delta(T)$ follows the BCS-prediction [21, 24]:

$$\frac{\Delta(T)}{\Delta(0)} \approx 1.74 \cdot \left[1 - \frac{T}{T_c}\right]^{1/2} \tag{2.3}$$

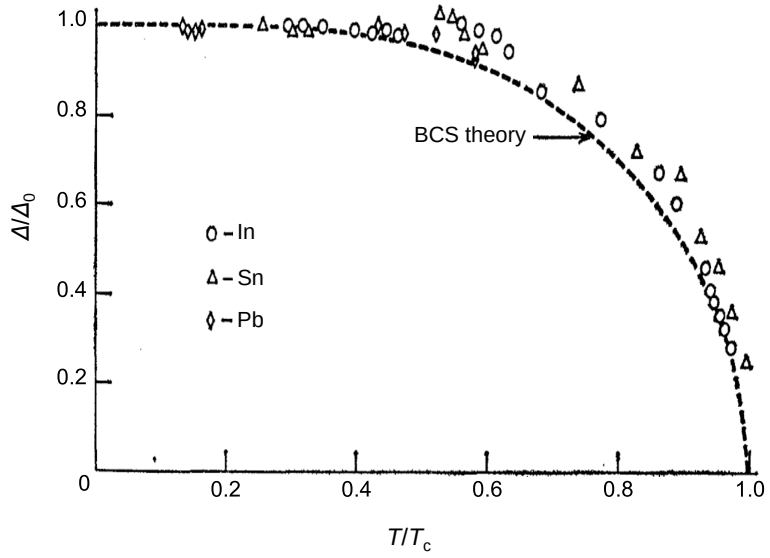

Figure 2.2: *The temperature dependence of the superconducting gap of In, Pb and Sn, which follows the BCS-prediction (dashed line). The vertical axis is the value of the gap Δ normalized to its $T = 0$ value Δ_0, plotted versus temperature T normalized to the critical temperature T_c. From [25].*

Figure 2.2 presents I. Giaever's early experimental results on the temperature dependence of the superconducting gaps of three BCS-superconductors, namely In, Pb and Sn [25]. Measurements follow the BCS prediction well, down to temperatures as low as 20% of T_c for the case of Pb.

Experimental confirmation of the BCS-theory has been obtained in measurements of the flux quantization of superconducting rings and the temperature dependence of the specific heat. The theory is moreover consistent with the isotope effect [26–28]. The gap dependence on the Debye frequency (Eq.

2.2) implies that the critical temperature T_c is proportional to the quantity M^{-a}, where M is the isotope mass and a is measured close to 0.5 for many BCS-superconductors. This is expected since $\omega_D \propto M^{-1/2}$.

From 2.2, it can be inferred that the gap Δ obeys:

$$\frac{2\Delta}{k_B T_c} = 3.527 \tag{2.4}$$

This relation is not always valid. Among other metals, Pb and Hg exhibit ratios higher than 4 [29], with Debye temperatures below 100 K. This is an indication of enhanced electron-phonon interaction, i.e. strong-coupling superconductors.

In addition to Eq. 2.4, from 2.2 it follows that [24]:

$$k_B T_c \simeq \hbar\omega \cdot exp\left[-\frac{1}{N_0 \cdot V}\right] \tag{2.5}$$

The critical temperature T_c is proportional to the average phonon frequency ω, with k_B the Boltzmann constant. A natural upper limit for T_c is set by the Debye frequency ω_D, which is the maximum oscillation frequency of the lattice and thus $\omega \leq \omega_D$ [30]. This means that T_c cannot exceed the Debye temperature T_D, defined as:

$$T_D = \frac{\hbar\omega_D}{k_B} \tag{2.6}$$

In practice, T_c is much smaller than T_D. In 1968, W. McMillan has proposed a theory for calculating approximate T_c-values for BCS-superconductors [31], which considered the strength of the electron-phonon coupling and the electron density at the Fermi level, along with material specific constraints. After refinement [32], the McMillan model is given by the expression:

$$T_c = \frac{\Omega_{av}}{1.2} \cdot exp\left[-\frac{1.04(1+\lambda)}{\lambda - \mu^*(1+0.62\lambda)}\right] \tag{2.7}$$

Here, Ω_{av} is a weighted average of the phonon frequencies (see Ref. [32]) and λ is a measure of the electron-phonon coupling strength. The quantity μ^* is the Morel-Anderson pseudo-potential [33,34] that accounts for the time scale difference between the electron-electron and electron-phonon interactions.

Within the McMillan model, the calculations performed for known superconductors of the time (common metals) found T_c-values which never exceeded 40 K. This value was often misinterpreted in the

community, as a generic temperature upper-limit for BCS superconductivity. On the other hand, a theoretical prediction for the highest critical temperature of metallic H_2 showed $T_c \geq 300$ K, which was introduced by N. Ashcroft at approximately the same time [35, 36].

In their work, Bardeen, Cooper and Schrieffer suggested that different conditions, other than the lattice-mediated attraction, can also lead to electronic pairing. For instance, these can be of magnetic [37], polaronic [38] or excitonic origin [39]. This implies the existence of alternative pathways for superconductivity, described by physics that does not necessarily comply with the BCS-picture.

2.1.2 Unconventional Behavior

Following the advent of the BCS-theory for conventional superconductivity, a number of compounds have been studied extensively in an effort to accordingly modify material properties and tailor new superconductors from scratch. Already in 1979, F. Steglich et al. reported superconductivity in the heavy-fermion compound $CeCu_2Si_2$ which, unlike all previous superconductors, exhibited strong magnetic many-body interactions [40]. In 1986, G. Bednorz and K. Müller discovered superconductivity in $Ba_xLa_{5-x}Cu_5O_{5(3-y)}$, an oxygen-deficient copper-oxide compound with a critical temperature of 30 K, by far the highest reported at the time [41]. This initiated research on copper-based, oxide compounds (cuprates) and other, in an attempt to discover superconductors with higher critical temperatures. A new field of high-temperature superconductivity was established and the objective of finding materials that are superconducting in room-temperature boosted motivation, owing to their extremely high application potential.

It soon became evident that the phonon-mediated electronic attraction picture was insufficient for describing these new superconductors. The term "unconventional superconductivity", which has been introduced in the 80's, is rather abstract and essentially categorizes all superconductors whose phenomenology is not consistent with the established BCS-framework. The main open question regarding such materials is their actual pairing mechanism.

Many unconventional superconductors, such as the cuprates and the iron-based family (pnictides), exhibit physical properties that vary widely as a function of charge carrier density. Scanning tunneling spectroscopy (STS) studies in cuprates and pnictides have revealed that in both families, competing orders coexist with superconductivity and that the sign of the order parameter changes at different parts of the Fermi surface [42]. One of the main mysteries is the rise of a pseudogap phase in the underdoped superconducting regime of the phase diagram of the cuprates. For instance, the existence of a pseudogap phase in $Y_{0.8}Ca_{0.2}Ba_2Cu_3O_{7-\delta}$ has been exemplified in specific heat measurements. The specific heat coefficient γ is found to decrease already at a much higher temperature onset (T^*) than T_c at lower doping, in contradiction with the same measurements at higher doping [43]. Common compound families

whose members have exhibited unconventional character in their superconducting state, in addition to the cuprates (the high-temperature superconductors) and the pnictides (the iron-based compounds), are the heavy-fermions and the organic superconductors. These compound families are generally characterized by complex phase diagrams [44–50].

Figure 2.3 illustrates a representative phase diagram for the cuprates. At a particular range of carrier concentration (p-type carriers in this case), superconductivity emerges (blue dome). The pseudogap regime (above the underdoped superconducting side) is still debated in the community, as its experimental signatures are not clearly understood [51–53]. Among other techniques, tunneling spectroscopy has revealed signs of preformed Cooper-pairs therein, which persist up to very high temperatures.

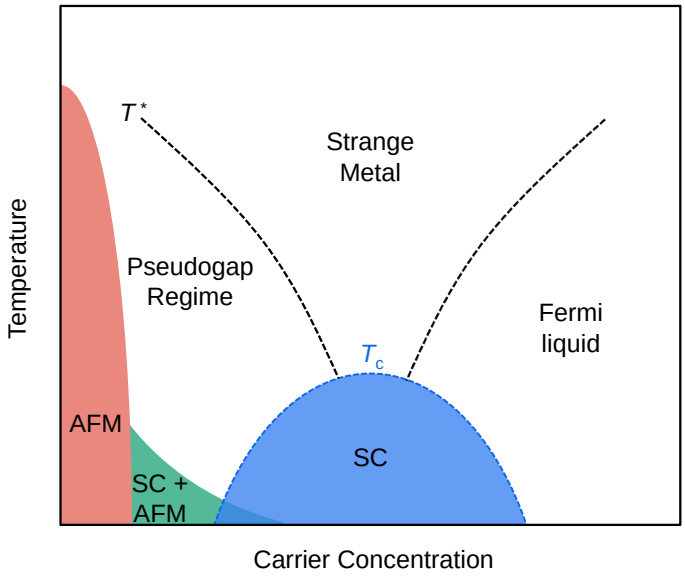

Figure 2.3: *Phase diagram of the copper-oxide superconductors. The superconducting dome (blue) is subdivided in three regions, with respect to the amount of doping: the optimally doped where* T_c *(dashed-blue line) is maximum, the underdoped for carrier concentrations less than the optimal doping and the overdoped for higher doping. In the red area, long-range antiferromagnetic (AFM) order exists. In the green, signatures of AFM and superconductivity coexist, as seen in many cuprate compounds. The normal state is also subdivided in the categories indicated, with different electronic behavior being exhibited in each. Note the temperature onset* T^* *of the pseudogap region. Reproduced from [54].*

At very low carrier concentrations, the cuprates' ground state exhibits anti-ferromagnetic order. It has been proposed that superconductivity often lies in the vicinity of an ordered state in the phase diagram (also for pnictides) [55]. Efforts undertaking the task of identifying the pairing mechanism of the superconducting ground state can partly explain some of the unusual features, but experiments always reveal contradictions [56]. One such is the Resonating Valence Bond (RVB) theory of P. W. Anderson [57, 58], still a controversial topic.

The ongoing research for new superconductors, as well as for understanding unconventional behavior, has yielded a huge number of superconducting compounds with exotic properties. Figure 2.4 presents a timeline for superconductivity from the beginning of the last century, tabulating compounds with respect to their critical temperature. The oxide superconductor $SrTiO_3$ (dark-yellow star in Fig. 2.4) was the predecessor of the high-temperature, copper-oxide superconductors. The superconductor with the highest T_c ever reported, the sulfur hydride system at 203 K, was discovered in 2015 [59]. This is astonishingly a BCS-superconductor, surpassing all known high-T_c materials, yet only under high pressure.

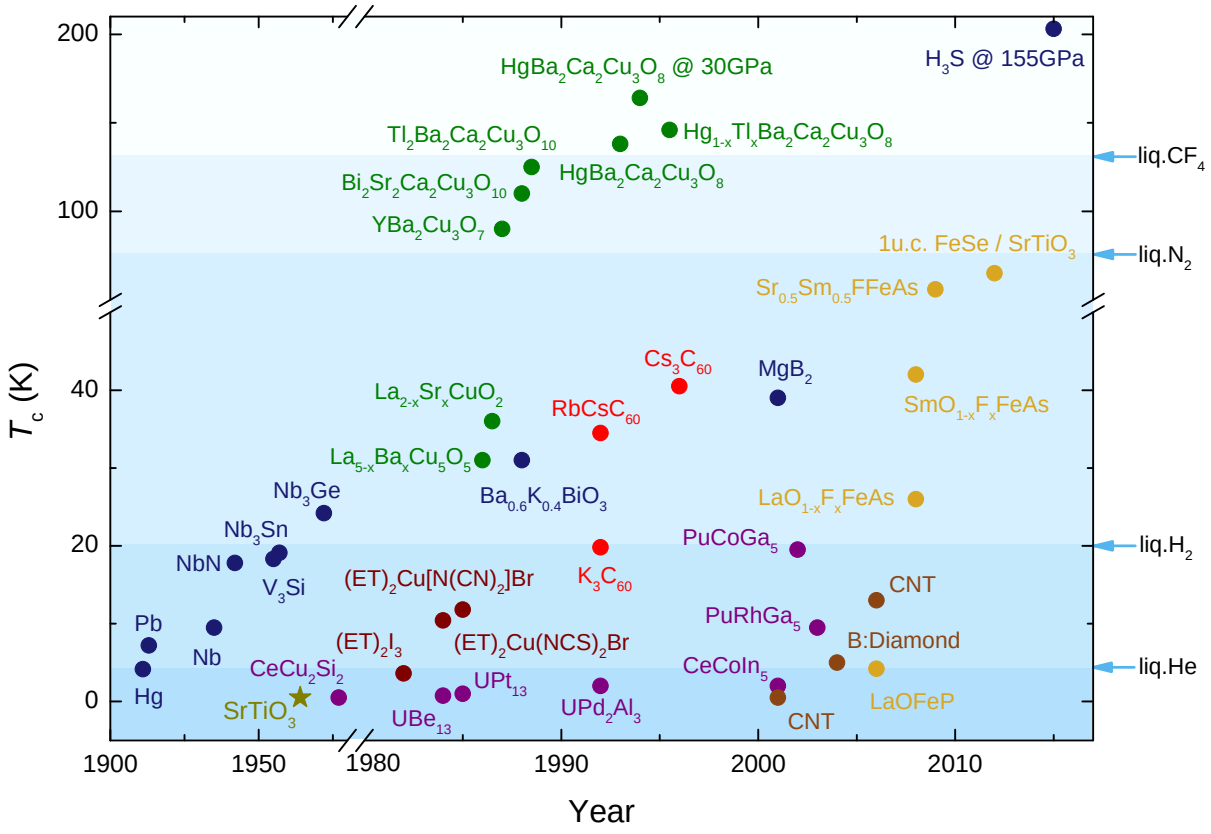

Figure 2.4: *The critical temperatures of representative compounds from important families of superconductors (in ambient pressure unless otherwise stated), listed with respect to year of discovery. The dark-blue points represent superconductors that are consistent with the BCS-framework, green points represent the cuprates and yellow points the iron-based superconductors (pnictides). Violet points stand for the heavy-fermion family, red for carbon-based superconductors and brown for carbon nano-tubes (CNT) and B-doped diamond. The dark-red points correspond to the 2D-(BEDT-TTF)$_2$X (or (ET)$_2$X) organic compounds, grown in the κ-phase [23]. The dark-yellow star, $SrTiO_3$ [60], the subject of this work, is also a BCS-superconductor. The T_c-value of the FeSe-monolayer on $SrTiO_3$ is taken from Ref. [61]. Note the breaks in the horizontal and vertical axes. The liquefaction temperatures of commonly used cryo-liquids are indicated by the blue arrows. The figure is a modification of Fig. 2.4 in Ref. [62].*

2.1.3 Superconductivity in Two Dimensions

In the cuprate family, superconductivity is mediated in the copper-oxide plane. These compounds consist of alternating stacks of CuO_2-building blocks with oxide-monolayers in between. For the first four monolayers, it is shown that with increasing number of CuO_2-planes per unit cell, the T_c increases [63]. Whether the dimension reduction accounts for the very high critical temperatures has been a subject of debate, with arguments against such hypothesis [64]. Lately a number of 2D systems have been reported to exhibit superconductivity. Some examples are the superconducting interface layer between La_2CuO_4 and $La_{1.55}Sr_{0.45}CuO_4$ [65], the 2D-organic BEDT-TTF salts [49, 66], the recently discovered FeSe superconducting monolayer grown on $SrTiO_3$ [61, 67] and the interface between $LaAlO_3$ and $SrTiO_3$ [68].

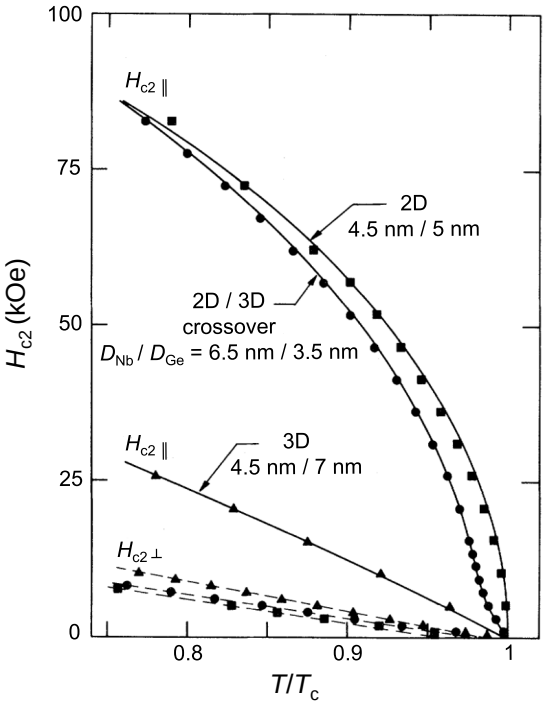

Figure 2.5: *Critical magnetic field dependencies on temperature (for fields perpendicular and parallel to the film-plane), for layered thin films of Nb and Ge. With constant Nb-thickness, the variation of Ge-film thickness alters the behavior of $H_{c2\|}(T)$, which transitions from strongly coupled 3D to decoupled 2D. From [70].*

The dimensional crossover of superconductivity has been studied in thin metallic films at low temperatures, by varying the film thickness. In Fig. 2.5, the superconducting critical field dependence on temperature of layered Nb/Ge films reveals a dimensional crossover from 3D to 2D, as the Ge thickness is increased. For Ge-thickness of 35 Å, the $H_{c\|}(T)$-dependence is 3D-like at $T \to T_c$ but rapidly switches to 2D as temperature decreases. An elaborate analysis of the layered structure effect on superconductivity is the Lawrence-Doniach model, which considers the difference in the effective mass between in-plane and out-of-plane direction. More information can be found in Refs. [21, 69].

A superconducting film is considered two-dimensional if its thickness is lower than the superconducting coherence length ξ. In the 2D-limit, transport properties of thin superconducting films are studied with respect to disorder, a parameter that can entirely suppress superconductivity. Interesting physics emerges at the transition of a superconducting phase to an insulating (SIT). The first SIT experiments were performed by I. Shalnikov in 1938, who studied thin films of Pb and Sn and determined the critical current dependence on film thickness [71]. Detailed information about the SIT of thin films can be found in Ref. [72]. From a the-

oretical view, the BKT-framework [73–75] establishes the SIT as a quantum phase transition at $T = 0$, where vortices unbind at quantum criticality, as disorder increases [76, 77].

Two-dimensional films and electron gases offer novel application potential owing to their high integrability in electronic devices. Discovery of the $LaAlO_3/SrTiO_3$ 2DES, on which a superconductor-to-insulator transition (SIT) can be tuned by an electric gate-field [78] is a relatively recent example.

2.2 Tunneling Spectroscopy

The tunneling effect, a quantum-mechanical process, refers to the propagation probability of an electron with energy E, from one classically allowed regime of potential energy $V < E$ to another, through a classically forbidden regime for which $V > E$. In more rigorous terms, the electron wavefunction ψ^2 inside this forbidden regime (barrier) maintains a finite value that decreases exponentially with increasing barrier thickness. The first theoretical framework for quantum tunneling was proposed by G. Gamow in 1928, in his attempt to understand alpha-radioactivity [79, 80]. It soon became evident that such concept is universal and essentially present in all physical systems.

For what concerns the field of condensed matter physics, when two conducting (metallic) materials are brought in direct proximity, with only a tiny insulating barrier (order of a few nm) in-between, net electron propagation can accordingly occur from one to the other, as long there's finite potential difference across this metal-insulator-metal junction [81]. Such barriers can be for instance thin insulating layers, grain boundaries, Schottky barriers, or even vacuum.

2.2.1 Inelastic Tunneling

Inelastic electron tunneling spectroscopy (IETS) has been established as a powerful tool for resolving electronic transitions or vibrational spectra of molecules, in tunneling junctions with metals separated by a classically forbidden region (barrier) [82]. The term inelastic refers to the case where the tunneling electron transfers part of its energy onto the lattice or any kind of impurity that is present, through scattering. Conversely, during elastic tunneling, the electronic energy transfer when scattering is zero. As will be later discussed, the latter is also exclusive at a small energy range around the chemical potential of tunnel junctions, a condition that allows the study of superconductivity [83].

Figure 2.6 depicts the two tunneling channels in a qualitative schematic. Finite bias across a tunnel junction of two metals misaligns their chemical potentials (μ_i). Provided the barrier is thin enough, the electronic wave-functions of the two metals overlap therein, leading to net electron-transfer that restores the equilibrium of μ_i (noted as $E_{F,i}$ in Fig. 2.6, at $T = 0$). Most electrons do not lose energy during tunneling and the elastic channel is the dominant contribution of the total tunneling current [84, 85]. The inelastic component (green arrow) involves finite energy transfer and depends on material properties (phonons, embedded molecular adsorbates, etc.). This channel is a useful probe for studying interface states or phonon modes, as will be seen in Ch. 4 and 5. The current (I) dependence of the elastic channel on applied bias (V) is linear. Assuming the existence of one inelastic channel (i.e. tunneling is assisted by a lattice-phonon of characteristic energy eV_{ph}), the current dependence is still linear but with a slope change at bias V_{ph}. This change induces a step-increase on the first and a peak on the second derivative of the I-dependence, all at an energy eV_{ph} that corresponds to the energy loss through the inelastic process.

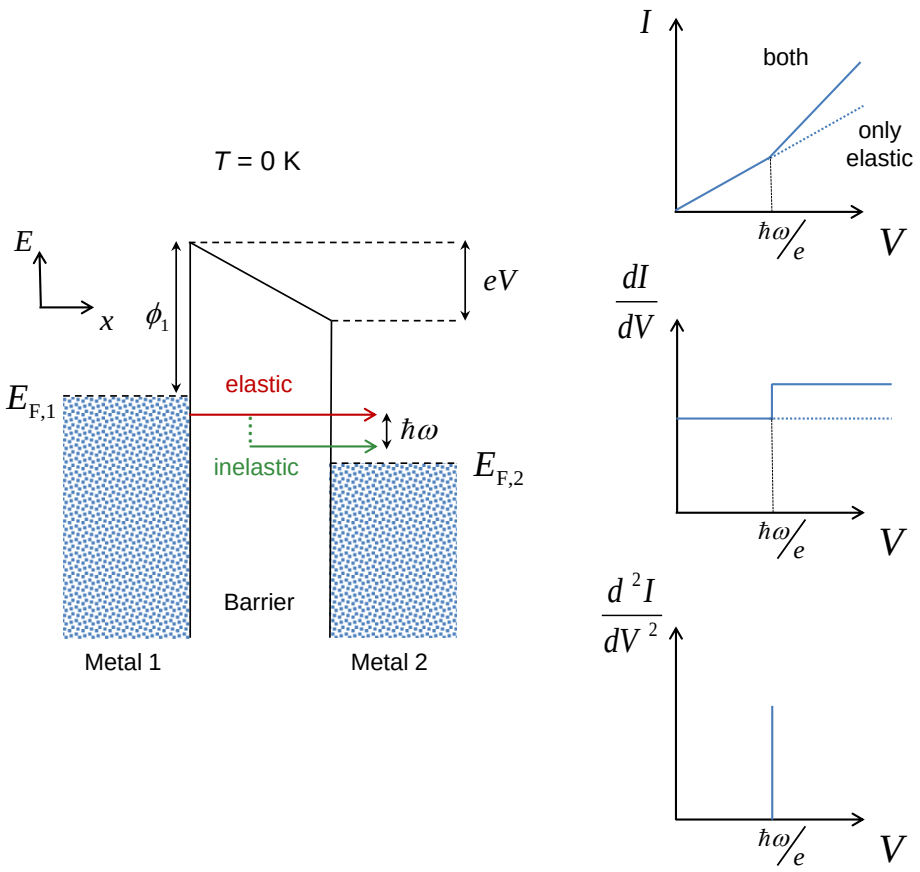

Figure 2.6: *A tunnel junction consisting of two metals and an insulating barrier at zero temperature, is illustrated on the left. Application of bias V across the junction shifts the Fermi level of metal 1 with respect to metal 2 and thereby net electron tunneling occurs. Tunneling channels are of two types: elastic (red) and inelastic (green).* $E_{F,1}$ *and* $E_{F,2}$ *are respectively the Fermi levels of the two metals,* ϕ_1 *is the work function of metal 1 and the quantity "*$\hbar\omega$*" is the electronic energy loss through the inelastic channel. On the right, the I,* dI/dV *and* d^2I/dV^2 *dependencies on applied bias V are illustrated, with (solid lines) and without the inelastic channel (dotted lines). The latter shows peaks (in reality of finite width) at energies that correspond to losses through inelastic processes (e.g. due to phonon scattering).*

The advantage of IETS with respect to other techniques such as Infrared, Raman and Electron Energy-Loss Spectroscopy, is the high spectral resolution that enables the accurate identification of phonon peaks and molecular vibrations. Lambe et al. have calculated the resolving power of IETS [82], yielding a fundamental limitation of $5.4\times k_B T$, in addition to broadening contributions from finite voltage-modulation that originates from the instrument [86,87]. Measuring in low temperatures improves the spectral resolution of IETS, as the line-width at half maximum ranges from approximately 100 meV at ambient temperature (experimentally non-practical), to less than a meV at the base temperature of a dilution refrigerator.

All the above describe the case of a tunnel junction that consists of two metallic electrodes, with constant DOS at the Fermi energy. The picture is different when one (or both) of the electrodes is a semiconductor [88] or a superconductor [24]. The next sections will briefly introduce the cases of metal-semiconductor junction or Schottky junctions, metal-insulator-superconductor (MIS) and superconductor-normal-superconductor junctions (SNS) [89].

2.2.2 The Metal-Semiconductor Junction

When metals and semiconductors are brought in contact, tunnel junctions can be created without an insulating layer in-between. This is a Schottky junction in which the high potential region (Schottky barrier) results from electron transfer from the semiconductor to the metal at thermal equilibrium [88, 90, 91]. The height of the Schottky barrier ideally equals the difference of the metallic work function and the semiconductor's electron affinity. Yet, electronic states that exist in the band gap of the semiconductor can also play a role, by pinning of the Fermi level. Upon contact, the chemical potential of the semiconductor matches that of the metal, with electrons transferring into the metallic side of the interface. This results in an excess of negative charge. The depleted or positively charged region in the semiconductor has a finite width W.

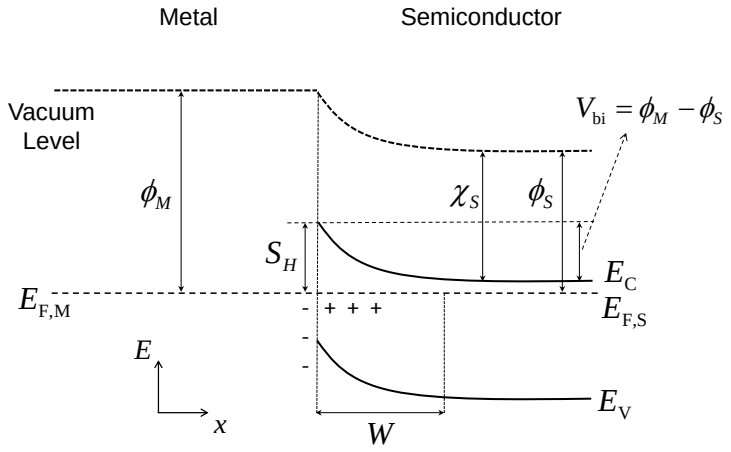

Figure 2.7: *The energy-band diagram across a Schottky junction at thermal equilibrium. Upon contact, the Fermi level $E_{F,S}$ of the semiconductor equals that of the metal ($E_{F,M}$). As a result, electrons accumulate at the metallic side of the interface while a positively charged region extends into the semiconductor, to a distance W. E_V and E_C are respectively the valence and conduction bands of the semiconductor, ϕ_S and χ_S the work function and electron affinity and ϕ_M is the metal work function. The quantity S_H is the height of the Schottky barrier at the interface. V_{bi} is the built-in potential due to work-function difference.*

Figure 2.7 illustrates a Schottky junction in thermal equilibrium, between a metal and an n-doped

semiconductor, with the metallic work function higher than that of the semiconductor. As the Fermi levels match, a position-dependent electrostatic potential emerges at the interface. Since the vacuum level is continuous, the Schottky barrier at the interface amounts to:

$$S_{\mathrm{H}} = \phi_{\mathrm{M}} - X_{\mathrm{S}} \tag{2.8}$$

Tunneling through Schottky barriers allows the determination of the chemical potential of semiconductors and identification of phonon modes, as in the case of $SrTiO_3$ [92, 93]. Typically, the built-in potential V_{bi} is determined by capacitance measurements [88]. By using tunnel spectroscopy, the difference between conduction band and chemical potential (Fermi degeneracy) can be quantified and thus the Schottky barrier height can be directly determined.

Next, the case of a heavily doped semiconductor is considered. In tunneling experiments this ensures that the applied voltage drops across the depletion region [90]. Figure 2.8 illustrates the effect of applied bias across a Schottky junction with a heavily n-doped semiconductor, at $T = 0$:

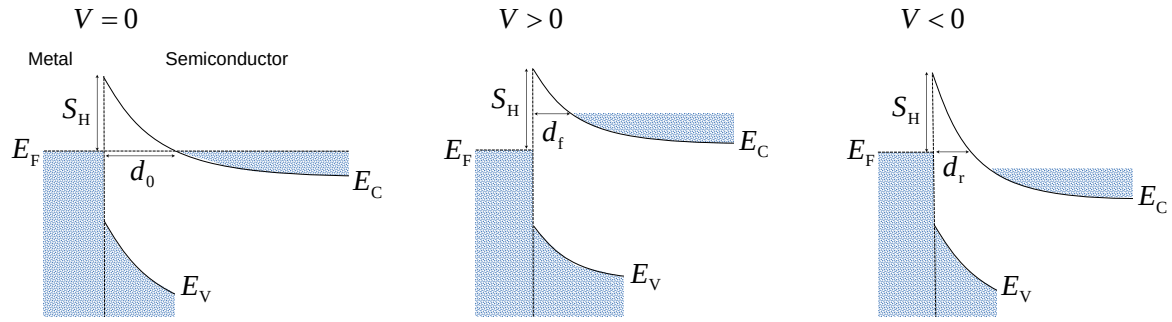

Figure 2.8: *A Schottky barrier between a heavily n-doped semiconductor at thermal equilibrium is shown on the left. In the middle, the application of forward bias across the junction reduces the barrier, as seen from the semiconductor. The case of reverse bias application is shown on the right, where the barrier increases. The Schottky barrier height S_{H} (measured from the metallic E_{F}) is constant in all cases. The quantities d_0, d_{f} and d_{r} are the barrier thickness for zero, forward and reverse bias application, respectively. Modified from Fig.1 of [94].*

On the left, the chemical potentials are aligned in thermal equilibrium. The difference with Fig. 2.7 is that the bottom of the conduction band is energetically lower than the Fermi level. The semiconductor is sufficiently doped to lie in the metallic side of the Mott transition, as the chemical potential lies above the bottom of the conduction band at equilibrium. In the middle, forward bias raises the chemical potential of the semiconductor with respect to the metal and thereby the barrier thickness d_{f} reduces with respect to d_0 of the zero bias case. On the right, reverse bias reduces the chemical potential and the barrier

thickness d_r is again reduced. It is evident that the Schottky barrier thickness is maximum at $V = 0$.

Assuming uniform doping concentration, the electrostatic potential in the depleted region of width W can be estimated [90, 94]:

$$U(x) = \frac{e^2 N_D (W-x)^2}{2\varepsilon} + eV - \mu_0 \tag{2.9}$$

In the above expression, x is measured from the interface and extends towards the semiconductor, while $0 < x < W$. N_D is the donor concentration, ε the dielectric constant and μ_0 the chemical potential (or Fermi degeneracy) of the semiconductor when $V = 0$. In addition to U, also the barrier width W depends on bias V:

$$W = \left[\frac{2\varepsilon (S_H + \mu_0 - V)}{eN_D} + eV - \mu_0 \right]^{1/2} \tag{2.10}$$

2.2.3 The Metal-Insulator-Superconductor Junction

The electron tunneling between two metals has been discussed in the beginning of the section. When a metal is superconducting at low temperatures, the tunneling characteristic differs from Fig. 2.6, for $0 < T < T_c$. The energy scale of the superconducting gap Δ is typically small (often in the order of $k_B T_c$), thus inelastic scattering processes from phonons become irrelevant. Due to the gap-opening at the DOS, the tunneling current dependence on applied bias is not linear for energies eV of the order of Δ.

Figure 2.9 demonstrates the influence of superconductivity on the $I-V$ characteristics. A superconducting gap of magnitude 2Δ appears at the density of states of the superconductor around the Fermi energy, at temperatures below T_c. At $T = 0$, the current dependence on applied bias drops to zero at a finite value $e|V| = \Delta$. For $T \neq 0$ and below T_c, thermally excited carriers in the superconductor occupy available states at energies $E \geq E_{F,S} + \Delta$ and the net tunneling current is finite for $V \neq 0$. This dependence is shown on the right diagram in Fig. 2.9.

The characteristic density of states of the superconductor, normalized to the normal state value of dI/dV, has the form [24]:

$$N(E) = \mathrm{Re}\left\{ \frac{|\mathrm{E}|}{(\mathrm{E}^2 - \Delta^2)^{1/2}} \right\} \tag{2.11}$$

E is measured from the Fermi level of the superconductor, Δ is the superconducting gap and $N(E)$ the DOS. Assuming that only one electrode is superconducting, the dependence of the conductance (dI/dV) on applied bias at $T \to 0$ is given by the expression [90, 95]:

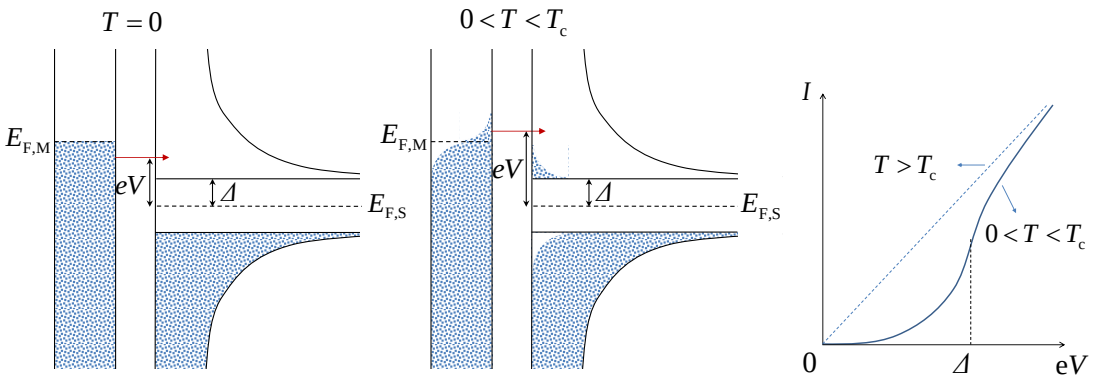

Figure 2.9: *The effect of a bias V applied across a tunnel junction between a metal and a superconductor.* $E_{\mathrm{F,M}}$ *and* $E_{\mathrm{F,S}}$ *are the Fermi energies of metal and superconductor, respectively. Blue shaded regions correspond to filled states while the empty (white) area within the lines are unoccupied, available states. At* $T = 0$ *(left diagram), a finite bias of magnitude* $e|V| > \Delta$ *results in (elastic) tunneling from the metal towards the superconductor (red arrow), through the insulating layer. The same holds for* $0 < T < T_{\mathrm{c}}$ *in the middle, where the electronic Fermi distribution broadens. As a result, the net tunneling current in the regime* $0 < e|V| < \Delta$ *is finite (diagram on the right). The dashed blue line is the* $I-V$ *dependence of the elastic channel for* $T > T_{\mathrm{c}}$.

$$\sigma = \int_{-\infty}^{\infty} N(E) \frac{-\partial f(E+eV)}{\partial V} dE \tag{2.12}$$

On this basis, tunneling measurements can be used to measure the DOS of superconductors. Studying more complex junctions, when both electrodes are superconducting, is also possible.

2.2.4 The Superconducting Tunnel Junction

When two superconducting materials are separated by a thin insulating barrier, the tunneling process (at $T \to 0$) is more complex [96].

Figure 2.10 shows the DOS of two superconductors in a tunnel junction, with their chemical potentials shifted by an external bias. Finite temperatures broaden the Fermi distribution function and available states above the Fermi level are partly occupied. Tunneling measurements are a good tool for determining the superconducting gaps from the $I-V$ characteristic. For two unequal gaps Δ_1 and Δ_2,

when V reaches $\frac{|\Delta_1 - \Delta_2|}{e}$, the tunneling current dependence shows a peak. At $\frac{\Delta_1 + \Delta_2}{e}$, the slope of I-dependence on energy eV is maximum.

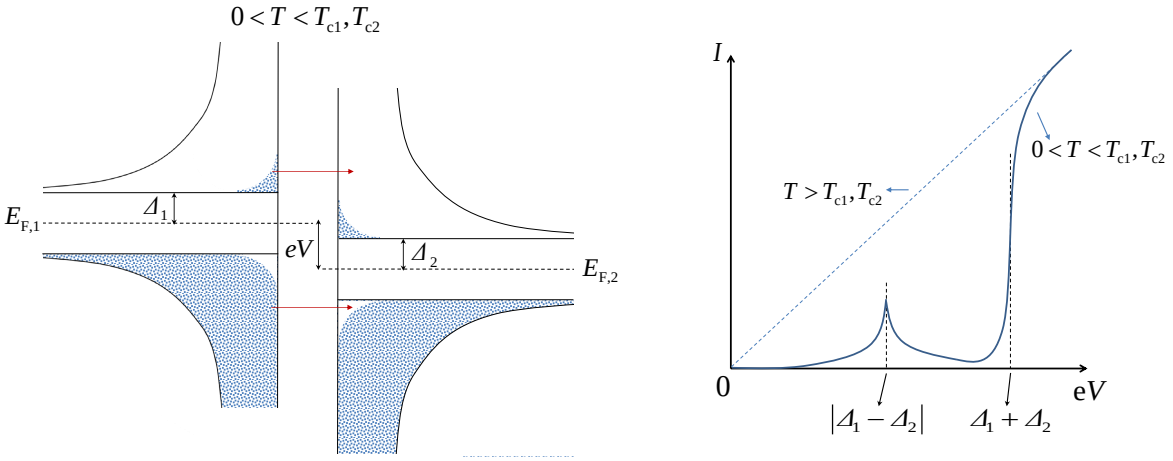

Figure 2.10: *Illustration of the tunneling process between two superconductors at low temperatures, with the respective dependence of the tunneling current I on energy eV. $E_{\mathrm{F,M}}$ and $E_{\mathrm{F,S}}$ are the Fermi energies of the superconductors and eV is their energy difference $|E_{\mathrm{F,M}} - E_{\mathrm{F,S}}|$. The red arrows on the left highlight net tunneling processes from filled states of the left into empty states of the right superconductor. The superconducting gap difference ($|\Delta_1 - \Delta_2|$) and sum ($\Delta_1 + \Delta_2$) can be determined by the features of the $I-V$ characteristic (right diagram). Modified from [21].*

The tunneling current dependence on bias V is given in Ref. [21]. The exact expression is of the form:

$$I_{ss} = \frac{G_{nn}}{e} \int_{-\infty}^{\infty} \frac{|E|}{[E^2 - \Delta_1^2]^{1/2}} \frac{|E + eV|}{[(E + eV)^2 - \Delta_2^2]^{1/2}} [f(E) - f(E + eV)] dE \tag{2.13}$$

Here, G_{nn} is the normal conductance value when $T > T_{c1}, T_{c2}$, $f(E)$ the Fermi distribution function, while the energy E is measured from the Fermi level of the junction at thermal equilibrium. Equation 2.13 implies that, at $T = 0$, with increasing bias V there is no net electronic tunneling current across the junction, until a minimum bias of $\frac{\Delta_1 + \Delta_2}{e}$ is reached. At this point, the DOS is infinite and yields a sharp discontinuous jump at the $I-V$ dependence towards the normal level. At $0 < T < T_{c1}, T_{c2}$, there is a negative dI/dV-region, at a bias range between $\frac{|\Delta_1 - \Delta_2|}{e}$ and $\frac{\Delta_1 + \Delta_2}{e}$, following a local maximum at $\frac{|\Delta_1 - \Delta_2|}{e}$.

In experiment, to accurately measure the peak location in the $I-V$, a voltage source is necessary to ensure stability of the measured tunneling current [21]. A current-source arrangement yields instabilities when measuring voltage signals, as Eq. 2.13 yields three voltage values as solutions for a given current.

2.3 The $LaAlO_3/SrTiO_3$ Interface Electron System

The pioneering work of A. Ohtomo and H.Y. Hwang in 2004 [68] has demonstrated the emergence of a two-dimensional electron system (2DES) at the interface between two band insulators of perovskite structure, the oxides $LaAlO_3$ and $SrTiO_3$. The latter has an indirect band gap of 3.25 eV [97] while $LaAlO_3$ exhibits a direct, broad-range energy band-gap from 5.6 to 6.5 eV [98–100]. $LaAlO_3$ and $SrTiO_3$ have similar lattice constants, respectively at 3.790 Å [101, 102] and 3.905 Å [103], thus construction of heterostructures with the two as building blocks is possible.

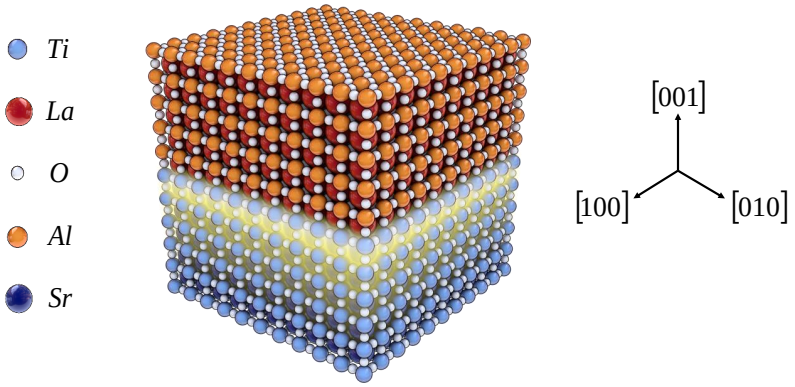

Figure 2.11: *Epitaxially grown $LaAlO_3$ on top of an $SrTiO_3$ substrate. The growth is along the [001] crystallographic direction. The 2DES emerges at the $SrTiO_3$ side, next to the interface (yellow shine). Modified from [104].*

In Fig. 2.11, an ideally grown heterostructure of $SrTiO_3$ and $LaAlO_3$ is shown, highlighting the emergent conducting interface. The 2D electron-system (2DES) extends about 10 nm into the $SrTiO_3$ substrate at low temperatures [105]. Typically, the $LaAlO_3$ layer is grown epitaxially by PLD on $SrTiO_3$-substrates (of [001]-orientation). A requirement for obtaining n-type conducting interfaces is a TiO_2-terminated $SrTiO_3$ substrate, because (SrO) or mixed terminations yield only insulating interfaces.

Soon after its discovery, the question regarding the origin of charge carriers that populate the interface of $LaAlO_3/SrTiO_3$ arose. The proposed scenario settles the polar discontinuity at the interface; that is the polar $LaAlO_3$ layer grown on-top of the non-polar $SrTiO_3$ substrate. Upon heteroepitaxy (and assuming $LaAlO_3$ is grown along the [001]-direction), the $(LaO)^+$ and $(AlO_2)^-$ monolayers have alternating net charges as opposed to the zero net charge of the (SrO) and (TiO_2) monolayers of the substrate. This polar discontinuity is compensated by electronic reconstruction [106], a mechanism illustrated in Fig. 2.12. The built-up of a finite electric field for each $LaAlO_3$ layer grown in the out-of-plane direction results in

a diverging electric potential V. Charge transfer of 0.5 electrons per unit lattice, from the surface to the TiO_2-monolayer at the interface, cancels the divergence out and the electric displacement is continuous.

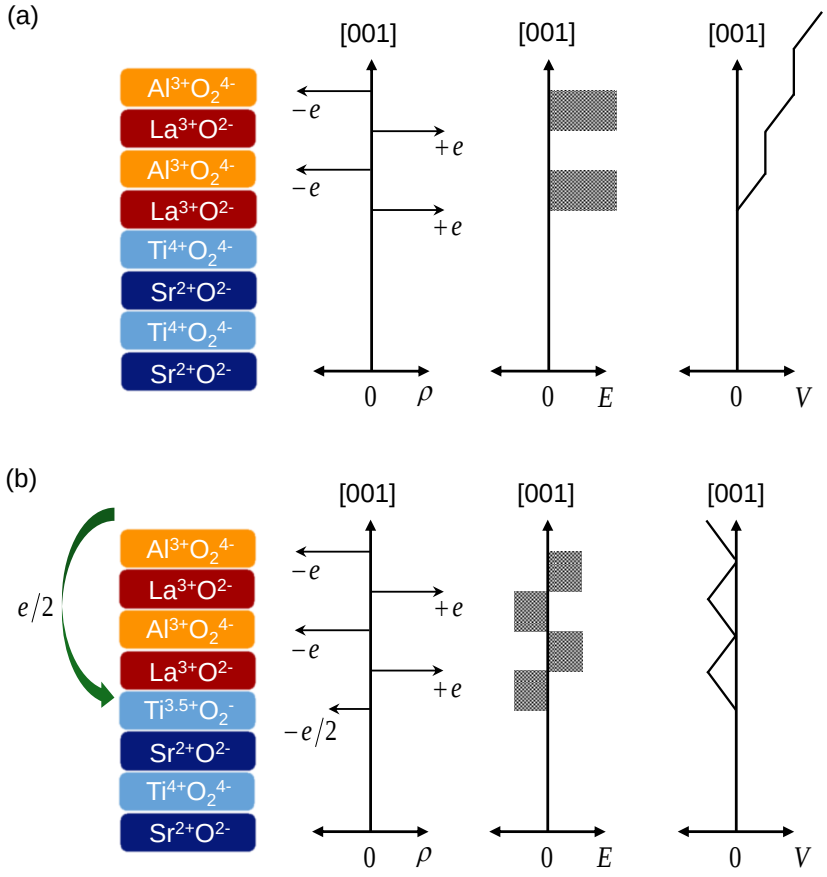

Figure 2.12: *(a) The monolayer-stacking across the interface in the absence of electronic reconstruction, where polar catastrophe is present. The alternating net charges $\pm\rho$ at the $LaAlO_3$ side give rise to a periodic electric field with positive average along the growth direction, which yields a diverging electric potential V. With more monolayers grown, the potential build-up increases. (b) The electronic reconstruction mechanism is shown, featuring the addition of extra 0.5 electrons per unit lattice, on the first TiO_2-monolayer at the interface. This settles the diverging electric potential shown in (a), with V now oscillating around a finite value. The electron transfer takes place from the topmost $(AlO_2)^-$ monolayer of the heterostructure (not shown). Reproduced from [107, 108].*

In parallel with the electronic reconstruction, additional contributions to the charge carrier density of the 2DES have been proposed. In work published by several groups it is claimed that O_2-vacancies contribute to conductivity [109–111], which originate from the $SrTiO_3$ substrate. Others have claimed intermixing of Sr and La atoms can also be a cause of the enhanced conductivity [112]. These effects may coexist as independent contributors, it is yet unlikely that reported carrier densities up to 10^{14}

cm^{-2} can be reached in the absence of reconstruction. Second harmonic generation (SHG) spectroscopy indeed supports this scenario, through measurements of the polarization profiles across $SrTiO_3$ substrates [113, 114]. On the other hand, conducting-AFM measurements have mapped out the 2DES-thickness of in-situ annealed and non-annealed samples and found differences in the conductivity values between the two. Thicknesses range from a few nanometers for the former, up to hundreds of micrometers for the latter [115]. A more complete picture with all aspects that concern the origin of charge carriers at the $LaAlO_3/SrTiO_3$ 2DES can be found in these reviews [116–118]. A recent work [119] supports that both contributions are simultaneously present on samples with crystalline $LaAlO_3$ grown on $SrTiO_3$ [001].

In 2006, S. Thiel et al. have demonstrated that, in addition to TiO_2-termination, the $LaAlO_3$ layer must be at least four unit-cells thick for the interface to be conducting [120]. A series of samples with $LaAlO_3$-thicknesses ranging from 0 to 15 u.c., grown at different temperatures, were measured. All samples with thickness $d \geq 4$ yielded conducting interfaces. Samples with 4 u.c. of $LaAlO_3$ were annealed for days and still sustained conducting interfaces, albeit with lower carrier densities than before. Since, the $LaAlO_3$-thickness threshold of four unit cells has been verified by a number of groups.

2.3.1 Superconductivity at the $LaAlO_3/SrTiO_3$ 2DEL

From the work of Reyren et al. in 2007 [121], the $LaAlO_3/SrTiO_3$ 2DES was found to be superconducting at temperatures below approximately 300 mK (see Fig. 2.13). This finding has guided numerous studies on understanding the properties of the superconducting ground state, in their vast majority by transport measurements [122–126], by tunneling spectroscopy [127–129] and also in theory [130–132].

The work of M. Breitschaft et al. combined scanning tunneling spectroscopy and DFT-calculations and has shown that electrons reside at the vicinity of the interface, trapped in potential wells formed by the TiO_6-octahedra [133]. These electrons exhibit strong correlations and thereby form a conducting electron system characterized as a two-dimensional electron-liquid (2DEL), which extends along the interface plane.

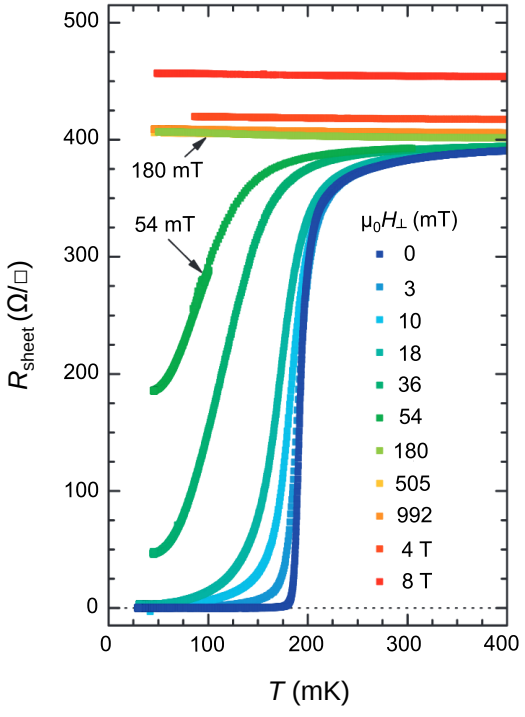

Figure 2.13: *The superconducting transition of a sample with 8 u.c. $LaAlO_3$. Superconductivity is destroyed at a critical magnetic field, in perpendicular orientation. From [121].*

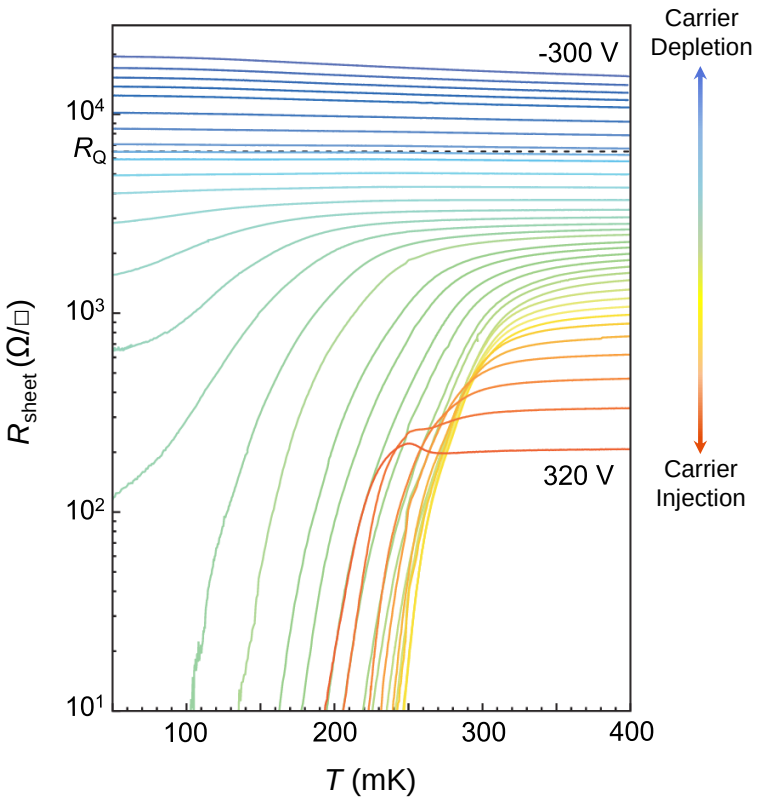

Figure 2.14: *The sheet resistance dependence on temperature, at 50 mK and at various gate voltages that correspond to different doping amount. The optimally doped region lies approximately at 100 V. From [122].*

Motivated by the work of S. Thiel, in 2008 Caviglia et al. [122] mapped out the superconducting dome of the $LaAlO_3/SrTiO_3$ 2DEL, by using the electric field effect [78] to reversibly tune the carrier density, and determined the critical temperature by transport measurements (Fig. 2.14). It was found that the 2DEL undergoes a quantum phase transition (QPT), from superconducting to insulating, at a gate-field of -140 V approximately, and that the superconducting transition is consistent with the BKT-behavior for 2D-systems [73–75]. In this particular sample, the critical temperature T_{BKT} near the QPT was found to scale with gate-field (δV) as: $T_{BKT} \propto (\delta V)^{zv}$, where the exponent zv was determined to be $2/3$. The 2D-nature of the superconducting $LaAlO_3/SrTiO_3$ 2DEL has been since extensively studied by several groups [123, 132, 134].

Transport measurements under perpendicular and parallel magnetic fields have revealed a large anisotropy of the in-plane and out-of-plane critical-field temperature dependence, from which the thickness of the superconducting 2DEL was determined to be approximately 10 nm [135]. The in-plane coherence length was determined to be 70 nm for a slightly overdoped sample with 4 u.c. $LaAlO_3$. In literature, it ranges from 40 nm to 200 nm and depends on doping as well as on the $LaAlO_3$-layer thickness [124, 136].

2.3.2 Interesting Phenomena at the $LaAlO_3/SrTiO_3$ 2DEL

The $LaAlO_3/SrTiO_3$ 2DEL is a system where fascinating physical phenomena are simultaneously manifested in reduced dimensions. In addition to superconductivity, the interface exhibits ferromagnetism, with the two coexisting at low temperatures [137–142]. In this highly correlated electron system, Rashba spin-orbit coupling (RSOC) has been reported [143, 144], while it is also argued that the spin-orbit interaction, with respect to carrier concentration, accounts for the Fermi surface reconstruction [145, 146]. Magneto-transport experiments have shown that the Rashba interaction rises steeply inside the superconducting dome, emerging at carrier densities near the quantum critical point of the SIT [147]. Due to the spin-orbit interaction, the potential existence of Majorana bound states at the 2DEL has been discussed [148, 149]. Recent information about all exciting physics of the $LaAlO_3/SrTiO_3$ electron system can be found in these reviews [150, 151].

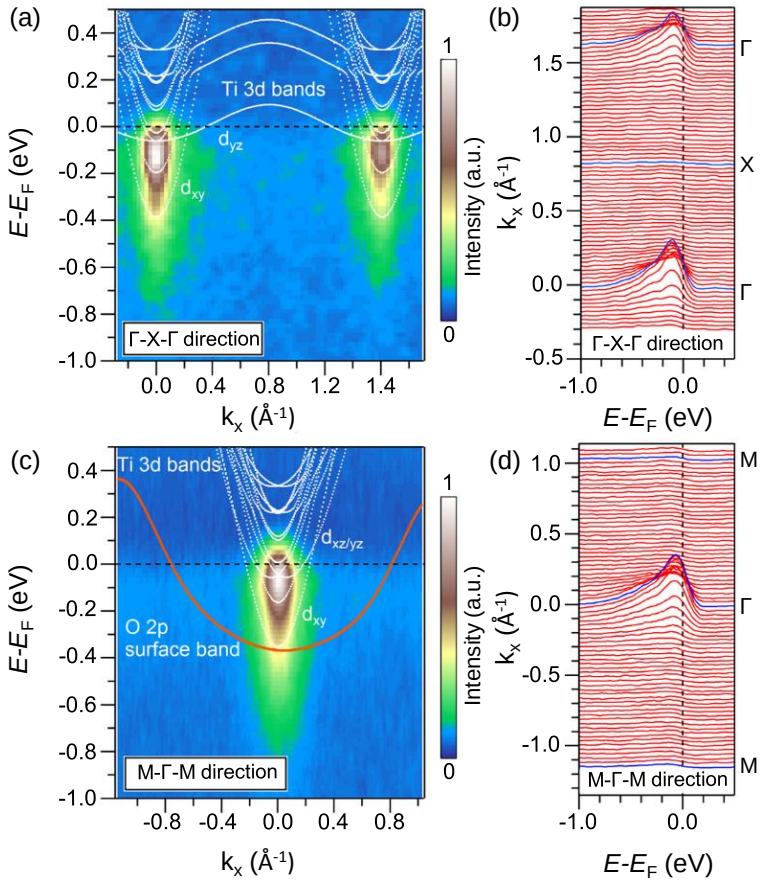

Figure 2.15: *SX-ResPES measurements and energy-band maps of the $LaAlO_3/SrTiO_3$ 2DES along the $\Gamma - X - \Gamma$ (a) and $M - \Gamma - M$ (c) directions with the electronic occupation shown by the intensity contours. The white and red lines are DFT-calculated band dispersions, using a GGA+U approximation. Respectively, (b) and (d) are energy distribution curves from (a) and (c). From [152].*

Density functional theory (DFT) calculations have revealed that electronic occupancy at the interface involves multiple subbands that coexist at the Γ-point [153, 154], while others have claimed that this multiple subband structure (where 2DEGs can be generated), is akin to $SrTiO_3$ and can manifest itself in other transition-metal oxides [155]. In the work of G. Berner et al., DFT calculations of the band structure of $LaAlO_3/SrTiO_3$ have been confirmed by soft x-ray, resonant photoelectron spectroscopy (SX-ResPES) [152]. Their results comparing theory and experiment are presented in Fig. 2.15.

The usage of $SrTiO_3$ substrates of [001]-orientation for growing $LaAlO_3/SrTiO_3$ samples is a common choice in the community. Yet, there are reports about emergent 2DEGs at interfaces with $LaAlO_3$ on $SrTiO_3$ of [110] and [111] orientations, or even with amorphous $LaAlO_3$ on $SrTiO_3$ [156, 157]. In the case of [110]-orientation, superconductivity is also present [158, 159].

In their recent work, G. Herranz et al. have mapped the energetic hierarchy between d_{xy} and the degenerate $d_{xz,yz}$ orbitals through electrostatic gating experiments [136]. $LaAlO_3$ was grown along the [001] and [110] crystallographic directions and it was found that this hierarchy is different for the two orientations. This must be considered in tunneling spectroscopy experiments, as the real-space extension of different orbitals can influence measurement since tunneling is essentially orbital-direction selective.

2.4 The Bulk, Doped-$SrTiO_3$ Crystal

Strontium titanate is a widely known perovskite oxide with large dielectric constant (of the order of 10^4) at low temperatures [160]. Its naturally occurring counterpart, tausonite, is an oxide mineral discovered in 1982 [161]; until then $SrTiO_3$ existed as a product entirely artificial. From early on, it was considered of high importance as a promising candidate for usage in modern electronics, particularly for very large scale integrated circuit (VLSI) devices and dynamic random access memories (DRAMs) [162–165], due to its high dielectric constant and has been therefore extensively studied. Its cubic structure undergoes a structural transition to tetragonal at approximately 105 K [166, 167]. At lower temperatures ($T_p \approx 37$ K), it transitions to a quantum paraelectric state [160, 168]. With an incipient ferroelectric character and thus a very high dielectric constant at liquid helium temperatures [169], it allows for electrostatic tuning of the $LaAlO_3/SrTiO_3$ 2DEL [120, 122].

Pure $SrTiO_3$ is a band insulator which can be doped with a variety of rare earth elements [170–173], so that both electronic and ionic conductivity are drastically increased. The type of doping depends on the oxidation level of the dopant with respect to the substituted ion at the $SrTiO_3$ lattice. An exception to the latter are the amphoteric Group III elements which may occupy either a Sr or a Ti site [174]. Typical single donors are for instance Al^{3+} and La^{3+} substituting on a Sr^{2+}-site, or Nb^{5+} and Ta^{5+} substituting on a Ti^{4+}-site. Similarly, single acceptors can be Fe^{3+} on a Ti^{4+}-site or Na^{1+} on a Sr^{2+}-site. Ion implantation is a common technique for doping an $SrTiO_3$ crystal.

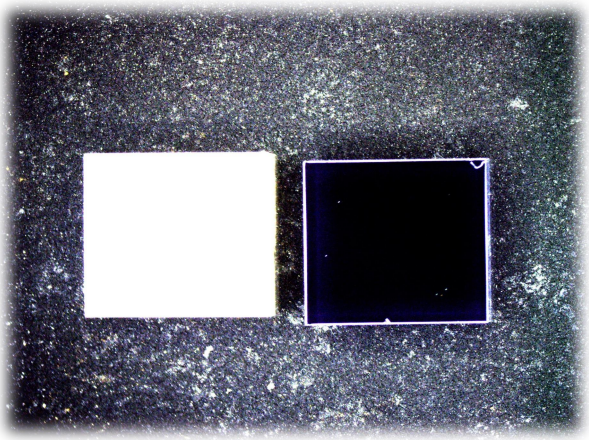

Figure 2.16: *A 5x5x1 mm undoped $SrTiO_3$-substrate (white) next to a 0.05 wt% Nb-doped $SrTiO_3$-substrate (black) (Crystec GmbH) on a glass plate, as seen through an optical microscope. The difference in their electrical and optical properties is (literally) black-and-white.*

In addition, it is also possible to electronically dope $SrTiO_3$ by O_2-reduction [175–178], either partly (on the surface) by cleaving in high vacuum, or completely, by annealing at high temperatures and low O_2-pressure. Removal of one O-atom renders two electrons free on the vacancy-site. Doping by this

method requires an a posteriori determination of the exact carrier concentration, which is typically done by Hall measurements.

By controlled doping, the carrier concentration of $SrTiO_3$ can be tuned within several orders of magnitude. Nb-doping as low as 0.05 wt% drastically changes the electronic and optical properties of $SrTiO_3$ (see Fig. 2.16) [178]. Donor-doping has been often preferred to O_2-reduction, especially for the study of thin films, because the dopant-concentration is more stable at temperatures higher than 100 ^{o}C [162]. Furthermore, doping over a large carrier concentration range (10^{17} to 10^{21} cm^{-3}) is better controlled by donor doping, with Nb being the most common single donor for $SrTiO_3$. On the other hand, it has been reported that O_2-reduction can provide semiconducting $SrTiO_3$ with carrier concentrations as low as 10^{15} cm^{-3} [163]. Such low electronic-concentration is not easy to obtain by ionic-substitution, as ion-donors are often rendered electrically inactive at small concentrations. This can be due to the presence of compensating-acceptors (impurities) whose electrical contribution can become relevant below a threshold dopant-concentration ($\approx$ 0.2 at% for Nb) [163].

Resistance measurements on doped $SrTiO_3$ reveal a Fermi-liquid behavior at low temperatures, i.e. a T^2-dependence over a wide doping range [179, 180]. This is an indication that electronic interactions are the main mechanism of scattering. Yet, the T^2-dependence of the resistivity is found to persist at very low carrier densities (the single-band regime) where the electron density is very low and the Fermi surface too small to allow for Umklapp events to occur [179]. It has been suggested that the T^2-dependence may be due to the polaronic nature of the quasi-particles [181] or the slightly anisotropic structure of the Fermi surface [182]. Interestingly, recent measurements have shown that the scattering rate is independent of the carrier density [180]; a behavior commonly featured in non-Fermi liquids.

2.4.1 $SrTiO_3$, the First Oxide Superconductor

In 1964, reduced $SrTiO_3$ was found to be superconducting [60]. Along with GeTe [183], they are the first semiconductors to ever exhibit superconductivity. Its doping-dependent T_c reaches 400 mK, a value close to the T_c of the $LaAlO_3/SrTiO_3$ 2DES. Interestingly, superconductivity is also present for carrier densities lower than 10^{18} cm^{-3}. The existence of a superconducting phase has been verified in measurements of the residual magnetization and critical field dependences on temperature, for reduced and Nb-doped $SrTiO_3$ samples, as well as in Hall measurements of the heat capacity down to 0.3 K (see Ref. [184]).

Since then, superconducting $SrTiO_3$ has been the subject of extensive research and its critical temperature has been determined by a number of groups. Figure 2.17 presents the T_c-dependence on carrier concentration n_s, as measured in a series of O_2-reduced and donor-doped $SrTiO_3$ samples [185]. The T_c dependence on n_s is maximum at approximately 10^{20} cm^{-3} and features a dome-shaped dependence [186], which is universal regardless of the method of doping [187].

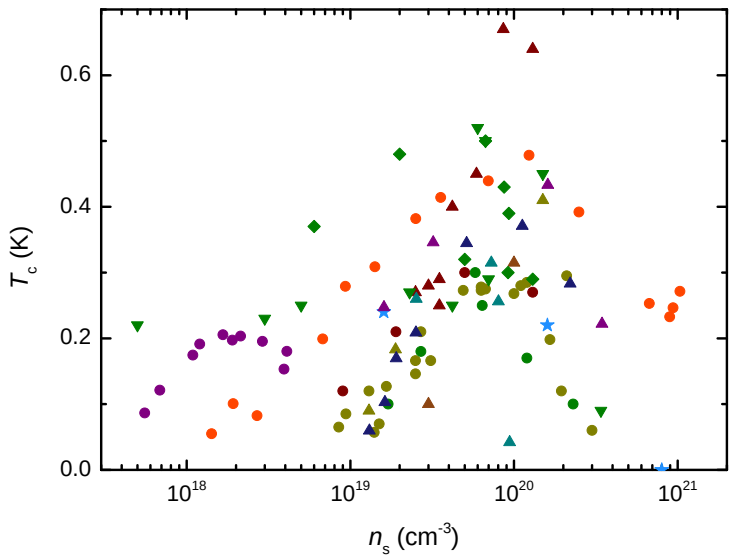

Figure 2.17: *Critical temperatures (T_c) of doped $SrTiO_3$ samples with respect to carrier concentration n_s. Each symbol type is assigned to a doping method: circles for O_2-reduced samples, triangles for Nb-doped, inverted triangles for Ba-doped, rhombi for Ca-doped and stars for La-doped. The colors in the graph indicate the origin of the data: green [188], dark yellow [189], dark red [190], violet [191], dark blue [192], light blue [187], brown [193], dark cyan [194] and orange [195].*

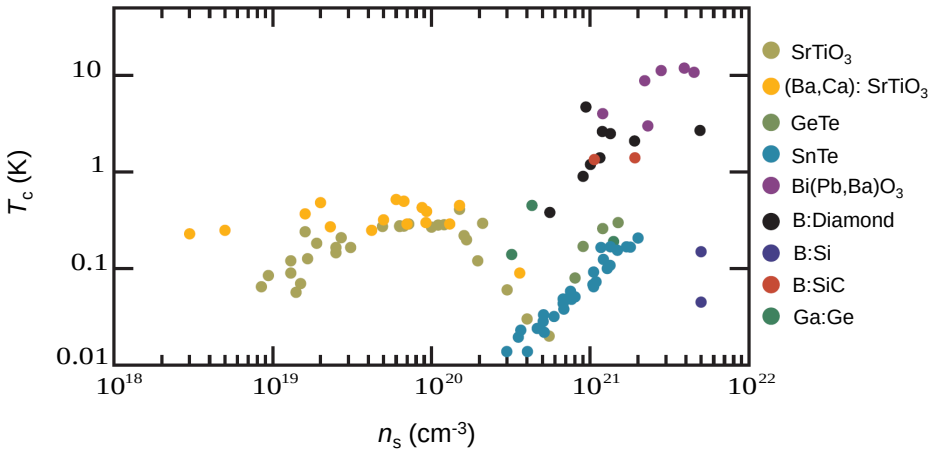

Figure 2.18: *The critical temperature dependence on carrier density for a variety of semiconductors. The data in the graph are from the following references: $SrTiO_3$ [187, 189], (Ba,Ca):$SrTiO_3$ [188], GeTe [183], SnTe [196], Ba(Pb,Bi)O_3 [197], B:Diamond [198–200], B:Si [201], B:SiC [202], Ga:Ge [203]. From [204].*

It is evident that superconductivity persists at very low carrier densities, as compared to other semiconductors and semi-metals that are also superconducting. Figure 2.18 presents a collective dataset of critical temperatures of superconducting semiconductors with respect to charge carrier density.

The Fermi surface of $SrTiO_3$ has been characterized as extremely small, of simple topology and barely anisotropic (see Refs. [182,205,206]). $SrTiO_3$ is also referred to as the most dilute superconductor [207]. The only known superconducting material at such low carrier densities is Bi, whose T_c is (very recently) reported to be below 1 mK at ambient pressure [208, 209]. Estimated values for the Debye temperature of $SrTiO_3$ vary; the lower estimate of 490 K [210] is higher than the reported T_c. Intriguingly, this estimate is also an order of magnitude higher than the Fermi temperature [207], a feature commonly seen in heavy-fermion compounds [211], but not in BCS-superconductors.

2.4.2 Multiband Superconductivity Studied by Tunneling

In 1980, experiments by G. Binnig et al. revealed two-band superconductivity in doped-$SrTiO_3$ [190]. Their explanation was based on a single-valley model for the conduction band (predicted by L. Mattheiss [212]), which can be replaced by a two-band (one heavy and one light band) model above a threshold carrier density of 10^{19} cm^{-3}. At this value, the Fermi level crosses the second electron-like band. As was later reported [181], this value coincides with the carrier density of the optimally doped region (maximum T_c) at the superconducting dome.

Tunneling measurements were performed in Nb-doped and also reduced-$SrTiO_3$ samples, using In as a second electrode, a common choice for tunneling on $SrTiO_3$ [92, 213], due to its relatively low work function. Owing to the emergence of Schottky barriers between metals and semiconductors, SIS junctions made of In and Nb-doped $SrTiO_3$ can be obtained at low temperatures (see previous section). As observed in Fig. 2.19, the tunneling spectra reveal two band gaps for $SrTiO_3$, both of which disappear at the critical temperature. This feature was only observed in highly doped samples and was attributed to the fact that the chemical potential resides well above the minimum of the second band.

In a separate work, Baratoff and Binnig showed that key ingredients to superconductivity are the two highest longitudinal optical phonon modes (LO3 and LO4) [214]. The doping density may drastically affect the electron-phonon coupling, as the electric field of the modes is screened by the charge carriers. It was hypothesized that low carrier densities allow stronger electron-phonon coupling. On this direction, S. Hayashi provided evidence that the coupling strength to the highest LO4 phonon mode is 2.5 times higher than to the LO3. He provided a quantitative analysis of the differential conductance $\mathrm{d}I/\mathrm{d}V(V)$ [93].

Henceforth, several groups have focused on investigating the superconducting phase of semiconducting $SrTiO_3$, with a few characteristic examples in [194,215–217]. Recently, by quantum oscillations measurements [191], X. Lin et al. have identified the two carrier concentration thresholds that correspond

to band-population onsets [181]. It was also found that as the second band is populated and $SrTiO_3$ enters the regime of two-band superconductivity, the strength of the electronic attraction decreases. Multiband signatures were also revealed by thermal conductivity measurements under magnetic fields [218].

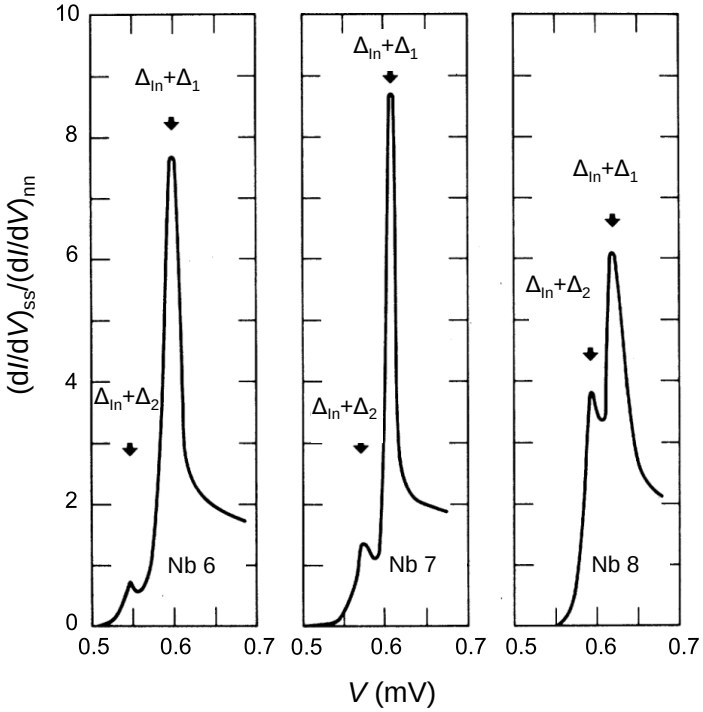

Figure 2.19: *A pronounced double superconducting gap feature in tunneling spectra from three tunnel junctions made of In and Nb-doped $SrTiO_3$. In this voltage range the two peaks are sums of the superconducting gap of In with each individual band gap of doped $SrTiO_3$. Each panel corresponds to a different sample, all of which are doped above the carrier concentration threshold for two-band superconductivity. The measurements are performed at 100 mK. From [190].*

In the last year, L. Gorkov has theoretically studied the superconducting mechanism of $SrTiO_3$ with respect to dopant concentration, and argued that the pairing interaction is assisted by several LO phonon modes with frequencies larger than E_F [219]. The doping method is also found to affect the dielectric constant and consequently pairing. The effect of plasma mediated pairing has been the research subject in the work of J. Ruhman et al., for samples with low carrier density [220]. Tunneling measurements in planar junction have been recently performed by Swartz et al. [221] and the electron-phonon coupling dependence on doping has been studied.

The potential link between 3D (bulk) and 2D ($LaAlO_3/SrTiO_3$ 2DEL) superconductivity has been partly addressed in theory and experiment [131, 155, 222]. The pairing mechanism and possible competing orders that destroy superconductivity in the underdoped and overdoped regimes, as well as the SIT at the quantum critical point, are issues not yet entirely understood.

References

[1] T. H. Levere: *Martinus van Marum: Life and Work*, v.1., p. 158-226, ed. by R.J. Forbes (Hollandsche Maatschappij der Wetenschappen), Haarlem, (1969).

[2] M. Faraday: *Experimental Researches in Chemistry and Physics*, p. 85-124, Taylor & Francis, London (1991).

[3] S. Reif-Acherman, Revisita Brasileira de Ensino de Fisica **33**, 2601 (2011).

[4] L. P. Cailletet, Comptes Rendus Hebdomadaires des Seances de l' Academie des Sciences **85**, 1213 (1877).

[5] R. Pictet, Comptes Rendus Hebdomadaires des Seances de l' Academie des Sciences **85**, 1214 (1877).

[6] D. van Delft and P. Kes, Phys. Today **63**, 38 (2010).

[7] P.-J.-C. Janssen, Comptes Rendus Hebdomadaires des Seances de l' Academie des Sciences **67**, 838 (1868).

[8] H. Kamerlingh-Onnes: *Through Measurement to Knowledge: The selected papers of Heike Kamerlingh Onnes 1853-1926*, ed. by K. Gavroglu and Y. Goudarolis, Kluwer, Dordrecht (1991).

[9] W. Buckel and R. Kleiner: *Superconductivity: Fundamentals and Applications*, 2nd Edition, WILEY-VCH Verlag GmbH & Co. KGaA, Weinheim, Germany (2004).

[10] W. Meissner and R. Ochsenfeld, *Ein neuer Effekt bei Eintritt der Supraleitfähigkeit*, Naturwissenschaften **21**, 787 (1933).

[11] C. J. Gorter and H. Casimir, Physica **1**, 306 (1934).

[12] C. J. Gorter and H. Casimir, Phyz. Z. **35**, 963 (1934).

[13] C. J. Gorter and H. Casimir, Z. Tech. Phys. **15**, 539 (1934).

[14] F. London and H. London, Proc. Roy. Soc. A **149**, 71 (1935).

[15] F. London and H. London, Physica **2**, 341 (1935).

[16] A. B. Pippard, Proc. Roy. Soc. A **203**, 210 (1950).

[17] A. B. Pippard, Proc. Camb. Phil. Soc. A **47**, 617 (1951).

[18] V. L. Ginzburg and L. D. Landau, J.E.T.P. USSR **20**, 2064 (1950).

[19] A. A. Abrikosov, Doklady Akademii Nauk SSSR **86**, 489 (1952).

[20] A. A. Abrikosov: *Type-II superconductors and the vortex lattice*, Nobel Prize lecture (2003).

[21] M. Tinkham *Introduction to Superconductivity*, 2nd Edition, Dover Publications Inc. Mineola, New York (1996).

[22] C. Enss and S. Hunklinger, *Low Temperature Physics*, Universität Heidelberg, Springer-Verlag Berlin, Heidelberg (2005).

[23] M. Dressel: *Lecture notes on Superconductivity*, University of Stuttgart 2011.

[24] J. Bardeen, L. N. Cooper and J. R. Schrieffer, Phys. Rev. **108**, 1175 (1957).

[25] I. Giaever and K. Megerle, Phys. Rev. **122**, 1101 (1961).

[26] E. Maxwell, Phys. Rev. **78**, 477 (1950).

[27] C. A. Reynolds, B. Serin, W. H. Wright and L. B. Nesbitt, Phys. Rev. **78**, 487 (1950).

[28] J. de Launay, Phys. Rev. **93**, 661 (1954).

[29] K. H. Bennemann and J. B. Ketterson: *The Physics of Superconductors Vol. I: Conventional and High-T_c Superconductors*, Springer-Verlag Berlin Heidelberg (2003).

[30] J. Klein, A. Leger, S. de Cheveigne, D. MacBride, C. Guinet, M. Belin and D. Defourneau, Solid State Commun. **33**, 1091 (1980).

[31] W. L. McMillan, Phys. Rev. **167**, 331 (1968).

[32] P. B. Allen and R. C. Dynes, Phys. Rev. B **12**, 905 (1975).

[33] P. Morel and P. W. Anderson, Phys. Rev. **125**, 1263 (1962).

[34] F. Marsiglio, J. Low Temp. Phys. **87**, 659 (1992).

[35] N. W. Ashcroft, Phys. Rev. Lett. **21**, 1748 (1968).

[36] J. M. McMahon, M. A. Morales, C. Pierleoni and D. M. Ceperley, Rev. Mod. Phys. **84**, 1607 (2012).

[37] I. I. Mazin and D. J. Singh, J. Phys. Chem. Sol. **59**, 2185 (1998).

[38] J. E. Hirsch, Phys. Rev. B **47**, 5351 (1993).

[39] A. Hamo, A. Benyamini, I. Shapir, I. Khivrich, J. Waissman, K. Kaasbjerg, Y. Oreg, F. von Oppen and S. Ilani, Nature **535**, 395 (2016).

[40] F. Steglich, J. Aarts, C. D. Bredl, W. Lieke, D. Meschede, W. Franz and H. Schäfer, Phys. Rev. Lett. **43**, 1892 (1979).

[41] J. G. Bednorz and K. A. Müller, Z. Phys. B: Cond. Matter **64**, 189 (1986).

[42] N.-C- Yeh, M. L. Teague, A. D. Bayer, B. Shen and H.-H. Wen, J. Phys. Conf. Ser. **400**, 022140 (2012).

[43] J. W. Loram, K. A. Mirza, J. R. Cooper and J. L. Tallon, Physica C **282**, 1405 (1997).

[44] D. C. Johnston, Adv. Phys. **59**, 803 (2010).

[45] J.-P. Paglione and R. L. Greene, Nature Phys. **6**, 645 (2010).

[46] I. I. Mazin, Nature **464**, 183 (2010).

[47] Y. Nakai, T. Iye, S. Kitagawa, K. Ishida, H. Ikeda, S. Kasahara, H. Shishido, T. Shibauchi, Y. Matsuda and T. Terashima, Phys. Rev. Lett. **105**, 107003 (2010).

[48] D. N. Basov and A. V. Chubukov, Nature Phys. **7**, 272 (2011).

[49] F. Kagawa, T. Itou, K. Miyagawa and K. Kanoda, Phys. Rev. B **69**, 064511 (2004).

[50] Y. Chen, W. B. Jiang, C. Y. Guo, F. Ronning, E. D. Bauer, T. Park, H. Q. Yuan, Z. Fisk, J. D. Thompson and X. Lu, Phys. Rev. Lett. **114**, 146403 (2015).

[51] N. F. Mott, Rev. Mod. Phys. **40**, 677 (1968).

[52] T. Kondo, R. Khasanov, T. Takeuchi, J. Schmalian and A. Kaminski, Nature **457**, 296 (2009).

[53] A. A. Kordyuk, Low Temp. Phys. **41**, 319 (2015).

[54] J. Orenstein and A. J. Millis, Science **288**, 468 (2000).

[55] W. Wu, J. Cheng, K. Matsubayashi, P. Kong, F. Lin, C. Jin, N. Wang, Y. Uwatoko and J. Luo, Nature Commun. **5**, 5508 (2014).

[56] A. J. Leggett, Nature Phys. **2**, 134 (2006).

[57] P. W. Anderson, Science **235**, 1196 (1986).

[58] P. W. Anderson, P. A. Lee, M. Randeria, T. M. Rice, N. Trivedi and F. C. Zhang, J. Phys. Cond. Matt. **16**, R755 (2004).

[59] A. P. Drozdov, M. I. Eremets, I. A. Troyan, V. Ksenofontov and S. I. Shylin, Nature **525**, 73 (2015).

[60] J. F. Schooley, W. R. Hosler and M. L. Cohen, Phys. Rev. Lett. **12**, 474 (1964).

[61] S. He, J. He, W. Zhang, L. Zhao, D. Liu, X. Liu, D. Mou, Y.-B. Ou, Q.-Y. Wang, Z. Li, L. Wang, Y. Peng, Y. Liu, C. Chen, L. Yu, G. Liu, X. Dong, J. Zhang, C. Chen, Z. Xu, X. Chen, X. Ma, Q. Xue and X. J. Zhou, Nature Mater. **12**, 605 (2013).

[62] P. J. Ray, MSc Thesis: *Structural Investigation of* $La_{2-x}Sr_xCuO_{4+y}$*: Following Staging as a Function of Temperature*, University of Copenhagen 2015.

[63] A. Schilling, M. Cantoni, J. D. Guo and H. R. Ott, Nature **363**, 56 (1993).

[64] E. S. Reich, Nature **501**, 474 (2013).

[65] A. Gozar, G. Logvenov, L. Fitting-Kourkoutis, A. T. Bollinger, L. A. Giannuzzi, D. A. Müller and I. Bozovic, Nature **455**, 782 (2008).

[66] F. Kagawa, K. Miyagawa and K. Kanoda, Nature Phys. **5**, 880 (2009).

[67] Q.-Y. Wang, Z. Li, W.-H. Zhang, Z.-C, Zhang, J.-S. Zhang, W. Li, H. Ding, Y.-B. Ou, P. Deng, K. Chang, J. Wen, K. He, J.-F. Jia, S.-H. Ji, Y.-Y. Wang, L.-L. Wang, X. Chen, X.-C. Ma, Q.-K. Xue, Chin. Phys. Lett. **29**, 037402 (2012).

[68] A. Ohtomo and H. Y. Hwang, Nature **427**, 423 (2004).

[69] W. E. Lawrence and S. Doniach: *Theory of layer structure superconductors*, E. Kanda ed., Academic Press of Japan, Kyoto (1971).

[70] S. T. Ruggiero, T. W. Barbee Jr., and M. R. Beasley, Phys. Rev. Lett. **45**, 1299 (1980).

[71] A. I. Shalnikov, Nature **142**, 74 (1938).

[72] A. M. Goldman and N. Markovic, Phys. Today **51**, 39 (1998).

[73] V. L. Berezinskii, Sov. Phys. JETP **32**, 493 (1971).

[74] V. L. Berezinskii, Sov. Phys. JETP **34**, 610 (1972).

[75] J. M. Kosterlitz and D. J. Thouless, J. Phys. C: Solid State Phys. **6**, 1181 (1973).

[76] B. I. Halperin and D. R. Nelson, J. Low Temp. Phys. **36**, 599 (1979).

[77] S. Doniach and B. A. Huberman, Phys. Rev. Lett. **42**, 1169 (1979).

[78] J. Mannhart, J. G. Bednorz, K. A. Mueller and D. G. Schlom, Z. Phys. B **83**, 307 (1991).

[79] G. Gamow, Nature **122**, 805 (1928).

[80] G. Gamow, Z. Phys. **51**, 204 (1928).

[81] J. C. Fischer and I. Giaever, J. Appl. Phys. **32**, 172 (1961).

[82] J. Lambe and R. C. Jaklevic, Phys. Rev. **165**, 821 (1968).

[83] J. Nicol, S. Shapiro and P. H. Smith, Phys. Rev. Lett. **5**, 461 (1960).

[84] K. W. Hipps and U. Mazur, *Inelastic Electron Tunneling Spectroscopy, Handbook of Vibrational Spectroscopy*, John Wiley & Sons Ltd, Chichester (2002).

[85] S. K. Khanna and J. Lambe, Science **220**, 1345 (1983).

[86] J. Klein, A. Leger, M. Belin, D. Defourneau and M. J. L. Sangster, Phys. Rev. B **7**, 2336 (1973).

[87] M. A. Reed, Materials Today **11**, 46-50 (2008).

[88] S. M. Sze, *Semiconductor Devices: Physics and Technology*, John Wiley and Sons, New York (1985).

[89] B. D. Josephson, Phys. Lett. **1**, 251 (1962).

[90] E. L. Wolf, *Principles of Electron Tunneling Spectroscopy*, 2nd Edition, Oxford University Press, New York (2012).

[91] R. Dalven, *Introduction to Applied Solid State Physics*, 2nd Edition, Plenum Press, New York and London (1990).

[92] Z. Sroubek, Solid State Commun. **7**, 1561 (1969).

[93] S. Hayashi, J. Phys. Soc. Jpn. **53**, 2350 (1984).

[94] J. W. Conley, C. B. Duke, G. D. Mahan and J. J. Tiemann, Phys. Rev. **150**, 466 (1966).

[95] I. Giaever, Phys. Rev. Lett. **5**, 147 (1960).

[96] I. Giaever, Phys. Rev. Lett. **5**, 464 (1960).

[97] K. van Benthem, C. Elsässer and R. H. French, J. Appl. Phys. **90**, 6156 (2001).

[98] S.-G. Lim, S. Kriventsov, T. N. Jackson, J. H. Haeni, D. G. Schlom, A. M. Balbashov, R. Uecker, P. Reiche, J. L. Freeouf and G. Lucovsky, J. Appl. Phys. **91**, 4500 (2002).

[99] L. F. Edge, D. G. Schlom, S. A. Chambers, E. Cicerelly, J. L. Freeouf, B. Hollander and J. Schubert, Appl. Phys. Lett. **84**, 726 (2004).

[100] Y. Y. Mi, Z. Yu, S. J. Wang, P. C. Lim, Y. L. Foo, A. C. H. Huan and C. K. Ong, Appl. Phys. Lett **90**, 181925 (2007).

[101] S. Geller and V. B. Bala, Acta Cryst. **9**, 1019 (1956).

[102] S. A. Hayward, F. D. Morrison, S. A. T. Redfern, E. K. H. Salje, J. F. Scott, K. S. Knight, S. Tarantino, A. M. Glazer, V. Shuvaeva, P. Daniel, M. Zhang and M. A. Carpenter, Phys. Rev. B **72**, 054110 (2005).

[103] J. G. Bednorz and H. J. Scheel, J. Crystal Growth **41**, 5 (1977).

[104] J. Zabaleta, V. S. Borisov, R. Wanke, H. O. Jeschke, S. C. Parks, B. Baum, A. Teker, T. Harada, K. Syassen, T. Kopp, N. Pavlenko, R. Valenti and J. Mannhart, Phys. Rev. B **93**, 235117 (2016).

[105] Z. Huang, X. Renshaw Wang, Z. Q. Liu, W. M. Liu, S. W. Zeng, A. Annadi, W. L. Tan, X. P. Qiu, Y. L. Zhao, M. Salluzo, J. M. D. Coey, T. Venkatesan and Ariando, Phys. Rev. B **88**, 161107(R) (2013).

[106] R. Hesper, L. H. Tieng, A. Heeres and G. A. Sawatzky, Phys. Rev. B **62**, 16046 (2000).

[107] N. Nakagawa, H. Y. Hwang and D. A. Muller, Nature Mater. **5**, 204 (2006).

[108] C. Richter PhD Thesis: *Experimental Investigation of Electronic and Magnetic Properties of $LaAlO_3$-$SrTiO_3$ Interfaces*, University of Augsburg 2012.

[109] A. Kalabukhov, R. Gunnarson, J. Börjesson, E. Olsson, T. Claeson and D. Winkler, Phys. Rev. B **75**, 121404(R) (2007).

[110] W. Siemons, G. Koster, H. Yamamoto, W. A. Harrison, G. Lucovsky, T. H. Geballe, D. H. A. Blank and M. R. Beasley, Phys. Rev. Lett. **98**, 196802 (2007).

[111] G. Herranz, M. Basletic, M. Bibes, C. Carretero, E. Tafra, E. Jacquet, K. Bouzehouane, C. Deranlot, A. Hamzic, J.-M. Broto, A. Barthelemy and A. Fert, Phys. Rev. Lett. **98**, 216803 (2007).

[112] P. R. Willmott, S. A. Pauli, R. Herger, C. M. Schlepütz, D. Martoccia, B. D. Patterson, B. Delley, R. Clarke, D. Kumah, C. Cionca and Y. Yacoby, Phys. Rev. Lett **99**, 155502 (2007).

[113] A. Rubano, T. Günter, T. Fink, D. Paparo, L. Marrucci, C. Cancellieri, S. Gariglio, J.-M. Triscone and M. Fiebig, Phys. Rev. B **88**, 035405 (2013).

[114] A. Savoia, D. Paparo, P. Perna, Z. Ristic, M. Salluzzo, F. Miletto Granozio, U. Scotti di Uccio, C. Richter, S. Thiel, J. Mannhart and L. Marrucci, Phys. Rev. **80**, 075110 (2009).

[115] M. Basletic, J.-L. Maurice, C. Carretero, G. Herranz, O. Copie, M. Bibes, E. Jacquet, K. Bouzehouane, S. Fusil and A. Barthelemy, Nature Mater. **7**, 621 (2008).

[116] S. A. Pauli and P. R. Willmott, J. Phys. Cond. Matter **20**, 264012 (2008).

[117] M. Huijben, A. Brinkman, G. Koster, G. Rijnders, H. Hilgenkamp and D. H. A. Blank, Adv. Mater. **21**, 1665 (2009).

[118] J. Pereiro, A. Petrovic, C. Panagopoulos and I. Bozovic, Phys. Express **1**, 208 (2011).

[119] Z. Q. Liu, C. J. Li, W. M. Lü, X. H. Huang, Z. Huang, S. W. Zeng, X. P. Qiu, L. S. Huang, A. Annadi, J. S. Chen, J. M. D. Coey, T. Venkatesan and Ariando, Phys. Rev. X **3**, 021010 (2013).

[120] S. Thiel, G. Hammerl, A. Schmehl, C. W. Schneider and J. Mannhart, Science **313**, 1942 (2006).

[121] N. Reyren, S. Thiel, A. D. Caviglia, L. F. Kourkoutis, G. Hammerl, C. Richter, C. W. Schneider, T. Kopp, A.-S. Ruetschi, D. Jaccard, M. Gabay, D. A. Muller, J.-M. Triscone and J. Mannhart, Science **317**, 1196 (2007).

[122] A. D. Caviglia, S. Gariglio, N. Reyren, D. Jaccard, T. Schneider, M. Gabay, S. Thiel, G. Hammerl, J. Mannhart and J.-M. Triscone, Nature **456**, 624 (2008).

[123] S. Gariglio, N. Reyren, A. D. Caviglia and J.-M. Triscone, J. Phys. Condens. Matter **21**, 164213 (2009).

[124] M. Ben Shalom, M. Sachs, D. Rakhmilevitch, A. Palevski and Y. Dagan, Phys. Rev. Lett. **104**, 126802 (2010).

[125] M. M. Mehta, D. A. Dikin, C. W. Bark, S. Ryu, C. M. Folkman, C. B. Eom and V. Chandrasekhar, Phys. Rev. B **90**, 100506(R) (2014).

[126] S. Caprara, D. Bucheli, N. Scopigno, J. Biscaras, S. Hurand, J. Lesueur and M. Grilli, Supercond. Sci. Technol. **28**, 014002 (2015).

[127] C. Richter, H. Boschker, W. Dietsche, E. Fillis-Tsirakis, R. Jany, F. Loder, L. F. Kourkoutis, D. A. Muller, J. R. Kirtley C. W. Schneider and J. Mannhart, Nature **502**, 528 (2013).

[128] H. Boschker, C. Richter, E. Fillis-Tsirakis, C. W. Schneider and J. Mannhart, Sci. Rep. **5** 12309 (2015).

[129] E. Fillis-Tsirakis, C. Richter, J. Mannhart and H. Boschker, New J. Phys. **18**, 013046 (2016).

[130] T. Schneider, A. D. Caviglia, S. Gariglio, N. Reyren and J.-M. Triscone, Phys. Rev. B **79**, 184502 (2009).

[131] J. M. Edge and A. V. Balatsky, J. Supercon. Nov. Magn. **28**, 2373 (2015).

[132] S. N. Klimin, J. Tempere, J. T. Devreese and D. van der Marel, Phys. Rev. B **89**, 184514 (2014).

[133] M. Breitschaft, V. Tinkl, N. Pavlenko, S. Paetel, C. Richter, J. R. Kirtley, Y. C. Liao, G. Hammerl, V. Eyert, T. Kopp and J. Mannhart, Phys. Rev. B **81**, 153414 (2010).

[134] J. A. Bert, K. C. Nowack, B. Kalisky, H. Noad, J. R. Kirtley, C. Bell, H. K. Sato, M. Hosoda, Y. Hikita, H. Y. Hwang and K. A. Moler, Phys. Rev. B **86**, 060503(R) (2012).

[135] N. Reyren, S. Gariglio, A. D. Caviglia, D. Jaccard, T. Schneider and J.-M. Triscone, Appl. Phys. Lett. **94**, 112506 (2009).

[136] G. Herranz, G. Singh, N. Bergeal, A. Jouan, J. Lesqueur, J. Gasquez, M. Varela, M. Scigaj, N. Dix, F. Sanchez and J. Fontcuberta, Nature Commun. **6**, 6028 (2015).

[137] A. Brinkman, M. Huijben, M. van Zalk, J. Huijben, U. Zeitler, J. C. Maan, W. G. van der Wiel, G. Rijnders, D. H. A. Blank and H. Hilgenkamp, Nature Mater. **6**, 493 (2007).

[138] D. A. Dikin, M. Mehta, C. W. Bark, C. M. Folkman, C. B. Eom and V. Chandrasekhar, Phys. Rev. Lett. **107**, 056802 (2011).

[139] N. Pavlenko, T. Kopp, E. Y. Tsymbal, G. A. Sawatzky and J. Mannhart, Phys. Rev. B **85**, 020407(R) (2012).

[140] J. A. Bert, B. Kalisky, C. Bell, M. Kim, Y. Hikita, H. Y. Hwang and K. A. Moler, Nature Phys. **7**, 767 (2011).

[141] F. Bi, M. Huang, S. Ryu, H. Lee, C.-W. Bark, C.-B. Eom, P. Irvin and J. Levy, Nature Commun. **5**, 5019 (2014).

[142] L. Li, C. Richter, J. Mannhart and R. C. Ashoori, Nature Phys. **7**, 762 (2011).

[143] S. Banerjee, O. Erten and M. Randeria, Nature Phys. **9**, 626 (2013).

[144] M. H. Fischer, S. Raghu and E.-A. Kim, New J. Phys. **15**, 023022 (2013).

[145] A. Fete, S. Gariglio, A. D. Caviglia, J.-M. Triscone and M. Gabay, Phys. Rev. B **86**, 201105(R) (2012).

[146] A. Joshua, S. Pecker, J. Ruhman, E. Altman and S. Ilani, Nature Commun. **3**, 1129 (2012).

[147] A. D. Caviglia, M. Gabay, S. Gariglio, N. Reyren, C. Cancellieri and J.-M. Triscone, Phys. Rev. Lett. **104**, 126803 (2010).

[148] M. Scheurer and J. Schmalian, Nature Commun. **6**, 6005 (2015).

[149] N. Mohanta and A. Taraphder, EPL **108**, 60001 (2014).

[150] S. Gariglio, M. Gabay, J. Mannhart and J.-M. Triscone, Physica C **514**, 189 (2015).

[151] S. Gariglio, M. Gabay and J.-M. Triscone, APL Mater. **4**, 060701 (2016).

[152] G. Berner, M. Sing, H. Fujiwara, A. Yasui, A. Saitoh, A. Yamasaki, Y. Nishitani, A. Sekiyama, N. Pavlenko, T. Kopp, C. Richter, J. Mannhart, S. Suga and R. Claessen, Phys. Rev. Lett. **110**, 247601 (2013).

[153] Z. S. Popovic, S. Satpathy and R. M. Martin, Phys. Rev. Lett. **101**, 256801 (2008).

[154] P. Delugas, A. Filippetti, V. Fiorentini, D. I. Bilc, D. Fontaine and P. Ghosez, Phys. Rev. Lett. **106**, 166807 (2011).

[155] A. F. Santander-Syro, O. Copie, T. Kondo, F. Fortuna. S. Pailhes, R. Weht, X. G. Qiu, F. Bertran, A. Nicolaou, A. Taleb-Ibrahimi, P. Le Fevre, G. Herranz, M. Bibes, N. Reyren, Y. Apertet, P. Lecoeur, A. Barthelemy and M. J. Rozenberg, Nature **469**, 189 (2011).

[156] G. Herranz, F. Sanchez, N. Dix and J. Fontcuberta, Sci. Rep. **2**, 758 (2012).

[157] G. E. D. K. Prawiroatmodjo, F. Trier, D. V. Christensen, Y. Chen, N. Pryds and T. S. Jespersen, Phys. Rev. B **93**, 184504 (2016).

[158] A. Annadi, Q. Zhang, X. Renshaw Wang, N. Tuzla, K. Gopinadhan, W. M. Lü, A. Roy Barman, Z. Q. Liu, A. Srivastana, S. Saha, Y. L. Zhao, S. W. Zeng, S. Dhar, E. Olsson, B. Gu, S. Yunoki, S. Maekawa, H. Hilgenkamp, T. Venkatesan and Ariando, Nature Commun. **4**, 1838 (2013).

[159] Y.-L. Han, S.-C. Shen, J. You, H.-O. Li, Z.-Z. Luo, C.-J. Li, G.-L. Qu, C.-M. Xiong, R.-F. Dou, L. He, D. Naugle, G.-P. Guo and J.-C. Nie, Appl. Phys. Lett. **105**, 192603 (2014).

[160] K. A. Müller and H. Burkard, Phys. Rev. B **19**, 3593 (1979).

[161] Mineral information and data: *http://www.mindat.org/min-3895.html*, 18-07-2016.

[162] T. Tomio, H. Miki, H. Tabata, T. Kawai and S. Kawai, J. Appl. Phys. **76**, 5886 (1994).

[163] A. Spinelli, M. A. Torija, C. Liu, C. Jan and C. Leighton, Phys. Rev. B **81**, 155110 (2010).

[164] W. A. Feil, B. W. Wessels, L. M. Tonge and T. J. Marks, J. Appl. Phys. **67**, 3585 (1990).

[165] T. Sakuma, S. Yamamichi, S. Matsubara, H. Yamaguchi and Y. Miyasaka, Appl. Phys. Lett. **57**, 2431 (1990).

[166] L. Rimai and G. A. de Mars, Phys. Rev. **127**, 702 (1962).

[167] R. A. Cowley, Phys. Rev. **154**, A981 (1964).

[168] K. A. Müller, W. Berlinger and E. Tosatti, Z. Phys. B: Cond. Matt. **84**, 277 (1991).

[169] M. L. Reinle-Schmitt, C. Cancellieri, D. Li, D. Fontaine, M. Medarde, E. Pomjakushina, C. W. Schneider, S. Gariglio, Ph. Ghosez, J.-M. Triscone and P. R. Wilmott, Nature Commun. **3**, 932 (2012).

[170] S. Hui and A. Petric, J. Electr. Soc. **149**, J1 (2002).

[171] A. Rocca, A. Liciulli, M. Politi and D. Diso, ISRN Ceramics **2012**, 926537 (2012).

[172] D. J. Cumming, J. A. Kilner and S. Skinner, J. Mater. Chem. **21**, 5021 (2011).

[173] L. J. Knott and J. C. Wright, J. Lumin. **60** & **61**, 227 (1994).

[174] A. C. Marquez PhD Thesis: *Advanced Si-pad Detector Development and $SrTiO_3$ Studies by Emission Channeling and Hyperfine Interaction Experiments*, University of Lisbon 2009.

[175] L. C. Walters and R. E. Grace, J. Phys. Chem. Solids **28**, 245 (1967).

[176] H. Uwe, H. Yamaguchi and T. Sakudo, Ferroelectrics **96** : **1**, 123 (1989).

[177] D. A. Tenne, I. E. Gonenli, A. Soukiassian, D. G. Schlom, S. N. Nakhmanson, K. M. Rabe and X. X. Xi, Phys. Rev. B **76**, 024303 (2007).

[178] H. P. R. Frederikse, W. R. Thurber and W. R. Hosler, Phys. Rev. **134**, A442 (1964).

[179] X. Lin, B. Fauque and K. Behnia, Science, **349**, 945 (2015).

[180] E. Mikheev, S. Raghavan, J. Y. Zhang, P. B. Marshall, A. P. Kajdos, L. Balents and S. Stemmer, Sci. Rep. **6**, 20865 (2016).

[181] D. van der Marel, J. L. M. van Mechelen and I. I. Mazin, Phys. Rev. B **84**, 205111 (2011).

[182] S. J. Allen, B. Jalan, S. Lee, D. G. Ouellette, G. Khalsa, J. Jaroszynski, S. Stemmer and A. H. MacDonald, Phys. Rev. B **88**, 045114 (2013).

[183] R. A. Hein, J. W. Gibson, R. Mazelsky, R. C. Miller and J. K. Hulm, Phys. Rev. Lett. **12**, 320 (1964).

[184] E. Ambler, J. H. Colwell, W. R. Hosler and J. F. Schooley, Phys. Rev. **148**, 280 (1966).

[185] H. Boschker, *Private Communication*, 2016.

[186] A. Quattropani and C. P. Enz, Phys. Lett. 26A, 100 (1967).

[187] H. Suzuki, H. Bando, Y. Ootuka, I. H. Inoue, T. Yamamoto, K. Takahashi and Y. Nishihara, J. Phys. Soc. Jpn. **65**, 1529 (1996).

[188] J. F. Schooley, H. P. R. Frederikse, W. R. Hosler and E. R. Pfeiffer, Phys. Rev. **159**, 301 (1967).

[189] C. S. Koonce, M. I. Cohen, J. F. Schooley, W. R. Hosler and E. R. Pfeiffer, Phys. Rev. **163**, 380 (1967).

[190] G. Binnig, A. Baratoff, H. E. Hoenig and J. G. Bednorz, Phys. Rev. Lett. **45**, 1352 (1980).

[191] X. Lin, G. Bridoux, A. Gourgout, G. Seyfarth, S. Krämer, M. Nardone, B. Fauque and K. Behnia, Phys. Rev. Lett. **112**, 207002 (2014).

[192] E. R. Pfeiffer and J. F. Schooley, Phys. Lett. **29A**, 589 (1969).

[193] P. Moetakef, J. R. Williams, D. G. Ouellette, A. P. Kadjos, D. Goldhaber-Gordon, S. J. Allen and S. Stemmer, Phys. Rev. X **2**, 021014 (2012).

[194] A. Leitner, D. Olaya, C. T. Rogers and J. C. Price, Phys. Rev. B **62**, 1408 (2000).

[195] J. F. Schooley, W. R. Hosler, E. Ambler and J. H. Becker, Phys. Rev. Lett. **14**, 305 (1965).

[196] J. K. Hulm, C. K. Jones, D. W. Deis, H. A. Fairbank and P. A. Lawless, Phys. Rev. **169**, 388 (1968).

[197] T. D. Thanh, A. Koma and S. Tanaka, Appl. Phys. **22**, 205 (1980).

[198] E. A. Ekimov, V. A. Sidorov, E. D. Bauer, N. N. Mel'nik, N. J. Curro, J. D. Thompson and S. M. Stishov, Nature **428**, 542 (2004).

[199] E. Bustarret, J. Kacmarcik, C. Marcenat, E. Gheeraert, C. Cytermann, J. Marcus and T. Klein, Phys. Rev. Lett. **93**, 237005 (2004).

[200] K. Winzer, D. Bogdanov and C. Wild, Physica C **432**, 65 (2005).

[201] E. Bustarret, C. Marcenat, P. Achatz, J. Kacmarcik, F. Levy, A. Huxley, L. Ortega, E. Bourgeois, X. Blase, D. Debarre and J. Boulmer, Nature **444**, 465 (2006).

[202] Z.-A- Ren, J. Kato, T. Muranaka, J. Akimitsu, M. Kriener and Y. Maeno, J. Phys. Soc. Jpn. **76**, 103710 (2007).

[203] T. Hermannsdörfer, V. Heera, O. Ignatchik, M. Uhlarz, A. Mücklich, M. Posselt, H. Reuther, B. Schmidt, K.-H. Heinig, W. Skorupa, M. Voelskow, C. Wündisch, R. Skrotzki, M. Helm and J. Wosnitza, Phys. Rev. Lett. **102**, 217003 (2009).

[204] Y. Kozuka PhD Thesis: *High Mobility Electrons and Two-Dimensional Superconductivity in $SrTiO_3$ Heterostructures*, University of Tokyo 2010.

[205] H. Uwe, R. Yoshizaki, T. Sakudo, A. Izumi and T. Uzumaki, Jpn. J. Appl. Phys. **24**, 335 (1985).

[206] H. Uwe, T. Sakudo and H. Yamaguchi, Jpn. J. Appl. Phys. **24**, 519 (1985).

[207] X. Lin, Z. Zhu, B. Fauque and K. Behnia, Phys. Rev. X **3**, 021002 (2013).

[208] O. Prakash, A. Kumar, A. Thamizhavel and S. Ramakrishnan, Science **355**, 52 (2017).

[209] K. Behnia, Science **355**, 26 (2017).

[210] G. P. Malik, *Superconductivity: A New Approach Based on the Bethe-Salpeter Equation in the Mean-Field Approximation, Chapter 10*, World Scientific Publishing Co. Pte. Ltd., London (2016).

[211] Z. Fisk, H. R. Ott, T. M. Rice and J. L. Smith, Nature **320**, 124 (1986).

[212] L. F. Mattheiss. Phys. Rev. B **6**, 4740 (1972).

[213] S. Shapiro, Phys. Rev. **140**, A169 (1965).

[214] A. Baratoff and G. Binnig, Physica **108B**, 1335 (1981).

[215] H. Vogt, Phys. Rev. B **38**, 5699 (1988).

[216] J. M. Edge, Y. Kedem, U. Aschauer, N. A. Spaldin and A. V. Balatsky, Phys. Rev. Lett. **115**, 247002 (2015).

[217] Y. Ishida, R. Eguchi, M. Matsunami, K. Horiba, M. Taguchi, A. Chainani, Y. Senba, H. Ohashi, H. Ohta and S. Shin, Phys. Rev. Lett. **100**, 056401 (2008).

[218] X. Lin, A. Gourgout, G. Bridoux, F. Jomard, A. Pourret, B. Fauque, D. Aoki and K. Behnia, Phys. Rev. B **90**, 140508(R) (2014).

[219] L. P. Gorkov, PNAS **113**, 4646 (2016).

[220] J. Ruhman and P. A. Lee, Phys. Rev. B **94**, 224515 (2016).

[221] A. G. Swartz, H. Inoue, T. A. Merz, Y. Hikita, S. Raghu, T. P. Devereaux, S. Johnston and H. Y. Hwang, arXiv: 1608.05621 (2016).

[222] R. M. Fernandes, J. T. Haraldsen, P. Wölfle and A. V. Balatsky, Phys. Rev. B **87**, 014510 (2013).

Chapter 3

Growth, Characterization and Equipment

The sample fabrication, characterization, growth procedures and the dilution refrigerator set-up are discussed in this chapter. $LaAlO_3/SrTiO_3$ samples were grown by Pulsed Laser Deposition (PLD). Fabrication of the tunnel junctions with doped-$SrTiO_3$ and metals was done using an electron-beam (E-beam) evaporator (for depositing Au, Pt, Ti and Al) and an effusion cell for In-deposition. The patterning of samples in measurement structures required treatment in a cleanroom, where steps of cleaning and photolithography take place. The vast majority of measurements were conducted in a dilution refrigerator system (all tunneling-spectroscopy measurements were exclusively done here), while characterization was mainly done by Atomic Force Microscopy (AFM).

3.1 Growing $LaAlO_3$ on $SrTiO_3$ by Pulsed Laser Deposition

The $LaAlO_3/SrTiO_3$ sample was fabricated by PLD at the University of Augsburg. A mm-thick $SrTiO_3$-substrate of [001]-orientation (CrysTec GmbH), was TiO_2-terminated via HF-etching, and a four-unit-cell-thick $LaAlO_3$-layer was grown on-top. During deposition, the O_2 partial pressure and temperature were held at 10^{-4} mbar and 780 °C respectively, while the $LaAlO_3$-target was ablated with an excimer-laser, with a fluence of 1 J/cm^2. The $LaAlO_3$-growth was monitored by Reflection High Energy Electron Diffraction (RHEED). A cross-sectional image of the $LaAlO_3/SrTiO_3$ sample, with a 30 nm Au-layer additionally grown on top of the $LaAlO_3$, is shown in Fig. 3.1. This was obtained by cross-sectional Scanning Transmission Electron Microscopy (STEM) [1].

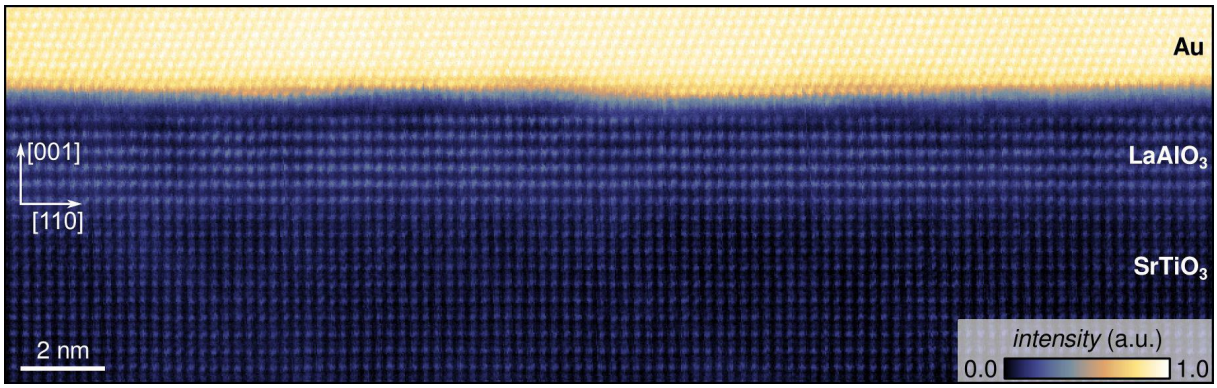

Figure 3.1: *High-angle annular dark-field STEM image from the cross section of an $LaAlO_3/SrTiO_3$ sample grown under the specified conditions. The epitaxially grown $LaAlO_3$ layer on $SrTiO_3$ [001] is clearly distinguished. On top of $LaAlO_3$, a Au-layer is additionally grown, as top electrode of the tunnel junction. Au-diffusion towards the interface was not observed. This image was taken at Cornell University by L. Fitting-Kourkoutis and D. A. Muller [1].*

The tunneling measurements are performed between the Au-layer on the insulating $LaAlO_3$-film (top electrode) and the $LaAlO_3/SrTiO_3$ 2DEL (bottom electrode) [1]. Accessing the 2DEL for measurement requires further treatment, as it is "buried" between the $LaAlO_3$ layer and $SrTiO_3$ substrate. This is achieved by Au-coated Ti-contacts that are constructed by Ar-milling of the $LaAlO_3$ film and partly of the $SrTiO_3$ substrate, followed by Ti-evaporation. This method allows reliable four-point resistivity and tunneling measurements.

Figure 3.2 depicts the layer sequence of a tunnel-device that is covered with Au. The $LaAlO_3/SrTiO_3$ 2DEL (light brown) is approximately 10 nm thick, extending from the interface towards the $SrTiO_3$ side. It is contacted by the Ti-probes that enable access from the top. An Ag-foil (here shown as an extra layer) at the bottom enables the electrostatic tuning of the 2DEL.

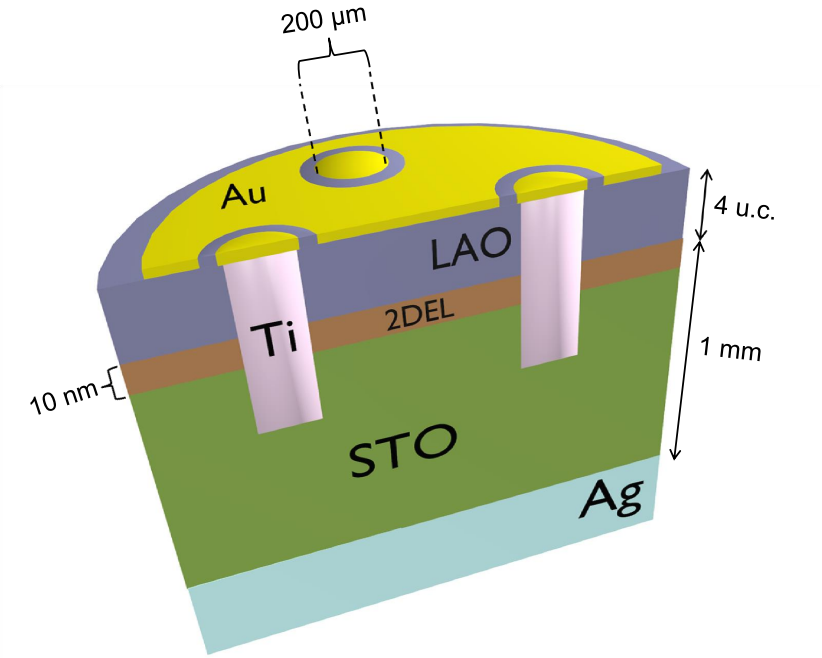

Figure 3.2: *A cross-sectional schematic of an $LaAlO_3/SrTiO_3$ device (defined as the area below the gold disk), within a PLD-grown sample. The 2DEL (brown layer) extends into the $SrTiO_3$ substrate (green). The Au-layer on top is grown atop the four u.c.-thick $LaAlO_3$ (violet). An Ag-foil, attached at the back of the substrate, serves as the gate electrode (light blue). The device area may vary slightly, with an approximate radius of the order of a millimeter.*

3.2 Electron-Beam and Thermal Evaporation

Au, Pt and Al are grown by electron-beam physical-vapor deposition (EBPVD). These metals were assessed as top electrodes of Schottky junctions with doped $SrTiO_3$. A thin Au-layer is typically grown on-top of all metals, to improve the bonding contact on metallic devices. The EBPVD technique is based on material-evaporation from a target that is bombarded by highly-kinetic electrons. A "CARRERA" high voltage power supply unit and an evaporation controller (Genius), from Ferrotec GmbH, are used to drive electrons through a filament, where electronic emission takes place. In presence of a magnetic field, the emitted electron-beam is forced into circular trajectory and directed towards the crucible stage that contains the target. Electron bombardment evaporates the desired material towards the patterned substrate and deposition takes place. Set-up and process are shown in Fig. 3.3.

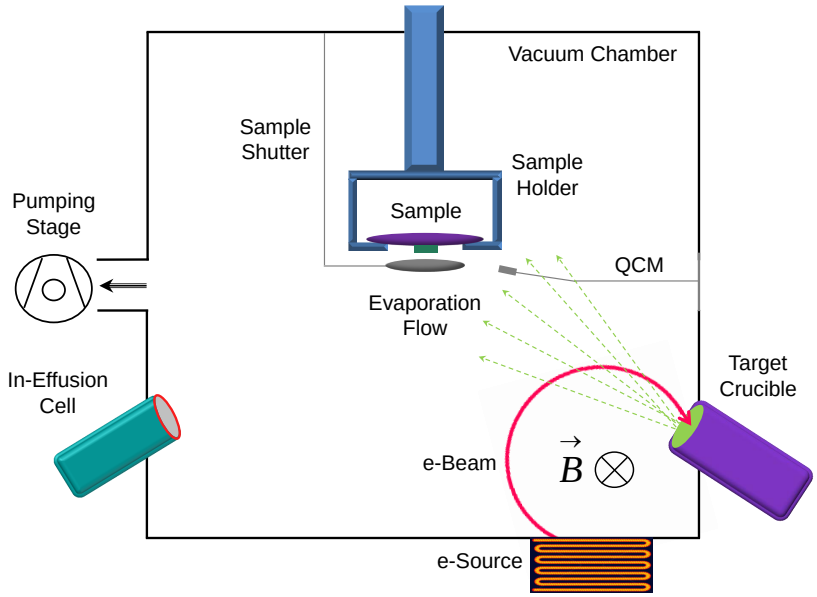

Figure 3.3: *An illustration of the front-view of the vacuum chamber where the electron-beam evaporation takes place, along with main components. The transfer disk on which the sample is glued (green), is mounted on the holder stage (blue) that can rotate during evaporation. The position of the crucible (violet) contains target material (light green) against the path of the emitted electron-beam (pink). The beam's trajectory is curved by a magnetic field, optimized to direct emitted electrons (from the hot filament shown at the bottom) towards the target. The evaporation flow is directed towards the sample and the QCM, as shown. With the latter one can keep track of the deposition rate. An effusion-cell for In-deposition (turquoise) is attached opposite to the E-beam evaporator in the chamber.*

Deposition takes place at a pressure range between 10^{-9} mbar to 10^{-7} mbar. The sample holder rotates at 14 rpm, while a quartz crystal monitor (QCM) at the direct proximity of the sample monitors the growth rate. The filament's emission current can be tuned via the evaporation-control unit and allows for tuning of the growth rate during deposition. Each metal is optimally evaporated under different values of the emission current. Au is typically deposited with a current of 225 mA, which corresponds to a rate of approximately 0.5 Å/s. Yet, these values are susceptible to change with respect to age and shape of the target-material inside the crucible, or filament degradation.

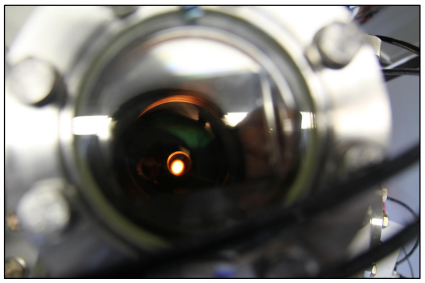

Figure 3.4: *View of the electron-irradiated Au-target in the crucible, through a top view-port of the e-beam evaporation chamber. The irradiation spot has a characteristic shine that is much more pronounced for Au than for Ag, Pt or Ti, visible from the outside.*

3.2.1 Indium-Growth with an Effusion Cell

Evaporation of In is done using an effusion cell unit also attached to the e-beam evaporation chamber, opposite to the crucibles, as shown in Fig. 3.3.

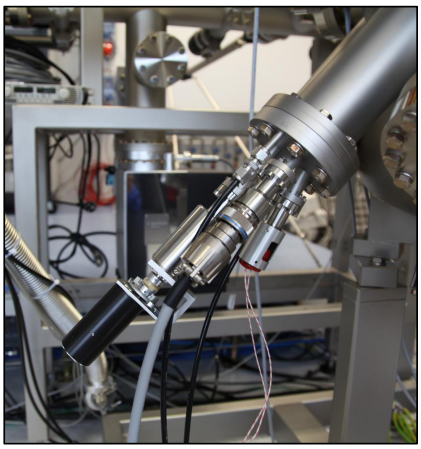

Figure 3.5: *View of the In effusion-cell, attached at the vacuum chamber (see Fig. 3.3), adjacent to the electron-beam evaporator.*

The In-target is heated inside a crucible by an electric current flowing through the attached main coil. A secondary coil is embedded on the hot-lip (the rim of the crucible) for keeping it at higher temperature, in order to prevent liquid-In from flowing out of the crucible and into the chamber. This is particularly important when cooling In inside the crucible below its melting point, which is approximately at 140 ^{o}C. The onset of In-evaporation is above 800 ^{o}C, while deposition of all In-films took place between 860 ^{o}C and 970 ^{o}C. The crucible temperature determines the metal deposition rate and is an optimization parameter.

3.3 Photolithography

Fabrication of samples with metal and $SrTiO_3$ Schottky-junctions requires patterning before deposition. The patterning is done by photolithography in a cleanroom. Substrates are cleaned in acetone and isopropanol, prior to ultra-violet (UV) irradiation. After cleaning, negative photoresist (AZ 5214E) is used to cover the substrate which is then spin-coated at 6000 rpm for 30 s. The substrate is then heated on a hot plate for 50 s and is transferred to a mask aligner for UV-irradiation for 6.5 s. A second heating step of 180 s follows, along with further irradiation for 90 s. By UV-exposure through Cr-masks, the desired structures are "imprinted" in the photo-resist layer. The non-exposed photoresist is removed after stirring the substrate for 15 s in a solution with developer (AZ 400K) and water, of proportion one-to-four, respectively. Typical structures are shown in Fig. 3.6.

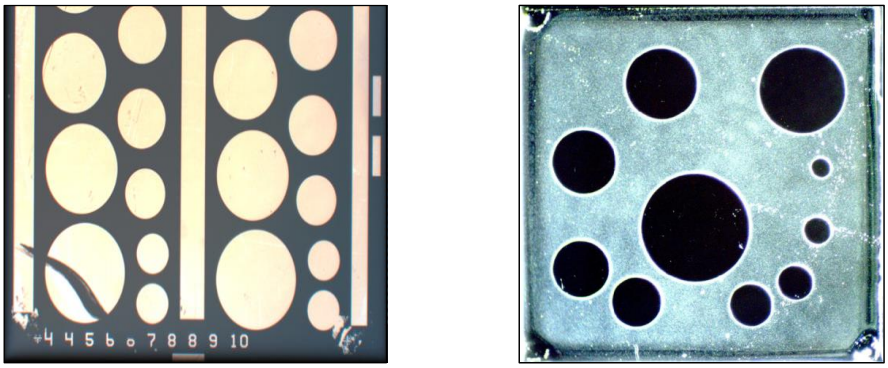

Figure 3.6: *Two 5x5 mm doped $SrTiO_3$ substrates with photoresist-patterned devices. Left: 50 nm In-devices. Right: a photoresist hard-mask just before metal deposition.*

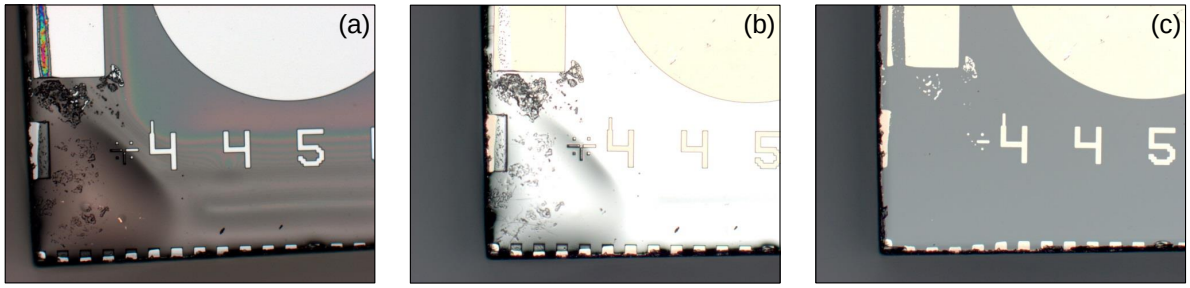

Figure 3.7: *Optical microscope images of a sample at different stages of the fabrication procedure. The same region is depicted in all cases. a) The bottom-left corner of a substrate patterned with photoresist, b) after deposition of a 50 nm In-layer and c) after lift-off. In (c), seen in yellow are substrate regions covered with In, which is the top electrode of the Schottky junction with the Nb-doped $SrTiO_3$ substrate.*

The cleanroom treatment yields the conditioning shown in Fig. 3.7a. The substrate is covered by photo-resist, apart from the washed-off regions of the circular devices and numbering, revealed after developing. Figure 3.7b depicts a substrate after thermal evaporation of a 50 nm In-film and 3.7c is the final stage of the fabrication process (after photoresist lift-off). The metallic devices on the substrate are then bonded with Au-wires for measurement.

3.3.1 Lift-off and Bonding

After metal evaporation, a lift-off step follows. The recipe involves dissolving the photoresist, Ag-paste remnants and other post-deposition contaminants in acetone for 8 min followed by another 8-min step in isopropanol, in an ultrasonic bath. Once the device structure is revealed, bonding follows. Au-wires connect each device with the sample-holder pins. Epoxy adhesive is used for gluing the wires on the metallic device and then baking at 100 °C. Al-wires are pressed into the substrate, enabling spectroscopy and four-point transport measurements. Circular metallic regions are bonded on the top with two Au-wires, while Al-wires contact the substrate. Figure 3.8 presents a sample of Nb-doped $SrTiO_3$ with thin layers of In and Au grown on top, bonded onto a 24-pin sample-holder. Often, a RuO_2-sensor is attached to the chip carrier in the direct proximity of the sample (not shown in the figure), in order to record temperature accurately in the the mK range.

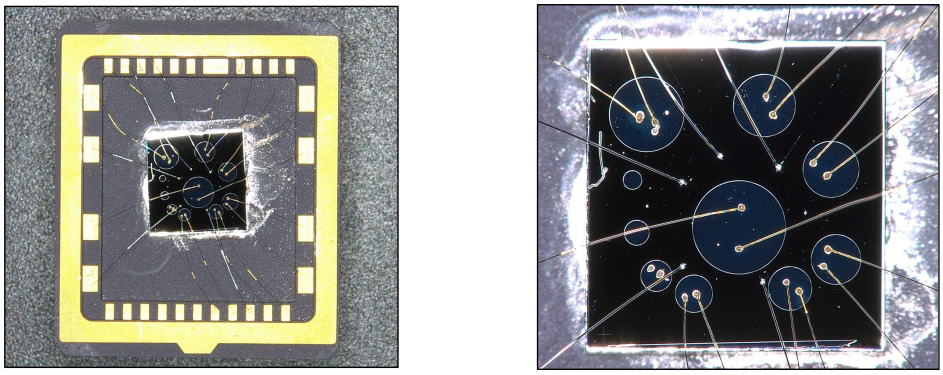

Figure 3.8: *A sample bonded onto a 24-pin holder (left). Circular devices with varying diameter are individually contacted. Two Au-wires are glued to each metallic device, while Al-wires are pressed into the substrate (seen on the right).*

3.4 Characterization by Atomic Force Microscopy (AFM)

The surface roughness of metallic films grown by PLD, EBPVD or thermal evaporation, is one criterion of the growth quality. Minimizing roughness is a crucial part in the optimization of the sample fabrication process. Also, substrate quality is often below the desired standards and the surface roughness is a condition easily assessed by AFM. Figure 3.9 shows AFM graphs of the step-edge of an $SrRuO_3$ device grown by PLD (3.9a) and an In-device grown by thermal evaporation (3.9b), on Nb-doped $SrTiO_3$. The surface roughness of the $SrRuO_3$-film is much lower as compared to the In-film.

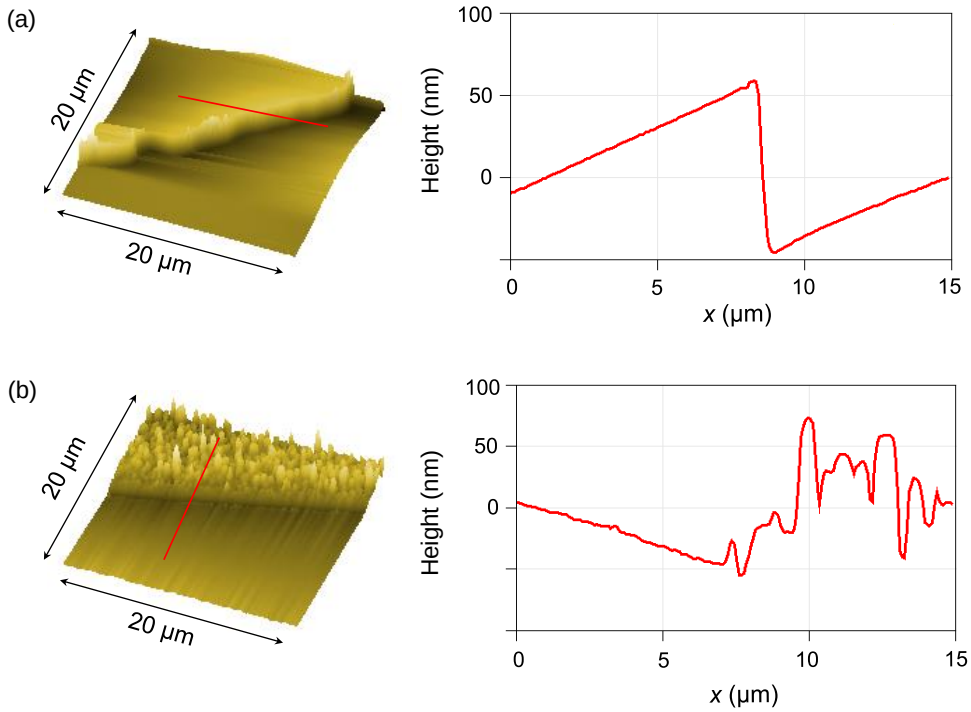

Figure 3.9: *3D-images of device step-edges (left), with the respective height profile (right) along the red line in the graph. (a) PLD-grown $SrRuO_3$ devices on doped-$SrTiO_3$. (b) 50 nm In-devices deposited by thermal evaporation on doped-$SrTiO_3$. The $SrRuO_3$/$SrTiO_3$ samples are patterned and Ar-milled into structure after PLD growth.*

It is evident that the PLD-grown $SrRuO_3$ film has minimal roughness as compared to the thermally evaporated In. The curves in the panels of Fig. 3.9 are tilted (i.e. they have a finite slope with respect to lateral dimensions), as the sample's surface is not parallel to the AFM-scanning plane. Substrates are typically flat in comparison to any thermally evaporated film that always features distinct height fluctuations. The edge of the In-device in Fig. 3.9b has a fluctuating thickness that is often lower than the intended 50 nm. This is probably due to masking in the proximity of the photoresist layer that is present during deposition and is later lifted-off.

In addition, (HF-etched) TiO_2-terminated substrates of Nb-doped $SrTiO_3$ have been prepared for Scanning Tunneling Microscopy (STM) studies, for which surface roughness should be as low as possible. Figure 3.10 shows the AFM scans of well and of poorly terminated substrates.

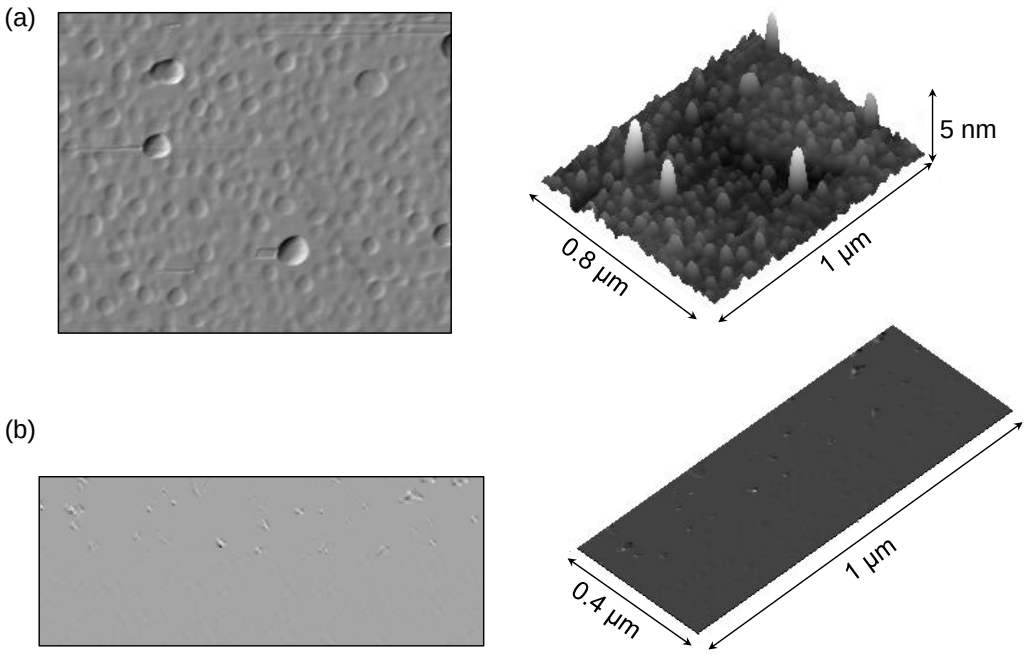

Figure 3.10: *(a) Top-view of an unsuccessfully terminated doped-$SrTiO_3$ crystal and its respective 3D image of the same dimensions. The surface is rather rough, featuring contamination-peaks that extend above the substrate plane. (b) Same, but this time with a successful termination, where contamination peaks are barely visible. Step-and-terrace structures have been observed in well-terminated Nb-doped $SrTiO_3$ substrates, in a smaller scale. Note that the scales here are smaller than those in Fig. 3.9.*

3.5 The Dilution Refrigerator Unit

Investigation of superconductivity at the $LaAlO_3/SrTiO_3$ interface and the bulk $SrTiO_3$ Schottky junctions requires the ability to measure at low temperatures and particularly below the critical temperature T_c of 300 mK. Since liquid-He temperature is not low enough, the usage of sophisticated equipment is essential for reaching the desired temperatures, that is practically close to absolute zero.

The system used is a Kelvinox AST Dilution Refrigerator (Oxford Instruments GmbH) and enables measurement at temperatures down to the mK-range. The coldest point of the system, the mixing chamber, can be cooled to 12 mK. The sample temperature can be as low as 30 mK, provided that high-vacuum is maintained (no exchange gas in the sample-environment), there are no magnetic field fluctuations (a typical heating source on such systems) and also that the measurement is conducted with sufficiently low currents for minimizing resistive heating.

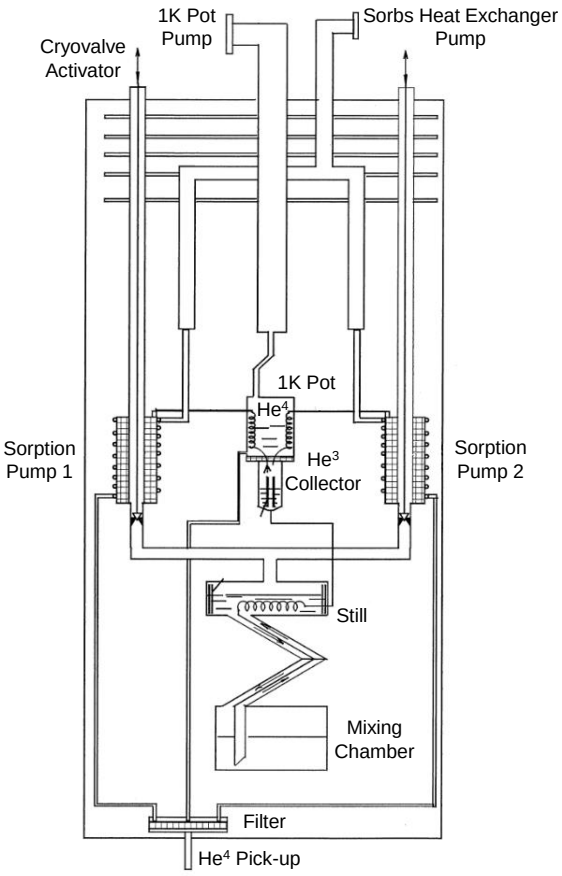

Figure 3.11: *A schematic of the Kelvinox Inner Vacuum Chamber (IVC), where the He^3/He^4-mixture circulates. The entire volume is under high-vacuum, with the insert surrounded by liquid-He. The sample (not shown) is positioned just below the mixing chamber, to which it is thermally connected by Cu-wires. The drawing is reprinted from the Oxford Instruments Ltd. operating manual.*

Figure 3.11 depicts a simple schematic of the fridge's tubular volume, or inner vacuum chamber (IVC insert) that enters the liquid-He cryostat, on a perpendicular-to-floor orientation. The cryostat-container (not shown here) is thermally shielded by vacuum on its outer shell and contains the liquid-He^4 bath into which the insert is immersed.

Cooling below 4.3 K is achieved by the combined usage of pumps, valves and heaters that can selectively heat particular components in order to cool-down a gas mixture of He^3 and He^4, of an approximate proportion of 50% each. The mixture circulates inside an independent circuit, passing through the sorption pumps, 1K-pot, "still" and mixing-chamber. The cooling of the entire IVC-circuitry is based on circulation of liquid He^4 through the pick-up gateway shown at the bottom of the figure. This is particularly designed to allow liquid He to flow into the IVC's components, while the IVC's vacuum environment is secured by an In-seal. External pumping on the sorption pumps and 1K-pot achieves continuous cooling by draining thermal energy from the highly energetic molecules of the He^4-bath, which are in gaseous form.

Below 3.2 K, both, He^3 and He^4 are in the liquid phase. In a 50-50 % concentration, the liquid-mixture is expected to undergo phase separation into its individual components, at an approximate temperature of 0.8 K [2]. This is achieved at the lowest point of the IVC, the mixing chamber. This condition of phase separation is the key to achieve maximum cooling power. Atoms from the He^3-rich phase efficiently transfer thermal energy onto the He^4-rich phase. Highly energetic atoms of the latter are directed towards the still. Pumping and heating the sorption pumps, "still" and 1K-pot can coordinate the process into equilibrium, where the phase-separated He^3 and He^4 reside permanently in the mixing chamber and constantly dispose of thermal energy. After a few hours of circulation, the system can reach equilibrium, which has the mixing chamber at base temperature (about 15 mK) and stable amounts of phase separated liquid He^3 and He^4. In this state the dilution fridge is ready for measuring the sample in the millikelvin regime.

For magnetic-field measurements, a Nb_3Sn superconducting coil magnet is embedded on the bottom of the cryostat, permanently immersed in the liquid-He^4 bath and surrounding the volume of the lower part of the insert. It can be driven either in manual or persistent mode, sustaining currents up to 120 A and capable of applying magnetic fields of ± 12 T on a perpendicular-to-floor orientation. The magnetic field orientation is essentially perpendicular to the sample's surface (the tilt of the sample's plane was measured below 9 degrees with respect to the floor), as the system lacks the ability to rotate the sample holder for angular field measurements.

References

[1] C. Richter, H. Boschker, W. Dietsche, E. Fillis-Tsirakis, R. Jany, F. Loder, L. F. Kourkoutis, D. A. Muller, J. R. Kirtley C. W. Schneider and J. Mannhart, Nature **502**, 528 (2013).

[2] C. Enss and S. Hunklinger, *Low Temperature Physics*, Universität Heidelberg, Springer-Verlag Berlin, Heidelberg (2005).

Chapter 4

Results: Tunneling Spectroscopy at the $LaAlO_3/SrTiO_3$ Heterointerface

In this chapter, measurements at the $LaAlO_3/SrTiO_3$ interface [1] are categorized into sections, each addressing a distinct framework. A brief introduction of the key experimental tool, tunnel spectroscopy, is presented. This is succeeded by a section about the $LaAlO_3/SrTiO_3$ superconductor, as studied through transport and tunneling spectroscopy. The following sections cover my work on the evolution of the superconducting features on the tunnel spectra with respect to gate-voltage, the investigation of the superconductor-to-metal-to-insulator transition and the nature of superconductivity in the presence of external, out-of-plane magnetic fields. Next, a section summarizes measurements of the temperature dependence of the critical field, along with implications of the observed behavior. The last section is a summary of the main results and discusses future experimental possibilities.

4.1 Tunneling Spectroscopy Using Planar Junctions

In 1960, the pioneering work of I. Giaever brought the first experimental manifestation of tunneling between two metallic films [2], a metal and a superconductor [3] and two superconductors [4], with aluminum oxide being the insulating barrier in all cases. Also through the work of J. Nicol et al. [5] it became evident that the observed non-linear region of the $I-V$ characteristics of a tunnel junction between a metal and a superconductor is directly related to the spectral density-of-states (DOS) around the Fermi level, as described in the BCS theory [6–8]. An elaborate description of the effect can be found in Ch. 2.

Scanning Tunneling Spectroscopy (STS) is generally known to be an excellent probe for studying the DOS of semiconducting thin films and 2DEGs. Studying the $LaAlO_3/SrTiO_3$ interface through STS, however, is a challenging task, a good example of which is the work of M. Breitschaft et al. [9]. In contrast to the planar tunnel-junction set-up, STM is suitable for measuring tunnel spectra at large voltages (order of volts) since the tunnel barrier can be tuned by adjusting the tip-sample distance. This is however more complicated in the case of $LaAlO_3/SrTiO_3$, as the tunnel barrier additionally includes the $LaAlO_3$ layer, which has to be at least four unit cells thick so that a conducting interface is obtained [10]. The $LaAlO_3$ layer not only reduces the tunneling probability, but can also alter the tunneling-current towards the interface due to possible contributions from its electronic surface states. With planar $LaAlO_3/SrTiO_3$ tunnel junctions, one does not only avoid the above but can also obtain higher energy resolution, owing to larger tunneling currents (of several orders of magnitude in comparison to STS) obtained over a wide sample area [11, 12]. Moreover, a planar junction enables measurements on a variety of instruments (cryostat, PPMS, dipsticks etc.). My investigation of superconductivity is therefore performed using planar tunnel junctions. A downside of the planar junctions, as compared to STS, is the inability to provide local information on the atomic scale.

In particular, electron-tunneling is explored between the $LaAlO_3/SrTiO_3$ 2DEL (bottom electrode) and a Au-layer (top electrode) that is grown on top of an $LaAlO_3$ layer that simultaneously acts as an insulating barrier. More details on the growth procedure are given in the previous chapter. In the case of tunneling within a broad energy range (order of hundreds of meV), inelastic processes (i.e. phonon assisted tunneling) may be relevant; the $I-V$ characteristics can thereby map part of the phonon spectrum of the electrode of interest. On the other hand, the superconducting DOS features a gap-opening at an energy scale of the order of 100 μeV around the Fermi energy, a range small enough that tunneling can be considered purely elastic. This implies that the tunneling-conductance is a good probe of the superconducting DOS around the Fermi energy.

Due to the group's history, all measurements presented in this chapter have been performed in a sample (T36) that was PLD-grown at the University of Augsburg. Absolute values of quantities such

as the tunnel resistance or the carrier-density change with back-gate fields typically vary from sample to sample. The growth parameter-window for high quality $LaAlO_3/SrTiO_3$ samples is usually small and also unique for a PLD-chamber. For the investigation of superconductivity, this quality essentially refers to low $LaAlO_3/SrTiO_3$ sheet resistance (also with respect to the tunneling resistance), clarity in observing superconducting signatures and also response to gate-field application. As seen in the work of my colleague L. Kürten, PLD-grown $LaAlO_3/SrTiO_3$ samples (at the Max-Planck-Institute) have featured well-conducting interfaces with sheet-resistances in the order of 100 Ω and can be tuned by back-gate voltages typically within the range -300 V < V_g < +300 V (for 1 mm thick $SrTiO_3$ substrates). Superconducting critical temperatures of these samples varied within the interval 200 mK to 300 mK.

4.1.1 Measurement technique

In tunneling measurements on $LaAlO_3/SrTiO_3$, both the top and bottom electrodes are only accessible for bonding from the sample's surface. The Au-layer (top electrode) is independent of the Au-pads that contact the interface (see previous chapter). When investigating the DOS, a direct (dc) and an alternating (ac) current component are summed and sourced to either the top (Au) or bottom ($LaAlO_3/SrTiO_3$ interface) electrode. In all transport measurements shown in this chapter, ac currents are sourced through a single Ti-contact to the 2DEL and drained to another which is grounded, while simultaneously recording the induced voltage drop across the interface using two separate contacts and a lock-in technique. This is a four-point resistance measurement. Direct-current measurements are not preferred in transport as they yield higher noise levels.

Figure 4.1 depicts the electronic configuration of a tunnel-measurement in detail. An SR830 Stanford Lock-In amplifier provides a constant ac-current component (below 10 Hz) through an output resistor typically of the order of 100 MΩ. The SR830 unit has 10 MΩ input impedance that enables reliable ac-measurements of the sheet resistance and also combined dc + ac tunneling measurements. The dc-component is provided by a current-source (Keithley 6430) in series with a sub-femto amplifier, as the applied currents for such measurements are in the pico-ampere range. The ac and dc current components are summed and sourced at the top electrode. This technique has yielded tunnel spectra with much higher signal-to-noise ratios (in comparison to pure dc-measurements), as the low-frequency ac-component is less sensitive to voltage spikes but at the same time not greatly affected by capacitive contributions across the junction. The ac-response is then fed into the SR830 input, whereas the dc-part is simultaneously recorded by a nanovolt-meter (Keithley 2182). Last, a source-meter (Keithley 2410) provides the high back-gate voltage necessary to tune the charge carrier concentration at the interface (see Refs. [13, 14]) through an Ag-foil attached to the back of the sample (Fig. 4.1). All electronic instruments are connected to the same ground as the $LaAlO_3/SrTiO_3$ interface and the cryostat. Measurements were initiated by

the K6430 source-current sweep that triggers measurement on the nanovolt-meter and the Lock-In after every step, all remotely controlled in a Labview interface. The gate-voltage source-meter independently applies the desired gate-field at the back of the $SrTiO_3$ substrate.

The ac-conductance measured with respect to the dc-response is considered a direct probe of the energy-dependent DOS. Measurements that aim to reveal the phonon modes of $SrTiO_3$ are typically done at 4.3 K and tunneling spectra are recorded within a larger energy interval [15]. In this case a source-meter unit (Keithley 2410) is used to source voltages in the order of hundred millivolts and record the induced current across the junction.

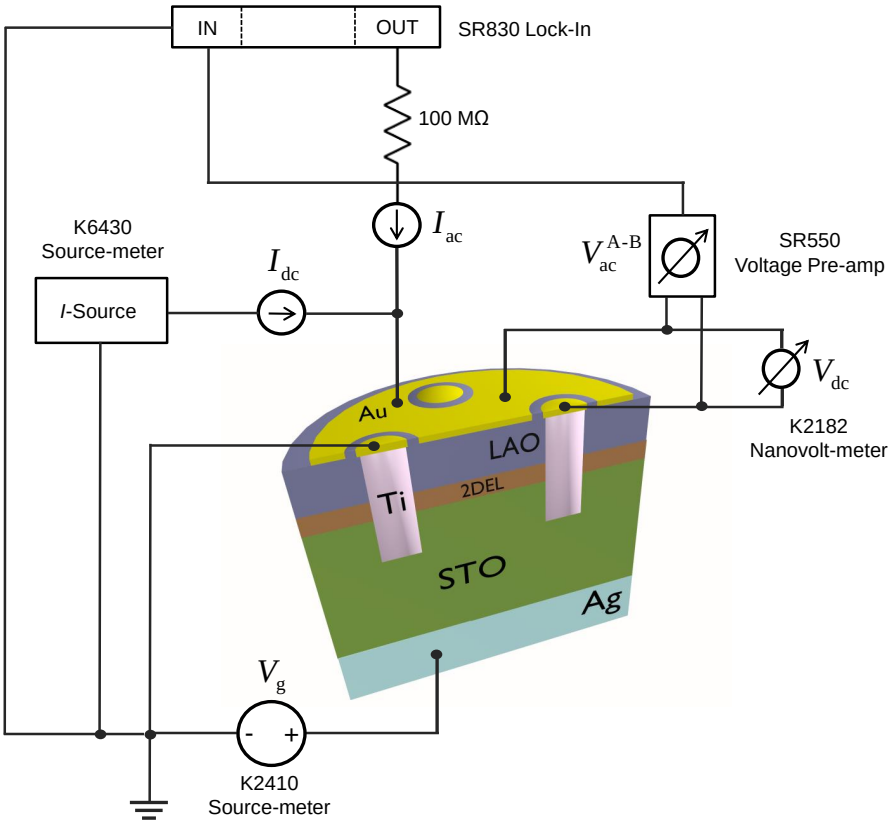

Figure 4.1: *Illustration of the tunneling spectroscopy measurement configuration. All instruments are connected as shown to an $LaAlO_3/SrTiO_3$-Au planar tunnel junction (a dimensional schematic is shown in Fig. 3.2, Ch. 3). The back-gate voltage V_g sourced to the Ag-foil below the $SrTiO_3$-substrate ranges in the interval -300 V < V_g < +300 V and is kept constant during a tunneling measurement. For the application of tunneling currents in the pico-ampere range, a sub-femto amplifier is serially connected to a Keithley 6430. A voltage preamplifier picks up the ac-response which is recorded with the SR830 unit. The ac-current component is constant, usually at 40 pA. The resistor at the signal output of the SR830 is of the order of 100 MΩ, while its input impedance is 10 MΩ (not shown). The tunnel resistance is in the order of 0.5 MΩ.*

Figure 4.2 shows an experimental observation of two $SrTiO_3$ phonon modes, with electrons tunneling from the $LaAlO_3/SrTiO_3$ 2DEL into the Au-layer on top of a four u.c. $LaAlO_3$ insulating barrier. The tunnel spectra are recorded at 50 mK and for several back-gate field values. The convention used in this chapter is: for $V < 0$ electrons tunnel out of the 2DEL and into the top electrode. Two phonon peaks are clearly visible at 60 and 100 meV and correspond to the LO3 and LO4 phonon modes of $SrTiO_3$ [16]. Indeed, their peak location does not vary with gate voltage; it is actually independent and an intrinsic feature of the $SrTiO_3$ structure. Moreover, this finding is direct evidence of tunneling between Au and the 2DEL.

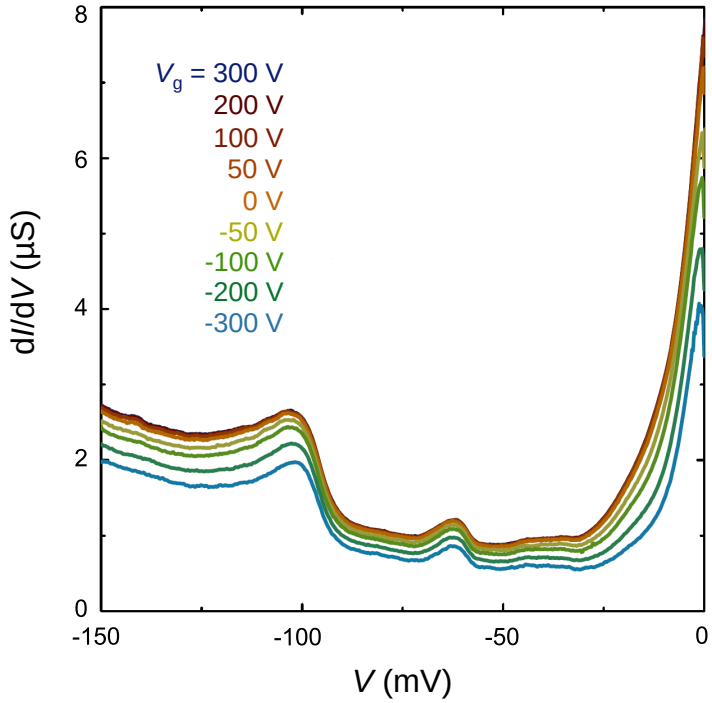

Figure 4.2: *Tunneling characteristics of the $LaAlO_3/SrTiO_3$ 2DEL at 50 mK. The energy scale here contains all phonon modes that can be resolved from the Fermi level up to 150 meV, and is about 1000 times larger than that of superconducting features. The color code highlights the different gate fields applied. Negative voltage values correspond to carrier depletion. From [15].*

4.2 The $LaAlO_3/SrTiO_3$ Phase Diagram

As shown by the pioneering work of Thiel et al. in 2006 [10] and Caviglia et al. in 2008 [13], reversible tuning of the charge carrier concentration at the $LaAlO_3/SrTiO_3$ 2DEL is possible, via the electric field effect [17]. This has enabled the extensive study of the superconducting ground state of $LaAlO_3/SrTiO_3$, with a number of scientific groups being involved in understanding the properties of the dilute 2D superconductor.

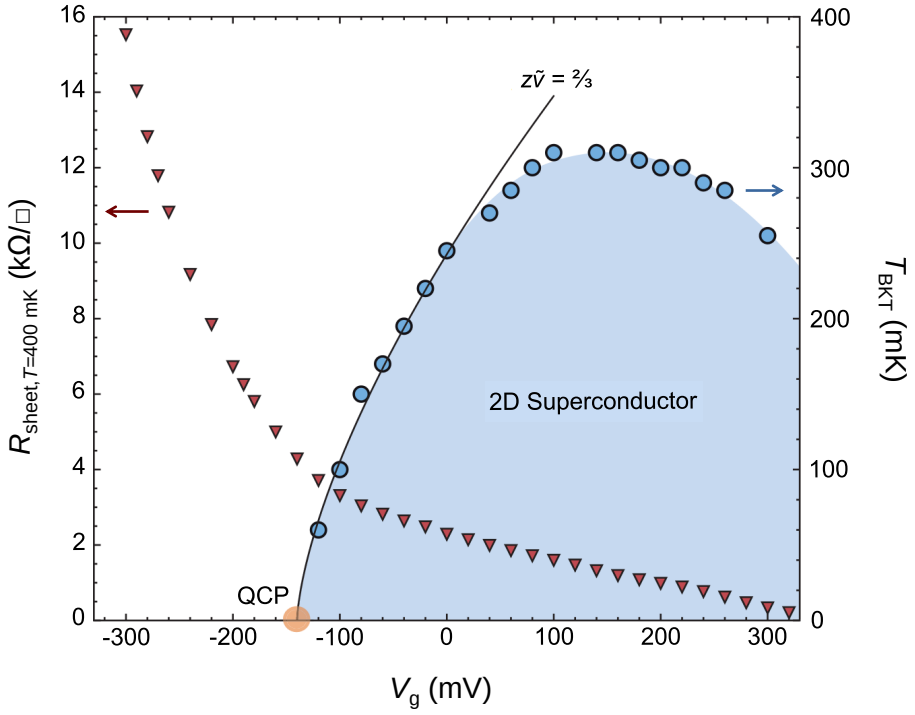

Figure 4.3: *The $LaAlO_3/SrTiO_3$ sheet resistance (red triangles) and the superconducting critical temperature T_c (blue circles) versus applied back-gate voltage V_g. The T_c dependence on V_g defines a superconducting dome, with a superconducting onset and a quantum critical point at $V_g \approx$ -150 V. From [13].*

The dielectric constant of $SrTiO_3$ is 300 at room temperature and increases by almost two orders of magnitude at 4.2 K. Such a high value is related to the incipient ferroelectric character of $SrTiO_3$ [10, 18] and allows for injection or withdrawal of charge carriers from the 2DEL, by applying positive or negative back-gate fields at the $SrTiO_3$ substrate, respectively. Figure 4.3 depicts the first experimental mapping of the $LaAlO_3/SrTiO_3$ phase diagram [13], using the electric field effect. Measurements of the resistivity with respect to temperature have been used to identify the superconducting onset at different charge carrier concentrations and thereby to extract the superconducting dome (blue circles in the Fig. 4.3).

In a similar manner, four-point resistivity measurements have been performed for defining the superconducting dome in my work with $LaAlO_3/SrTiO_3$ [14]. The T_c in my sample was determined while

tuning the charge carrier density by the gate voltage. The criterion used for determining T_c is the temperature at which resistivity drops below the measurement noise-level. The underdoped, optimally doped and overdoped superconducting regions could be revealed. Figure 4.4 depicts the $R(T)$-curves at different values of the back-gate field, along with the top-view of the measurement configuration.

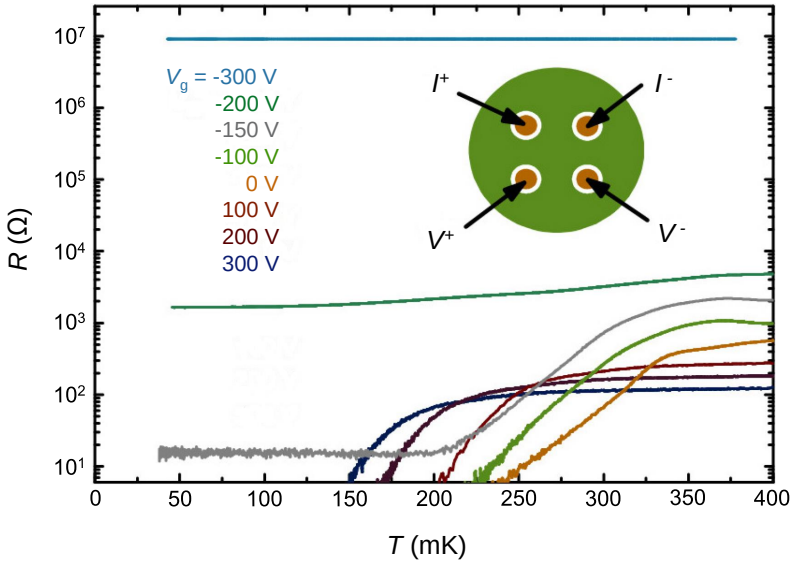

Figure 4.4: *R(T)-curves at different values of the back-gate field. For this particular sample, gate voltages of -200 V and -300 V withdraw more charge carriers than the minimum required for macroscopic superconductivity. At V_g = 0, the $LaAlO_3/SrTiO_3$ system shows the highest critical temperature and is thus considered to lie within the optimally doped superconducting region. The measurement configuration is shown at the top right corner, with green depicting the gold electrode and brown the interface contacts. From [14].*

The optimally doped region occurs at approximately zero back-gate voltage. The phase diagram extends from the resistive state (metallic or insulating), to the underdoped, optimally doped and overdoped superconducting regions, respectively within a gate-voltage span from -300 V to +300 V. The carrier density was measured to be approximately 2×10^{13} cm^{-2}, in the absence of back-gate fields. The carrier-density change with gate-field has been estimated by $C(V)$-spectroscopy at 7×10^{10} cm^{-2} V^{-1} at the base temperature [14, 19]. This dependence, although accurate for low values of the gate-field, departs from linearity when the absolute value increases to the order of hundred volts. This is because the dielectric constant of $SrTiO_3$ is gate-field dependent. The change of the carrier density for high gate-fields cannot be directly measured. I therefore present all data as a function of the gate voltage V_g rather than of the carrier concentration n_s.

4.2.1 Temperature and Gate Voltage Dependent Tunnel Spectra

As discussed before, tunneling spectroscopy gives the opportunity to measure the DOS of a superconductor. This section presents tunneling measurements of the 2DEL's DOS in the entire phase diagram, from 50 mK up to 700 mK. The first measurements aimed to map the temperature dependence of the DOS around E_F in the superconducting state. As inferred from Fig. 4.4, the $LaAlO_3/SrTiO_3$ 2DEL shows a critical temperature of about 300 mK at the optimally doped region, in good agreement with literature [20, 21].

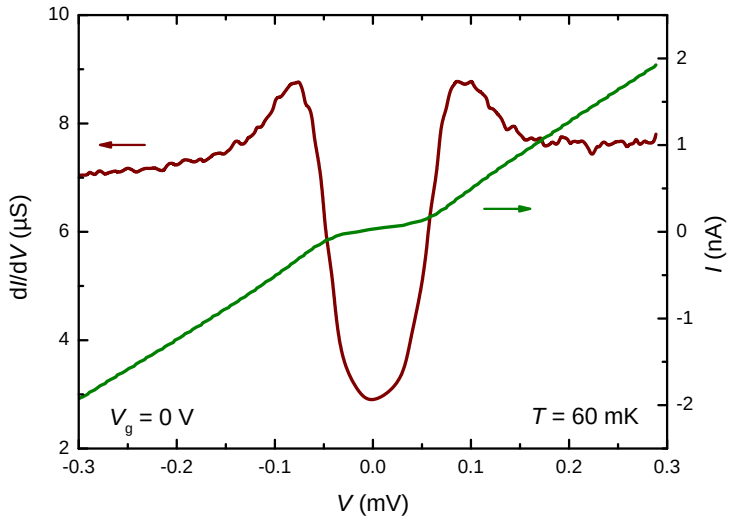

Figure 4.5: *A tunnel-spectrum and a $dI/dV(V)$ curve (brown) featuring the quasiparticle excitation peaks and the superconducting gap in the DOS of the $LaAlO_3/SrTiO_3$ 2DEL. Data were recorded at 60 mK, with no back-gate field applied. The dc-voltage sweep probes the energy-range where the gap and the excitation peaks emerge from the normal state conductance level, around the Fermi energy ($V = 0$). The $I-V$ characteristic (green) is also plotted.*

The I - V characteristic and the respective dI/dV-dependence (this is the ac-conductance as a function of dc-voltage), at zero gate-field and at 60 mK, are presented in Fig. 4.5. The superconducting gap in the DOS and the quasiparticle peaks are clearly visible (brown curve). The gap is in the order of 60 μeV. As discussed, the non-linearity of the I - V characteristics (green curve) is due to opening of the superconducting gap at the DOS of the $LaAlO_3/SrTiO_3$ 2DEL, as evidenced in the figure.

Important information on the superconducting properties is embedded in the evolution of the dI/dV with respect to temperature. Figure 4.6 shows the $dI/dV(V)$ characteristics as a function of temperature, from T = 60 mK to $T > T_c$. Each of the four panels corresponds to a different region in the phase diagram, based on the characterization by transport. In the entire gate-field range of investigation, the superconducting features are clearly visible and always evolve with temperature in the same manner,

i.e. the gap gradually disappears as the conductance reaches its normal state value (background) with increasing temperature. The background conductance level shows a V-shape that is attributed to an Altshuler-Aronov reduction of the DOS near the Fermi energy [22]. Interestingly, the superconducting gap is largest at the extremely underdoped region and decreases with increasing gate-field. This behavior is particularly pronounced when comparing the curves of all panels at 60 mK.

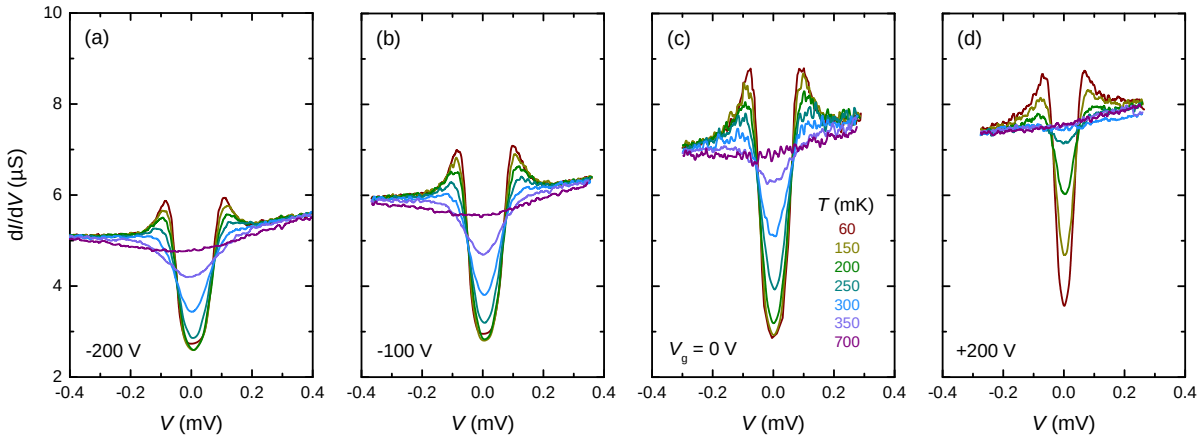

Figure 4.6: *The temperature-dependent tunnel spectra measured at four different regions of the phase diagram. a) the extremely-underdoped or resistive region, b) the underdoped, c) the optimally doped and d) the overdoped superconducting region. All four panels have the same scale. The color code used to distinguish the measurement temperatures is also identical (shown in (c)).*

Figure 4.7 presents the gate-voltage dependence of the tunnel spectra at three fixed temperature-values, i.e. 60 mK, 250 mK (this value is chosen to investigate close to but below T_c) and 400 mK. In these plots, the effect of the back-gate field can be directly observed; that is the charge carrier depletion at negative bias application. The normal conductance level surrounding the superconducting features gradually decreases, following the gate-field decrease, since the chemical potential μ approaches the edge of the conduction band where the DOS is smaller. This effect is also visible in Fig. 4.6. Positive fields however do not increase the normal conductance which is attributed to the fact that additional carriers start populating a different band which does not participate in tunneling [15, 23]. Therefore, the conductance background has a constant value as the positive gate field increases. The conductance value at the center of the gap is not zero, but finite. The measurements take place at finite temperatures (the base temperature T_{base} of the dilution fridge is approximately $0.16 \times T_c$) and thus the I - V characteristic for $0 < eV < \Delta$ is non-zero (see Fig. 2.9 in Ch. 2).

As discussed in Ch. 2, the features of tunnel-spectra carry information about the superconducting gap Δ and the quasiparticle lifetime broadening Γ. The $dI/dV(V)$ characteristics yield the DOS close to E_F for $LaAlO_3/SrTiO_3$, so Δ and Γ can be determined by fitting the measured curves. The temperature dependence of these two parameters provides information about the superconducting nature of the 2DEL.

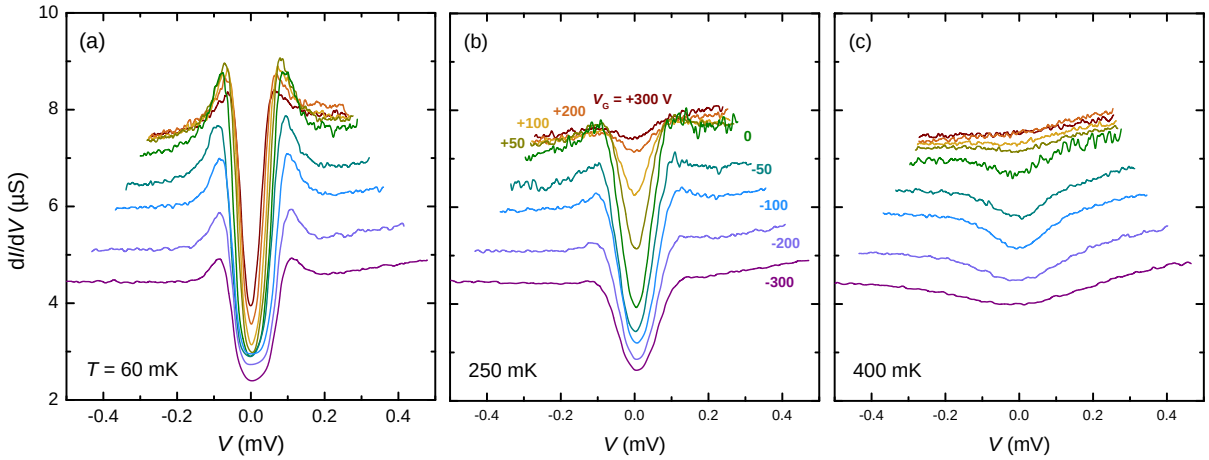

Figure 4.7: *The gate voltage dependent tunnel spectra. The V_g-evolution a) at 60 mK, b) at 250 mK, very close to T_c in the optimally doped region, and c) at 400 mK where no superconducting features are present at the overdoped, but with DOS-gap signatures at the optimally doped, underdoped and resistive regions.*

4.2.2 Determination of the Superconducting Gap and the Quasiparticle Excitation Peak Broadening from the Tunnel Spectra

From the tunnel spectra, the gap at the DOS and the quasiparticle-peak broadening can be quantified if one takes into account the BCS-expression of the DOS-structure for arbitrary energy E [6, 7]:

$$\rho_s(E) = \rho_n(E_F)\frac{|E-E_F|}{\left[(E^2-E_F^2)-\Delta_0^2\right]^{1/2}} \tag{4.1}$$

Here, $\rho_s(E)$ stands for the quasiparticle DOS, $\rho_n(E_F)$ is the (normal) background density of states at the Fermi level in the absence of superconductivity, which is assumed constant for energies close to E_F. The quantity Δ_0 is the real amplitude of the complex order parameter $\Delta = \Delta_0 e^{i\phi}$, with $|\Delta|^2 = \Delta_0^2$. It is half the magnitude of the gap in the DOS. In the above expression, $\rho_s(E)$ is zero for $|E| < E_F + \Delta_0$ (the term on the right becomes imaginary), reaches infinity at $E = E_F + \Delta_0$ and reduces rapidly towards $\rho_n(E_F)$ for $|E| > E_F + \Delta_0$.

In more practical terms, setting $E_F = 0$ and assuming a small energy interval around the Fermi energy, the normalized quasiparticle DOS can be obtained by the expression:

$$\rho(E) = \mathrm{Re}\left\{\frac{|\mathrm{E}|}{(\mathrm{E}^2 - \Delta_0^2)^{1/2}}\right\} \tag{4.2}$$

The real amplitude Δ_0 of the complex order parameter will be from now on denoted as Δ for simplicity. BCS-theory predicts that the $I-V$ characteristic (at $T = 0$) is discontinuous at an interval of 2Δ symmetrically extending around the Fermi energy. In experiments however and at finite temperatures, the $I-V$ is continuous and $\rho(E)$ has a finite slope at $E = |\Delta|$. This can be also observed in tunnel spectra, even at base temperature, where finite broadening of the quasiparticle peaks is present. This feature is attributed to the finite lifetime of a quasiparticle excitation, as discussed by Dynes et al. [24]. This broadening can be quantified by modifying Eq. 4.2 with the addition of an imaginary, energy-independent part to the energy E. This expression, although valid close to the Fermi energy (order of $k_B T$), is weak for $E >> |\Delta|$ as additional terms that consider self-energy effects would be required [24, 25]. One therefore obtains the new form for the normalized quasiparticle DOS:

$$\rho(E,\Gamma) = \mathrm{Re}\left\{\frac{\mathrm{E} - \mathrm{i}\Gamma}{[(\mathrm{E} - \mathrm{i}\Gamma)^2 - \Delta^2]^{1/2}}\right\} \tag{4.3}$$

Equation 4.3 can be used in the expression for the differential conductance between a metal (assuming constant DOS) and a superconductor [8]:

$$\frac{dI}{dV}(V) = G_0 + G_1 \int_{-\infty}^{\infty} \rho(E,\Gamma)\frac{-\partial f(E+eV)}{\partial V} dE \tag{4.4}$$

In the above expression, "f" is the Fermi-distribution function. The quantity $\frac{-\partial f(E+eV)}{\partial V}$ is sharply peaked and positive at $E = -eV$ and at the $T \to 0$ limit it yields $\rho(-eV) = \rho(eV)$. This satisfies the requirement for finite energy of the order of the superconducting gap Δ, so that tunneling into the superconductor can occur. G_1 is the normal background conductance while G_0 accounts for additional, independent contributions to the conductance (i.e. leakage currents) and is found to be zero throughout my analysis.

The fitting model for the tunnel spectra uses the expression 4.4 with the DOS-structure of 4.3. The entire treatment assumes s-wave symmetry for the $LaAlO_3/SrTiO_3$ 2D superconductor. This assumption is supported by the agreement of the fitting results to a conventional BCS temperature dependence. The model also takes into account the Altshuler-Aronov suppression of the conductance at the Fermi level,

which yields a V-shaped background centered at E_F in the tunnel spectra. Two linearly extrapolated lines, one from the far positive and the other from the far negative side of the spectrum (away from the quasiparticle spectral region) merge at $V = 0$ and define the normal conductance background when fitting the superconducting DOS. Figure 4.8 graphically presents the fitting of a tunnel spectrum. At low temperatures, the fitting is fairly accurate across the phase diagram, however as $T \to T_c$ the errors of the extracted values for Δ and Γ become larger.

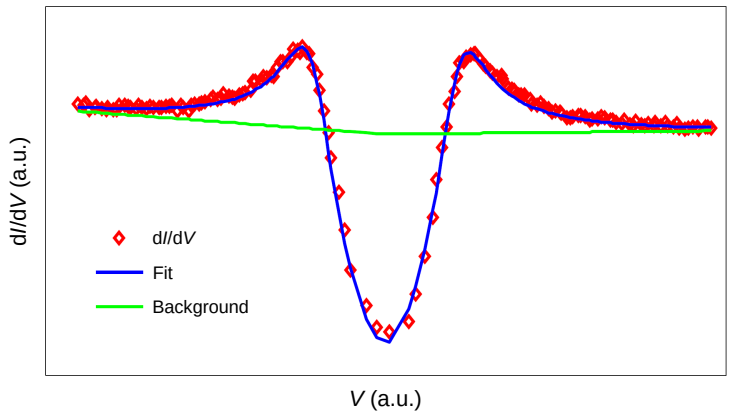

Figure 4.8: *The fitting model applied (using MATLAB) on the tunneling characteristics of $LaAlO_3/SrTiO_3$. In this particular case, V_g = +50 V, H = 0 T and T = 60 mK. The red rhombi are experimental points from $dI/dV(V)$ measurements. The blue line is the actual fitting model and the green lines stand for the V-shaped background which was always assumed.*

Figure 4.9 shows the extracted values of Δ and Γ with respect to temperature for the optimally doped superconducting region (V_g = 0). The broadening of the quasiparticle peak dependence on temperature ($\Gamma(T)$) is opposite to that of the superconducting gap. This is expected when the superconductivity is suppressed at finite temperatures and is consistent in the entire phase diagram. At temperatures far below T_c, the quasiparticle peaks yield low Full Width at Half Maximum (FWHM). Theoretically, at $T = 0$, the quasiparticle DOS shows a singularity [25,26]. As temperature increases, the thermal phonon population increases accordingly and induces a finite spectral width on the peaks around the superconducting gap due to energy loss of quasiparticles that scatter inelastically with phonons. Above a threshold temperature (still below T_c), the quasiparticle scattering rate becomes comparable to the Cooper-pair recombination rate (which is always higher at $T \to 0$) [25]. This is the point where scattering becomes dominant and the quasiparticles are now more likely to transmit energy to the thermally induced phonons [27]. Thereby the quasiparticle peaks in the tunnel spectra broaden with increasing temperature, as is evident by the increase of Γ, before superconductivity is destroyed. Yet, there is a possibility of other scattering

mechanisms besides phonons that can lead to broadened quasiparticle peaks in the tunnel spectra of $LaAlO_3/SrTiO_3$. A definite conclusion of the exact nature of the quasiparticle scattering cannot be inferred from the data.

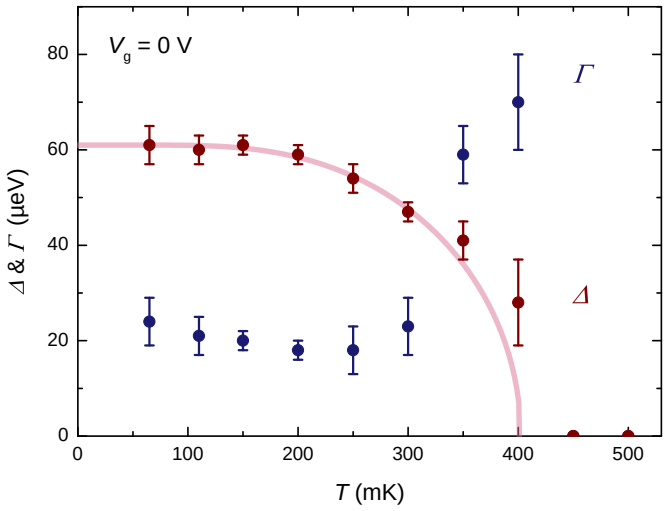

Figure 4.9: *Plot of $\Delta(T)$ (brown points) and $\Gamma(T)$ (blue points) dependencies, at $V_g = 0$ V. The superconducting gap Δ follows the BCS-dependence on temperature well (pink curve), while Γ, although relatively constant at temperatures below T_c, increases at higher temperatures until superconductivity vanishes. When the critical temperature is surpassed, the Δ and Γ values are zero.*

An additional contribution to the broadening of the peaks comes from the Fermi-distribution function. As temperature increases, $f(E)$ "smears-out" and the measured $dI/dV(V)$ spectra do not reflect the DOS structure of the 2DEL entirely accurately, but appear broader than the DOS. This additional smearing becomes already significant at intermediate temperatures, before the onset of superconductivity.

In Fig. 4.10, the $\Delta(T)$ and $\Gamma(T)$ characteristics are presented for nine V_g-values. The superconducting gap is not only preserved in the resistive regime (-300 V and -200 V), but also decreases with increasing gate-voltage. The temperature dependence of the gap follows the BCS-expectation very well (pink curves), in both the optimally doped and overdoped regions. In the regimes of depletion ($V_g < 0$) and for T close to T_c, the uncertainty is relatively large when fitting the tunneling characteristics with the Dynes-model. Therefore, a departure of $\Delta(T)$ from the BCS-trend is observed. The dependence of Γ on T is also consistent in the entire phase diagram.

An indication of the pairing interaction strength and robustness of the superconducting ground state is reflected in the ratio of Δ and Γ. The Δ / Γ dependence on T is plotted in Fig. 4.11, for the same V_g-values seen in Fig. 4.10. The ratio is enhanced at back-gate voltages of -50 V, 0 V and 50 V, compared to other regions in the phase diagram, as these values correspond to the optimally doped superconducting region.

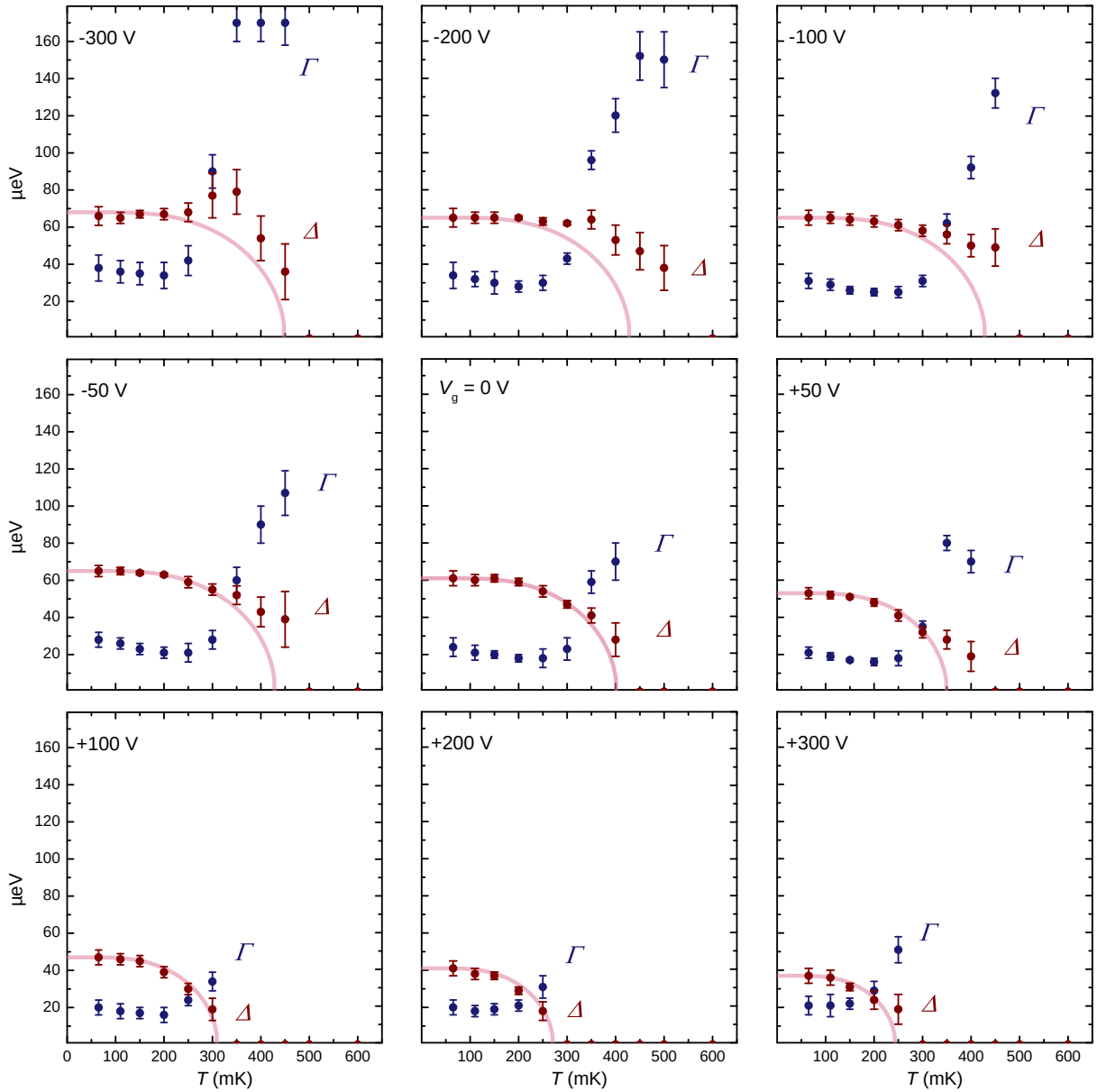

Figure 4.10: *From top-left to bottom-right panel, the Δ(T) (brown points) and Γ(T) (blue points) characteristics are given as a function of increasing gate voltage, starting from far into the resistive state (V_g = -300 V) until the far overdoped superconducting region (V_g = +300 V). The pink curves represent the BCS temperature-dependence of Δ. For Δ(0) I assume the value of Δ measured at the lowest temperature and also $2\Delta/k_BT_c$ = 3.527 [26]. At large negative gate fields (especially at -300 V), already from intermediate temperatures, the Δ values deviate from a pure BCS temperature-dependence owing to an increased model-inconsistency in fitting the superconducting features that extend over the entire data range. The error bars denote the deviation of the values derived from fitting each spectrum, which is performed typically from three to five times with different horizontal offsets. Larger temperature deviations induce additional errors to the measurements at 60 mK and 100 mK. All axes have the same scale.*

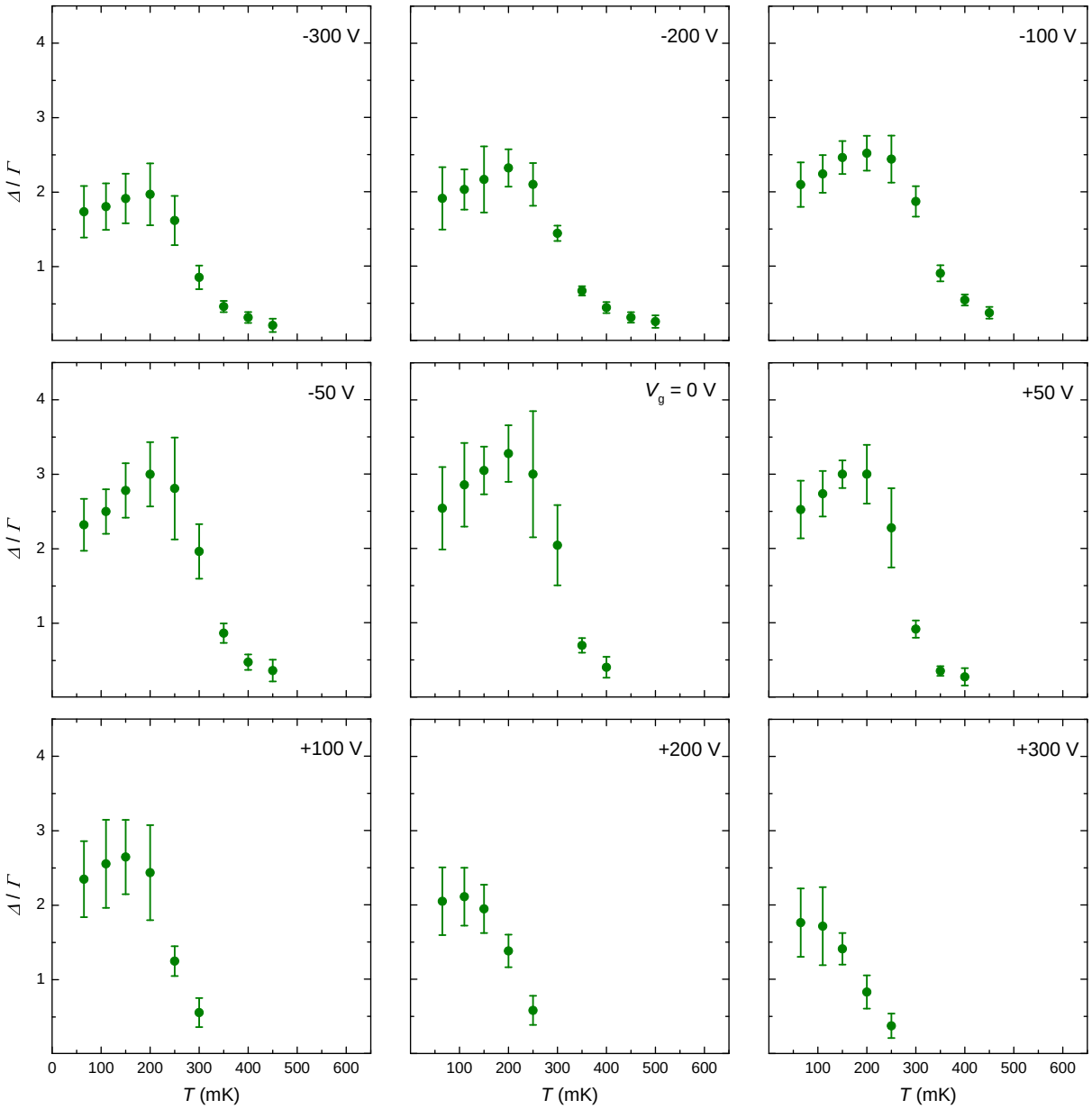

Figure 4.11: *From top-left to bottom-right panel, the $\Delta/\Gamma(T)$ ratio is presented. It is qualitatively similar in almost all regions except at +200 V and +300 V, and increases slightly with increasing temperature up to 200 mK before it rapidly drops to zero at the critical temperature of the respective region. The error bars feature the propagated deviations from those calculated for Δ and Γ.*

A peculiar feature that can be seen in 4.11, is that the ratio increases for $T \leq 200$ mK, before dropping to zero at T_c. This is in contrast to the expected gradual suppression of the superconductivity with increasing temperature. Owing to an increased uncertainty at the lowest temperatures, especially in extracting parameter Γ from the spectra, this is possibly a fitting-related artifact that appears in the calculation of Δ/Γ, albeit the general consistency in the extraction of Δ. It might yet be interesting to elaborate on the dependence of the broadening parameter Γ in other superconductors, i.e. the cuprates.

As $T \rightarrow T_c$ for all gate voltages, the uncertainty again increases. This is principally due to the large broadening of the quasiparticle peaks that extends to almost the entire data range. The Altshuler-Aronov suppression of the DOS in the absence of superconductivity may still yield finite values for Δ when fitting the data. Thus when the absolute value is surpassed by the uncertainty margin, Δ is considered zero.

Figure 4.12 presents the Δ/Γ-ratio with respect to V_g. According to the tunneling spectroscopy data, superconductivity is most prominent in the optimally doped and persists in the entire doping range of investigation, in contradiction with the $R(T)$-measurements of the phase diagram that yields finite resistance for the gate voltages of -200 V and -300 V (see Fig. 4.4).

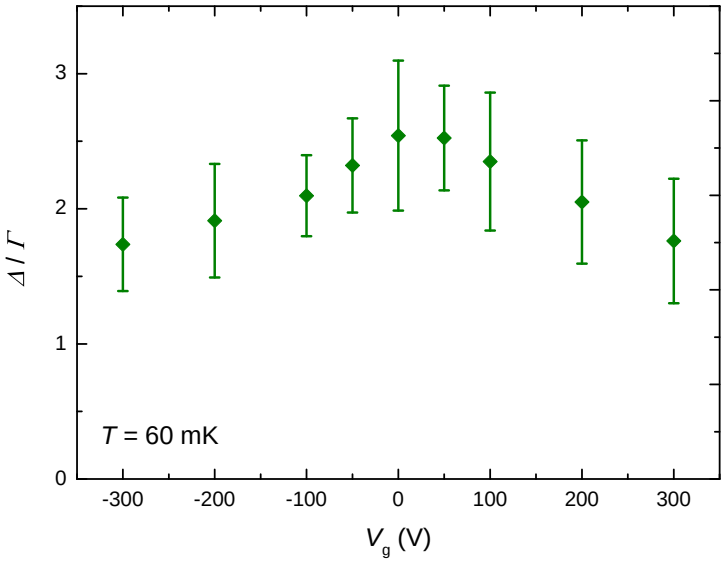

Figure 4.12: *The Δ / Γ-dependence on back-gate voltage at base temperature, as calculated shown in Fig. 4.11. The ratio is an indication of the superconducting strength in the phase diagram, and shows a maximum at the optimally doped region.*

4.2.3 Pseudogap Behavior of the $LaAlO_3/SrTiO_3$ 2DEL

The spectroscopic investigation of the 2DEL phase diagram offers an alternative view on the evolution of superconductivity with carrier concentration. So far we have seen in this section that superconducting properties are preserved on the tunnel spectra for all gate-voltages (see Figs. 4.6 and 4.10). This finding seems to contradict the transport results. In Fig. 4.4, sheet-resistance measurements on the same sample have mapped the phase diagram of the superconducting 2DEL and yielded finite resistance at the far negative gate-voltage regime (-200 and -300 V). It seems puzzling that in the very depleted (resistive) region superconducting features are still visible in tunneling, although macroscopic ($R(T)$-defined)

superconductivity is absent.

The disappearance of the superconducting features in tunneling is the criterion used for marking the onset of superconductivity itself. In contrast to expectations that transport and spectroscopy characterize the superconducting state similarly, our findings point to a different scenario, summarized in Fig. 4.13.

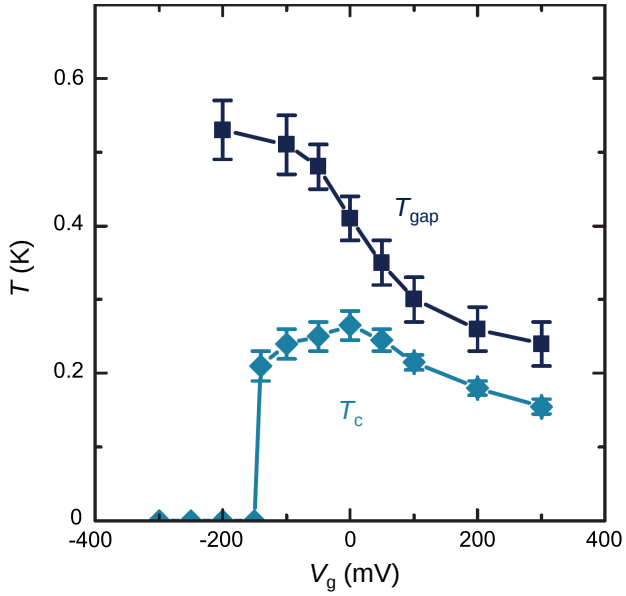

Figure 4.13: *The superconducting dome of $LaAlO_3/SrTiO_3$ as mapped by transport and tunneling spectroscopy. The light blue curve marks the onset of superconductivity (T_c) as extracted by the $R(T)$-measurements. At a threshold-value of V_g close to -150 V and lower, finite resistance can be measured at the entire temperature range of investigation (down to 50 mK) and macroscopic superconductivity is destroyed. The dark blue curve corresponds to the superconducting onset revealed by tunneling spectroscopy (T_{gap}) and defined as the temperature at which the superconducting features (gap and quasiparticle peaks) in the DOS vanish completely. From [14].*

The light-blue curve illustrates the superconducting onset at different gate voltages that correspond to the doping level of the superconductor and exhibits the dome-shape superconducting region in a temperature-versus-doping phase diagram for $LaAlO_3/SrTiO_3$. The dark-blue curve corresponds to the critical temperatures determined by tunneling spectroscopy. The two curves, although similar in the overdoped regime, deviate in the optimally-doped and further at lower doping. Moreover, instead of dropping to zero, the tunneling-defined superconducting onset increases with decreasing V_g until -300 V, the lower voltage-limit for electrostatic tuning in this sample.

On one hand, a finite resistance measurement is undoubtedly evidence for disappearance of superconductivity by strong depletion. The decrease of T_c with decreasing charge carrier density is due to either emergent competing orders or weakening of the superconducting phase coherence. In the case that

phase coherence exists in the extremely depleted regime, a decrease in the superfluid density can account for the observed decrease of T_c [28]. Measurements performed by Bert et al. on $LaAlO_3/SrTiO_3$ [29] indeed report on a drastic decrease of the superfluid density upon carrier depletion.

On the other hand, the imprint of superconductivity on the tunnel spectra, with the superconducting features preserved at carrier densities low enough to yield finite resistance, is reminiscent of the pseudogap phase seen in the high temperature superconductors [30–32]. Figure 4.14 summarizes the resemblance into a simple, qualitative graphic.

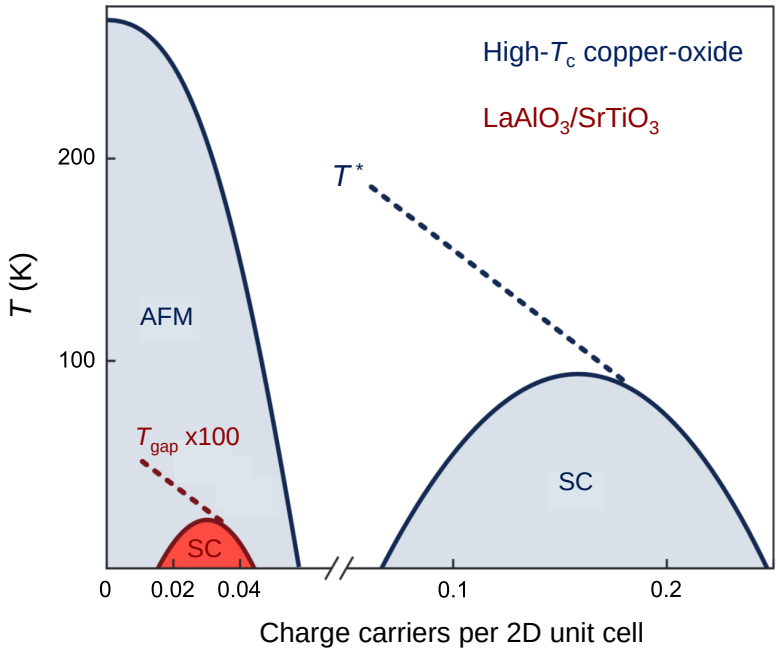

Figure 4.14: *The superconducting dome of the $LaAlO_3/SrTiO_3$ interface (red-filled area), 100-times enlarged, presented on a temperature versus charge-carrier doping diagram. For comparison, a qualitative phase diagram of the high-temperature, copper-oxide superconductors (light-blue areas) is embedded in the graph. There is a striking similarity in the behaviors of T^* and T_{gap}, with respect to the superconducting dome for each case. From [14].*

The similarity of T^* for the cuprate superconductors [33, 34] and the T_{gap}-curve yielded by tunnel spectroscopy is conspicuous. T_{gap} follows T_c in the overdoped region but increases rapidly before the optimally doped and deep into the carrier-depleted regime. Yet, from these measurements, little can be said about the resistive region ($V_g \leq$ -150 V). Investigations on the nature of superconductivity in this region have been carried out by studying the magnetic field dependence of the tunnel spectra. They will be presented in detail in a separate section.

At this point, the pseudogap-like behavior seen on $LaAlO_3/SrTiO_3$ is of particular importance, as it is possible that the physics of this regime is similar to that of the pseudogap regime seen in the cuprates. The superconducting features of the tunnel-spectra point to a conventional, s-wave symmetry and the

Δ-dependence on temperature, complying with the BCS picture. It is yet unclear what mechanism drives the pertaining superconductivity in the highly-depleted region, where pairing other than s-wave is also a possibility. An equally interesting question is whether pseudogap behavior and two dimensional superconductivity are related. Extending this hypothesis further, other two-dimensional systems can provide an additional overview. A relevant example is the FeSe monolayer grown on $SrTiO_3$ (doped and undoped) [35–37]. This system exhibits superconductivity up to very high temperatures; however a pseudogap behavior has not been reported so far.

The pseudogap behavior seen on $LaAlO_3/SrTiO_3$ has triggered high interest in the community and consequently motivated several studies to interpretation-attempts and also to extending the investigation in similar systems. Some of the examples can be found in Refs. [37–40].

4.2.4 The Role of the Electron-Phonon Coupling

For a better understanding of the pseudogap behavior seen on $LaAlO_3/SrTiO_3$, additional work has been carried out (see H. Boschker et al. [15]), which focused on the investigation of the pairing mechanism and in particular the strength of the electron-phonon coupling, in different regions of the phase diagram of the 2DEL.

By tunneling within a larger energy range (order of 100 meV) around the Fermi energy, the phonon modes of $SrTiO_3$ (see Fig. 4.2) were resolved. The electron-phonon spectral function and chemical potential evolution across the phase diagram were determined and the electron-phonon coupling was calculated. It was found that there exists pronounced coupling to longitudinal optical (LO) phonon modes of $SrTiO_3$, in particular to the LO3 and LO4 modes, although coupling to acoustical modes could not be excluded from the data. The McMillan parameter λ [41] that accounts for the coupling strength has been extracted from the electron-phonon spectral function $a^2F(\omega)$, using the expression:

$$\lambda = 2\int_0^\infty a^2F(\omega)/\omega \cdot d\omega \tag{4.5}$$

Figure 4.15 shows the evolution of λ, μ, T_{gap} and T_c with gate-voltage. It appears that electron-phonon coupling is larger for negative V_{g} and increases with increasing carrier depletion. On the other hand, the chemical potential increases with increasing gate-voltage until the overdoped superconducting region. There both dependencies reach a plateau and are no longer affected by the V_{g}-increase. This work provides evidence that the increased electron-phonon coupling in the underdoped regime can account for the increased value of T_{gap}. Albeit a low superfluid density, the electron-phonon coupling is pronounced owing to a small Fermi surface and the large phonon energies (60 meV and 100 meV) which are not screened by plasmonic excitations [15, 42]. In the overdoped side, the chemical potential is independent

of gate-voltage. This suggests that injected charge carriers populate one or more different bands [23,43] that do not participate in tunneling; they do however suppress superconductivity via Coulomb scattering and thereby T_{gap} and T_c decrease.

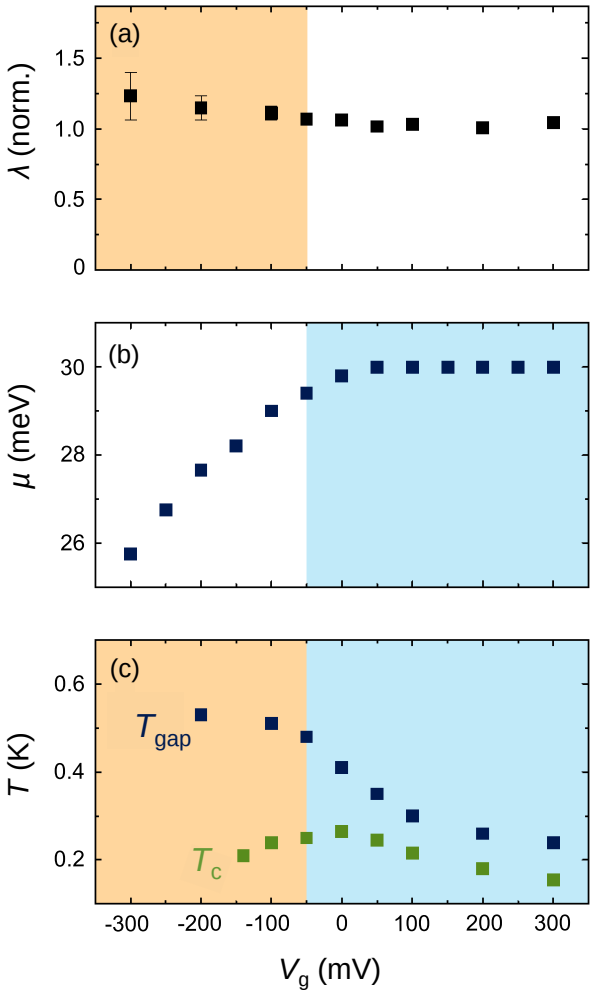

Figure 4.15: *The gate-voltage dependence of (a) the electron-phonon coupling strength λ, normalized to the value in the overdoped region, (b) the chemical potential μ and (c) the superconducting onsets T_{gap} and T_c as described in the previous section. As shown, λ is enhanced in the underdoped regime and increases with decreasing gate-voltage, whereas it remains constant in the overdoped regime. Also μ increases with increasing gate-voltage until it saturates to approximately 30 meV in the overdoped regime. The T_{gap} and T_c dependencies are presented for a qualitative comparison. From [15].*

4.3 Longevity of the Superconducting Properties

The extreme sensitivity to growth parameters demands that series of measurements are performed on a single sample, that can often take place more than a year apart. To eliminate the possibility of an aging effect or any permanent structural change due to the field-effect gating on this sample, measurements of the superconducting gap were repeated. This is for checking whether important properties (i.e. the superconducting gap, tuning of the charge carriers) have degraded over time. The experiments shown in this section were performed during a time span of years. We found that the sample showed consistent results during this time. Figure 4.16 shows both sets of values for the superconducting gap, taken in 2013 and 2014.

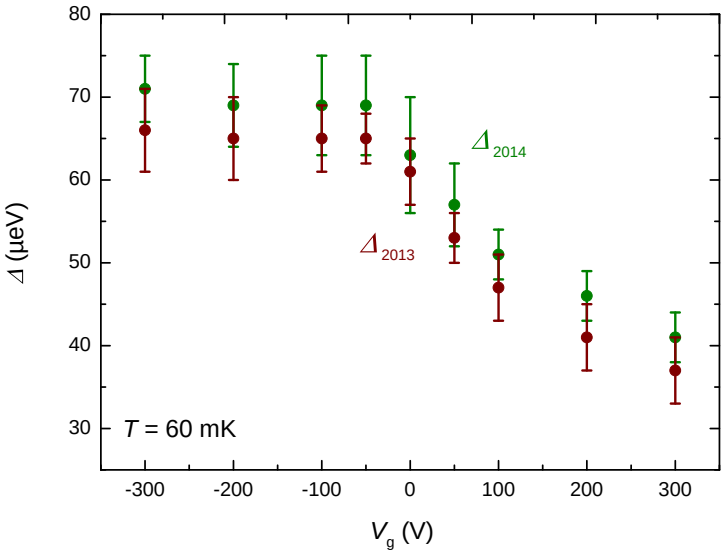

Figure 4.16: *The Δ-dependence on V_g for two sets of measurements. The brown points are measurements from 2013, green points are from 2014. The fitting routine applied on the tunnel spectra (introduced in the previous section) is identical for both cases. The error margins correspond to deviations of the fitting model applied typically between three to five times on each curve, while varying the dc-voltage offset.*

The gap-values obtained in 2014 are slightly larger than those of 2013 [14]. This systematic deviation may be due to slow O_2-diffusion processes that can affect the carrier concentration in the 2DEL through time. Yet, the $\Delta(V_g)$-dependence is essentially identical in both measurement-sets.

The quasiparticle lifetime broadening parameter Γ has been also re-evaluated. The Δ/Γ ratio comparison is presented in Fig. 4.17. Verifying our expectation from the $\Delta(V_g)$ dependencies, the superconducting profiles reflected in the Δ/Γ ratio are very similar. The superconducting condensate is weakened at the far overdoped (+100 V, +200 V and +300 V) regions. Most importantly, the superconducting domes of 2013 and 2014 almost match, with the optimally doped region residing always at zero back-

gate field in the sample.

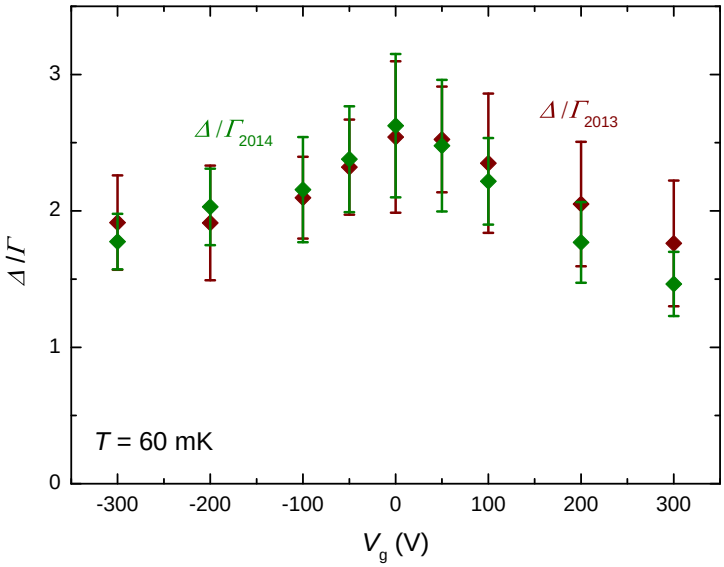

Figure 4.17: *The Δ/Γ ratios from measurements of 2013 (brown) and of 2014 (green). Both $\Delta(V_g)$-dependencies are qualitatively similar and within the error margins assigned to each experimental point.*

In the next sections, an additional parameter, an external magnetic field oriented perpendicular to the 2DEL plane is introduced. The robustness of the superconducting ground state of $LaAlO_3/SrTiO_3$ through time and during intensive gating allows us to do such measurements.

4.4 The Superconductor-to-Metal-to-Insulator Transition across the Phase Diagram

With the introduction of the localization theory by P. W. Anderson [44], numerous studies have been carried out to understand how disorder affects transport. Reduced dimensionality plays a special role, as the effect of disorder is enhanced in confined dimensions. The emergence of superconductivity in metallic systems at low temperatures has offered novel research potential, with substantial experimental work addressing the transition from the superconducting to the insulating state by tuning disorder [45–51]. A.I. Shalnikov presented the first experiments on the investigation of the superconductor-to-insulator transition (SIT) of Pb and Sn films, in 1938 [52].

SITs are quantum phase transitions (QPTs). These are transitions between two quantum phases at zero temperature, driven by external parameters such as disorder or magnetic field. $R(T)$-measurements have shown that disorder reduction in thin films (by increasing thickness) drives a transition from an insulating to a superconducting state. This occurs at a particular value of the film's resistance [46, 47], known as the quantum-resistance of paired electrons ($R_Q = h/4e^2 \approx 6.45\ k\Omega$).

There are numerous examples of thin metallic films exhibiting an SIT. There exist cases, however, in which the evolution from the superconducting to the insulating state is not as sharp, with a metallic state intervening the superconducting and the insulating ones. These cases are experimental manifestations of the so-called SMIT [53–63]. These transitions can be generally induced by tuning disorder or the charge carrier concentration, while Cooper pairs reportedly exist even in the insulating state [64–78]. The $LaAlO_3/SrTiO_3$ 2DEL exhibits an SMIT, as is evident from $R(T)$ and $R(H)$ measurements performed by a number of groups [13, 79–85].

The emergence of the pseudogap-like behavior, owing to an enhanced electron-phonon coupling in the carrier-depleted regime, asks for a detailed investigation of the nature of the Cooper-pairs. Given the unique perspective of the superconducting DOS offered by tunneling spectroscopy, it is important to characterize the transition to the depleted regime of the 2DEL [13]. This section will elaborate on the investigation of the SMIT on $LaAlO_3/SrTiO_3$ through transport measurements of the sheet resistance, while tuning the gate-voltage and sweeping magnetic fields perpendicular to the interface-plane.

4.4.1 Evolution of the 2DEL Resistance with Perpendicular Magnetic Fields

Transport measurements have been employed to map the SMIT-crossover by measuring the $LaAlO_3/SrTiO_3$ sheet resistance as a function of temperature and gate voltage. Of particular interest here, is the finite sheet resistance in the depleted regime.

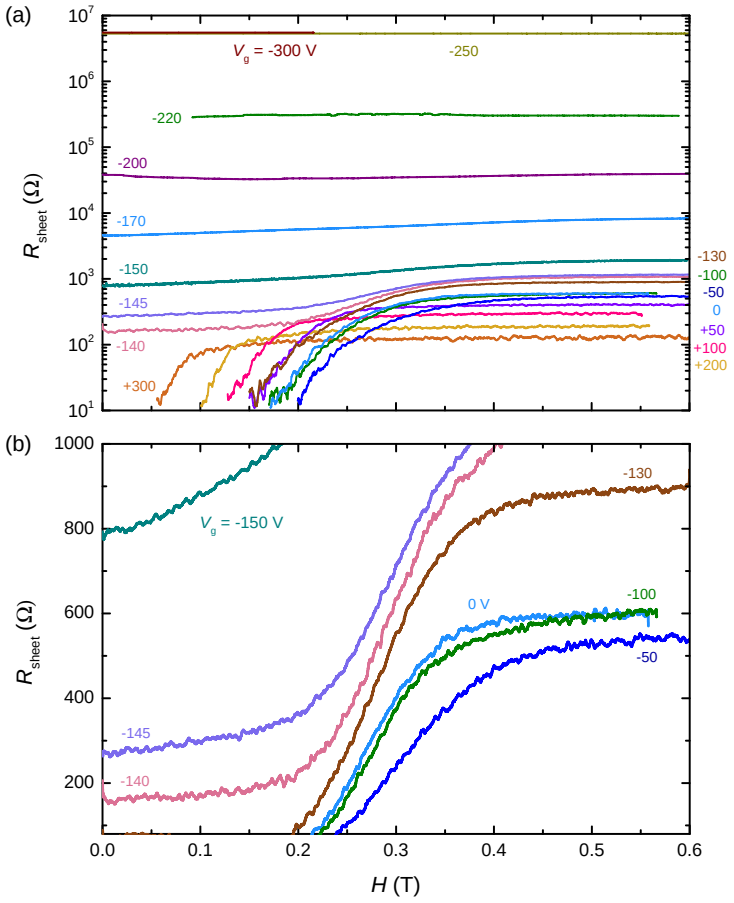

Figure 4.18: *(a) The R(H)-dependence across the phase diagram as a function of gate-field (values shown in volts next to each curve), plotted on a logarithmic scale. Curves for V_g > -150 V have been smoothed, as the measurement noise rises drastically for R_{sheet} < 50 Ω. (b) The same measurements, plotted on a linear scale, with the focus on the SMIT crossover. At -140 V < V_g < -130 V, finite resistance emerges, even at H = 0. The temperature is 60 mK and the magnetic field is swept at a rate of 5 mT/min.*

Figure 4.18 presents the resistance-versus-magnetic field measurements performed on the 2DEL, by applying ac-currents of 5 nA and 8.333 Hz and simultaneously recording the ac-voltage. This reference frequency value is kept constant throughout this work, in order to avoid possible low-frequency noise sources of the lab. An SR830 Lock-In amplifier is used for the ac-measurements, while the back-gate voltage is applied by a source-meter. The current has been kept low enough to prevent heating that might either suppress superconductivity or destroy the interface, with the downside being the high noise-level

in recording resistance. The magnetic-field sweep-rate is also restricted to 5 mT/min, to avoid (as much as possible) the induced heating on the sample that is particularly enhanced at the regime between 0 and 100 mT (see Appendix C).

In 4.18a, the 2DEL's SMIT can be observed on a semilogarithmic plot. The magnetic field dependence of the resistance marks the critical field where superconductivity is suppressed. Outside the superconducting dome, finite resistance is measured even at $H \to 0$, with an increasing magnitude as the back-gate voltage decreases. The sheet resistance at -300 V (brown curve) and at -250 V (dark-yellow curve) has increased several orders of magnitude, to approximately 5 MΩ. At such high resistances, it is possible that the measurement's accuracy is reduced owing to the 10 MΩ lock-in input impedance that is now in the same order of magnitude as the sheet-resistance. Regarding the SMIT-crossover, panel 4.18b shows $R(H)$ curves that correspond to the optimally doped, underdoped and SMIT-regions, on a linear scale. Finite resistance emerges at a gate field between -130 V and -140 V (brown and pink $R(H)$-curves respectively). This lies well within our expectations from the $R(T)$-measurements [14] mentioned in the beginning of the chapter.

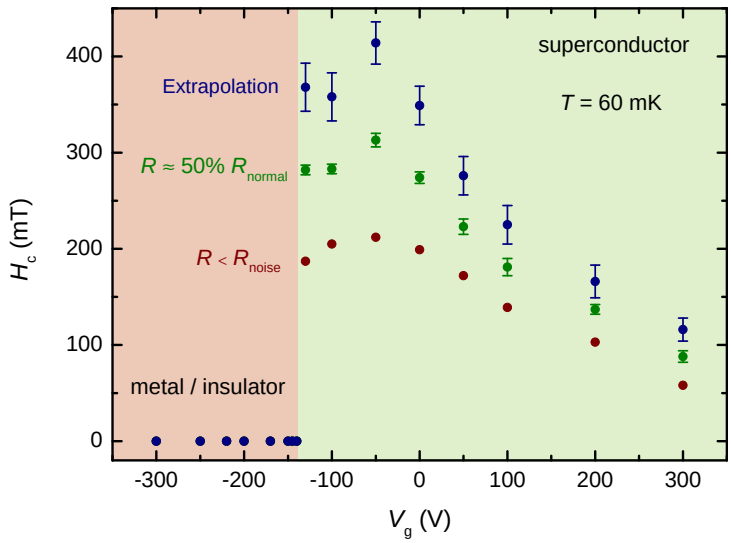

Figure 4.19: *The H_c dependence on gate voltage, as derived from the $R(H)$-curves of Fig. 4.18. The three extraction criteria are illustrated: The $R < R_{\text{noise}}$ considers the field-point where the sheet resistance goes below the noise limit, the $R \approx 50\% R_{normal}$ where it drops to half of its normal state value, and last the magnetic field that corresponds to the intersection of linear extrapolations. The superconducting and resistive regimes are shown in light-green and light-red background font, respectively.*

From the $R(H)$-dependencies one can extract the superconducting onset with respect to perpendicular magnetic field, similar to the $R(T)$-treatment. Three criteria have been assigned to extract the critical field value H_c from the $R(H)$-curves. The first is the magnetic field at which the resistance R drops

below the noise level, the second is when R drops to 50% of its initial value and the third considers the intersection of two linear extrapolations of the normal state sheet resistance and of the steep $R(H)$-regime (see Ref. [86]). In all three cases, the maximum magnetic field until which superconductivity is sustained lies in the $R(T)$-defined underdoped region, at -50 V, implying that the carrier concentration at 0 V is optimal for maximizing the superconducting T_c, but it does not yield the maximum H_c (see Fig. 4.19).

However, the $R(H)$-curves are not measured sequentially in time. Looking closer in 4.18b, the normal state resistance for V_g = 0 V is astonishingly higher than that for -50 V and approximately equal to the -100 V curve, in contradiction with the $R(T)$-measurements shown in Fig. 4.4. It is possible that during the measurement time-span (about one week) the sheet conductance changes, with any such disturbance being reflected in the $R(H)$-characteristics and thus in the determination of H_c, especially when measuring sheet resistances in the order of 100 Ω. On the other hand, one cannot exclude imperfect device-geometry effects, as the ac-current flows in random directions around the device and towards the drain, rather than in a well-defined path. Parameters T and H, respectively in $R(T)$ and $R(H)$ measurements, could also influence the current flow in a different manner.

The Superinsulator State

It has been argued in literature, that $R(H)$-measurements can be a good probe for studying a superinsulator state. [87–92]. This is a novel ground state that is distinct from the normal metallic state that is obtained by destroying superconductivity by a magnetic field. It manifests itself in systems which are close to a disorder driven SIT [92]. In experiment, such a state features a peak of the magnetic-field dependent resistance, at the point of the superconducting transition from the normal state (Fig. 4.20). We have not seen the emergence of the superinsulator state in the $R(H)$-measurements of $LaAlO_3/SrTiO_3$.

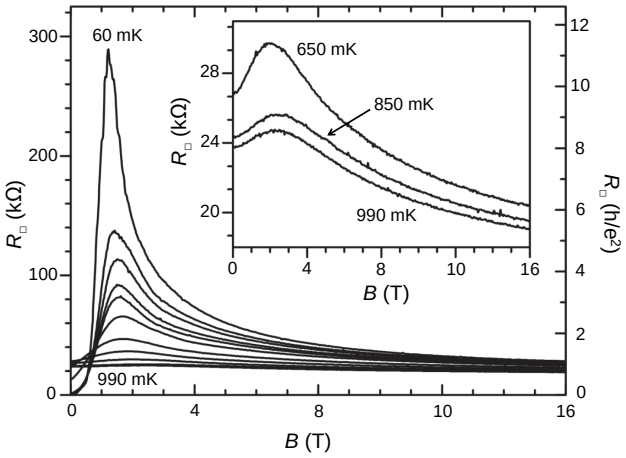

Figure 4.20: *The non-monotonic variation of the sheet-resistance of TiN-films with magnetic field, at various temperatures. Reproduced from [92].*

The next section will describe our tunneling spectroscopy measurements under out-of-plane magnetic fields. Given the transport-characterized SMIT of the $LaAlO_3/SrTiO_3$ 2DEL, it is important to understand how the phase-coherent superconducting state evolves with carrier depletion, from the superconducting dome towards the resistive regime.

4.5 The Phase-Coherent Resistive Regime of the $LaAlO_3/SrTiO_3$ Superconductor

The discovery of pseudogap-like behavior on the $LaAlO_3/SrTiO_3$ superconductor [14], in parallel with the work on investigating the pairing mechanism [15], has triggered interest in unraveling the physics that governs the carrier depleted regime in the vicinity of the underdoped superconducting region. The magnetic field dependence of superconductivity can provide information on the nature of the Cooper-pairs, the effects of vortices and the likelihood of a coherent superconducting-like ground state, at a regime where the ultra-low charge carrier density can no longer sustain macroscopic superconductivity. This regime will be referred to as "resistive" in this section. As discussed, the $LaAlO_3/SrTiO_3$ 2DEL exhibits a carrier-density driven SMIT [13, 14, 79–85, 93]. In contrast to early experiments from Caviglia et al. [13] where the quantum critical point is very close to the quantum-resistance for pairs, we and several others [14, 84, 85, 93] observe that the gate-voltage range at which $dR/dT \approx 0$ is rather large. The intervening metallic phase between superconductor and insulator is arguably bosonic in nature [60], with Cooper-pairs not only existing but also participating in transport.

Regardless of the sharpness of the transition to the resistive region, an interesting question is whether Cooper-pairs preserve phase-coherence. These are either localized into superconducting puddles which do not "communicate", or form an incipient superconducting ground state that is governed by vortex physics and is therefore characterized by an order parameter and a critical magnetic field. A key-technique for identifying which of the two scenarios holds for $LaAlO_3/SrTiO_3$ is applying an external magnetic-field perpendicular to the interface plane. The effect of the field in each case is fundamentally different: localized, incoherent pairs survive until the Zeeman-energy is strong enough to induce pair-breaking, whereas if global coherence pertains, the breaking is driven by penetration of the superconducting state with vortices.

Thus, tunneling spectroscopy under external magnetic fields is the tool of choice to study superconductivity in the resistive regime, with the aim to determine the critical field H_c across the phase diagram. Although transport measurements can also yield the value of H_c within the superconducting state, they fail to provide a realistic measure in the resistive region where macroscopic superconductivity is suppressed.

4.5.1 Magnetic Field Dependent Tunnel Spectra

The persisting superconducting features across the QCP seen in the section on temperature-dependent tunneling is already an indication of Cooper-pairs existing in the insulating regime. The evolution of tunneling spectra with magnetic field at different gate-fields provide more evidence on the matter, as it may well be that outside the (transport defined) superconducting dome the features evolve differently.

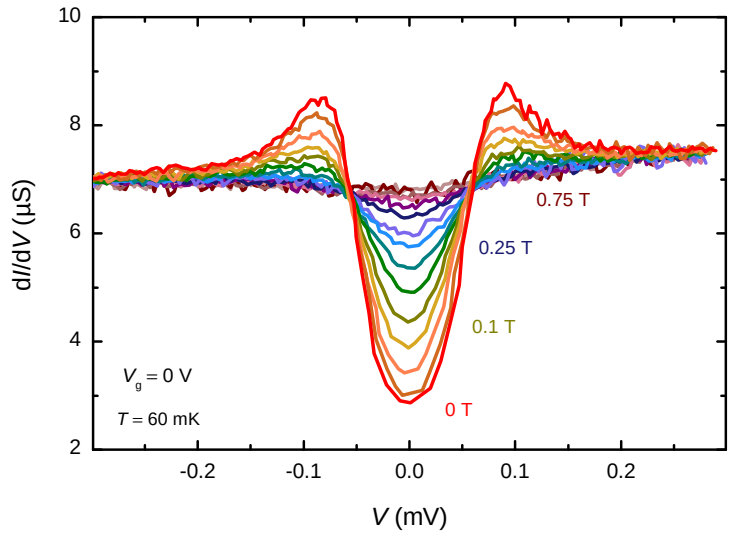

Figure 4.21: *The $dI/dV(V)$ spectra measured at different magnetic fields, at the lowest temperature of 60 mK. The curves were obtained at several values of magnetic field, with an incremental step of 0.025 T for $H < 0.2$ T, while the field-values above 0.2 T are: 0.25, 0.3, 0.4, 0.5, 0.75 and 1 T. The smooth destruction of superconductivity with increasing magnetic field is directly seen. From [86].*

Figure 4.21 depicts the $dI/dV(V)$ evolution with magnetic field at the optimally doped region. At 0 T (red curve), the superconducting gap and quasiparticle peaks are prominent. As the field increases, the gap closes and the quasiparticle peaks get broader, until superconductivity almost vanishes at approximately 0.25 T. At higher fields the conductance level does not change further (up to 1 T). The temperature of the experiments presented in this section is kept constant at the lowest possible value of 60 mK (unless explicitly stated).

Figure 4.22 summarizes the tunneling spectroscopy experiments regarding the magnetic field dependence. The take-home message is the smooth evolution of all tunnel spectra with H, for V_g-biases probing the entire phase diagram. Starting from the superconducting ground state ($H = 0$) in all regions, the superconducting features disappear with increasing field into an Altshuler-Aronov type conductance background. The critical magnetic field for each region is different, starting from 300 mT in the resistive and underdoped, to 215 mT and 90 mT in the optimally doped and overdoped regions, respectively. Once

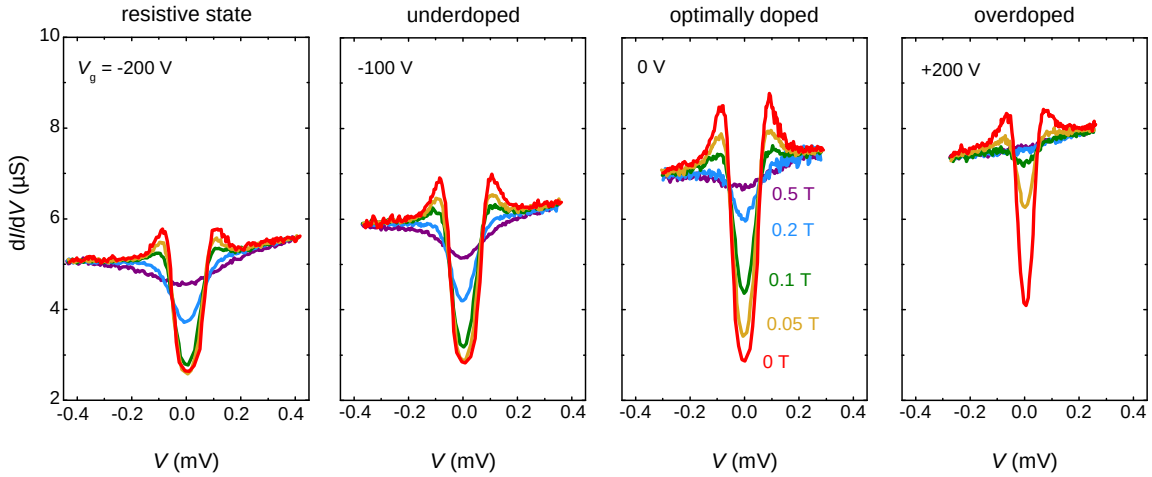

Figure 4.22: *The dependence of the $dI/dV(V)$ characteristics on magnetic field H, at different gate-fields. The superconducting gap for the fields of +200, 0, -100, -200 V is suppressed at H = 90, 215, 300 and 300 mT, respectively. In the resistive state, the quasiparticle excitation peaks are visible even though macroscopic superconductivity is not sustained. From [86].*

again, the gate-voltage effect on the charge carrier density defines the normal conductance background level, similarly to the first section. Intriguingly, the quasiparticle excitation peaks are preserved even at the resistive state. This is an indication of preserved phase coherence [94], between superconducting puddles that are too small to sustain macroscopic superconductivity in transport measurements, down to the lowest temperature.

This gradual suppression of the superconducting features is associated with BCS type-II superconductivity. One needs to take into account that all measured spectra originate from electron-tunneling across planar junctions, of a size much larger than the superconducting length scales (coherence length, normal vortex distance at the presence of magnetic field etc). Magnetic fields induce vortices and thereby, for fields close to the critical field, the DOS-reduction (at $V = 0$) is an average superconducting suppression over the device area.

4.5.2 The Critical Field at Base Temperature

Quantifying the robustness of superconductivity against the external magnetic field is the next step. In Fig. 4.23 the criterion that marks the superconducting onset is illustrated. For each V_g, one can track the evolution of the minimum of the $dI/dV(H)$-characteristics (i.e. $dI/dV|_{V=0}$), with increasing magnetic field. For extremely low ac-currents (order of 40 pA), the Fermi level of Au practically probes the $LaAlO_3/SrTiO_3$ superconducting gap and the conductance value is exclusively dependent on the states

influenced by superconductivity. Therefore an increase of the $dI/dV|_{V=0}$ value with increasing magnetic-field would indicate suppression of the superconductivity. The magnetic field value beyond which the conductance reaches a plateau (see Fig. 4.23) is the upper critical field. The intersection of two linear extrapolations, one from the plateau and one from the steepest region of the $dI/dV(V=0,H)$ curves, yields the experimentally determined values for the upper critical field of the $LaAlO_3/SrTiO_3$ 2DEL. This field will be henceforth referred to as the critical field H_c of the system.

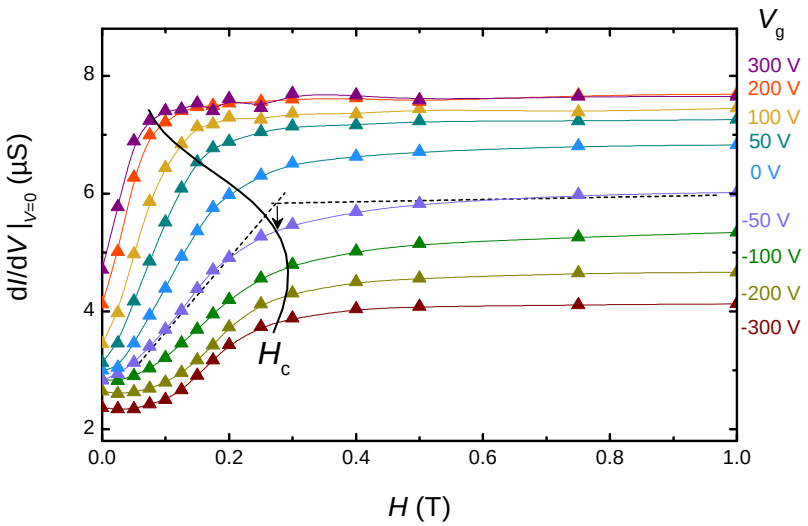

Figure 4.23: *The $dI/dV(V=0,H)$ characteristics for gate fields between -300 V and +300 V. The magnetic field H is altered in steps, to induce the least possible heating on the sample due to gradients. This is a plot of the spectral minima from all recorded spectra at nine values of V_g. The method used to derive H_c is graphically shown in the figure. From [86].*

In addition to determining the critical field experimentally, measurements of the superconducting gap Δ from our previous work yield the coherence length values for $LaAlO_3/SrTiO_3$, by using the BCS theory [26]. Assuming conventional superconductivity for $LaAlO_3/SrTiO_3$ and also that the Fermi velocity v_F remains constant in the entire phase diagram, the estimated critical field can be derived as follows:

$$H_c = \frac{\pi \cdot \Phi_0}{2} \left(\frac{\Delta}{\hbar \cdot v_F} \right)^2 \tag{4.6}$$

Equation 4.6 is derived from the BCS model [26]:

$$\xi_{0,BCS} = \frac{\hbar \cdot v_F}{\pi \cdot \Delta} \tag{4.7}$$

and also from the Ginzburg-Landau expression for the coherence length, namely:

$$H_c = \frac{\Phi_0}{2\pi \cdot \xi_0} \tag{4.8}$$

with the magnetic flux quantum $\Phi_0 \approx 2.07 \cdot 10^{-15}$ T·m^2.

For a clean superconductor, the Ginzburg Landau coherence length ξ_0 equals $\xi_{0,BCS}$. As will be discussed in the next section, the superconducting 2DEL is indeed towards the clean limit, as corroborated by measurements of the $H_c(T)$-dependence. Expression 4.6 determines H_c for $T << T_c$ and can provide a reference measure for the experimental values derived from Fig. 4.23, based on independent measurements of the superconducting gap Δ (discussed in the previous sections). Figure 4.24a presents the measured H_c curve dependence with back-gate field, along with the values derived from the BCS-treatment. The Fermi velocity v_F has been treated as a fitting parameter during calculations, with an obtained value of $1.1 \cdot 10^4$ m/sec. This is slightly lower than the literature value for $LaAlO_3/SrTiO_3$ [95], yet it is close to the expected $1.5 \cdot 10^4$ m/sec for bulk $SrTiO_3$ [96] which is in the order of the sound velocity [97]. The two H_c-dependencies on gate voltage V_g match very well. This is an indication of conventional, BCS behavior of the 2D superconductor. Given the good agreement of the calculated and measured H_c-values, the constant value of v_F is itself evidence of clean superconductivity in the 2DEL.

An interesting finding from the estimated $H_c(V_g)$-dependence is the gradual evolution across the SMIT-crossover. The superconducting ground state of $LaAlO_3/SrTiO_3$, although weakened by charge carrier depletion at V_g = -200 V, still preserves Cooper-pairing in its resistive state.

Figure 4.24b presents the measured values for the coherence length ξ_0, derived from Eq. 4.7. As discussed in the beginning, the Cooper-pairs may exist in isolated superconducting puddles, of a smaller size than the measured coherence length and within the area of the planar junction, and thereby sustain the overall superconducting character seen in the tunnel spectra. This hypothesis implies localization of the charge carriers, whose wavefunction is suppressed within a length-scale smaller than ξ [98, 99]. However, this is in contradiction with our measured tunnel spectra, due to the observed persistence of the quasiparticle peaks upon charge carrier depletion, past the SMIT-crossover. The peaks are an indication of a sustained, long-range superconducting order [94, 100, 101], fact which is corroborated by the gradual (not sharp) evolution of the critical field in the phase diagram and at the resistive region.

In addition, the scenario of pertaining, phase-coherent superconductivity at the resistive region is supported by the significant difference between the measured H_c-data and the Clogston-Chandrasekhar prediction [102, 103] (H_c^{CC}-limit). This is a low-limit estimate of the upper critical field for conventional superconductors, with magnitude proportional to the superconducting gap, reading:

$$H_c^{CC} = \frac{\Delta}{\sqrt{2} \cdot \mu_B} \tag{4.9}$$

Here, μ_B is the Bohr-magneton. Assuming a g-factor of 2, and the value $\Delta = 66\ \mu$eV which is constant in the resistive region, H_c^{CC} is estimated at about 0.8 T. This value does not include spin-orbit coupling contributions that are present on $LaAlO_3/SrTiO_3$ and can increase this limit to even greater values [104, 105].

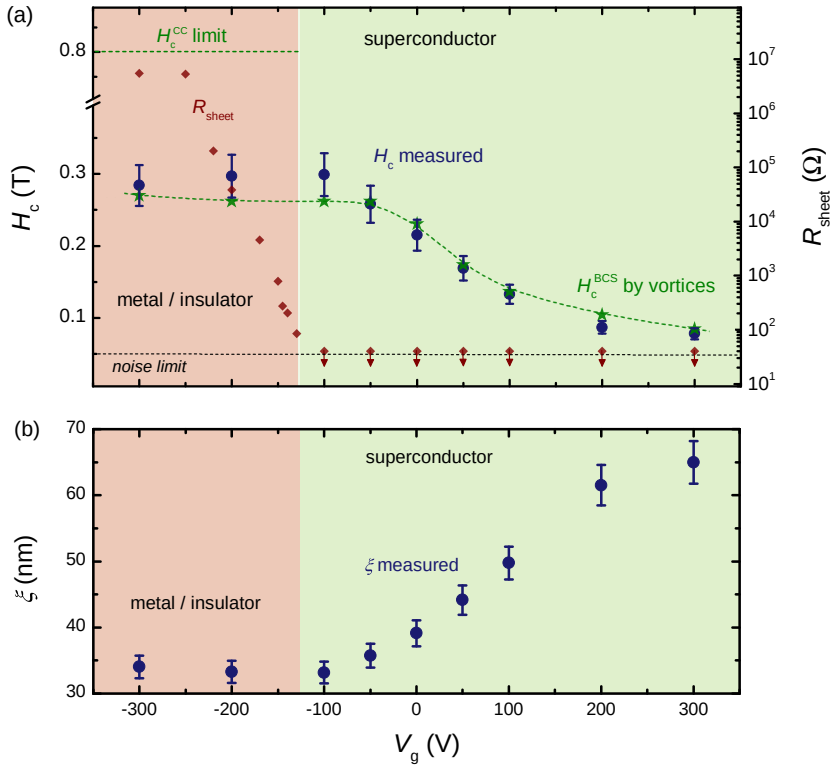

Figure 4.24: *(a) The dependencies of the measured critical-field (blue points) and the BCS-derived from Eq. 4.6 (green stars) on V_g are shown. Both curves match quite well, under the assumption of a constant v_F. The dark-red rhombi are measurements of the sheet resistance of $LaAlO_3/SrTiO_3$ in the absence of magnetic fields, illustrating the transition from macroscopic superconductivity to a resistive state (sheet resistance above the noise limit). The calculated Clogston-Chandrasekhar prediction for the lowest value of the critical field is shown at the top left corner. (b) The coherence length dependence on V_g, as derived from Eq. 4.7. From [86].*

The work presented in this section is conclusive on a persisting, coherent superconducting behavior of the charge carriers at the resistive, or pseudogap-like regime of the 2D $LaAlO_3/SrTiO_3$ interface electron system. Table 4.1 summarizes the obtained results from the magnetic field dependent tunnel spectra. The in-plane coherence length $\xi_{\parallel}$ is calculated from the H_c-measured values through Eq. 4.7, while the H_c^{BCS} is determined by Eq. 4.6 using the measured values of the superconducting gap Δ (from Ref. [14]). The $R_{sheet,H=0}$ values (brown rhombi in Fig. 4.24a) match the values shown in Fig. 4.18, for $H = 0$.

Table 4.1: The measured superconducting features of $LaAlO_3/SrTiO_3$ with respect to V_g.

Gate-Voltage V_g (V)	Measured H_c (T)	Measured $\xi_{\parallel}$ (nm)	Zero-Field R_{sheet} (Ω)	Δ (μeV)	Calculated H_c^{BCS} (T)
-300	0.284 ± 0.028	34.1 ± 1.70	5.5×10^6	66	0.270
-200	0.297 ± 0.030	33.3 ± 1.67	3.8×10^4	65	0.262
-100	0.299 ± 0.030	33.2 ± 1.66	< 40	65	0.262
-50	0.258 ± 0.026	35.7 ± 1.79	< 40	65	0.262
0	0.215 ± 0.022	39.1 ± 1.96	< 40	61	0.230
+50	0.169 ± 0.017	44.1 ± 2.21	< 40	53	0.174
+100	0.133 ± 0.013	49.8 ± 2.49	< 40	47	0.137
+200	0.087 ± 0.009	61.5 ± 3.08	< 40	41	0.104
+300	0.078 ± 0.008	64.5 ± 3.25	< 40	37	0.085

In the last section, the temperature dependence of the critical field H_c in different regions of the phase diagram will be discussed. It has been suggested that the $H_c(T)$-dependence can be a useful tool for revealing multiband superconducting behavior [106–108].

4.6 Temperature and Gate Voltage Dependence of the Critical Field

Concluding this chapter, I have investigated whether the 2D $LaAlO_3/SrTiO_3$ electron system is a multiband superconductor [106, 109–111]. Theoretically, multiband superconductivity has been introduced only a few years after BCS-theory itself [112–114] and $SrTiO_3$ is the first superconductor whose tunneling spectra showed two superconducting gap signatures in the DOS [115].

This is due to the fact that more than one bands can cross the Fermi-level and at the same time participate in the superconducting condensate. The presence of additional superconducting carriers in a second band may affect superconductivity in the first, depending on the gap-difference, effective masses etc. A simple case is illustrated in Fig. 4.25, where the temperature-dependence of the order parameter of an s-band is drastically affected by the presence of a superconducting d-band with more carriers. In more complex systems with several bands crossing the Fermi level, the interaction could be different.

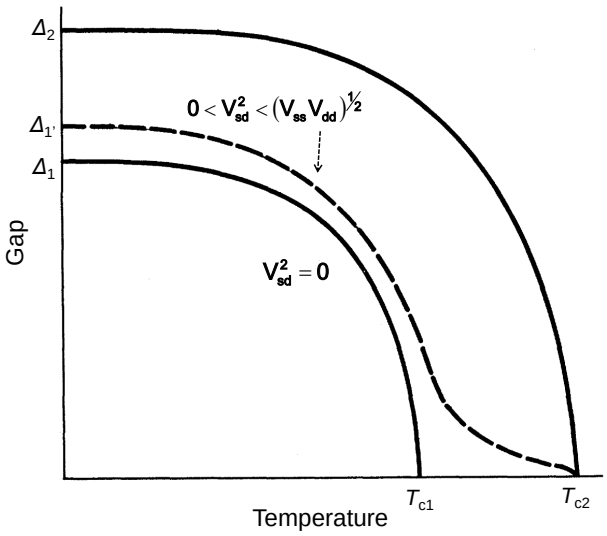

Figure 4.25: *Temperature dependence of the order parameters of a two-band superconductor. Δ_1 and Δ_2 are the superconducting gaps of the s and d-band respectively, in the absence of interband interaction. As soon as $V_{sd}^2 > 0$, i.e. interaction between the carriers of the two bands appears, the gap-dependence of the s-band (with less carriers) follows $\Delta_{1'}$. Reproduced from [112].*

After its superconducting character was revealed, it was believed that $SrTiO_3$ shows a many-valley band structure [116]. It soon became evident that this is not the case [117–120], with different bands being identified to reside at the center of the Brillouin zone [121]. In their tunneling measurements, G. Binnig et al. [115] identified two superconducting order parameters, one of which exhibited exotic, non-BCS temperature dependence that was very similar to the Δ_1'-dependence in Fig. 4.25, in the presence of interband interaction. It is anticipated that the multiband tunneling features observed on $SrTiO_3$ are present also in the $LaAlO_3/SrTiO_3$ superconducting 2DEL.

With or without interaction between the bands, multigap features would ideally be resolved by tunneling spectroscopy. However, the superconducting gap-dependence on temperature also depends on the experimental probe. In the planar junction case, tunneling takes place from the top-electrode (Au) towards the [001]-oriented $SrTiO_3$-substrate and is therefore spatial-orientation selective for the degen-

erate $d_{xz,yz}$ orbitals [43, 84]. Tunneling spectroscopy measurements have not revealed signatures of a second gap from the additional band that is populated by carrier injection [23]. Depending on its size, it is possible that the second gap is masked by the broad superconducting features of the first.

The critical magnetic field H_c is directly related to the superconducting gap Δ (see previous section) and is at the same time easily determined by experiment. Measurements of its temperature dependence can be a useful tool for revealing multiband signatures of the superconducting state or even unconventional behavior [26, 106] of the $LaAlO_3/SrTiO_3$ 2DEL.

4.6.1 Measurements

In order to accurately measure H_c, the $dI/dV(V=0,H)$-dependence is used, similarly to the previous section. This time however, the magnetic field is not increased in steps; it is swept constantly with a rate of 5 mT per minute. This allows for a more accurate observation of the superconducting suppression by monitoring the conductance behavior. An ac-current of 40 pA is typically applied (no dc component). The downside of sweeping the magnetic field in a constant rate is the induced heating on the sample due to rapid field-change. This heating is particularly prominent in the magnetic field region between 0 and 100 mT and is cryostat-dependent. Low sweep rates ensure reduced heating because the field change is slower. An elaborate discussion on the heating-effect can be found in Appendix C.

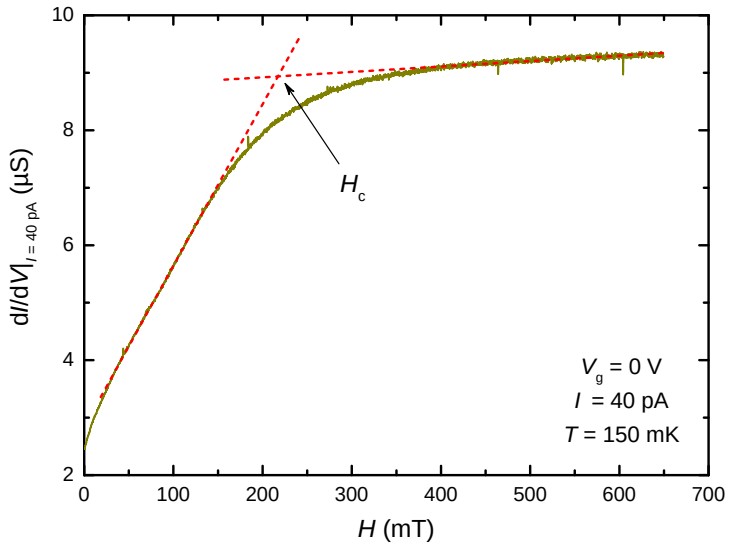

Figure 4.26: *The H_c extraction technique from the $dI/dV(V=0)$-dependence on H is shown. This is in the optimally doped region, at 150 mK. The H_c-value is in all cases extracted as indicated.*

Figure 4.26 illustrates the H_c-extraction method. The steep rise of $dI/dV(V=0)$ with H is fitted linearly, along with the plateau at higher fields. We use the intersection of the two linear fits (red lines in the graph) as the critical magnetic field H_c for each temperature and gate-voltage value. Often, sweeping

the magnetic field up and down reveals a hysteretic-like behavior that is not systematic or temperature dependent. In these cases, the average value of H_c extracted from both sweep directions is considered. Using this method, the $dI/dV(V=0,H)$-dependence can determine H_c for all carrier densities.

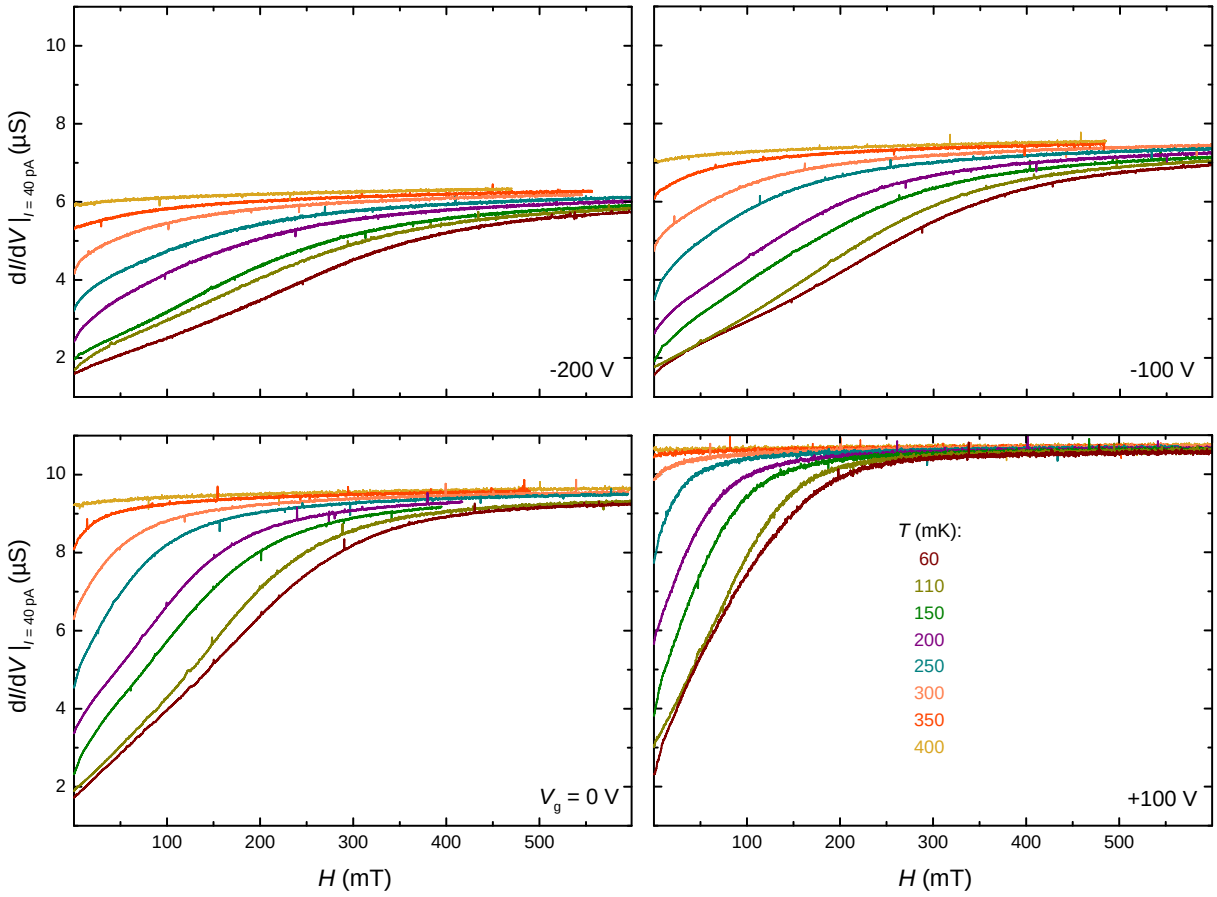

Figure 4.27: *The $dI/dV(V=0)$-dependence on magnetic field, at different temperature steps and regimes of the phase diagram. The color code for temperature is shown on the bottom-right panel and is the same for all panels. The magnetic field sweep rate is the same in all cases, while an ac-current of 40 pA is constantly sourced through the tunnel junction. Four regions are investigated (at gate-fields of -200, -100, 0 and +100 V) that correspond to the resistive, underdoped, optimally doped and overdoped region.*

Figure 4.27 presents the $dI/dV(V=0,H)$-dependence at various temperatures, for the resistive (-200 V), underdoped (-100 V), optimally doped (0 V) and the overdoped (+100 V) regions. For each of the four cases, the $dI/dV(V=0,H)$-evolution is measured at eight temperature-steps. The evolution across the phase diagram is qualitatively similar. In all cases, the gradual suppression of superconductivity with field is evident. For temperatures above 300 mK, the conductance increase is minimal, rapidly approaching a plateau when the magnetic field is increased. An interesting observation is that the steepest transition (the difference between the normal conductance plateau and $dI/dV(V=0,H=0)$ happens at the overdoped region where the excess of carriers at the interface raises the normal conductance level.

Yet, the conductance suppression at $H = 0$ (about 2 μS) in this region is similar to the other regions, despite a superconducting gap smaller than in the optimally doped region. Figure 4.28 presents the H_c-values extracted from the data of Fig. 4.27. Down to the lowest temperature of 60 mK, the $H_c(T)$-dependence is linear to a good approximation.

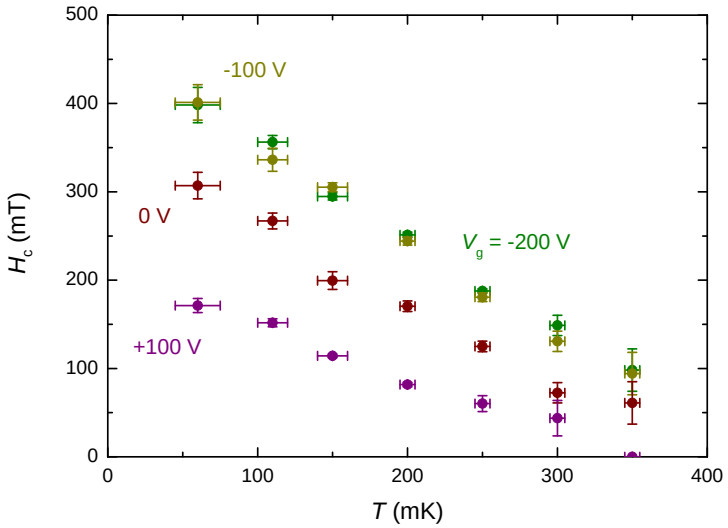

Figure 4.28: *The critical field dependence on temperature, for four V_g-values. Each experimental point is extracted by the linear extrapolation method from the respective $dI/dV(V = 0, H)$-curve of Fig. 4.27. The error margins reflect the uncertainty of the extraction method used, that is increased for the higher and lower temperatures. This is due to a reduced number of fitted-points at the respective $dI/dV(V = 0, H)$ steep-rise and plateau regimes. Errors in temperature are due to field-gradient induced heating, which is very pronounced at base temperature.*

To verify the observed linear behavior, the results were compared to measurements performed on a different sample by my colleague L. Kürten [122]. Figure 4.29 presents the measured critical fields of both samples with respect to T/T_c, at different values of V_g. In all cases, the $H_c(T)$-dependence is linear in the temperature range $0.16 \times T_c < T < T_c$. The absolute values of H_c measured in the two samples differ. It is yet important to realize that the electrostatic tuning does not affect different samples in the same manner, owing to differences in the carrier densities and mobilities that emerge during growth. The latter has been verified in the work of my colleague A. Teker, who focused on the growth optimization of $LaAlO_3/SrTiO_3$ samples with ultra-high mobilities [123]. The superconducting ground state of sample P-LUK11 was in the overdoped regime for V_g = 0, in contrast to sample T36 (discussed in this work) which was in the optimally-doped regime. In addition, the carrier density (and thereby T_c) of sample P-LUK11 in the V_g-range -100 V < V_g < + 100 V did not vary significantly.

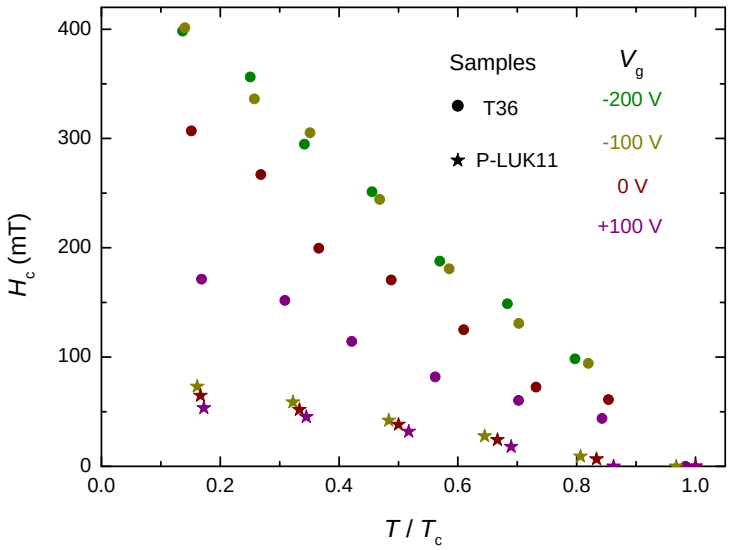

Figure 4.29: *The H_c-dependence on the ratio T / T_c for sample T36 discussed in this work (circles) and sample P-LUK11, grown by L. Kürten (stars). The color code specifies the different values of the gate voltage. A linear dependence is seen in both samples.*

4.6.2 Implications of the observed linear $H_c(T)$-Dependence

The observed behavior is not similar to the BCS-prediction for bulk, type-II superconductors, which has the form [7, 26]:

$$H_c(T) = H_c(0)\left[1 - \left(\frac{T}{T_c}\right)^2\right] \tag{4.10}$$

For superconductors in confined dimensions, the picture is more complicated. Owing to an increased effective mass in the out-of-plane direction, the coherence length is reduced [26]. This anisotropy rises below a certain sheet thickness and linearizes the $H_c(T)$-dependence. It is expected that the 2D-confinement realized in the $LaAlO_3/SrTiO_3$ 2DEL, can account for a linear H_c dependence on temperature in the regime $T \to T_c$ [26, 124–127]. Indeed, the temperature-dependence of the critical field has been already measured down to 100 mK for a slightly overdoped $LaAlO_3/SrTiO_3$ sample. Transport measurements in the work of Reyren et al. [128] have shown that there exists anisotropy between the temperature dependences of the in-plane and out-of-plane critical fields, attributed to reduced dimensionality. Our measurements even down to 50 mK still exhibit linear $H_c(T)$-dependences in the phase diagram.

$LaAlO_3/SrTiO_3$ interfaces have mean free paths ℓ ranging from 25 nm [129] (range of the in-plane coherence length ξ that is typically above 50 nm [128, 130]) up to the μm range [131]. The mean free path of the bulk, doped $SrTiO_3$ is approximately 60 nm [96]), as reference. The $LaAlO_3/SrTiO_3$ 2DEL is considered to be at the border between clean ($\ell > \xi$) and dirty ($\ell < \xi$) superconductors. Golubov et al. [132] have investigated the influence of electron-electron interactions of dirty superconducting thin films, which yield a positive curvature on the H_c as temperature decreases. Such feature is not observed in our measurements at temperatures far from T_c. Within the Werthamer-Helfand-Hohenberg (WHH) theory [133], the effects of Pauli paramagnetism and impurity scattering tend to reduce H_c as $T \to 0$. Given the linear temperature dependence of H_c down to about one sixth of T_c, we conclude that the 2DEL is at the clean limit. This is corroborated by the constant value of the Fermi velocity in the entire phase diagram, as a consequence of the good agreement between the measured values of H_c and the BCS-derived based on independent measurements of the superconducting gap [14, 86].

Proximity to a Second Band and Multiband Superconductivity

Theoretical [134, 135] and experimental work have illustrated that multi-layers of alternating superconducting - normal metals [136], or a thin superconductor embedded in a bulk [137], often exhibit H_c (T)-dependence with positive curvatures. This effect is due to a proximity-induced suppression of the pair potential which yields lower T_c and H_c values than the conventionally expected. In $LaAlO_3/SrTiO_3$, the carrier population of a second band can potentially give rise to a similar effect. In case the order parameter of the second band (possibly of a much higher effective mass) is not equal to the first, the critical field H_c measured in tunneling can be smaller. As observed in Fig. 4.28, the shape of the H_c (T)-dependence at the overdoped region (+100 V) is approximately linear. Intriguingly, our tunneling measurements have not been able to resolve multiband behavior on the $LaAlO_3/SrTiO_3$ 2DEL, neither in the tunneling characteristics of the planar junctions, nor in the $H_c(T)$-dependence (as described in Ref. [106]).

Anisotropy of the Fermi Surface

In addition to low-dimensionality, there exist other possible explanations for the extended linear behavior. It has been suggested that anisotropy of the Fermi surface can induce deviations on the conventional $H_c(T)$-dependence.

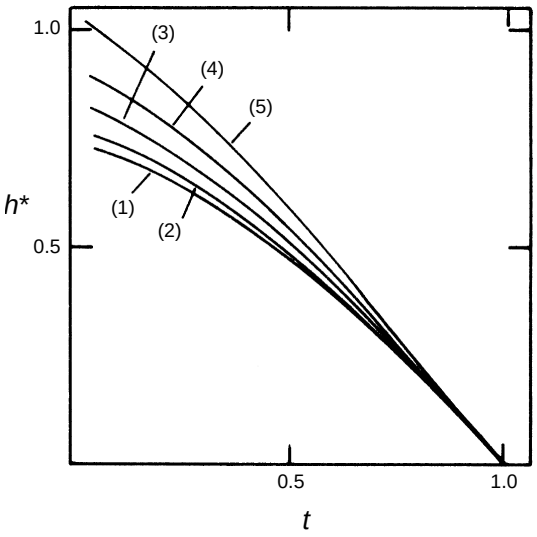

Figure 4.30: *Calculated normalized critical fields for materials with distorted Fermi surfaces, as a function of temperature (normalized to T_c). The indices correspond to increasing anisotropy magnitude in the absence of impurity scattering (i.e. clean limit). Reproduced from [138].*

Youngner and Klemm have theoretically established that the shape of the Fermi surface can influence the temperature dependence of H_c [138]. The increase of the Fermi surface anisotropy linearizes the $H_c(T)$-dependence, which departs from the expected isotropic dirty-limit curve predicted by Helfand et al. [133, 139]. This feature is illustrated in Fig. 4.30 where the critical field dependence is plotted against the ascended temperature for various amounts of (in this case hexagonal) anisotropy.

On the other hand, impurity scattering may cancel the anisotropy-induced effects. As was shown in parallel, increasing disorder pushes the dependence towards the dirty-limit, where anisotropy plays no significant role. Disorder refers to the ratio of the electron scattering length to the coherence length.

To sum up, the linear dependence of H_c down to 50 mK is an indication of a clean superconductor, while any disorder-induced plateau is absent in the entire temperature range of the tunneling measurements. The Fermi surface anisotropy effect cannot be excluded from the data. In this sample, there exist no clear multiband signatures in the temperature dependence of H_c in the phase diagram.

4.7 Chapter Summary

This chapter has presented in detail all experiments performed at the superconducting $LaAlO_3/SrTiO_3$ 2DEL. The technique applied was tunneling spectroscopy, in order to acquire direct information about the DOS-evolution with gate voltage, temperature and perpendicular magnetic fields. Additional transport measurements of the sheet resistance have been used in the investigation of the superconducting 2DEL. Fabrication of $LaAlO_3/SrTiO_3$ planar junctions has offered the possibility to perform all these measurements directly at the same sample and, moreover, tune each of the three parameters mentioned inside a cryostat. The main results are summarized in the following paragraphs.

The DOS Evolution across the Phase Diagram of $LaAlO_3/SrTiO_3$

Through tunneling spectroscopy measurements and by using the electric field-effect, I have investigated how superconductivity evolves in different regions of the phase diagram. The perspective offered by the tunneling measurements (as compared to transport) on determining the $LaAlO_3/SrTiO_3$ critical temperature has led to experimental and theoretical work on unraveling the origin of the pseudogap-like behavior [14]. As an analogue to the pseudogap phase seen in the layered high-T superconductors, the cuprates, the emergence of such behavior on a totally different 2D system like $LaAlO_3/SrTiO_3$ has offered astonishing implications and posed questions. This has, most importantly, motivated us to further investigate the phonon mediated electron-pairing on $LaAlO_3/SrTiO_3$ (Boschker et al. [15]).

Investigation of the SMIT and Nature of Cooper Pairing at the Resistive Regime

The disappearance of superconductivity at the quantum critical point, by tuning the charge carrier density, has been long addressed in the community. Yet, following the emergence of the pseudogap behavior, the question regarding the pairing nature of the very underdoped regime arose. Signatures of an SMIT scenario in the $R(T)$ and $R(H)$ measurements have been confirmed on our samples and suggested that this transition on $LaAlO_3/SrTiO_3$ is bosonic in character. In addition, the tunnel spectra evolution with perpendicular magnetic fields has demonstrated that superconducting phase coherence pertains deep inside the depleted regime, where finite resistance is measured by transport.

The Expectation for Multiband Behavior on $LaAlO_3/SrTiO_3$

The $H_c(T)$-dependence was chosen as a tool to investigate the existence of emergent multiband features. Superfluid density measurements of the $LaAlO_3/SrTiO_3$ 2DEL performed by Bert et al. [29] have ruled out multiband behavior through bands with very different gap sizes. However, in the case of similar coupling strength for the bands, $H_c(T)$-measurements provide a better probe for mapping multiband signatures, since the opening of the superconducting gap may occur at similar temperatures.

Concluding this experimental chapter, tunneling spectroscopy and other measurements presented in this work have contributed to the field of two-dimensional superconductivity, by studying a novel 2D electron system of the oxide community, the $LaAlO_3/SrTiO_3$ interface. Progress has been made in understanding how superconducting properties evolve with charge carrier density. There's still room for more however.

In the last years, there exist a number of reports on superconductivity at the interface of $LaAlO_3$ grown atop $SrTiO_3$ (110) and (111) orientations [140–142]. By growing on such substrates, one can explore superconductivity on $LaAlO_3/SrTiO_3$ from a different angle in k-space, as tunneling from the top is orbital selective.

Other potential for future work is the fabrication of in-plane Josephson junctions with $LaAlO_3/SrTiO_3$ and a conventional superconductor. Motivated by the anisotropy of the Fermi surface, a phase sensitive probe, like a dc-SQUID (i.e. as described by Wollman et al. for YBCO [143]) can resolve anisotropies of the Fermi surface (or even an exotic pairing symmetry). This is achieved by monitoring the critical current dependence on perpendicular magnetic fields [144–146].

Last, an equally exciting challenge is already at hand. The link between 2D superconductivity on $LaAlO_3/SrTiO_3$ and its bulk counterpart, the doped-$SrTiO_3$, has not been entirely addressed by experiment. The next chapter will elaborate on spectroscopy measurements on the bulk $SrTiO_3$ superconductor, by fabricating Schottky junctions and using tunneling spectroscopy to probe the DOS.

References

[1] A. Ohtomo and H. Y. Hwang, Nature **427**, 423 (2004).

[2] J. C. Fischer and I. Giaever, J. Appl. Phys. **32**, 172 (1961).

[3] I. Giaever, Phys. Rev. Lett. **5**, 147 (1960).

[4] I. Giaever, Phys. Rev. Lett. **5**, 464 (1960).

[5] J. Nicol, S. Shapiro and P. H. Smith, Phys. Rev. Lett. **5**, 461 (1960).

[6] J. Bardeen, L. N. Cooper and J. R. Schrieffer, Phys. Rev. **108**, 1175 (1957).

[7] W. Buckel and R. Kleiner: *Superconductivity: Fundamentals and Applications*, 2nd Edition, WILEY-VCH Verlag GmbH & Co. KGaA, Weinheim, Germany (2004).

[8] E. L. Wolf, *Principles of Electron Tunneling Spectroscopy*, 2nd Edition, Oxford University Press, New York (2012).

[9] M. Breitschaft, V. Tinkl, N. Pavlenko, S. Paetel, C. Richter, J. R. Kirtley, Y. C. Liao, G. Hammerl, V. Eyert, T. Kopp and J. Mannhart, Phys. Rev. B **81**, 153414 (2010).

[10] S. Thiel, G. Hammerl, A. Schmehl, C. W. Schneider and J. Mannhart, Science **313**, 1942 (2006).

[11] Y. Li and N. Mason, Appl. Phys. Lett. **102**, 023102 (2013).

[12] J. G. Rodrigo, H. Suderow and S. Vieira, Eur. Phys. J. B **40**, 483 (2004).

[13] A. D. Caviglia, S. Gariglio, N. Reyren, D. Jaccard, T. Schneider, M. Gabay, S. Thiel, G. Hammerl, J. Mannhart and J.-M. Triscone, Nature **456**, 624 (2008).

[14] C. Richter, H. Boschker, W. Dietsche, E. Fillis-Tsirakis, R. Jany, F. Loder, L. F. Kourkoutis, D. A. Muller, J. R. Kirtley C. W. Schneider and J. Mannhart, Nature **502**, 528 (2013).

[15] H. Boschker, C. Richter, E. Fillis-Tsirakis, C. W. Schneider and J. Mannhart, Sci. Rep. **5**, 12309 (2015).

[16] H. Vogt, Phys. Rev. B **38**, 5699 (1988).

[17] J. Mannhart, J. G. Bednorz, K. A. Mueller and D. G. Schlom, Z. Phys. B **83**, 307 (1991).

[18] M. L. Reinle-Schmitt, C. Cancellieri, D. Li, D. Fontaine, M. Medarde, E. Pomjakushina, C. W. Schneider, S. Gariglio, Ph. Ghosez, J.-M. Triscone and P. R. Wilmott, Nature Commun. **3**, 932 (2012).

[19] C. Richter PhD Thesis: *Experimental Investigation of Electronic and Magnetic Properties of $LaAlO_3$-$SrTiO_3$ Interfaces*, University of Augsburg 2012.

[20] N. Reyren, S. Thiel, A. D. Caviglia, L. F. Kourkoutis, G. Hammerl, C. Richter, C. W. Schneider, T. Kopp, A.-S. Ruetschi, D. Jaccard, M. Gabay, D. A. Muller, J.-M. Triscone and J. Mannhart, Science **317**, 1196 (2007).

[21] S. Gariglio, N. Reyren, A. D. Caviglia and J.-M. Triscone, J. Phys. Condens. Matter **21**, 164213 (2009).

[22] B. Altshuler and A. Aronov, Solid State Commun. **30**, 115 (1971).

[23] A. Joshua, S. Pecker, J. Ruhman, E. Altman and S. Ilani, Nature Commun. **3**, 1129 (2012).

[24] R. C. Dynes, V. Narayanamurti and J. P. Garno, Phys. Rev. Lett. **41**, 1509 (1978).

[25] S. B. Kaplan, C. C. Chi, D. N. Langenberg, J. J. Chang, S. Jafarey and D. J. Scalapino, Phys. Rev. B **14**, 4854 (1976).

[26] M. Tinkham *Introduction to Superconductivity*, 2nd Edition, Dover Publications Inc. Mineola, New York (1996).

[27] P. Hu, R. C. Dynes, V. Narayanamurti, H. Smith and W. F. Brinkman, Phys. Rev. Lett. **38**, 361 (1977).

[28] Y. J. Uemura, G. M. Luke, B. J. Sternlieb, J. H. Brewer, J. F. Carolan, W. N. Hardy, R. Kadono, J. R. Kempton, R. F. Kiefl, S. R. Kreitzman, P. Mulhern, T. M. Riseman, D. L. Williams, B. X. Yang, S. Uchida, H. Takagi, J. Gopalakrishnan, A. W. Sleight, M. A. Subramanian, C. L. Chien, M. Z. Cieplak, G. Xiao, V. Y. Lee, B. W. Statt, C. E. Stronach, W. J. Kossler and X. H. Yu, Phys. Rev. Lett. **62**, 2317 (1989).

[29] J. A. Bert, K. C. Nowack, B. Kalisky, H. Noad, J. R. Kirtley, C. Bell, H. K. Sato, M. Hosoda, Y. Hikita, H. Y. Hwang and K. A. Moler, Phys. Rev. B **86**, 060503(R) (2012).

[30] D. S. Marshall, D. S. Dessau, A. G. Loeser, C.-H. Park, A. Y. Matsuura, J. N. Eckstein, I. Bozovic, P. Fournier, A. Kapitulnik, W. E. Spicer and Z.-X. Shen, Phys. Rev. Lett. **76**, 4841 (1996).

[31] A. G. Loeser, Z.-X. Shen, D. S. Dessau, D. S. Marshall, C. H. Park, P. Fournier and A. Kapitulnik, Science **273**, 325 (1996).

[32] H. Ding, T. Yokoya, J. C. Campuzano, T. Takahashi, M. Randeria, M. R. Norman, T. Mochiku, K. Kadowaki and J. Giapintzakis, Nature **382**, 51 (1996).

[33] A. Damascelli, Z. Hussain and Z.-X Shen, Rev. Mod. Phys. **75**, 473 (2003).

[34] O. Fischer, M. Kugler, I. Maggio-Aprile, C. Berthod and C. Renner, Rev. Mod. Phys. **79**, 353 (2007).

[35] J.-F. Ge, Z.-L. Liu, C. Liu, C.-L Gao, D. Qian, Q.-K. Xue, Y. Liu and J.-F Jia, Nature Mater. **14**, 285 (2014).

[36] Y. Sun, W. Zhang, Y. Xing, F. Li, Y. Zhao, Z. Xia, L. Wang, X. Ma, Q.-K. Xue and J. Wang, Sci. Rep. **4**, 6040 (2014).

[37] S. He, J. He, W. Zhang, L. Zhao, D. Liu, X. Liu, D. Mou, Y.-B. Ou, Q.-Y. Wang, Z. Li, L. Wang, Y. Peng, Y. Liu, C. Chen, L. Yu, G. Liu, X. Dong, J. Zhang, C. Chen, Z. Xu, X. Chen, X. Ma, Q. Xue and X. J. Zhou, Nature Mater. **12**, 605 (2013).

[38] D. Bucheli, S. Caprara and M. Grilli, Supercond. Sci. Technol. **28**, 045004 (2015).

[39] M. S. Scheurer and J. Schmalian, Nature Commun. **6**, 6005 (2015).

[40] N. Mohanta and A. Taraphder, Phys. Rev. B **92**, 174531 (2015).

[41] W. L. McMillan, Phys. Rev. **167**, 331 (1968).

[42] A. Baratoff and G. Binnig, Physica **108B**, 1335 (1981).

[43] G. Berner, M. Sing, H. Fujiwara, A. Yasui, A. Saitoh, A. Yamasaki, Y. Nishitani, A. Sekiyama, N. Pavlenko, T. Kopp, C. Richter, J. Mannhart, S. Suga and R. Claessen, Phys. Rev. Lett. **110**, 247601 (2013).

[44] P. W. Anderson, Phys. Rev. **109**, 1492 (1958).

[45] M. Ma and P. A. Lee, Phys. Rev. B **32**, 5658 (1985).

[46] D. B. Haviland, Y. Liu and A. M. Goldman, Phys. Rev. Lett. **62**, 2180 (1989).

[47] A. M. Goldman and N. Markovic, Phys. Today **51**, 39 (1998).

[48] A. Yazdani and A. Kapitulnik, Phys. Rev. Lett. **74**, 3037 (1995).

[49] J. M. Valles, R. C. Dynes and J. P. Garno, Phys. Rev. Lett. **69**, 3567 (1992).

[50] M. P. A. Fischer, G. Grinstein and S. Girvin, Phys. Rev. Lett. **64**, 587 (1990).

[51] P. A. Lee and T. V. Ramakrishnan, Rev. Mod. Phys. **57**, 287 (1985).

[52] A. I. Shalnikov, Nature **142**, 74 (1938).

[53] D. Ephron, A. Yazdani, A. Kapitulnik and M. R. Beasley, Phys. Rev. Lett. **76**, 1529 (1996).

[54] N. Mason and A. Kapitulnik, Phys. Rev. Lett. **82**, 5341 (1999).

[55] Y. Seo, Y. Qin, C. L. Vicente, K. S. Choi and Y. Joon, Phys. Rev. Lett. **97**, 057005 (2006).

[56] Y. Qin, C. L. Vicente and J. Yoon, Phys. Rev. B **73**, 100505(R) (2006).

[57] V. Humbert, F. Couedo, O. Crauste, L. Berge, A.-A. Drillien, C. A. Marrache-Kikuchi and L. Dumoulin, J. Phys. Conf. Ser. **568**, 052012 (2014).

[58] Y. Li, C. L. Vicente and J. Yoon, Phys. Rev. B **81**, 020505(R) (2010).

[59] S. Park, J. Shin and E. Kim, Sci. Rep. **7**, 42969 (2014).

[60] P. Phillips and D. Dalidovich, Science **302**, 243 (2003).

[61] H. M. Jaeger, D. B. Haviland, A. M. Goldman and B. G. Orr, Phys. Rev. B **34**, 7 (1986).

[62] N. Mason and A. Kapitulnik, Phys. Rev. B **64**, 060504(R) (2001).

[63] C. Christiansen, L. M. Hernandez and A. M. Goldman, Phys. Rev. Lett. **88**, 037004 (2002).

[64] M. P. A. Fischer, P. B. Weichman, G. Grinstein and D. S. Fischer, Phys. Rev. B **40**, 546 (1989).

[65] T. I. Baturina, A. Y. Mironov, V. M. Vinokur, M. R. Baklanov and C. Strunk, Phys. Rev. Lett. **99**, 257003 (2007).

[66] B. Sacepe, C. Chapelier, T. I. Baturina, V. M. Vinokur, M. R. Baklanov and M. Sanquer, Nature Commun. **1**, 140 (2010).

[67] Y. Dubi, Y. Meir and Y. Avishai, Nature **449**, 876 (2007).

[68] J. Biscaras, N. Bergeal, S. Hurand, C. Feuillet-Palma, A. Rastogi, R. C. Budhani, M. Grilli, S. Caprara and J. Lesqueur, Nature Mater. **12**, 542 (2013).

[69] M. D. Stewart Jr, A. Yin, J. M. Xu and J. M. Valles Jr, Science **318**, 1273 (2007).

[70] R. P. Barber Jr, L. M. Merchant, A. La Porta and R. C. Dynes, Phys. Rev. B **49**, 3409 (1994).

[71] A. E. White, R. C. Dynes and J. P. Garno, Phys. Rev. B **33**, 3549 (1986).

[72] S. M. Hollen, H. Q. Nguyen, E. Rudisaile, M. D. Stewart Jr, J. Shainline, J. M. Xu and L. M. Valles Jr, Phys. Rev. B **84**, 064528 (2011).

[73] S. Poran, E. Shimshoni and A. Frydman, Phys. Rev. Lett. **84**, 014529 (2011).

[74] D. Sherman, G. Kopnov, D. Shahar and A. Frydman, Phys. Rev. Lett. **108** 177006 (2012).

[75] Y. Noat, V. Cherkez, C. Brun, T. Cren, C. Carbillet, F. Debontridder, K. Ilin, M. Siegel, A. Semenov, H.-W. Hübers and D. Roditchev, Phys. Rev. B **88**, 014503 (2013).

[76] A. T. Bollinger, G. Dubuis, J. Yoon, D. Pavuna, J. Misewich and I. Bozovic, Nature **472**, 458 (2011).

[77] X. Shi, G. Logvenov, A. T. Bollinger, I. Bozovic, C. Panagopoulos and D. Popovic, Nature Mater. **12**, 47 (2012).

[78] M. Chand, G. Saraswat, A. Kamlapure, M. Mondal, S. Kumar, J. Jesudan, V. Bagwe, L. Benfatto, V. Tripathi and P. Raychaudhuri, Phys. Rev. B **85**, 014508 (2012).

[79] T. Schneider, A. D. Caviglia, S. Gariglio, N. Reyren and J.-M. Triscone, Phys. Rev. B **79**, 184502 (2009).

[80] M. M. Mehta, D. A. Dikin, C. W. Bark, S. Ryu, C. M. Folkman, C. B. Eom and V. Chandrasekhar, Phys. Rev. B **90**, 100506(R) (2014).

[81] S. Caprara, D. Bucheli, N. Scopigno, J. Biscaras, S. Hurand, J. Lesueur and M. Grilli, Supercond. Sci. Technol. **28**, 014002 (2015).

[82] Y.-H. Lin, J. Nelson and A. M. Goldman, Physica C **514**, 130 (2015).

[83] D. A. Dikin, M. Mehta, C. W. Bark, C. M. Folkman, C. B. Eom and V. Chandrasekhar, Phys. Rev. Lett. **107**, 056802 (2011).

[84] G. Herranz, G. Singh, N. Bergeal, A. Jouan, J. Lesqueur, J. Gasquez, M. Varela, M. Scigaj, N. Dix, F. Sanchez and J. Fontcuberta, Nature Commun. **6**, 6028 (2015).

[85] C. Bell, S. Harashima, Y. Kozuka, M. Kim, B. G. Kim, Y. Hikita and H. Y. Hwang, Phys. Rev. Lett. **103**, 226802 (2009).

[86] E. Fillis-Tsirakis, C. Richter, J. Mannhart and H. Boschker, New J. Phys. **18**, 013046 (2016).

[87] V. M. Vinokur, T. I. Baturina, M. V. Fistul, A. Y. Mironov, M. R. Baklanov and C. Strunk, Nature **452**, 613 (2008).

[88] M. Ovadia, D. Kalok, B. Sacepe and D. Shahar, Nature Phys. **9**, 415 (2013).

[89] M. Ovadia, D. Kalok, I. Tamir, S. Mitra, B. Sacepe and D. Shahar, Sci. Rep. **5**, 13503 (2015).

[90] D. M. Basko, I. L. Aleiner and B. L. Altshuler, Phys. Rev. B **76**, 052203 (2007).

[91] V. Y. Butko and P. W. Adams, Nature **409**, 161 (2001).

[92] T. I. Baturina and C. Strunk, Phys. Rev. Lett **98**, 127003 (2007).

[93] S. Hurand, A. Jouan, C. Feuillet-Palma, G. Singh, J. Biscaras, E. Lesne, N. Reyren, A. Barthelemy, M. Bibes, C. Ulysse, X. Lafosse, M. Pannetier-Lecoeur, S. Caprara, M. Grilli, J. Lesueur and N. Bergeal, Sci. Rep. **5**, 12571 (2015).

[94] B. Sacepe, T. Dubouchet, C. Chapelier, M. Sanquer, M. Ovadia, D. Shahar, M. Feigel'man and L. Ioffe, Nature Phys. **7**, 239 (2011).

[95] Y. Nakamura and Y. Yanase, J. Phys. Soc. Jpn. **82**, 083705 (2013).

[96] X. Lin, Z. Zhu, B. Fauque and K. Behnia, Phys. Rev. X **3**, 021002 (2013).

[97] A. Koreeda, R. Takano and S. Saikan, Phys. Rev. Lett. **99**, 265502 (2007).

[98] P. W. Anderson, J. Phys. Chem. Solids **11**, 26 (1959).

[99] A. A. Abrikosov and L. P. Gorkov, Sov. Phys. JETP **8**, 1090 (1959).

[100] M. V. Feigel'man, L. B. Ioffe, V. E. Kravtsov and E. A. Yuzbashyan, Phys. Rev. Lett. **98**, 027001 (2007).

[101] M. V. Feigel'man, L. B. Ioffe, V. E. Kravtsov and E. Cuervas, Ann. Phys. **325**, 1390 (2010).

[102] B. S. Chandrasekhar, Appl. Phys. Lett. **1**, 7 (1962).

[103] A. M. Clogston, Phys. Rev. Lett. **9**, 266 (1962).

[104] A. D. Caviglia, M. Gabay, S. Gariglio, N. Reyren, C. Cancellieri and J.-M. Triscone, Phys. Rev. Lett. **104**, 126803 (2010).

[105] M. Kim, Y. Kozuka, C. Bell, Y. Hikita and H. Y. Hwang, Phys. Rev. B **86**, 085121 (2012).

[106] J. M. Edge and A. V. Balatsky, J. Supercon. Nov. Magn. **28**, 2373 (2015).

[107] G. P. Mikitik, Zh. Eksp. Teor. Fiz. **101**, 1042 (1992).

[108] A. Gurevich, Phys. Rev. B **67**, 184515 (2003).

[109] S. Caprara, J. Biscaras, N. Bergeal, D. Bucheli, S. Hurand, C. Feuillet-Palma, A. Rastogi, R. C. Budhani, J. Lesueur and M. Grili, Phys. Rev. B **88**, 020504(R) (2013).

[110] R. M. Fernandes, J. T. Haraldsen, P. Woelfle and A. V. Balatsky, Phys. Rev B **87**, 014510 (2013).

[111] V. K. Guduru, A. McCollam, J. C. Maan and U. Zeitler, J. Kor. Phys. Soc. **63**, 437 (2013).

[112] H. Suhl, B. T. Matthias and L. R. Walker, Phys. Rev. Lett. **3**, 552 (1959).

[113] V. A. Moskalenko, Phys. Met. Metallov. **8**, 25 (1959).

[114] V. A. Moskalenko, M. E. Palistrant and V. M. Vakalyuk, Sov. Phys. Usp. **34**, 717 (1991); arXiv:cond-mat/0309671v1.

[115] G. Binnig, A. Baratoff, H. E. Hoenig and J. G. Bednorz, Phys. Rev. Lett. **45**, 1352 (1980).

[116] M. L. Cohen, Phys. Rev. **134**, A511 (1964).

[117] F. Kuchar and P. Frankus, Solid State Commun. **16**, 181 (1975).

[118] J. Appel, Phys. Rev. **180**, 508 (1969).

[119] Z. Zinamon, Philos. Mag. **21**, 347 (1970).

[120] T. Jarlborg, Phys. Rev. B **61**, 9887 (2000).

[121] D. van der Marel, J. L. M. van Mechelen and I. I. Mazin, Phys. Rev. B **84**, 205111 (2011).

[122] L. Kürten, C. Richter, N. Mohanta, T. Kopp, A. Kampf, J. Mannhart and H. Boschker (submitted 2017).

[123] A. Teker, *Private Communication*, Max-Planck-Institute, Stuttgart (2016).

[124] S. T. Ruggiero, T. W. Barbee Jr., and M. R. Beasley, Phys. Rev. Lett. **45**, 1299 (1980).

[125] M. Tinkham, Phys. Rev. **129**, 2413 (1962).

[126] M. Tinkham, Rev. Mod. Phys. **36**, 268 (1964).

[127] R. E. Miller and G. D. Cody Phys. Rev.**173**, 494 (1968).

[128] N. Reyren, S. Gariglio, A. D. Caviglia, D. Jaccard, T. Schneider and J.-M. Triscone, Appl. Phys. Lett. **94**, 112506 (2009).

[129] M. Ben Shalom, C. W. Tai, Y. Lereah, M. Sachs, E. Levy, D. Rakhmilevitch, A. Palevski and Y. Dagan, Phys. Rev. B **80**, 140403(R) (2009).

[130] M. Ben Shalom, M. Sachs, D. Rakhmilevitch, A. Palevski and Y. Dagan, Phys. Rev. Lett. **104**, 126802 (2010).

[131] M. Hosoda, Y. Hikita, H. Y. Hwang and C. Bell, Appl. Phys. Lett. **103**, 103507 (2013).

[132] A. A. Golubov and V. V. Dorin, J. Low Temp. Phys. **78**, 375 (1990).

[133] N. R. Werthamer, E. Helfand and P. C. Hohenberg, Phys. Rev. **147**, 295 (1966).

[134] K. R. Biagi, J. R. Clem and V. G. Kogan, Phys. Rev. B **33**, 3100 (1986).

[135] K. R. Biagi, V. G. Kogan and J. R. Clem, Phys. Rev. B **32**, 7165 (1985).

[136] D. Neerinck, K. Temst, H. Vanderstraeten, C. van Haesendonck, Y. Bruynseraede, A. Gilbert and I. K. Schuller, J. Phys. Cond. Matt. **2**, 6287 (1990).

[137] D. R. Tilley and R. Ward, Solid State Commun. **8**, 1983 (1970).

[138] D. W. Youngner and R. A. Klemm, Phys. Rev. B **21**, 3890 (1979).

[139] E. Helfand and N. R. Werthamer, Phys. Rev. B **147**, 288 (1966).

[140] G. Herranz, F. Sanchez, N. Dix and J. Fontcuberta, Sci. Rep. **2**, 758 (2012).

[141] Y.-L. Han, S.-C. Shen, J. You, H.-O. Li, Z.-Z. Luo, C.-J. Li, G.-L. Qu, C.-M. Xiong, R.-F. Dou, L. He, D. Naugle, G.-P. Guo and J.-C. Nie, Appl. Phys. Lett. **105**, 192603 (2014).

[142] A. Annadi, Q. Zhang, X. Renshaw Wang, N. Tuzla, K. Gopinadhan, W. M. Lü, A. Roy Barman, Z. Q. Liu, A. Srivastana, S. Saha, Y. L. Zhao, S. W. Zeng, S. Dhar, E. Olsson, B. Gu, S. Yunoki, S. Maekawa, H. Hilgenkamp, T. Venkatesan and Ariando, Nature Commun. **4**, 1838 (2013).

[143] D. A. Wollman, D. J. van Harlingen, J. Giapintzakis and D. M. Ginsberg, Phys. Rev. Lett. **74**, 797 (1995).

[144] H. J. H. Smilde, A. A. Golubov, Ariando, G. Rijnders, J. M. Dekkers, S. Harkema, D. H. A. Blank, H. Rogalla and H. Hilgenkamp, Phys. Rev. Lett. **95**, 257001 (2005).

[145] D. J. van Harlingen, Rev. Mod. Phys. **67**, 515 (1995).

[146] D. J. van Harlingen, Physica C **317**, 410 (1999).

Chapter 5

Results: Tunneling Spectroscopy using Doped-$SrTiO_3$ Schottky Junctions

In this chapter, the doped-$SrTiO_3$ superconductor, the bulk counterpart of the 2D electron system that is generated by the $LaAlO_3/SrTiO_3$ interface, is studied in detail. The chapter starts with a brief introduction about tunneling into semiconducting $SrTiO_3$ and questions about its superconducting ground state. The measurements section is divided in two parts. The first presents tunnel measurements in a large energy range where inelastic tunneling processes are present. The second contains measurements restricted within a small energy window around E_F, where superconducting features are resolved and their evolution with temperature and magnetic field is discussed. Concluding this chapter, the main outcome of the study of bulk $SrTiO_3$ is summarized. Possible extensions of my research are discussed for future experiments.

5.1 Electron Tunneling in Junctions of Doped-$SrTiO_3$ and Indium

With the fabrication of two-dimensional electron gases in $SrTiO_3$ based heterostructures and particularly in the $LaAlO_3/SrTiO_3$ 2DEL in 2004 [1], bulk doped-$SrTiO_3$ has regained attention as a superconductor of extremely low carrier density. Although its superconducting ground state has been extensively studied decades ago [2, 3], several questions still remain open. The survival of superconductivity at carrier densities as low as $5{\cdot}10^{17}$ cm^{-3} is a mystery, as the Cooper-pairs exist in an ultra small Fermi surface (with Fermi energy of approx. 1 meV) on top of a 3.2 eV band gap [4]. The dome-like dependence of T_c on carrier concentration n_s is a feature uncommon for conventional BCS-superconductors [2]; yet a salient property of the high-temperature superconductors [5]. Through the study of superconductivity in doped-$SrTiO_3$ and other oxides with high dielectric constants, G. Bednorz and K. A. Muller proposed that this dome-like dependence originates from the T_c-dependence on the electron phonon coupling constant [6]. According to their concept, with increasing electron-phonon coupling at low temperatures, the emergent superconducting phase is suppressed by strong localization owing to the rise of Jahn-Teller polarons [7, 8]. Whether the coupling to longitudinal optical (LO) phonon modes can account for superconductivity in the dilute regime of $SrTiO_3$ and the relation to its two-dimensional counterpart, the $LaAlO_3/SrTiO_3$ 2DEL, still are questions that are not fully understood.

The dispersion of the lowest unoccupied bands at the Γ-point of the Brillouin zone of $SrTiO_3$ has been calculated [9]. In the [001]-direction, a heavy band along the Ti-O bond, centered at the Γ-point, is energetically the lowest. It is succeeded by two lighter bands at higher energies that are parabolic. For carrier concentrations of the order of 10^{19} cm^{-3}, at least two bands are occupied, thus $SrTiO_3$ is a likely candidate for multiband superconductivity, if sufficiently doped. Tunneling spectroscopy [10] and thermal conductivity measurements [11] have found multiband signatures in optimally doped $SrTiO_3$.

In 1969, Z. Sroubek performed tunneling measurements between In and Nb-doped $SrTiO_3$ [12]. By measuring the differential resistivity, the chemical potential and effective mass were determined for each sample. Figure 5.1 presents the $I-V$ characteristics of such tunnel junctions at different Nb-doping concentrations. They show rectifying behavior. Electron tunneling experiments in doped-$SrTiO_3$ is a useful method for studying the evolution of the superconducting DOS. Tunneling measurements in planar junctions of metals (top electrode) and semiconducting $SrTiO_3$ (bottom electrode) have been performed already long ago, with Au, In, Al, Ir and Pt being the most common counter electrodes (see Ch. 2, section 2.2.2). Indium is the preferred metal, as it yields junctions with low Schottky barriers and consequently tunneling currents high enough to resolve intrinsic features of the semiconducting $SrTiO_3$ substrate (i.e. phonon modes, the DOS around the Fermi energy at low temperatures).

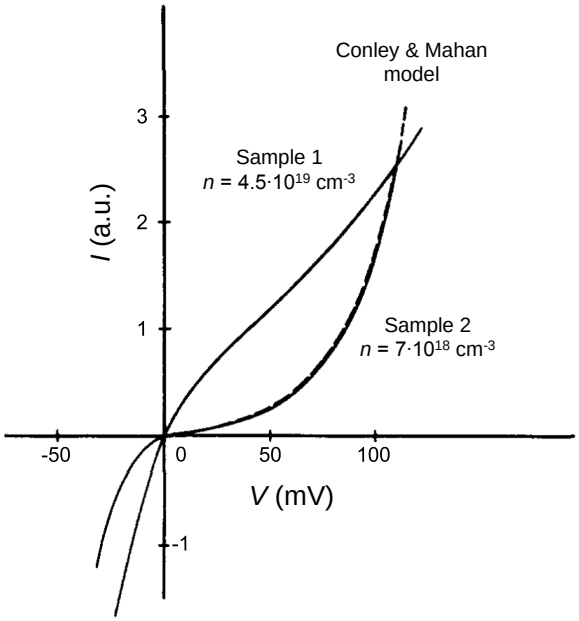

Figure 5.1: *The $I-V$ characteristics of two samples with tunnel junctions of In and Nb-doped $SrTiO_3$ of different carrier concentrations. The dashed line is the theoretical prediction of Ref. [13]. From [12].*

My work aims to provide information about the superconducting ground state of semiconducting $SrTiO_3$, by using tunneling spectroscopy at ultra low temperatures and in the presence of magnetic fields. Multiband superconductivity has been reportedly seen in tunnel measurements [12] and can be possibly resolved either in the tunnel spectra at the mK-range or in the temperature dependence of the critical magnetic field.

Commercially purchased Nb-doped substrates with varying carrier concentration (the doping ranges from 0.01 wt% to 1 wt%) were used in the fabrication of high-quality tunnel junctions, to resolve superconducting features in the tunnel spectra and multiband signatures for the highly-doped. In this carrier-density range, $SrTiO_3$ exhibits superconductivity [2, 14] with $T_c(n_s)$ having a dome-like shape. The carrier concentration dependence on doping is listed in Table 5.1, for the range where semiconducting $SrTiO_3$ is superconducting at low temperatures. Considering that Nb-dopants are single-donors (see Ch. 2), the atomic weight of Nb is 92.91 and also assuming an $SrTiO_3$ density of 5.11 gr/cm^{-3}, the absolute number of carriers in each substrate has been determined, for a nominal substrate-size of $5\times5\times1$ mm. From this number, the charge carrier density n_s could be calculated (column "Calculated n_s" in Tab. 5.1). In addition, Hall-measurements were performed at $T = 2$ K, in a PPMS set-up, in order to verify the calculated values. The measured values for n_s are generally in very good agreement with those calculated, in the entire doping range. Small deviations between measured and calculated values can be either due to dopant-segregation or due to electrically inactive (e.g. compensated by impurities) dopants within a substrate. As these deviations can be intrinsic to individual substrates, in this work I consider the calculated n_s as a nominal value for the carrier density.

Table 5.1: Carrier concentrations of Nb-doped $SrTiO_3$ substrates with respect to doping.

Nb-Doping (weight %)	Absolute Number of Carriers ($\times 10^{18}$)	Calculated n_s ($\times 10^{20}$ cm^{-3})	Measured n_s at T = 2 K ($\times 10^{20}$ cm^{-3})
1	8.28	3.31	3.24 ± 0.06
0.7	5.80	2.32	2.30 ± 0.04
0.5	4.14	1.66	1.75 ± 0.08
0.35	2.90	1.16	1.09 ± 0.06
0.2	1.66	0.66	0.60 ± 0.03
0.1	0.83	0.33	0.32 ± 0.02
0.05	0.41	0.17	0.14 ± 0.03
0.01	0.08	0.03	0.04 ± 0.01

For the discussion of tunnel junction characteristics, it is meaningful to categorize all measured samples with respect to their individual characteristics, i.e. substrate doping concentration and the thicknesses of the metallic layers deposited. Table 5.2 contains all the information about the characteristics of the tunnel junctions fabricated with Nb-doped $SrTiO_3$ substrates[1] and metals In, Au and Al. Those listed are only the samples mentioned in the discussion of this chapter and of the Appendices A and B.

Table 5.2: List of samples mentioned in this chapter and in the Appendix.

Sample	$SrTiO_3$ substrate Nb-doping wt%	Indium Thickness (nm)	Gold Thickness (nm)	Aluminum Thickness (nm)
P09	0.5	–	20	50
P11	0.5	50	30	–
P13	0.05	–	100	–
P19	0.5	100	40	–
P21	0.5	100	40	–
P22	0.1	–	100	–
P23	0.5	–	100	–
P31	0.5	50	30	–
P24 - P34[1]	0.5	50 - 150	0 - 30	–
P36	0.5	150	20	–

[1] In the P24 - P34 sample group, an undoped $SrTiO_3$ and a sapphire substrate were additionally used for metallic film growth.

5.2 Measurements: Non-linear *I-V* Characteristics at 4.3 K

The vast majority of tunneling measurements was performed in junctions of Nb-doped $SrTiO_3$ (0.5 wt%) with In-films, of thicknesses between 50 nm and 150 nm. For comparison, junctions with Al and Au as top electrodes were also manufactured. In the case of Al-junctions the Schottky barrier was extremely low, with the tunnel resistance close to zero (sample P09 in Tab. 5.2). Junctions with Au have generally yielded large Schottky barriers whose height was found to anti-correlate with the Nb-doping concentration (samples P13, P22 and P23 in Tab. 5.2). Still, it was found large in all cases, as compared to barriers in junctions with In and $SrTiO_3$. All tunnel junctions were fabricated by thermally evaporating metals on top of Nb-doped $SrTiO_3$ substrates (the process is described in Ch. 3). Circular devices with various sizes are individually contacted and by four-point measurements the $I-V$ characteristic of each junction is recorded. In the notation used in this chapter, for $V > 0$ electrons tunnel out of the $SrTiO_3$ substrate and into the metallic top electrode.

Figure 5.2 shows the $I-V$ characteristics of two tunnel junctions with Au and In as top electrodes. It is evident that the tunneling current in the case of In is higher, despite the smaller device size. In all other samples with Au as top electrode, on Nb-doped $SrTiO_3$ of smaller dopant-concentration, the tunneling currents obtained were order of magnitudes smaller than in sample P23 shown in Fig. 5.2.

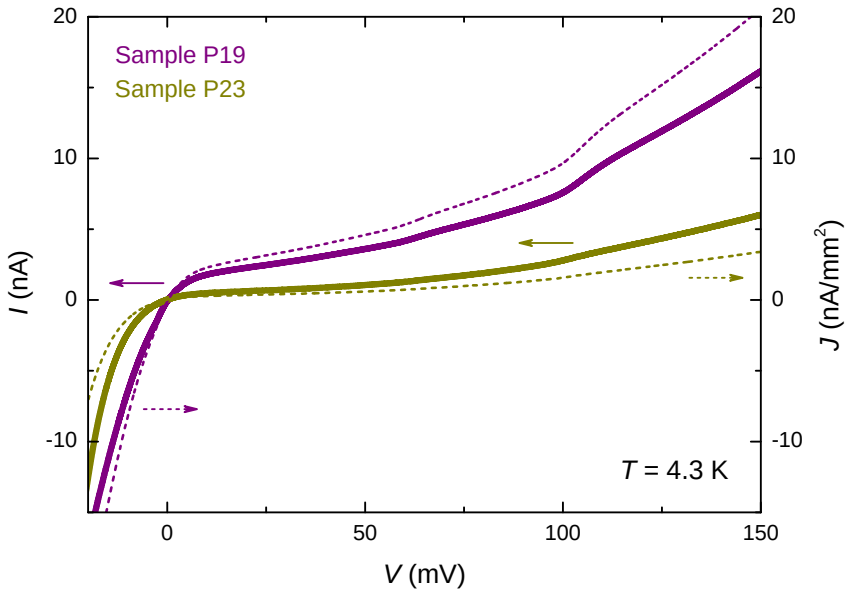

Figure 5.2: *I - V characteristics of tunnel junctions with $SrTiO_3$, doped with 0.5 wt% Nb. The violet curve is measured in a junction where a 100 nm In-layer (1 mm in diameter) is the top electrode (sample P19). The dark-yellow curve is from a junction with Au as top electrode, on a device 100 nm thick and 1.5 mm in diameter (sample P23). The dashed lines show the current density of each junction with respect to applied bias (right y-axis).*

The difference between the current densities of In-$SrTiO_3$ and Au-$SrTiO_3$ junctions can be explained by the difference in the work functions of Au and In. Gold has a work function that is approximately 1 eV higher, as compared to that of In at 4.12 eV (value taken from [15]), which typically yields larger Schottky barriers in such junctions. Within the Schottky-Mott theory [16, 17], the magnitude of the barrier is given by Eq. 2.8 in Ch. 2. Yet, the surface treatment is of high importance when fabricating metal-semiconductor junctions, as the Schottky barrier might be drastically affected by surface states. Several theories calculate the height of the Schottky barrier based on material parameters and are summarized in this review [18]. The covalency of the semiconductor is also known to play a role on the pinning of the Fermi level, in which case the material work function is not the key factor [19]. This pinning can be in some cases due to metal-induced gap-states [20], or due to native defects and surface states [21, 22].

5.2.1 Assessing the Schottky Junctions

Since the semiconductor's surface is one of the crucial factors that determine the shape of the Schottky barrier, several samples were grown under different conditions. The aim was to: a) check whether the barrier features are sustained over the entire $SrTiO_3$ substrate and b) study the dependence of the tunneling current on the junction-area. This was done by measuring the conductance across circular junctions of varying diameter on the same sample. It was found that the absolute value of the tunneling conductance increases with increasing device area, yet not showing a linear dependence.

Figure 5.3 shows the $I-V$ characteristics of tunnel junctions on sample P36, at 4.3 K.

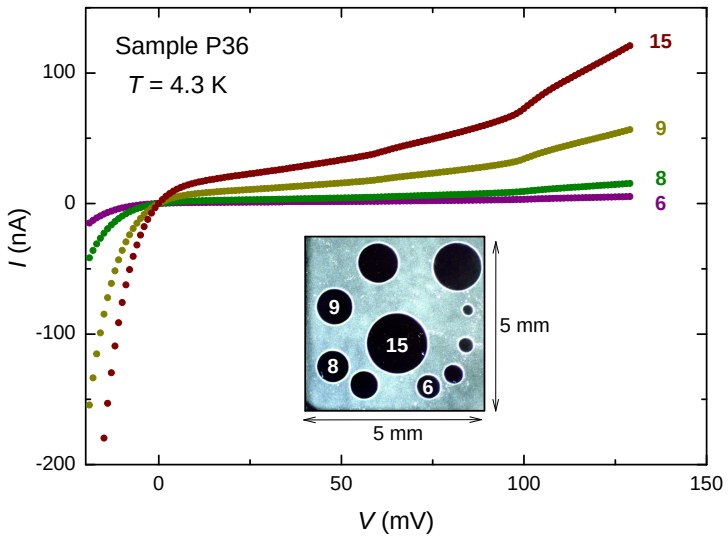

Figure 5.3: *The I - V characteristics from circular tunnel devices of different size on the same sample. Devices 6, 8, 9 and 15 respectively have diameters of 0.6, 0.8, 0.9 and 1.5 mm, with their exact location on the sample as indicated. In the voltage region between zero and 120 mV, the largest device exhibits the highest tunneling current.*

In Fig. 5.4a the tunneling conductances are plotted as a function of V. Junction 6 exhibits low tunneling current and the otherwise prominent phonon-mode features lie in a noisy background. As the device size increases the tunneling current is enhanced and the signal-to-noise ratio of the $\mathrm{d}I/\mathrm{d}V(V)$ dependence improves. The LO2 mode at approximately 34 mV is resolved in the characteristic of junction 15. The LO3 and LO4 modes are clearly distinguishable in all devices (see Table 5.3).

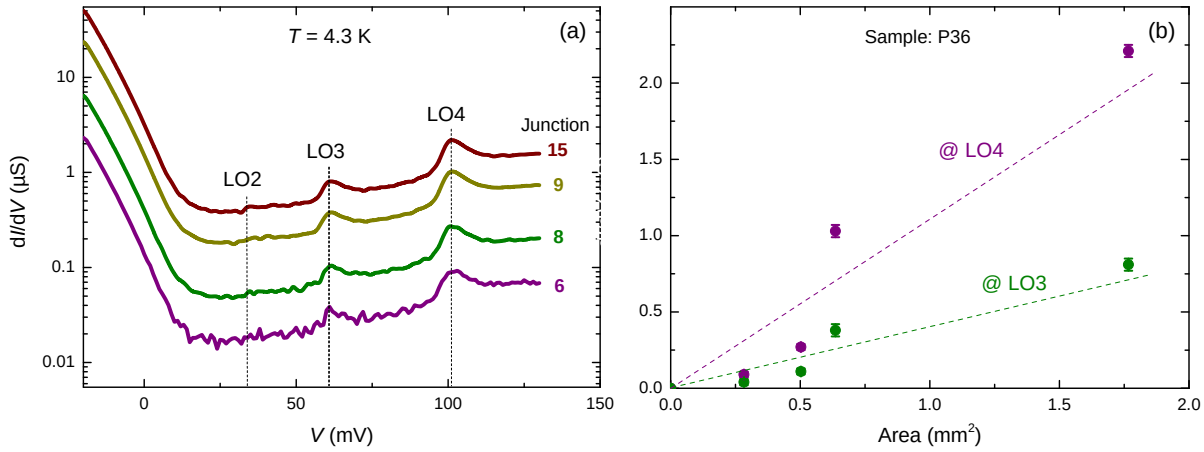

Figure 5.4: *(a) The dI/dV (V) dependences measured in the junctions of sample P36 are presented on a semilogarithmic plot. Junction 15 yielded tunneling currents high enough to resolve the LO2 mode, along with LO3 and LO4. The lines drawn in the vicinity of each phonon mode on the characteristics are used for calculating the conductance dependence on area (shown on the right) and do not correspond to precise phonon energies. (b) The absolute values of the dI/dV (V) at voltages that correspond to the LO3 (green points) and LO4 (purple points) modes in (a), with respect to junction area. The dI/dV-dependences are not exactly linear for either voltage value. The dashed lines are guides to the eye.*

To quantify the tunneling current increase with respect to device area, the absolute values of the conductance at voltages that correspond to the LO3 and LO4 modes are considered. Figure 5.4b presents the conductance dependence as a function of device area. With increasing tunneling-area the conductance also increases, yet not linearly. The dependence resembles an exponential growth for the three smaller junctions, but not for the largest (on this sample) with a diameter of 1.5 mm. It is therefore evident that the absolute value of the tunneling current is sensitive to location, even within the same substrate, and does not solely depend on the area of the tunnel junction. This explains why junctions measured on different samples do not always exhibit similar absolute values of their tunneling measures, albeit being often of similar size.

5.2.2 Resolving the Phonon Modes of Nb-doped $SrTiO_3$ by Tunneling Measurements

One of the goals of my work is the fabrication of junctions with Schottky barriers that yield tunneling currents high enough to resolve phonon modes consistently. It has been therefore concluded that In is the best candidate. As realized when optimizing the fabrication procedure, the Schottky barrier properties are quite sensitive to the substrate condition (especially when the $SrTiO_3$ crystals are etched in Ar) and also the metal growth rate, thus Fermi level pinning is a possibility in my junctions. In Fig. 5.5, the characteristic phonon peaks in the dI/dV are observed in the Schottky junction of doped $SrTiO_3$ and In.

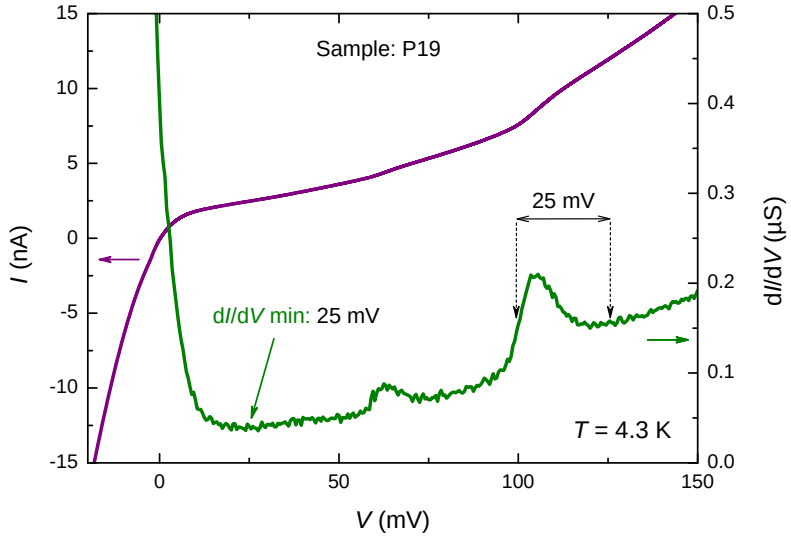

Figure 5.5: *The conductance (dI/dV) dependence on bias V (green curve) for the junction with In as top electrode. Two peaks appear in the range 25 meV to 150 meV, which correspond to longitudinal optical phonon modes of $SrTiO_3$. The minimum at approximately 25 mV marks the bottom of the conduction band. A region of 25 meV is also indicated at the regime of the most prominent inelastic feature. It is measured from the point where the slope (d^2I/dV^2 (V)) is maximum until the voltage where tunneling is mainly elastic and offers an alternative way of determining the value of the chemical potential [23].*

By monitoring the magnitude of the tunneling conductance across the junction, information on the onset of the conduction band can be obtained. In this sample, the minimum of the $dI/dV(V)$ dependence is approximately at 25 mV. For $V < 25$ mV, the conductance increases sharply as the empty states of the conduction band are now available for electrons to tunnel into from the metallic side. With bias increasing further from 25 mV, the conductance slowly increases due to elastic as well as due to phonon-assisted (inelastic) tunneling. It has been argued that inelastic tunneling gives more accurate information about the structure at the edge of the conduction band in MIS and Schottky junctions [23]. This is because tunneling electrons through the inelastic channel have higher energy than those through the elastic channel at the edge of the conduction band. The shape of the concave part at the right side of

an inelastic feature in the dI/dV is also known to depend on temperature [23, 24]. With no substantial discrepancy on the exact location of the chemical potential, as determined from the elastic and inelastic channels, it is concluded that the Fermi level lies approximately at 25 meV above the conduction band edge of $SrTiO_3$ in this particular junction. Meanwhile, for $V > 25$ mV, the elastic dI/dV background increases with increasing voltage, in the entire range of investigation. This comes as a result of a barrier-thickness decrease as the applied bias increases.

Under the assumption of a parabolic, non-degenerate band and considering this value for the chemical potential μ_F (measured from the bottom of the conduction band), an approximation of the effective mass m^* can be obtained by the expression [12, 13]:

$$\mu_F = \frac{\hbar^2}{2m^*}(3\pi^2 n_s)^{2/3} \tag{5.1}$$

The carrier concentration n_s for Nb-doping of 0.5 wt%, has been calculated at $1.66{\cdot}10^{20}$ cm^{-3} (see Table 5.1). Assuming an uncertainty of ± 1 meV for the estimation of the chemical potential μ_F from the dI/dV characteristic, an estimate for the effective mass $m^* = (4.4 \pm 0.2){\cdot}m_e$ is obtained, where m_e is the free electron mass. This value corresponds to the DOS effective mass of an electron in the conduction band. This estimate is remarkably close to the one determined by recent specific heat [11] and quantum oscillation measurements [25], at $4.2{\cdot}m_e$, for a sample with $n_s = 2.6{\cdot}10^{20}$ cm^{-3}. According to that work, when the carrier concentration exceeds a threshold value of $2{\cdot}10^{19}$ cm^{-3}, the chemical potential lies above the edge of the three bands, but with the majority of carriers residing in the lowest and heaviest. Earlier estimates of the mean effective mass in the conduction band have shown values of $5{\cdot}m_e$ (spin susceptibility measurements [26]) and $6{\cdot}m_e$ to $13{\cdot}m_e$ (transport measurements [27]). From the tunneling perspective, such values for the effective mass of an electron in the conduction band are extremely large for tunneling to occur in the first place. Yet, the dielectric constant ε in the Schottky region is much lower due to the electrostatic potential across the junction. This simply means that the effective tunneling mass is much smaller than the calculated DOS effective mass at $4.4{\cdot}m_e$.

The elastic and inelastic tunneling regimes are shown in Fig. 5.6, where the dI/dV-profile is measured over an extended voltage range. The Fermi level of $SrTiO_3$ lies inside the conduction band at equilibrium ($V = 0$). In the elastic regime, the conductance decreases exponentially with increasing bias V, not following the square-root energy-dependence of the DOS in 3D-space. Assuming parabolic bands, it is implied that the conductance is not directly proportional to the DOS. Yet on this extended V-range, changes in the Schottky barrier height may play a dominant role in the $\mathrm{d}I/\mathrm{d}V(V)$ dependence, invalidating the assumption of completely parabolic bands. This change is (seemingly) induced by the applied voltage, while population of states within the barrier itself is also a possibility during tunneling.

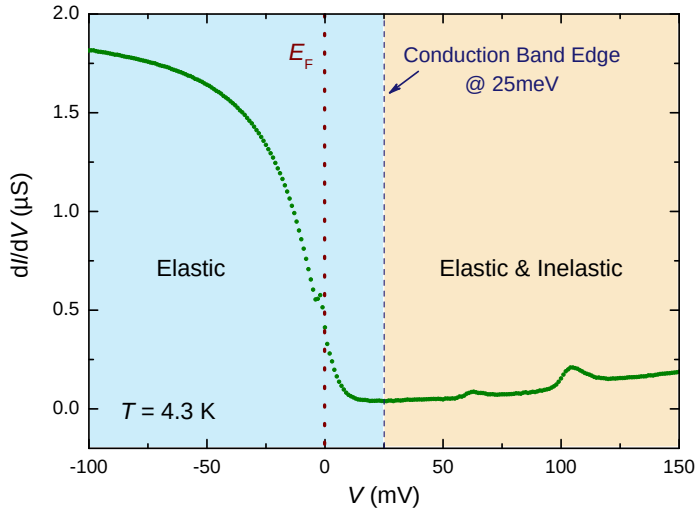

Figure 5.6: *The conductance dependence on applied bias, on an extended scale. Two regimes are highlighted, illustrating the bias-range where tunneling is only through the elastic channel (light blue) and through both, elastic and inelastic channels (light brown). The Fermi level and the onset of the conduction band are indicated, with phonon modes present for V > 25 mV.*

The energies of the phonon modes in the $\mathrm{d}I/\mathrm{d}V(V)$ can be precisely determined by plotting the second derivative of the tunneling current. The two maxima in the $\mathrm{d}^2I/\mathrm{d}V^2$ (V) spectrum correspond to the longitudinal optical modes LO3 and LO4, with energies respectively at 59 meV and 100.5 meV, as observed in Fig. 5.7. These values are very close to those reported by Hyper-Raman (HR) Spectroscopy [28], as well as to the tunneling determined values for $LaAlO_3/SrTiO_3$ [29, 30].

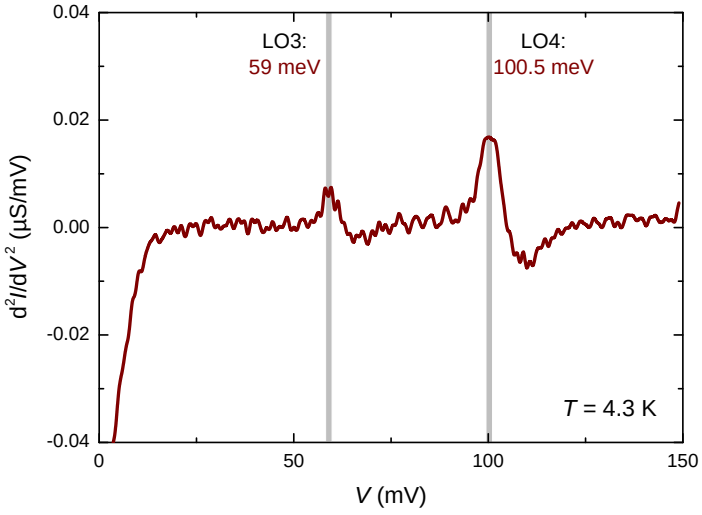

Figure 5.7: *The d^2I/dV^2 (V) spectrum of the tunnel junction featuring two longitudinal optical phonon modes (LO3 and LO4) of the Nb-doped $SrTiO_3$ substrate.*

The LO3 and LO4 modes are clearly resolved in this sample. In other samples in which higher tunneling currents were flowing across the Schottky junction, it was possible to observe a small conductance increase at an energy of 34 meV that corresponds to the LO2 mode (sample P36 in Fig. 5.4a). The LO1 mode, as well as transverse optical (TO) modes that are lower in energy, were not observed. The extracted experimental values are summarized in Table 5.3, along with values from literature.

Table 5.3: The identified phonon modes of $SrTiO_3$, as compared with literature.

Phonon Mode	HR-Spectroscopy (eV)	Tunneling ($LaAlO_3/SrTiO_3$) (eV)	This Work (eV)
LO2	33	33.5	34 ± 0.5
LO3	58.8	59.4	59 ± 0.5
LO4	98.6	98.1	100.5 ± 0.5

An estimation of the electron-phonon interaction strength was derived by S. Hayashi et al. for tunnel junctions with In and O_2-reduced $SrTiO_3$ [23, 31]. Fig. 5.8 shows their data, plotted along with my measurements with Nb-doped $SrTiO_3$. Sample P19 seemingly has more distinct inelastic features with respect to the elastic tunneling background on this voltage range.

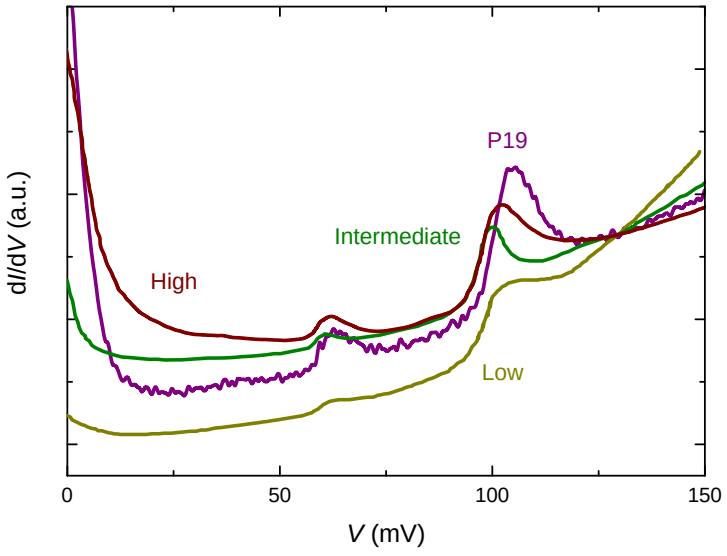

Figure 5.8: *Tunneling data from Ref. [23, 31] for doped $SrTiO_3$ crystals, with carrier concentrations (from low to high) of $2.1{\cdot}10^{19}$, $3.6{\cdot}10^{19}$ and $3{\cdot}10^{20}$ cm^{-3} at 1.75 K. My data at 4.3 K from sample P19 (violet curve) is also plotted. All curves are normalized to the conductance value at 130 mV.*

The ratio of the conductance-change of the LO3 and LO4 modes in the O_2-reduced samples exhibits an increase with increasing chemical potential (i.e. induced by doping by O_2-reduction). As is evident, the applied potential changes the Schottky barrier. This is seen by the elastic tunneling background which has a finite slope, an effect more pronounced at lower doping. Such barrier change is also present in our case with Nb-doping. Measurements on substrates with different doping levels are required for further analysis of the bias-effect on the Schottky barrier height.

5.3 Measurements: Tunneling Spectroscopy on Superconducting $SrTiO_3$

By fabricating tunnel junctions with In and semiconducting $SrTiO_3$, we aim to study the superconducting ground state of the latter. Using a dilution refrigerator set-up (see Ch. 3), tunnel spectroscopy measurements were performed at temperatures as low as 40 mK in perpendicular magnetic fields. The technique is essentially similar to the case of $LaAlO_3/SrTiO_3$, as described in Ch. 4, with the main difference being the simplicity of the fabrication procedure.

Having established that such junctions are a reliable template for tunneling measurements, superconducting features are expected to be present below the critical temperature of one or both electrodes. However, there exist complications in the fabrication process, which hinder the simultaneous observation of the superconducting gaps of In and $SrTiO_3$ in the same sample. An elaborate discussion can be found in Appendices A and B.

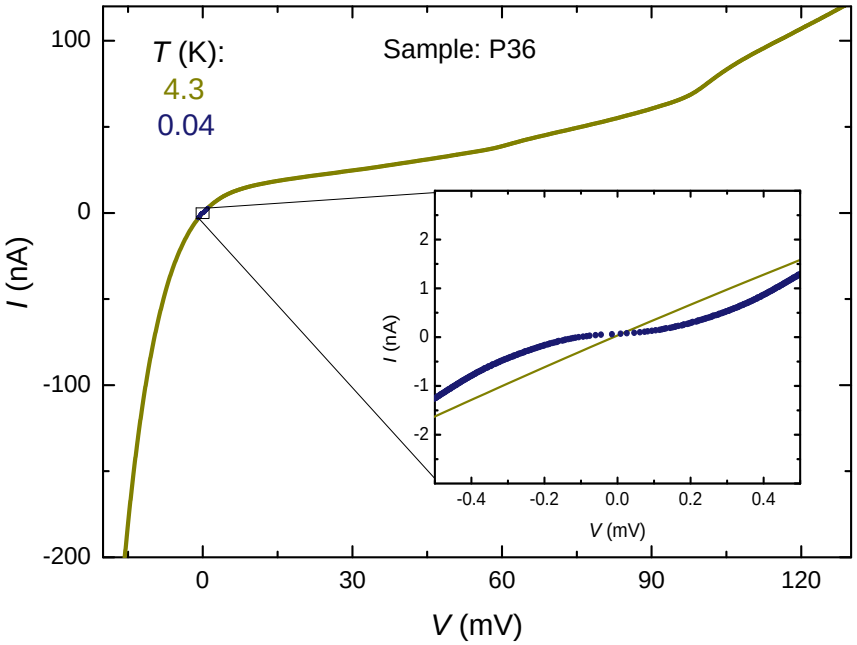

Figure 5.9: *The $I-V$ characteristics measured on device 15 of sample P36 at 4.3 K and at 40 mK. The inset shows the opening of the superconducting gap of In (dark-blue curve) which emerges below the critical temperature at 3.4 K [15].*

Figure 5.9 displays the opening of a superconducting gap at 40 mK, as seen in the $I-V$-characteristic of a tunnel junction. At this temperature, both In and doped $SrTiO_3$ are expected to be superconducting. The gap of doped $SrTiO_3$ is an order of magnitude smaller than that of In, of which there exists no clear sign in the $I-V$ characteristics in this sample. Tunneling measurements in such junctions, performed by G. Binnig et al. [10], have determined the value of the In-gap to be approximately 535 μeV. In that work, double-gap features were also observed in the tunneling characteristics of such junctions.

5.3.1 Tunneling into the Superconducting DOS of Doped-$SrTiO_3$

The optimization of the fabrication procedure for improving the junction quality involved etching of the $SrTiO_3$ substrates (prior to In-deposition) in an Ar-atmosphere. In addition to removing impurities, this process dopes the surface of the semiconductor by inducing O_2-vacancies. This way, the shape of the Schottky barrier can be varied in a semi-controlled manner, with the etching-time being a tuning parameter.

A thin layer of Au is typically deposited on top of the In-film for improving the wire-contacts to the devices. It was found that upon depositing 30 nm of Au on a 50 nm In-film, the latter is not superconducting anymore. A detailed investigation can be found in Appendix A, where thin films of In and Au of various thicknesses were grown on Nb-doped $SrTiO_3$ crystals and the superconducting critical temperature of In was monitored as a function of thickness ratio. As was evident, during deposition Au particles are embedded into the (soft) In-film until a certain depth and induce disorder. The critical temperature of the superconducting state is suppressed with increasing level of disorder.

The junctions of sample P11 were manufactured by etching the substrate in Ar-atmosphere for 5 minutes and depositing 50 nm In and 30 nm Au by thermal evaporation. Tunneling spectroscopy measurements take place between the non-superconducting In-Au film and Nb-doped $SrTiO_3$ (0.5 wt%).

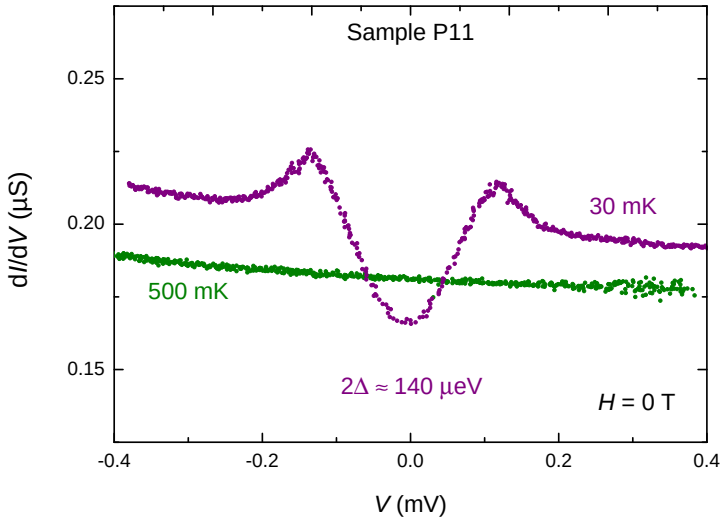

Figure 5.10: *The dI/dV (V) characteristics measured on sample P11, across a circular junction of diameter 1.2 mm, at 30 mK (violet) and at 500 mK (green) in the absence of magnetic fields. The opening of a superconducting gap Δ in the DOS around E_F, of the order of 70 μeV at base temperature, is evident.*

Figure 5.10 presents tunneling data from sample P11. A superconducting gap of approximately 70 μeV with a temperature onset below 500 mK is observed in the tunneling characteristics. Measurements on a larger scale, at the mK-regime and at 4.2 K have ruled out the possibility that this gap is due to

superconductivity in the In-Au film. As observed in 5.10, the conductance background is not constant during consecutive runs at varying temperature. This instability in the background conductance possibly originates from the inhomogeneous Schottky-depleted region along the metal-superconductor interface. It results in an increased uncertainty when estimating the superconducting gap Δ and particularly the quasiparticle lifetime broadening parameter Γ.

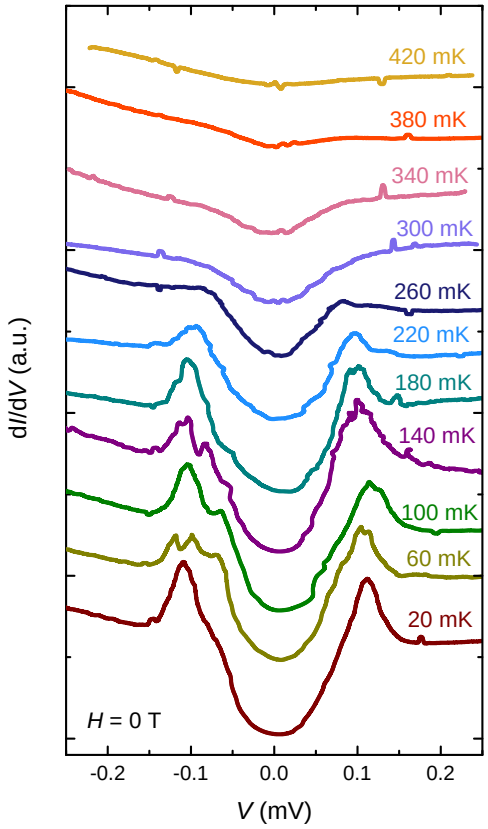

Figure 5.11: *The tunneling spectra evolution from sample P11 with increasing temperature, measured across a circular junction of 0.7 mm in diameter. The denoted temperature values correspond to the temperature of the mixing chamber. At approximately 380 mK, the superconducting features vanish completely. The spectra have been smoothened and offset for clarity.*

The evolution of the superconducting DOS in the tunnel spectra with increasing temperature is shown in Fig. 5.11. At base temperature (20 mK on the mixing chamber), the superconducting gap of $SrTiO_3$ is in the order of 70 μeV and gradually disappears as the temperature increases. Superconducting signatures vanish completely at approximately 380 mK. Features that mostly appear as peaks in the $\mathrm{d}I/\mathrm{d}V(V)$ characteristics at various temperatures are not systematic and are attributed to measurement noise that possibly originates from the Schottky barrier instability.

By fitting the tunnel spectra with the Dynes-model [32] (see previous chapter), the superconducting gap Δ could be determined up to T = 260 mK. At higher temperatures the uncertainty is large enough

to surpass the absolute value of the gap and fitting does not provide meaningful results. Figure 5.12 presents the experimentally determined values for Δ with respect to temperature. The T-dependence of the gap is BCS-like, although the BCS-ratio equals approximately 4.34, assuming $\Delta(0) = 71$ μeV at $T = 0$ and $T_c = 380$ mK. The latter value for T_c is considered, since the superconducting features of the tunneling characteristics of Fig 5.11 vanish approximately at this temperature. Such increased value of the BCS-ratio is reminiscent of the strongly coupled superconductors Pb and Hg [33]. Yet, owing to the increased uncertainty in fitting the tunnel spectra, there is little validity in arguments regarding the coupling strength of superconducting $SrTiO_3$ that are based on the $\Delta(T)$-dependence.

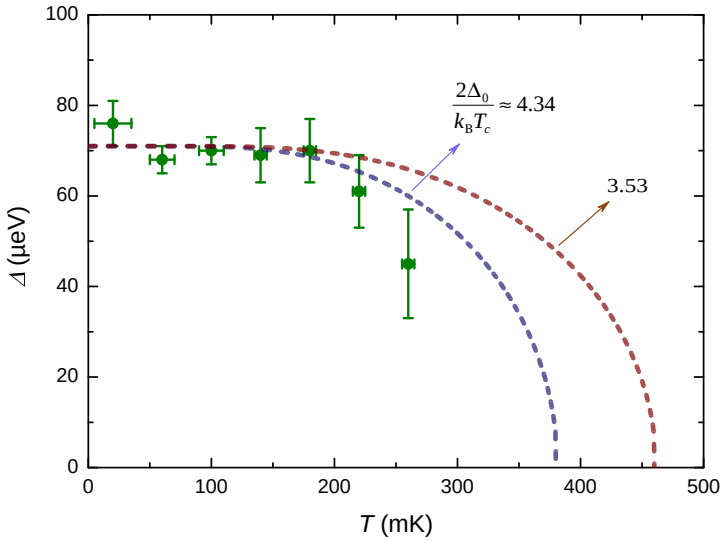

Figure 5.12: *The temperature dependence of the superconducting gap of Nb-doped $SrTiO_3$. The theoretical BCS-dependences assuming a ratio of 3.53 (light brown) and 4.34 (violet) are indicated by the dashed lines. For the latter, a critical temperature of 380 mK is assumed, based on the disappearance of superconductivity in the tunnel spectra of Fig. 5.11.*

The Nb-doping level of 0.5 wt% corresponds to a carrier concentration $n_s = 1.66{\cdot}10^{20}$ cm^{-3}. According to quantum oscillations measurements [25], for $n_s \geq 1.5{\cdot}10^{18}$ cm^{-3}, the chemical potential lies inside at least two bands at the Γ-point. As discussed earlier, multiband superconductivity has been observed in semiconducting $SrTiO_3$ [10,11]. Owing to the junction's inhomogeneity, the $dI/dV(V)$ characteristics are too noisy for a possible resolution of a multiband structure in the gap temperature dependence. A scenario is possible, in which superconductivity in two (or more) bands manifests itself out of electron-phonon interactions for which the intraband coupling constants are similar. In this case the respective superconducting gaps would be of the same order of magnitude and thus difficult to resolve directly from the tunnel spectra. It has been recently reported that the temperature dependence of the upper critical field is a better probe for detecting multiband signatures, particularly in the case where the coupling

constants within each band are of similar magnitude [34]. Therefore, more tunneling measurements for the experimental determination of the critical magnetic field of Nb-doped $SrTiO_3$ were performed.

5.3.2 Magnetic Field Dependent Tunnel Spectroscopy on Doped-$SrTiO_3$

The effect of a magnetic field on the tunnel spectra (applied parallel to the tunneling-direction) is displayed in Fig. 5.13. The minimum field required to entirely suppress the superconducting features at base temperature is approximately 20 mT. The superconducting gap and quasiparticle excitation peaks appear increased at a finite field, with a maximum in the range between 2 and 3 mT. This is due to residual magnetic flux in the dilution fridge setup which is constant during experiments and is compensated in all following magnetic field measurements.

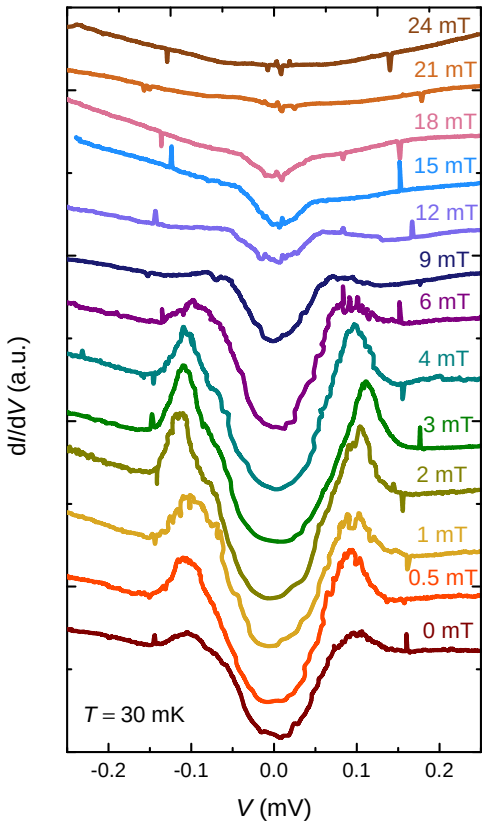

Figure 5.13: *The tunneling spectra evolution with increasing magnetic field. The field is oriented parallel to the tunneling direction. Fields of the order of 20 mT suppress the superconducting features entirely. The spectra have been smoothened and offset for clarity.*

The gradual suppression of the superconducting features seen in $SrTiO_3$ is reminiscent of the magnetic field suppression of superconductivity in $LaAlO_3/SrTiO_3$ (see previous chapter). A big difference lies in the absolute values of the critical fields. In the latter case and for positive gate voltages in the slightly overdoped regime, critical fields as high as 170 mT (one order of magnitude higher) were re-

quired to suppress superconductivity entirely [35]. On bulk $SrTiO_3$, such low values for the critical field have been observed in more than one samples throughout this work. In resonant microwave measurements between doped $SrTiO_3$ and Pb at low temperatures, performed by M. Thiemann et al. at the University of Stuttgart (the experiments were conducted on the same series of Nb-doped $SrTiO_3$ substrates) [36], critical fields between 15 mT and 35 mT have been also observed (at T = 60 mK).

The Fermi velocity of doped $SrTiO_3$ has been reported at $1.5{\cdot}10^4$ m/s [4]. Under the assumption that $SrTiO_3$ is a clean superconductor, this value yields a critical field H_c of 168 mT which is far away from the observed H_c of Fig 5.13. Conversely, a critical field of 18 mT corresponds to a Fermi velocity of $4.5{\cdot}10^4$ m/s; a value that is closer to the range reported in Ref. [37] for the $LaAlO_3/SrTiO_3$ interface. This difference of the Fermi velocities makes sense if one considers the chemical potential. The carrier concentration in my sample is higher than in those investigated in Ref. [4], thus the chemical potential lies possibly in an energy range of higher dispersion in k-space. This finding can be the subject of future investigation in follow-up measurements.

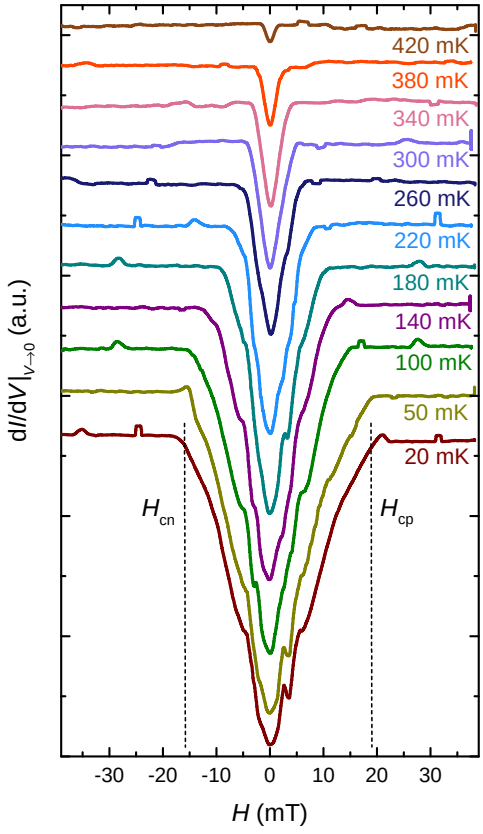

Figure 5.14: *The $dI/dV|_{V=0}$ (H)-dependence at different temperatures. In each curve, the critical field of doped $SrTiO_3$ determines the onset of the plateaus at large magnetic fields. Superconducting signatures are present in the entire temperature range. Curves have been smoothened and offset for clarity.*

For the determination of the critical field by tunnel spectroscopy, the technique already used for $LaAlO_3/SrTiO_3$ is applied (see also Ref. [35]). The absolute value of the tunneling conductance $dI/dV|_{V=0}$ is measured as the magnetic field is swept from -50 to 50 mT, under fixed-temperature and for T-steps in the range 30 mK < T < 420 mK. Figure 5.14 presents a selection of the dataset of the $dI/dV|_{V=0}$ (H) dependence. Suppression of the superconducting state by magnetic field and temperature is highlighted in this plot. Interestingly, a weak suppression of the conductivity (by superconductivity) across the junction is observed even up to 420 mK, although at high temperatures superconducting signatures are absent in the tunnel spectra of Fig. 5.11. At lower temperatures some of the curves exhibit local extrema that might appear as a particular structure. They are byproducts of additional heating during the magnetic-field sweep which is enhanced at the field range 0 mT < H < 100 mT and highly depends on the sweep rate. This effect is present for temperatures up to 180 mK and is a large error source in the determination of the critical field, thus the field sweep-rate has been kept at 5 mT per minute or less. Such effects appear frequently in dilution refrigerator systems. A more detailed study of the heating effect can be found in Appendix C.

The curves in Fig. 5.14 have been offset to compensate for trapped flux, so that minimum conductance corresponds to nominally zero magnetic field. The value of the critical field H_c at each temperature is the average of the individually extracted H_{cp} and H_{cn}, respectively, for positive and negative fields.

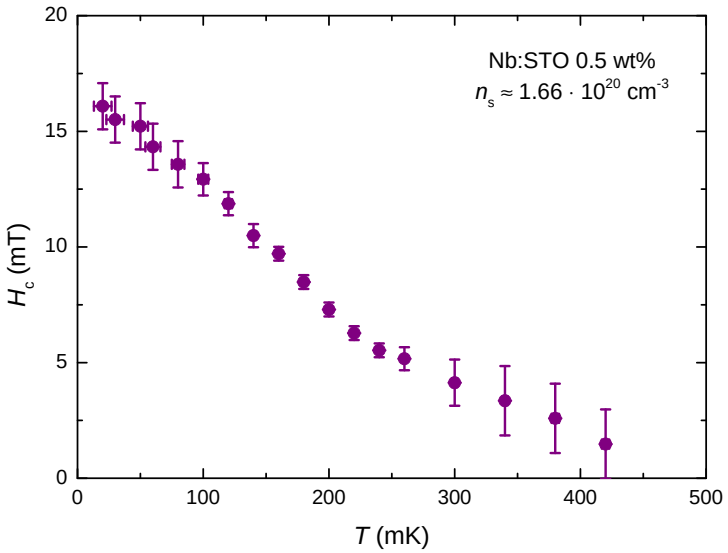

Figure 5.15: *Temperature dependence of the critical field of an $SrTiO_3$ sample with a doping level corresponding to the overdoped region, as determined by tunneling spectroscopy.*

The temperature dependence of H_c is shown in Fig. 5.15. The uncertainty is increased at very low temperatures due to the field-sweep-induced heating, and also close to T_c due to the small number of experimental points, as the $dI/dV|_{V=0}$ (H) suppression is only tiny. According to our tunneling spec-

troscopy method, the absolute values found for this sample are lower than those recently reported in the work of X. Lin et al. [11,25]. Their latest thermal conductivity measurements show a bulk upper critical field of about 60 mT at the lowest temperature, as compared to 16 mT that we see in tunneling. At the same time, according to their resistivity estimate, H_c already exceeds 100 mT at intermediate temperatures below T_c. These discrepancies between the two methods are intriguing and it is therefore necessary to examine superconductivity in bulk $SrTiO_3$ by using a variety of experimental approaches.

An interesting outcome of the magnetic field dependent measurements is the shape of the H_c-vs-T dependence, where a small but distinct positive curvature is present between 200 and 250 mK. At this doping range, more than one bands cross the Fermi level [11,38] and multiband superconductivity is a possible scenario. This dependence is reminiscent of the two-band signature reported in Ref. [34] for bulk $SrTiO_3$, in the scenario of two-band superconductivity in the dirty limit.

Modeling the $H_c(T)$-dependence of doped-$SrTiO_3$

The temperature dependence of the upper critical field has been calculated by A. Gurevich for the two-band superconductor MgB_2, in the presence of non-magnetic impurities from which both, interband and intraband scattering components are considered. The exact calculation can be found in Ref. [39]. Assuming a magnetic field H parallel to the c-axis and also that the impurity concentration does not affect T_c, a linearized form of the Usadel equations [40] for each band is obtained:

$$2\omega f_1 - D_1^{ab}\vec{\Pi}_a\vec{\Pi}_b f_1 = 2\Delta_1 \tag{5.2}$$

$$2\omega f_2 - D_2^{ab}\vec{\Pi}_a\vec{\Pi}_b f_2 = 2\Delta_2 \tag{5.3}$$

In the above expressions, ω is the Matsubara frequency and $\vec{\Pi} = \vec{\nabla} + 2\pi i\vec{A}/\phi_0$, with ϕ_0 the magnetic flux quantum and $\vec{A}$ the vector potential. The solutions of equations 5.2 and 5.3 are meaningful when the in-plane diffusivities D_i are isotropic, i.e. $D_i^{ab} = D_i\,\delta_{ab}$, with the Kronecker δ_{ab}. In the gauge $A_y = H\cdot x$ (where $x \parallel a$ and $y \parallel b$ in the crystal lattice), the Green functions f_i and the order parameters Δ_i of band i $(=1,2)$ obtain the following forms, respectively:

$$f_i(x,\omega) = \frac{\Delta_i(x)}{\omega + \pi H D_i/\phi_0} \tag{5.4}$$

$$\Delta_i(x) = \Delta_i'(x)\,e^{-\pi H x^2/\phi_0} \tag{5.5}$$

A generic expression for the order parameter is given in Refs. [41,42]:

$$\Delta_i = 2\pi T \sum_{\omega>0}^{\omega_D} \sum_i \lambda_{ii'} f_{i'}(\vec{r}, \omega) \tag{5.6}$$

Here, ω_D is the Debye-frequency, T the temperature and $\lambda_{ii'}$ is in our case a 2D-matrix with the intraband coupling constants ($i = i'$) as elements in its diagonal, and the interband coupling constants ($i \neq i'$) as off-diagonal elements. Substituting the expressions 5.4 and 5.5 in Eq. 5.6, one can obtain expressions for the amplitude of the superconducting order parameters:

$$\Delta_1' = \lambda_{11}[l - U(h)]\Delta_1' + \lambda_{12}[l - U(\eta h)]\Delta_2' \tag{5.7}$$

$$\Delta_2' = \lambda_{22}[l - U(\eta h)]\Delta_2' + \lambda_{21}[l - U(h)]\Delta_1' \tag{5.8}$$

where $U(x) = \psi(1/2+x) - \psi(1/2)$ with $\psi(x)$ the Digamma function, $l = \ln\left(\frac{2\gamma\omega_D}{\pi T}\right)$ with γ the Euler constant, $\eta = \frac{D_2}{D_1}$ and $h = \frac{H_c D_1}{2\Phi_0 T}$.

At this point, it is convenient to express the critical temperature T_c as a function of the Debye frequency ω_D [43]:

$$T_c = 1.14\,\omega_D\, e^{-(\lambda_p - \lambda_0)/2w} \tag{5.9}$$

The parameters λ_p, λ_0 and w depend on the coupling constants $\lambda_{ii'}$ as: $\lambda_p = \lambda_{11} + \lambda_{22}$, $\lambda_m = \lambda_{11} - \lambda_{22}$, $\lambda_0 = \sqrt{\lambda_m^2 + 4\lambda_{12}\lambda_{21}}$ and $w = \lambda_{11}\lambda_{22} - \lambda_{12}\lambda_{21}$. There exists a non-trivial solution to the system of Eq. 5.7 and 5.8, under a condition which provides an equation for the T-dependence of the critical field H_c:

$$\alpha_0[\ln t + U(h)][\ln t + U(\eta h)] + \alpha_2[\ln t + U(\eta h)] + \alpha_1[\ln t + U(h)] = 0 \tag{5.10}$$

In the above expression $t = \frac{T}{T_c}$, while the parameters $\alpha_j\,(j = 0, 1, 2)$ contain the dependence on the coupling constants: $\alpha_0 = \frac{2w}{\lambda_0}$, $\alpha_1 = 1 + \frac{\lambda_m}{\lambda_0}$ and $\alpha_2 = 1 - \frac{\lambda_m}{\lambda_0}$.

It is difficult to solve Eq. 5.10 analytically as a function of H_c and t, as one needs to work around the divergence of the Digamma functions $\psi(h)$ and $\psi(\eta h)$ at $T \to 0$. In addition to that, non-trivial solutions may exist in the entire set of real numbers. Yet the solutions of $H_c/H_{c,T\to 0}\,(t)$ can be approximated numerically (e.g. in *Mathematica*) in a straightforward manner and one can also narrow down to the real, positive solutions.

The solutions of Eq. 5.10 for $H_c/H_c(0)$ as a function of t are presented in Fig. 5.16. The coupling constants $\lambda_{ii'}$ are fixed to values that are found in literature for $SrTiO_3$. Two such sets have been found, one in Ref. [38] corresponding to the plots of 5.16a and another in Ref. [44] yielding the curves plotted in 5.16b. The $H_c(T)$ data from Fig. 5.15 measured in sample P11 is plotted as well, without the error bars for clarity. For the experimental points I have considered T_c = 440 mK because superconducting signatures are still present at T = 420 mK according to measurements shown in Fig. 5.14, while $H_c(0)$ has been set to 16.5 mT; a value slightly higher than the measurement at base temperature (see Fig. 5.15). Although superconducting signatures may exist up to 18 mT according to Fig. 5.13, the latter value is chosen to take into account a possible underestimation of the H_c-values extracted from Fig 5.14, complying with the extraction method. The ratio of the diffusivities η is a dimensionless tuning parameter and is let to freely evolve within a range of several orders of magnitude. The curvature of $\frac{H_c}{H_c(0)}(t)$ is sensitive to both, the coupling constants $\lambda_{ii'}$ and η.

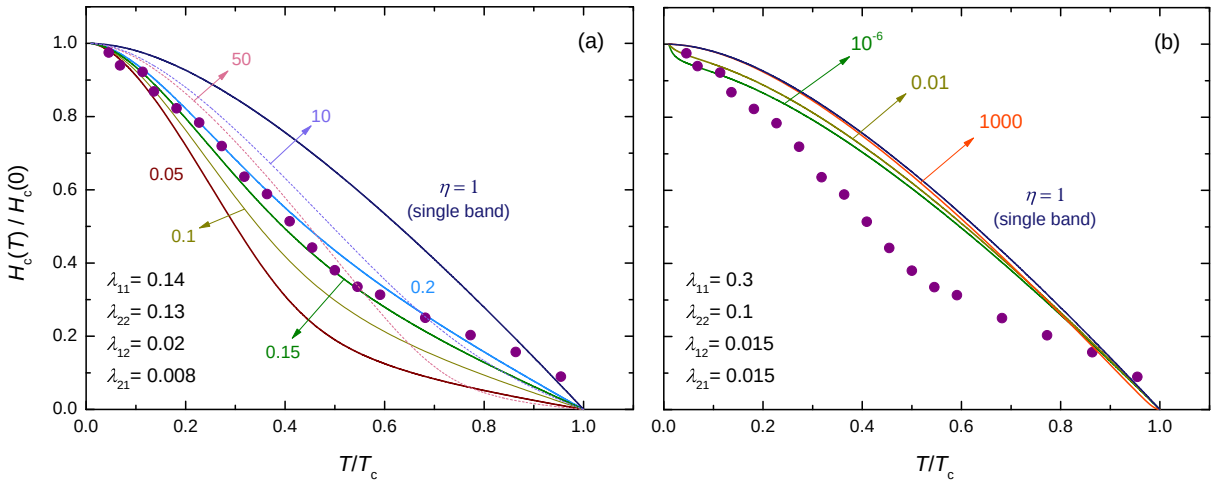

Figure 5.16: *The $H_c/H_c(0)$ dependence on T/T_c for the $SrTiO_3$ coupling constants given in the work of (a) Fernandes et al. [38] and (b) Bussman-Holder et al. [44]. The diffusivity ratio η is tuned (as indicated within each graph) while the coupling constants $\lambda_{ii'}$ are fixed. For the set of $\lambda_{ii'}$ in (a) the model approximates the measurement results from sample P11 well, in contrast to (b) where η inflicts minute changes to the dependence and does not comply with measurement.*

The electron diffusivity D describes the rate at which electrons flow within a band, measured in units of m^2/s and for which $D = v_F^2 \tau$, where v_F is the Fermi velocity and τ the scattering time. It is a quantity characteristic of the energy band. As is evident in Fig. 5.16, the measured dataset is described well by the solution of Eq. 5.10 and the coupling constants from Ref. [38]. The positive curvature at $T \approx 0.5\,T_c$ is reproduced best in 5.16a assuming $D_2 \approx 0.2\,D_1$ for the diffusivities.

This model from A. Gurevich was initially calculated for evaluating the H_c temperature dependence of MgB_2, as well as its angular dependence. MgB_2 is a two-band superconductor with two distinct superconducting gaps that correspond respectively to two bands of σ and π characters. Adding impurities on bulk MgB_2 [45] is a common technique to enhance its upper critical field, frequently done by proton [46] or neutron [47] irradiation. This impurity scattering, as well as the resulting interband effects, are taken into account in the model. Bulk $SrTiO_3$ resembles the properties of MgB_2 in the sense that the d_{xy} and the set of $d_{xz,yz}$ bands preserve the orthogonality of the σ and π bands. Impurities can also be present and induce scattering in $SrTiO_3$, which can be intrinsic in nature and/or possibly enhanced upon doping with Nb. This two-band model has been also used in the work of F. Hunte et al. [48] for interpreting the temperature dependence of H_c in the newly discovered superconductor $LaFeAsO_{0.89}F_{0.11}$.

Multiband superconductivity in $SrTiO_3$ has been so far reported in the early tunneling measurements of G. Binnig et al. [10] and in the more recent work of X. Lin et al. [11] by thermal conductivity measurements. This possibility is highlighted in the theoretical work of R. Fernandes et al. [38], where they also argue about the similarity of the bulk $SrTiO_3$ superconductor to the superconducting $LaAlO_3/SrTiO_3$ 2DEL. The recent work of S. Klimin et al. [49] demonstrates the emergence of multiband superconductivity in both, bulk $SrTiO_3$ and the $LaAlO_3/SrTiO_3$ interface, mediated by Fröhlich interactions of electrons and LO-phonons. Although, experimentally, there exists no evidence on multiband superconductivity at the $LaAlO_3/SrTiO_3$ interface, investigating the case of bulk $SrTiO_3$ further through tunnel spectroscopy is now particularly motivating and also essential for understanding the physics of superconductivity at the dilute limit.

5.4 Chapter Summary

In this chapter, I have presented the outcome of my work on understanding the bulk $SrTiO_3$ superconductor by tunneling spectroscopy using planar junctions. Given the revived interest in the properties of $SrTiO_3$, which comes in parallel with the understanding of the $LaAlO_3/SrTiO_3$ 2DEL, this study provides valuable information because it offers an alternative experimental tool for gaining insight into the superconducting properties. This is particularly important, as any possible connection between superconductivity in 2D ($LaAlO_3/SrTiO_3$ interface) and in 3D (semiconducting bulk $SrTiO_3$) can be directly examined by this approach.

Signatures of Multiband Superconductivity detected on bulk $SrTiO_3$

The ability to resolve the main phonon modes that account for superconductivity on $SrTiO_3$ proves that the method developed works effectively. The H_c-dependence on temperature shown in Figs. 5.15 and 5.16 demonstrates the possibility that magnetic-field dependent tunneling spectroscopy is a reliable way to analyze multiband signatures. According to my measurements, Nb-doping of $SrTiO_3$ by 0.5 wt%, which amounts to a carrier density n_s of approximately $1.66{\cdot}10^{20}$ cm^{-3}, shifts the chemical potential above the edge of a second (possibly degenerate) band. Distinct superconducting features are thereby revealed in the temperature dependence of the critical field. Within this scenario, carriers that mediate superconductivity reside in two non-degenerate bands of diffusivity ratio 5:1, with interband scattering present. Yet, extending the analysis to a broader range of doping is necessary for a verification. Reproducing this result under optimized fabrication conditions is also important after improving junction stability, especially since the tunneling conductance background fluctuates at the temperature dependent measurements. The samples investigated in this particular study are all in the slightly overdoped regime.

Potential for Future Investigation

Scanning tunneling spectroscopy combined with photoelectron spectroscopy measurements have been already performed on bulk $SrTiO_3$ [50–53], in an effort to investigate surface reconstructions with increasing doping content. STM-measurements in the mK-range can also offer a reliable alternative for probing the superconducting DOS of $SrTiO_3$ below T_c. Such local measurements however require attention, because the work function difference between tip and bulk $SrTiO_3$ might drastically affect the tunnel barrier.

In addition, investigating samples doped with La instead of Nb may also be interesting, as this dopant substitutes on a Sr-site rather than on a Ti-site. Dopant-clustering or segregation can be well monitored by STM techniques.

The elegance of studying superconductivity on $SrTiO_3$ by tunneling within Schottky junctions lies in the simplicity. Upon proper surface treatment via etching in Ar-atmosphere and a clean evaporation procedure, the Schottky barrier can provide a homogeneous insulator between metals and the doped $SrTiO_3$ substrate for reliable tunneling conditions. Yet this may entail complications as well, as the Schottky barrier is often unstable over macroscopic dimensions and during measurement. In my work, room for improving the fabrication procedure exists, so that the error margins in the calculation of the superconducting gap Δ and the critical field H_c may decrease. This mainly concerns the Ar-etching process which up until now has not been fully optimized. A recent work [54] has featured measurements in MIS tunnel-junctions with $SrTiO_3$, where a thin $LaAlO_3$ layer is the insulator and the electron-phonon coupling strength has been studied as a function of doping. Having an insulating layer instead of the Schottky barrier can be a good solution for the junction stability issue, although it adds more parameters in the fabrication procedure. In the particular case of using $LaAlO_3$, it is unclear whether incipient conductivity at the interface of $LaAlO_3$ and $SrTiO_3$ affects the study of the bulk.

References

[1] A. Ohtomo and H. Y. Hwang, Nature **427**, 423 (2004).

[2] J. F. Schooley, W. R. Hosler and M. L. Cohen, Phys. Rev. Lett. **12**, 474 (1964).

[3] C. S. Koonce, M. I. Cohen, J. F. Schooley, W. R. Hosler and E. R. Pfeiffer, Phys. Rev. **163**, 380 (1967).

[4] X. Lin, Z. Zhu, B. Fauque and K. Behnia, Phys. Rev. X **3**, 021002 (2013).

[5] J. E. Hirsch: *High-Tc Copper Oxide Superconductors and Related Novel Materials*, Chapter 9, Springer Series in Material Science 255, Springer (2017).

[6] G. Bednorz and K. A. Müller, Rev. Mod. Phys. **60**, 585 (1988).

[7] B. K. Chakraverty, J. Phys. Lett **40**, L99 (1979).

[8] B. K. Chakraverty, J. Phys. **42**, 1351 (1981).

[9] D. van der Marel, J. L. M. van Mechelen and I. I. Mazin, Phys. Rev. B **84**, 205111 (2011).

[10] G. Binnig, A. Baratoff, H. E. Hoenig and J. G. Bednorz, Phys. Rev. Lett. **45**, 1352 (1980).

[11] X. Lin, A. Gourgout, G. Bridoux, F. Jomard, A. Pourret, B. Fauque, D. Aoki and K. Behnia, Phys. Rev. B **90**, 140508(R) (2014).

[12] Z. Sroubek, Solid State Commun. **7**, 1561 (1969).

[13] J. W. Conley and G. D. Mahan, Phys. Rev. **161**, 681 (1967).

[14] H. Suzuki, H. Bando, Y. Ootuka, I. H. Inoue, T. Yamamoto, K. Takahashi and Y. Nishihara, J. Phys. Soc. Jpn. **65**, 1529 (1996).

[15] *http://environmentalchemistry.com/ - Periodic Table of the Elements*, October 2016.

[16] W. Schottky, Z. Physik, **113**, 367 (1939).

[17] N. F. Mott, Proc. Roy. Soc. **171**, 27 (1939).

[18] R. T. Tung, Mater. Sci. Eng. R. **35**, 1 (2001).

[19] M. Mrovec, J.-M. Albina, B. Meyer and C. Elsässer, Phys. Rev. B **79**, 245121 (2009).

[20] V. Heine, Phys. Rev. **138**, 1689 (1965).

[21] R. T. Tung, Phys. Rev. Lett. **84**, 6078 (2000).

[22] R. T. Tung, Phys. Rev. B **64**, 205310 (2001).

[23] S. Hayashi and R. Aoki, J. Phys. Soc. Jpn. **50**, 2613 (1981).

[24] R. Stratton: *Tunneling Phenomena in Solids*, ed. E. Burstein and S. Lundqvist, p.117, Plenum Press New York (1969).

[25] X. Lin, G. Bridoux, A. Gourgout, G. Seyfarth, S. Krämer, M. Nardone, B. Fauque and K. Behnia, Phys. Rev. Lett. **112**, 207002 (2014).

[26] H. P. R. Frederikse and G. A. Candela, Phys. Rev. **147**, 583 (1966).

[27] H. P. R. Frederikse, W. R. Thurber and W. R. Hosler, Phys. Rev. **134**, A442 (1963).

[28] H. Vogt, Phys. Rev. B **38**, 5699 (1988).

[29] C. Richter PhD Thesis: *Experimental Investigation of Electronic and Magnetic Properties of $LaAlO_3$-$SrTiO_3$ Interfaces*, University of Augsburg 2012.

[30] H. Boschker, C. Richter, E. Fillis-Tsirakis, C. W. Schneider and J. Mannhart, Sci. Rep. **5** 12309 (2015).

[31] S. Hayashi, J. Phys. Soc. Jpn. **53**, 2350 (1984).

[32] R. C. Dynes, V. Narayanamurti and J. P. Garno, Phys. Rev. Lett. **41**, 1509 (1978).

[33] K. H. Bennemann and J. B. Ketterson: *The Physics of Superconductors Vol. I: Conventional and High-T_c Superconductors*, Springer-Verlag Berlin Heidelberg (2003).

[34] J. M. Edge and A. V. Balatsky, J. Supercon. Nov. Magn. **28**, 2373 (2015).

[35] E. Fillis-Tsirakis, C. Richter, J. Mannhart and H. Boschker, New J. Phys. **18**, 013046 (2016).

[36] M. Thiemann, M. Beutel, M. Scheffler and M. Dressel, *Private Communication*, 1. Physikalisches Institut, University of Stuttgart (2017).

[37] Y. Nakamura and Y. Yanase, J. Phys. Soc. Jpn. **82**, 083705 (2013).

[38] R. M. Fernandes, J. T. Haraldsen, P. Wölfle and A. V. Balatsky, Phys. Rev. B **87**, 014510 (2013).

[39] A. Gurevich, Phys. Rev. B **67**, 184515 (2003).

[40] K. D. Usadel, Phys. Rev. Lett. **25**, 507 (1970).

[41] G. Eilenberger, Z. Phys. **214**, 195 (1969).

[42] A. I. Larkin and Y. N. Ovchinnikov, JETP **28**, 1200 (1969).

[43] H. Suhl, B. T. Matthias and L. R. Walker, Phys. Rev. Lett. **3**, 552 (1959).

[44] A. Bussmann-Holder, A. R. Bishop and A. Simon, Ferroelectrics **400**, 19 (2010).

[45] C. Buzea and T. Yamashita, Supercond. Sci. Technol. **14**, R115 (2001).

[46] Y. Bugoslavsky, L. F. Cohen, G. K. Perkins, M. Polichetti, T. J. Tate, R. Gwilliam and A. D. Caplin, Nature **411**, 561 (2001).

[47] M. Eisterer, M. Zehetmayer, S. Tönies, H. W. Weber, M. Kambara, N. Hari Babu, D. A. Cardwell and L. R. Greenwood, Supercond. Sci. Technol. **15**, L9 (2002).

[48] F. Hunte, J. Jaroszynski, A. Gurevich, D. C. Larbalestier, R. Jin, A. S. Sefat, M. A. McGuire, B. C. Sales, D. K. Christen and D. Mandrus, Nature **453**, 903 (2008).

[49] S. Klimin, J. Tempere, J. T. Devreese and D. van der Marel, J. Supercond. Nov. Mag. **30**, 757 (2017).

[50] Y. L. Chen, J. Wang, C. M. Hiong, R. F. Dou, J. Y. Yang and J. C. Nie, J. Appl. Phys. **112**, 023703 (2012).

[51] M. R. Castell, Surf. Sci. **505**, 1 (2002).

[52] M. S. J. Marshall, D. T. Newell, D. J. Payne, R. G. Egdell and M. R. Castell, Phys. Rev. B **83**, 035410 (2011).

[53] T. Matsumoto, H. Tanaka, T. Kawai and S. Kawai, Surf. Sci. Lett. **278**, L153 (1992).

[54] A. G. Swartz, H. Inoue, T. A. Merz, Y. Hikita, S. Raghu, T. P. Devereaux, S. Johnston and H. Y. Hwang, arXiv: 1608.05621 (2016).

Chapter 6

Summary

Solid-state physics has seen rapid development from the last century until today, owing to its constant provision of a plethora of scientific and technological advances. Oxide materials and artificially constructed, oxide-based heterostructures draw increasing attention, both as model systems from which science harvests ingredients for the understanding of a variety of intriguing physical phenomena, and because of their far-reaching potential for application [1]. Electronic systems which are as highly-functional as the $LaAlO_3/SrTiO_3$ interface are rare, as the emergent high-mobility two-dimensional electron system (2DES) exhibits ferromagnetism, incipient ferroelectricity, piezoelectricity, Rashba spin-orbit coupling, superconductivity and high electronic correlations; properties that may also coexist with one another. The possibility of tuning its electrical properties by external parameters such as a gate-field, temperature, pressure and magnetic-field makes the $LaAlO_3/SrTiO_3$-2DES the scientific analogue of a multi-tool. This versatility has been put in good use during this thesis, with the aim to investigate the $LaAlO_3/SrTiO_3$ interface superconducting ground state in the regime of strong depletion and in the presence of magnetic fields. For this purpose I have investigated $LaAlO_3/SrTiO_3$ samples, grown by pulsed-laser-deposition. Using this system, planar tunnel junctions were constructed that allowed for tunneling spectroscopy measurements. The resemblance of the $LaAlO_3/SrTiO_3$ 2DES to the high-temperature superconductors undoubtedly adds value to the findings of this work. These are summarized in the following lines.

A pseudogap-like phase has been observed in the underdoped regime of the $LaAlO_3/SrTiO_3$ superconducting 2DES [2]. Combined transport and tunneling spectroscopy measurements in the planar junction configuration have shown that the opening of the superconducting gap in the DOS persists with increasing depletion of charge carriers well outside the superconducting dome in the phase diagram. Although finite resistance is measured in this regime, the temperature at which the gap appears resembles the onset T^* of the pseudogap region seen in the cuprates. This finding led to the conjecture that, perhaps, the rise of such pseudogap phases is inherent in the 2D-character of superconductivity, manifesting

itself in the 10 nm thick $LaAlO_3/SrTiO_3$ 2DES and in the alternating CuO_2 planes within the cuprate structure. Moreover, throughout these measurements values of the superconducting gap Δ and quasiparticle lifetime-broadening parameter Γ and also of the critical temperature T_c have been determined for $LaAlO_3/SrTiO_3$ interfaces. Further investigation of its nature has revealed that by depleting from the optimally doped region, the electron-phonon coupling strength increases and accounts for the persisting superconducting behavior within the macroscopically resistive regime at very low doping [3].

Transport measurements at T = 50 mK were performed while tuning the carrier concentration and sweeping magnetic fields in the perpendicular-to-interface orientation, to investigate the superconductor-to-insulator transition by carrier depletion. It was found that the onset of finite resistance R at zero magnetic field occurred at a gate-field V_g between -130 V and -140 V, yet the absolute value of $R_{H=0}$ only saturates at $V_g \geq$ -250 V, in the MΩ range. This gradual suppression of superconductivity with depletion is in accordance with $R(T)$-measurements [2] and underlines the existence of an intermediate metallic phase between the superconducting and the insulating phases. This transition in $LaAlO_3/SrTiO_3$, induced by tuning the carrier concentration, has thus been characterized as a superconductor-metal-insulator transition (SMIT). One aim of these measurements was to investigate the possible existence of the "superinsulator" phase, identified by several authors in thin metallic films. Such a phase has not been observed during my transport measurements at the $LaAlO_3/SrTiO_3$ 2DES.

The nature of superconductivity in the entire phase diagram and particularly across the SMIT has been investigated by magnetic-field-dependent tunneling spectroscopy. The tunnel spectra evolution with fields applied perpendicular to the interface has been studied in detail, at carrier concentrations that correspond to the overdoped, optimally doped, underdoped and resistive (which can be characterized as metallic or insulating) regimes. In all four cases the evolution is gradual, with the experimentally determined upper critical field H_c varying smoothly across the phase diagram and particularly at the SMIT region [4]. This finding substantiates the scenario that the superconducting ground state is governed by vortex-penetration with increasing magnetic field and also that phase coherence is preserved well inside the resistive regime. Such understanding is corroborated by the presence of quasiparticle excitation peaks in the tunnel spectra in the region of extreme depletion. In addition, my measurements provide precise calculations of the critical field H_c, the coherence length ξ, as well as an estimate of the Fermi velocity v_F of the $LaAlO_3/SrTiO_3$ superconductor, as a function of gate-voltage V_g.

The temperature dependence of H_c, from 50 mK up to T_c, has been measured in the overdoped, optimally doped, underdoped and resistive regions in the phase diagram. A linear dependence down to the lowest temperature has been measured in all four regions, which would imply that the superconductor is in the clean limit. This assumption is also supported by the excellent agreement between the measured values of the critical field H_c and those derived by the BCS-expression (through independent measurements of the superconducting gap Δ), which yield a constant Fermi velocity in the entire phase diagram at low temperatures. Yet, it is also possible that the linearity originates from the anisotropy induced by confined-dimensionality, or from the incipient multiband character of superconductivity at the ground state of $LaAlO_3/SrTiO_3$. My data is not conclusive on the latter and therefore further measurements with more samples are required to shed light on this question.

In addition to superconductivity at the $LaAlO_3/SrTiO_3$ 2DES I have also investigated the doped-$SrTiO_3$ superconductor (as the bulk counterpart of the superconducting 2D-interface), which is the first oxide semiconductor to ever exhibit superconductivity. Its fundamental importance lies in the fact that superconductivity emerges at ultra-low carrier densities and that it has opened the route to the invention of the copper-oxide based compounds. A combined investigation of this system through tunneling spectroscopy along with the $LaAlO_3/SrTiO_3$ 2DES, can unravel new aspects of the observed superconductivity therein. It is still intriguing that a manifestation of two-band superconductivity has been reported for doped $SrTiO_3$ [5, 6] but not yet for the $LaAlO_3/SrTiO_3$ interface, albeit the apparent similarity of the energy band structure and hierarchy at the Fermi level.

In this thesis also, planar tunnel junctions of Nb-doped $SrTiO_3$ and In have been fabricated and analyzed. Tunneling spectroscopy measurements were conducted between the In-film and the bulk $SrTiO_3$ crystal, through the Schottky barrier that emerges at the interface of the two and acts as the tunneling barrier. Measurements performed within broad energy ranges (of the order of 100 meV) have resolved the two highest longitudinal optical phonon modes (LO3 and LO4) in agreement with literature. This indicates that tunneling through these junctions is a simple but reliable technique to investigate the spectral DOS at the Fermi energy. Yet, the downside of using the Schottky barrier configuration for tunneling is the instability during measurement (as opposed to having a thin insulating layer between In and $SrTiO_3$). The barrier is sensitive to the applied bias and this often yields a rather noisy background in the tunnel spectra. This has been made clear throughout my work and can be a useful take-home message for any successors.

My main objective when investigating Nb-doped $SrTiO_3$ (in the overdoped regime) was to study the superconducting properties of its ground state. The superconducting gap Δ and critical field H_c have been measured, and their temperature dependence has been studied. In the former case, a superconducting gap of the order of 75 μeV has been measured at base temperature, slightly higher than that of the $LaAlO_3/SrTiO_3$ interface. Its temperature dependence yields a BCS-ratio higher than 4, which is only seen in strongly coupled superconductors. The critical field dependence on temperature has revealed signs of two band behavior, with a positive curvature at about $0.5\times T_c$, as has been suggested by theory [7]. A model constructed for studying the two-band superconductor MgB_2 [8] and using literature values for the coupling constants of $SrTiO_3$ [9] approximates my data well, in the scenario that carriers that participate in superconductivity reside in two bands with diffusivity ratio 5:1. This finding needs to be corroborated by future measurements performed in Nb-doped substrates of various Nb-doping concentrations.

In conclusion, my thesis has contributed to understanding superconductivity at the $LaAlO_3/SrTiO_3$ 2DES and at the doped-$SrTiO_3$ crystal. It has succeeded an ongoing effort of my group from the past and has uncovered several intriguing superconducting properties of the two most dilute superconductors known today. The usage of tunneling spectroscopy in planar junctions as a tool for probing the DOS has been proven crucial and combining with transport measurements is a powerful method to unravel novel physical phenomena in superconductors. As an immediate follow-up of this thesis I suggest the thorough investigation of the superconducting properties in doped $SrTiO_3$ in the entire phase diagram, as well as the investigation of $LaAlO_3/SrTiO_3$ interfaces where $LaAlO_3$ is either amorphous [10] or grown on $SrTiO_3$ [110] and [111] [11,12]. Although technologically extremely challenging, fabrication of junctions where electrons tunnel into the $LaAlO_3/SrTiO_3$ 2DES from the side (as in the dc-SQUID configuration described in Ref. [13] for YBCO) may offer an alternative viewpoint on the fascinating properties of this delicate system. The greater puzzle of high-temperature superconductivity still has several pieces missing. It is perhaps through those endless hours of optimization, measurement and analysis, of one of extremely many novel superconducting compounds that progress is made in the community and the mysteries of today are knowledge of tomorrow.

References

[1] M. Lorenz et al., J. Phys. D: Appl. Phys. **49**, 433001 (2016).

[2] C. Richter, H. Boschker, W. Dietsche, E. Fillis-Tsirakis, R. Jany, F. Loder, L. F. Kourkoutis, D. A. Muller, J. R. Kirtley C. W. Schneider and J. Mannhart, Nature **502**, 528 (2013).

[3] H. Boschker, C. Richter, E. Fillis-Tsirakis, C. W. Schneider and J. Mannhart, Sci. Rep. **5**, 12309 (2015).

[4] E. Fillis-Tsirakis, C. Richter, J. Mannhart and H. Boschker, New J. Phys. **18**, 013046 (2016).

[5] G. Binnig, A. Baratoff, H. E. Hoenig and J. G. Bednorz, Phys. Rev. Lett. **45**, 1352 (1980).

[6] X. Lin, A. Gourgout, G. Bridoux, F. Jomard, A. Pourret, B. Fauque, D. Aoki and K. Behnia, Phys. Rev. B **90**, 140508(R) (2014).

[7] J. M. Edge and A. V. Balatsky, J. Supercon. Nov. Magn. **28**, 2373 (2015).

[8] A. Gurevich, Phys. Rev. B **67**, 184515 (2003).

[9] R. M. Fernandes, J. T. Haraldsen, P. Wölfle and A. V. Balatsky, Phys. Rev. B **87**, 014510 (2013).

[10] G. E. D. K. Prawiroatmodjo, F. Trier, D. V. Christensen, Y. Chen, N. Pryds and T. S. Jespersen, Phys. Rev. B **93**, 184504 (2016).

[11] G. Herranz, G. Singh, N. Bergeal, A. Jouan, J. Lesqueur, J. Gasquez, M. Varela, M. Scigaj, N. Dix, F. Sanchez and J. Fontcuberta, Nature Commun. **6**, 6028 (2015).

[12] G. Herranz, F. Sanchez, N. Dix and J. Fontcuberta, Sci. Rep. **2**, 758 (2012).

[13] D. A. Wollman, D. J. van Harlingen, J. Giapintzakis and D. M. Ginsberg, Phys. Rev. Lett. **74**, 797 (1995).

Appendix

A: Tuning the Critical Temperature of Superconducting Indium Films

Indium thin films are deposited by thermal evaporation (see Ch. 3), usually succeeded by E-beam evaporation of a thin Au-layer. The latter step is crucial for good quality contacts that ensure low-noise during electrical measurement in the tunnel junctions between In and doped-$SrTiO_3$. A qualitative analysis has been performed within the sample series P24 - P34 (listed in Table 5.2), focusing on the superconducting T_c of the In-Au multi-layer.

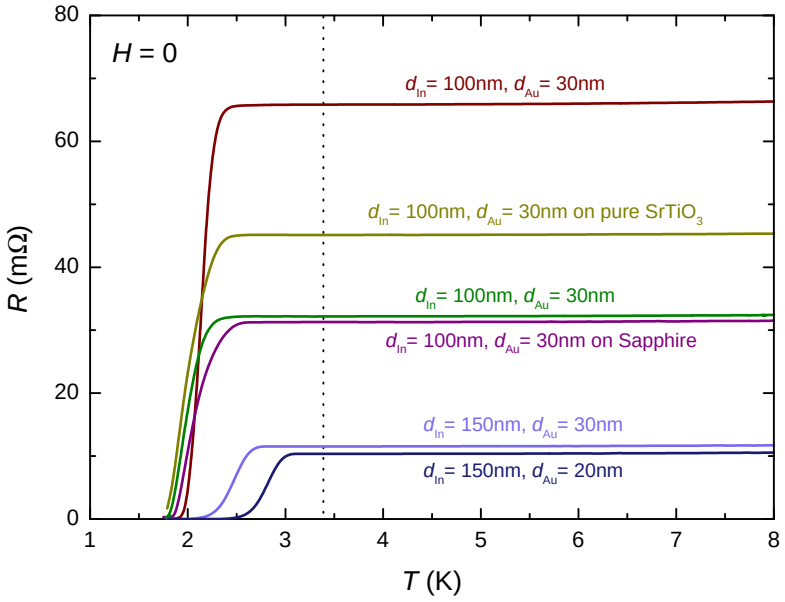

Figure 1: *The R(T)-characteristics of In-Au films on Nb-doped $SrTiO_3$, pure $SrTiO_3$ and Sapphire substrates, as measured with a PPMS in the van-der-Pauw configuration. In addition to the substrate-type, the Au and In film-thicknesses also vary as indicated. The onset of the transition to the superconducting state varies particularly with respect to the film-thickness ratio of In and Au. The dotted line marks the superconducting onset of bulk In, at 3.41 K.*

The superconducting critical temperatures (T_c) of In-Au films grown on various substrates and with different thicknesses have been determined, by measuring the $R(T)$-characteristics with a PPMS. The

temperature of the In-crucible (T_{cr}) varied within the interval 860 ^{o}C < T_{cr} < 970 ^{o}C during film growth. Metallic films of identical characteristics were grown at different starting temperatures within this range and showed no significant variation in the measured T_c. Figure 1 summarizes measurements performed on a representative subset of samples. A transition to the superconducting state of the In-Au film should ideally be present at 3.41 K, i.e. the T_c of In [1]. This is however not the case in these measurements, as the superconducting onset of the In-Au film is observed at lower temperatures. Here, T_c is determined as the temperature at which resistance drops to 50 % from the normal level.

The main conclusion inferred from these measurements is that T_c is essentially insensitive to the substrate on which the film is deposited and to the growth temperature. With fixed thicknesses (100 nm for In and 30 nm for Au, i.e. $d_{In}/d_{Au} = 3.33$), the values of T_c vary slightly from 1.9 K to 2.1 K for all samples. Yet with increasing ratio d_{In}/d_{Au}, i.e. of the In-thickness over Au-thickness, the measured T_c is enhanced towards that of bulk In at 3.41 K. Particularly at $d_{In}/d_{Au} = 5$ (d_{In} = 150 nm, d_{Au} = 30 nm), T_c is measured at 2.4 K and at $d_{In}/d_{Au} = 7.5$ (d_{In} = 150 nm, d_{Au} = 20 nm) T_c is 2.8 K. It is thus evident that, for In-Au film-thickness in the order of a few hundreds of nanometers, the film T_c increases with increasing d_{In}/d_{Au}-ratio and is expectedly upper-limited by the bulk-In T_c at 3.41 K. These results are shown in Fig. 2, where the measured values for the In-Au film T_c correspond to the curves of Fig. 1.

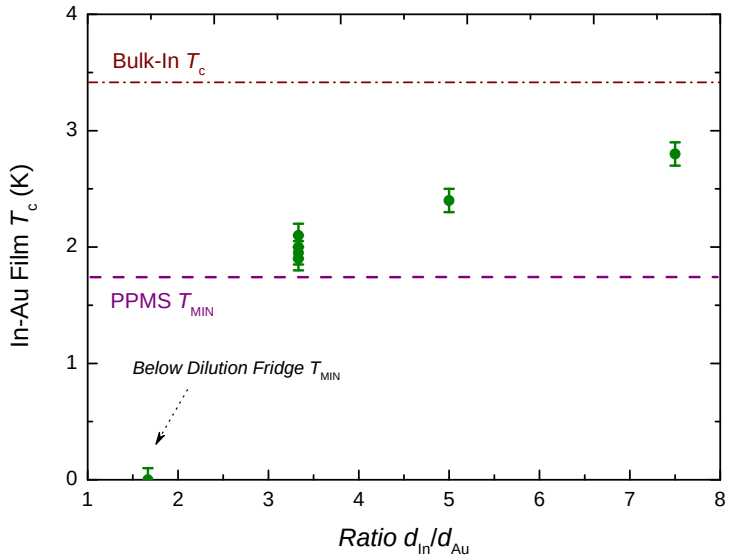

Figure 2: *The superconducting critical temperatures of In-Au films as a function of the ratio d_{In}/d_{Au}. The values of T_c are determined from the characteristics of Fig. 1, taking the $R \to 50\,\%$ criterion. Metallic films with $d_{In}/d_{Au} = 1.67$ did not feature superconductivity down to the mK-regime, as measured in the dilution refrigerator.*

It is evident that as the ratio $d_{\mathrm{In}}/d_{\mathrm{Au}}$ increases, the measured T_{c} approaches that of bulk-In. Films grown with 50 nm In and 30 nm Au were not superconducting down to 1.75 K. Sample P11 (see Ch. 5) belongs to that category and was measured in the dilution refrigerator down to the mK-regime, showing no superconducting signatures from the In-Au film.

The dependence of the In-Au film T_{c} on the ratio $d_{\mathrm{In}}/d_{\mathrm{Au}}$ leads to the assumption that Au-deposition has an impact on the homogeneity of the In-film which is grown shortly before. Since In is a soft metal, it is likely that Au particles are embedded inside the In-film during deposition and induce disorder high enough to suppress macroscopic superconductivity in the entire film. From an empirical perspective, samples with very thin Au films (20 nm and less) did not have the distinct Au-color on top, in contrast to all samples with 30 nm thick or more Au-films. In order to verify this hypothesis, secondary ion-mass spectroscopy (SIMS) measurements were performed on a sample with 50 nm In and 30 nm Au on a doped-$SrTiO_3$ substrate. Elaborate information on the SIMS method for interface and depth analysis can be found in Ref. [2]. The measurements are presented in Fig. 3.

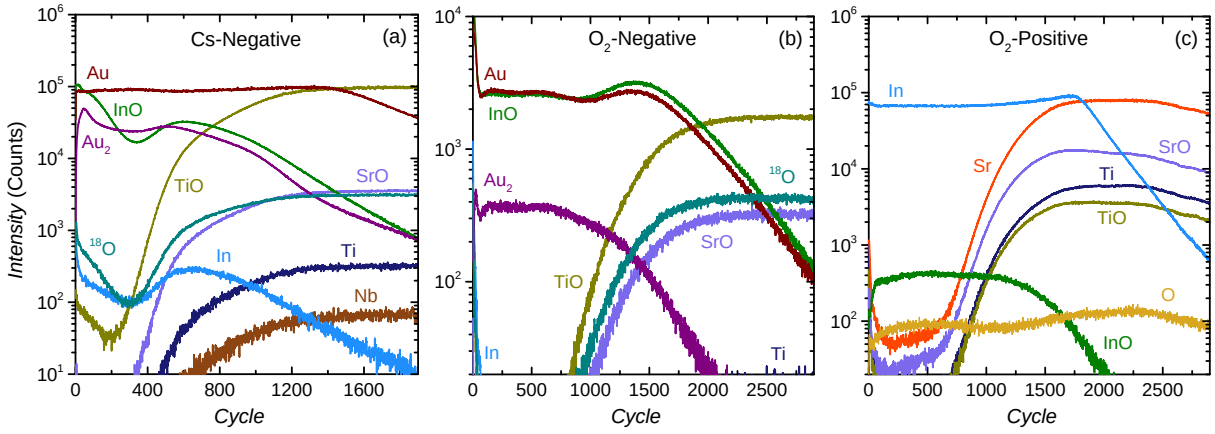

Figure 3: *Dynamic SIMS measurements for bulk analysis of sample P31, with 30 nm Au and 50 nm In on $SrTiO_3$ doped with Nb (0.5 wt%). Two types of ion-species, namely Cs and O_2, have been used to sputter the sample and individually investigate positive and negative elements: a) Cs for negative, b) O_2 for negative and c) O_2 for positive. These measurements offer only qualitative information, as there exists no direct correspondence of the measured intensity to ionic concentration. The increasing number of sputter-ion pulses provides depth resolution within about 100 nm from the surface.*

In Fig. 3, all curves correspond to elements of the $SrTiO_3$ substrate, Nb-dopants, Au and In. Each panel shows measurements that are taken in the same location, from the sample's surface towards the bulk. Lower intensity curves which indicate the presence of C, S, F and K impurities have been removed for clarity. In SIMS, the measured intensities do not relate directly to carrier concentration of the respective elements, as the ionization probabilities after sputtering with the ionic source (in this case Cs or O_2)

may drastically vary. Yet, qualitative information can be obtained from the data, regarding the element profiles with respect to depth (cycle number).

In all panels, the interface location in the horizontal axis is evidenced by the emergence of intensity curves from the substrate ionic-species, i.e. Nb, Ti, O, ^{18}O, Sr, SrO and TiO. These ingredients give out a stable signal with increasing number of cycles, following a relatively steep rise as the interface is probed. Note that the positive and negative channels are particularly sensitive to different ionic species. For instance, Au and Nb are clearly observed in panel 3a while In and Sr are present in panel 3c. Oxygen can be also used as a sputter parameter for the negative channel (panel 3b), yet the measured intensity for all species is reduced by two orders of magnitude, as compared to the other two panels.

The SIMS measurements verify the hypothesis suggested by the $R(T)$-characteristics measured in the PPMS (see Fig. 1). The profiles of In, InO, Au and Au_2 in all cases are similar with respect to depth, with no clear signature of an interface between the 50 nm In-film and the 30 nm Au-film that is deposited on top. The metallic film is essentially composed of In and Au, with the latter reaching the interface with the Nb-doped $SrTiO_3$ substrate (see panel 3a). In parallel, the presence of InO, appearing in all panels, implies that the In-film which is the top electrode in my tunnel junctions is partly oxidized. Note that InO is present not only in the negative O_2-channel but also in the Cs-channel (Fig. 3). This finding is important when discussing the Schottky barrier homogeneity and can be one of the main sources of the observed noise in my tunneling measurements. In addition, XRD-measurements have verified the presence of InO in another sample of the same characteristics.

From these measurements, it becomes evident that further optimization of the fabrication process is required. This optimization should target two main issues. The first is ensuring low oxidation in the top electrode. This can be however difficult for the particular study of superconductivity in the Schottky junction configuration, as the grown sample cannot be transferred and measured in-situ in the dilution refrigerator. Still, there is room for reducing the time between growth and cooling down to 4.2 K so that the oxidation level is also reduced. This has been suggested in the work of G. Binnig et al., on similar measurements with doped-$SrTiO_3$ [3]. Yet, oxidation cannot be completely avoided, as O_2 is already in abundance within the substrate itself. An alternative approach would be to include an additional insulating layer between metal and semiconducting $SrTiO_3$. This extra insulator would be less affected by the oxidation of any metallic film and can potentially reduce the induced noise in a tunneling measurement. A good candidate for this purpose is $LaAlO_3$, or AlO_2 in combination with Al as top electrode. The second issue to be addressed, is increasing the ratio $d_{\mathrm{In}}/d_{\mathrm{Au}}$ so that the In-layer at the proximity of the interface is unaffected by the evaporation of Au. This would ensure a good quality SIS junction with semiconducting $SrTiO_3$ substrates and can possibly also reduce the oxidation level in the interface region. Conversely, the impact of Au can prove itself useful, as by tuning the thickness-ratio one can systematically study superconductivity on doped-$SrTiO_3$ in both SIS and MIS configurations.

B: In-gap Features in the dI/dV Characteristics

Tunneling measurements on Schottky junctions made of In and doped-$SrTiO_3$, when both are superconducting, were performed. Signatures of the superconducting gap of In were resolved in the dI/dV-characteristics in my junctions, measured in the order of 500 μeV, which is in agreement with the tunneling measurements of G. Binnig et al. [3]. In addition, measurements of the magnetic field dependence of the tunneling conductance at $V \to 0$ (measurement process described in Ch. 4 & 5) with increasing temperature in steps, have shown that this gap in the DOS persists well above 800 mK. Its critical field was measured in the order of 20 mT, which is in a reasonable range for type-I superconductivity and happens to be close to that measured for doped-$SrTiO_3$ (sample P11, Ch. 5).

Ideally, at temperatures below the T_c of both superconductors, SIS-junctions are expected to exhibit tunneling characteristics with additional features due to tunneling-contributions from Josephson currents [4] and, possibly, signatures of two superconducting gaps. These were not observed in the tunneling characteristics in my samples, neither did the tunnel spectra resemble characteristics of typical MIS-junctions. Ac-measurements have revealed an intriguing increase in the dI/dV (V) at $V \to 0$, in all spectra, which is highly sensitive in the application of magnetic fields perpendicular to the junction plane.

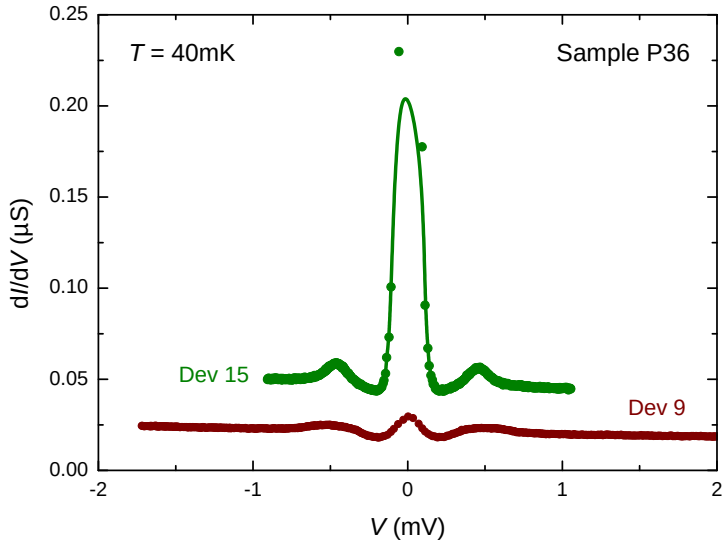

Figure 4: *Tunneling spectra at 40 mK featuring large zero-bias peaks, in Schottky junctions of 150 nm In and 20 nm Au on Nb-doped* $SrTiO_3$. *Zero-bias peaks were observed in all devices, which in some cases surpassed the normal state conductance background at the vicinity of the Fermi level.*

The dI/dV (V) characteristics measured in sample P36 are plotted in Fig 4 and show the emergence of zero-bias features in all devices. The absence of a double superconducting-gap structure on the dI/dV

(V), at energies $(\Delta_{\mathrm{In}} - \Delta_{\mathrm{SrTiO_3}})/e$ and $(\Delta_{\mathrm{In}} + \Delta_{\mathrm{SrTiO_3}})/e$, is in this case puzzling. It is possible that owing to the difference in the energy scales of the two gaps, in addition to low junction quality that increases noise in measurement, the resolution of double-gap structures in the tunnel spectra is hindered by the broadening of the In quasiparticle excitation peaks at $\approx \pm$ 500 mV.

Zero-bias conductance peaks appear often in tunneling measurements, in MIS and SIS junctions [5–14]. Kondo scattering from magnetic impurities can often lead to the rise of such peaks in tunneling spectra, yet in this case superconductivity is a competing order and the peaks disappear below the superconducting critical temperature [6]. In SIS junctions, provided that the tunnel resistance is small enough, Josephson tunneling can take place and thereby lead to increase of the conductance at $V \to 0$. Tunneling spectroscopy measurements in SIS junctions of high-temperature superconductors, particularly with YBCO [6, 7, 10, 11], BSCCO [5, 6, 13] and LSCO [5], have also demonstrated the emergence of zero-bias peaks. Yet, the temperature dependence of these peaks in my samples was measured up to 300 mK and intriguingly showed no significant change; therefore interpreting their existence based on tunneling within SIS junctions is not meaningful.

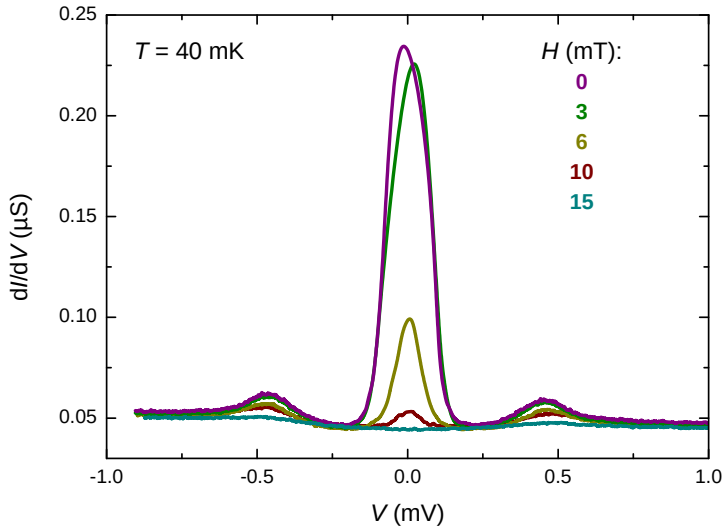

Figure 5: *Tunnel spectra from device 15, at perpendicular magnetic fields and at 40 mK. The suppression of the zero-bias and quasiparticle excitation peaks is gradual, until a field of approximately 15 mT at which they disappear.*

Under the application of magnetic fields, such peaks are often suppressed. This has been seen before in tunneling between noble metals and high-temperature superconductor junctions [5, 12]. Andreev reflection processes, between the superconducting In and the inhomogeneous doped-$SrTiO_3$ surface are also a possibility, as the tunnel resistance may vary over the macroscopically sized junction [8–10, 15]. As reported in other cases in literature, splitting of the peak has been observed, which is indicative of

scattering from magnetic impurities [16]. References [17, 18] give a detailed view of the emergence of zero-bias peaks in tunneling spectroscopy.

In order to establish that the observed features are linked to superconductivity, I performed measurements in perpendicular magnetic fields. The tunnel spectra are shown in Fig. 5. By application of small magnetic fields (in the order of a few mT), the quasiparticle excitation and zero-bias peaks simultaneously vanish. This leads to the assumption that the zero-bias peak in the spectra is a feature associated with superconductivity in the In-film. Splitting of the peak was not observed during any measurement under perpendicular magnetic fields in my samples. Interestingly, the disappearance of the superconducting characteristics is gradual, rather than sharp, albeit In being a type-I superconductor. In this sample, a Au-layer of 20 nm was evaporated on top of the 150 nm thick In-film. As discussed in Appendix A for this configuration, Au-atoms still induce disorder in the underlying In-film and thereby its T_c is reduced. Thus this gradual suppression probably originates from the induced disorder in the superconducting In-film.

Further investigation was performed, aiming to uncover the origin of such peak, through tunneling measurements with varying the frequency and phase of the ac-current applied across the junction. It was observed that the emergence of zero-bias peaks depended highly on the phase of the applied current. In parallel, measurements with no ac-current component (only dc-currents were applied), showed no signatures of zero-bias conductance increase in the spectra. In the latter case, the noise level was significantly increased.

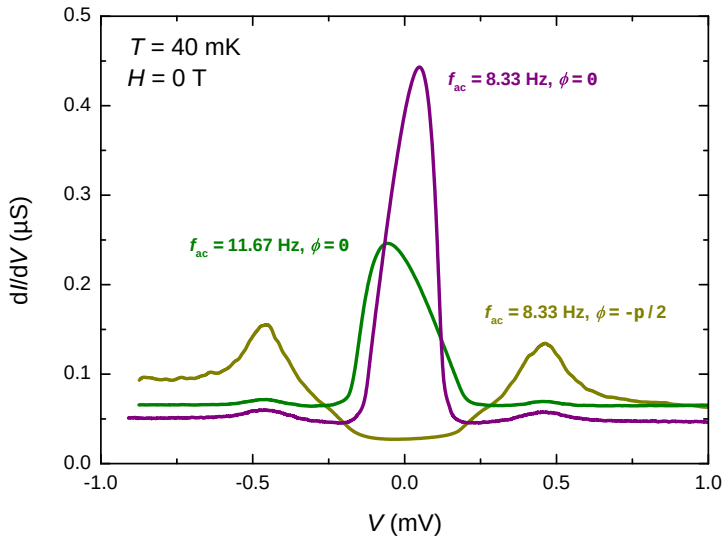

Figure 6: *Tunnel spectra from the ac-measurements, in which the frequency f and phase ϕ of the applied ac-current vary. The absolute value of the conductance is sensitive to f. Intriguingly, spectra measured at $\phi = -\pi/2$ with respect to lock-in reference do not exhibit zero-bias peaks.*

Figure 6 presents the dependence of the tunnel spectra on the frequency and phase of the ac-current. By changing the phase by $-\pi/2$, the zero bias peak disappears. Similar but not as pronounced features have been observed in other samples with In and Nb-doped $SrTiO_3$ (Sample P21, Tab. 5.2). Additional measurements with magnetic fields have shown that as soon as $H < H_{c,In}, H_{c,N:STO}$, the junction's out-of-phase component of the measured voltage dominates the measurement. Thus, it might be meaningful to investigate such effect further by calculating the junction's capacitance, considering the Schottky depletion region and observe how it varies with device size. Capacitive artifacts as these described here may appear frequently in ac-measurements and can be possibly misinterpreted as intrinsic properties of the sample. Low junction quality is likely to lead to the emergence of such peaks.

In the current stage the SIS junction fabrication procedure requires further optimization. The growth conditions of the In film is a crucial factor that determines the junction's homogeneity. From the measurements described in Appendix A, it is now possible to tailor MIS or SIS junctions between doped-$SrTiO_3$ and In/Au. The resolution of the superconducting gap of In was successful, yet the signatures of two gaps in the tunnel spectra (as seen in Ref. [3]) were not observed. Optimizing the Ar-etching step prior to In growth might be the key factor to not only create a more stable Schottky barrier but also tune its height and thereby the junction characteristics.

C: Magnetic-Field-Sweeps Induce Heating

Throughout all magnetic-field dependent tunneling measurements, the field was swept at constant rates, from 0 to several Tesla. It was noticed that, particularly at the sub-T regime, there is pronounced heating as the field is swept. This required further investigation as the temperature-increase, although small, can be a significant fraction of the critical temperatures of the superconducting $LaAlO_3/SrTiO_3$ 2DEL and doped-$SrTiO_3$. The magnitude of the induced heating depends highly on the sweep rate, a restriction that has forced me to perform very slow sweeps at low magnetic fields, typically of the order of 10 mT per minute and even less at the range 0 to 100 mT.

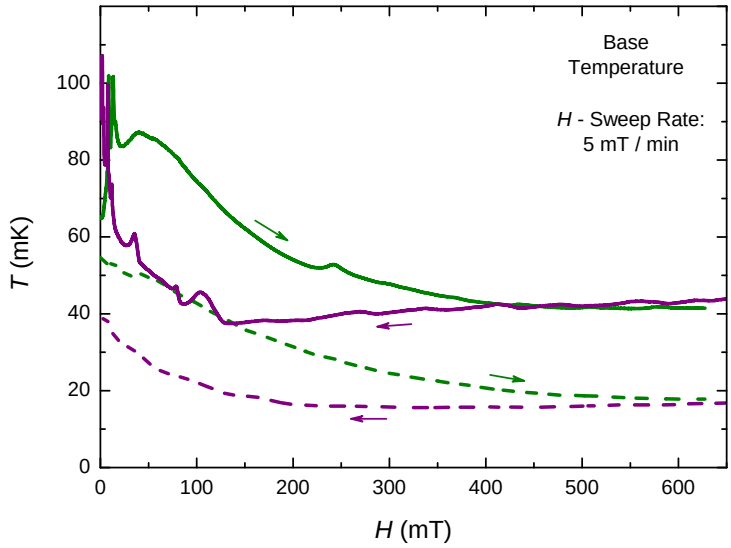

Figure 7: *Temperature fluctuations with varying magnetic field, at a rate of 5 mT per minute. The dashed lines correspond to the temperature of the mixing chamber in the dilution fridge and the solid lines are recorded by a RuO_2 temperature sensor (model RX-102A, Lakeshore Cryotronics Inc.) at the sample's direct proximity. The arrows indicate the sweep-direction for the respective curve, while generally violet indicates down-sweeps and green indicates up-sweeps.*

Figure 7 presents the effect discussed, for a typical measurement close to base temperature of the dilution refrigerator. The starting temperature of the mixing chamber was approximately 50 mK, owing to heating contributions from applying a large back-gate field (up to $\pm$ 300 V for $LaAlO_3/SrTiO_3$). In the range 0 to 100 mT, the field-sweep induces heating that is sensed by the RuO_2 sensor (solid lines) attached to the chip carrier, despite the low sweep-rate. The sensor of the mixing chamber (dashed lines) records only a tiny temperature increase, not visible in this graph. This finding substantiates the following hypotheses: (a) the rise in temperature originates from magnetic moments in the chip carrier with the bonded-sample, thermally connected to the mixing chamber, and is not fully compensated by cooling, (b) the temperature instability is due to low magnetic-field induced errors that are often a

characteristic of RuO_2 sensors [19]. The heating evolution with field-sweep has been monitored also at higher temperatures, setting the temperature at the mixing chamber to a constant value and initiating a sweep. Figure 8 presents measurements up to 350 mK.

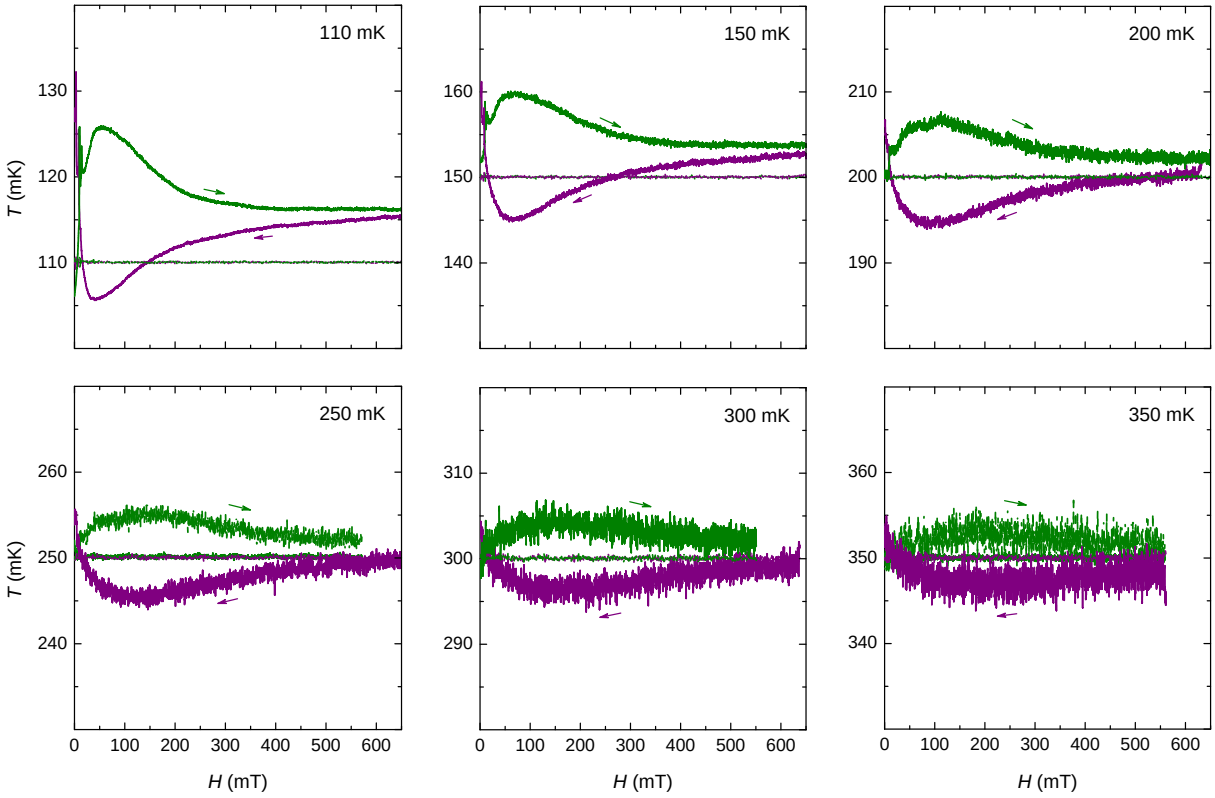

Figure 8: *Similar to Fig. 7, the heating induced by the field sweep (constant at 5 mT per minute), starting at preset temperatures in the mixing chamber, indicated at the top right corner of each panel. At low-fields (up to 100 mT) magnetization effects are pronounced, with the temperature rising when sweeping up and decreasing when sweeping the field down. This increase and decrease are higher in magnitude at lower starting temperatures. At higher starting temperatures magnetization effects are less pronounced, but the temperature fluctuations are enhanced in the entire field range. Note that the vertical scale extent in all panels is kept constant (40 mK), but depicts different temperature ranges.*

At lower preset temperatures, sweeping the field up induces sample-heating that relaxes after 100 mT, approximately. The reverse happens when sweeping the field down, where demagnetization effects take place and the temperature drops rapidly until the 100 mT mark. This effect (for both sweep-directions) decreases as the initial temperature at the mixing chamber is set to higher values. In parallel, as the latter increases, thermal fluctuations also increase and are present at the entire magnetic field range. During the sweep at all preset temperatures, a heater attached to the mixing chamber keeps temperature at a fixed value (in feedback operation), which shows only tiny fluctuations at very low magnetic fields and for the lower preset temperatures. From these measurements and especially due to the decreasing

temperature profiles as the field is swept towards zero, magnetization effects at the sample's vicinity is a likely explanation. All sample holders used in this work (see Ch. 3) exhibit small magnetization, which can be verified simply by approaching them to small permanent magnets of the order of a few mT (typical household magnets). Yet, possible sensor errors at the low magnetic regime and thereby the scenario of virtual heating contributions cannot be ruled-out by these data, as it is difficult to ascertain whether the power-heater at the mixing chamber totally compensates the temperature fluctuations in the vicinity of the sample.

Similar fluctuations are also seen in other laboratories with dilution refrigerator systems [20]. They are taken into account when estimating all error margins for temperature throughout this work. The heating/cooling profiles did not vary significantly with respect to the large back-gate fields applied in measurements at the $LaAlO_3/SrTiO_3$ interface.

References

[1] B. T. Matthias, T. H. Geballe and V. B. Compton, Rev. Mod. Phys. **35**, 414 (1963).

[2] C. W. Magee and R. E. Honig, Surf. Int. Anal. **4**, 35 (1982).

[3] G. Binnig, A. Baratoff, H. E. Hoenig and J. G. Bednorz, Phys. Rev. Lett. **45**, 1352 (1980).

[4] B. D. Josephson, Phys. Lett **1**, 251 (1962).

[5] L. Alff and R. Gross, Adv. Solid State Phys. **38**, 453 (2007).

[6] A. M. Cucolo, Physica C **305**, 85 (1998).

[7] K. Hirata, K. Yamamoto, K. Iijima, J. Takada, T. Terashima, Y. Bando and H. Mazaki, Appl. Phys. Lett. **56**, 683 (1990).

[8] E. Zhitlukhina, I. Devatov, O. Egorov, M. Belogolovskii and P. Seidel, Nanoscale Res. Lett. **11**, 58 (2016).

[9] M. Popinciuc, V. E. Caldo, X. L. Liu, A. R. Akhmerov, T. M. Klapwijk and L. M. K. Vandersypen, Phys. Rev. B **85**, 205404 (2012).

[10] T. Kusumori and I. Iguchi, J. Appl. Phys. Jpn. **31**, L956 (1992).

[11] J. S. Tsai, I. Takeuchi, J. Fujita, T. Yoshitake, S. Miura, S. Tanaka, T. Terashima, Y. Bando, K. Iijima and K. Yamamoto, Physica C **153**, 1385 (1988).

[12] J. W. Ekin, Y. Xu, S. Mao, T. Venkatesan, D. W. Face, M. Eddy and S. A. Wolf, Phys. Rev. B **56**, 13746 (1997).

[13] I. Shigeta, T. Uchida, Y. Tominari, T. Arai, F. Ichikawa, T. Fukami, T. Aomine and V. M. Svitsunov, J. Phys. Soc. Jpn. **69**, 2743 (2000).

[14] J. Takada, T. Terashima, Y. Bando, H. Mazaki, K. Iijima, K. Yamamoto and K. Hikita, Appl. Phys. Lett. **53**, 2689 (1988).

[15] F. Miao, S. Wijeratne, Y. Zhang, U. C. Coskun, W. Bao and C. N. Lau, Science **317**, 5844 (2007).

[16] M. Covington, M. Aprili, E. Paraoanu and L. H. Greene, Phys. Rev. Lett. **79**, 277 (1997).

[17] T. Walsch, Int. J. Mod. Phys. B **06**, 125 (1992).

[18] J. Mannhart and H. Hilgenkamp, Physica C **317**, 383 (1999).

[19] Lakeshore Cryotronics Inc., *Cryogenic Temperature Sensor Characteristics* © (2017).

[20] J. Falson, *Private Communication*, Max-Planck-Institute, Stuttgart (2016).

List of Abbreviations

AFM : Atomic-Force Microscopy or AntiFerroMagnetic

BCS : Bardeen-Cooper-Schrieffer

BKT : Berezinskii–Kosterlitz–Thouless

CNT : Carbon NanoTubes

DFT : Density Functional Theory

DOS : Density Of States

DRAM : Dynamic Random-Access Memory

EBPVD : Electron-Beam Physical-Vapor Deposition

FWHM : Full-Width at Half-Maximum

GGA : Generalized Gradient Approximation

GL : Ginzburg-Landau

HF : Hydrogen-Fluoride

HR : Hyper-Raman

HTS : High-Temperature Superconductors

IETS : Inelastic Electron Tunneling Spectroscopy

IVC : Inner Vacuum Chamber

LO : Longitudinal Optical

MIS : Metal-Insulator-Superconductor

PLD : Pulsed Laser Deposition

PPMS : Physical Property Measurement System

QCM : Quartz Crystal Monitor

QCP : Quantum Critical Point

QPT : Quantum Phase Transition

RHEED : Reflection High-Energy Electron Diffraction

RSOC : Rashba Spin-Orbit Coupling

RVB : Resonating Valence Bond

SHG : Second-Harmonic Generation

SIMS : Secondary Ion Mass Spectrometry

SIS : Superconductor-Insulator-Superconductor

SIT : Superconductor-Insulator Transition

SMIT : Superconductor-Metal-Insulator Transition

SNS : Superconductor-Normal-Superconductor

STEM : Scanning Transmission Electron Microscopy

STM : Scanning Tunneling Microscopy

STS : Scanning Tunneling Spectroscopy

SX-ResPES : Soft X-ray Resonant Photo-Electron Spectroscopy

TO : Transverse Optical

UV : Ultra-Violet

VLSI : Very-Large-Scale Integration

WHH : Werthamer-Helfand-Hohenberg

XRD : X-Ray Diffraction

2DEG : Two-Dimensional Electron-Gas

2DEL : Two-Dimensional Electron-Liquid

2DES : Two-Dimensional Electron-System

Acknowledgment Note

Concluding this thesis, I would like to express my sincere gratitude towards all those who have contributed in my efforts these years. They are people that have supported, guided and generally dedicated some of their time to help me finalize this work, both directly and indirectly. All this input has helped me grow a lot as a scientist and also as a person.

I want to thank Prof. J. Mannhart for offering the opportunity to pursue my PhD in such a fascinating topic. In addition to his key-contribution to the scientific part, I particularly thank him for always providing motivation in our scheduled meetings. Such communication has been a timely support, often at tough periods in this 4-year experience.

I deeply thank Dr. Hans Boschker for a constant supervision of my work, from day one till this very moment. His insight and technical expertise have been a priceless help to my scientific steps in and out of the lab, not to mention his willingness for discussions on problems of any nature. I certainly value the extent of our communication on a professional and also personal level, it being anywhere from our noisy Magnetlabor to some random pub of the city. Thanks a lot Hans, it has been great working with you.

Big part of my acknowledgment I want to direct to the superconducting team of the Mannhart department as a whole, which currently includes my colleague and officemate Lukas Kürten, in addition to Hans and myself. I did enjoy a great collaboration with you guys and have benefited a lot from our combined discussions. Also, keeping our good-old dilution fridge in one piece for so long was anything but easy. To a former member of this team, Dr. Christoph Richter, I also owe a great deal as his work has preceded mine and provided a solid ground for my study of the $LaAlO_3/SrTiO_3$ interface.

The technicians of my department have contributed a lot in many aspects, from repairing all kinds of fancy equipment to resolving software issues and generally maintaining great conditions in any lab I've entered. Thank you Manfred Schmid, Ingo Hagel, Wolfgang Winter, Sabine Seiffert and Konrad Lazarus. I explicitly acknowledge the help of Dr. Wolfgang Braun, who along with Lukas guided me for the installation of the In-Effusion cell.

To Marion Hagel I am particularly grateful for bonding a million of my samples in such a precise manner. I also appreciate the efforts of Yvonne Link for the thermal evaporation of metallic films on my samples, in the early stages of my work. I thank Tolga Acartürk and Helga Hoier, respectively for performing SIMS and XRD measurements for me. Having also benefited from discussions with scientists and good friends outside my group, I want to thank Dr. Eslam Khalaf and Dr. Hadj Mohamed Benia.

I am very thankful to Prof. Martin Dressel for undertaking the task of being in my committee and for reviewing my work. I am also thankful to Prof. Maria Daghofer for being willing to chair my defense and to Dr. Marko Burghard for externally supervising parts of my PhD-work in the first years.

I greatly appreciate the help I received from people that are no longer in the group. For all scientific discussions, lab guidance and support, I thank my former colleagues Rene, Carsten, Georg, Florian, Bhagwati and of course Takayuki. Also, many thanks to Jone for reviewing parts of my thesis and to Lukas for turning my summary into a Zusammenfassung..

The awesome office environment I had the luck to be in, I'm certainly going to miss. Yeliz, Ali, Lukas (wow you appear often in this note!) and formerly Cyril, thank you guys for the nice and relaxed times we had together. We should find a way to keep up the wine sessions - the next one is on me.

The interplay of discussion and fun in the MHA-group, often in areas with high alcohol concentration, has certainly played a constructive part in finalizing this work. Iman, thank you for the countless beer sessions mate. For my coffee sessions - danke schön Ali. My neighbors Robin and Pascal, props to your good spirit & attitude and also to your bbq-skills, es war wirklich toll. To the Mediterranean squad (now scattered across the continent), Yeliz, Jone, Cyril and Marco: I won't forget those times guys, cheers!

I also want to thank our newer members for keeping the spirit up: Prosper, Wolfgang III, Maren, Sogol and Gena (who never hesitated to invade my office in the search of alcohol). Last but not least, I'm grateful to the valuable support of our group's secretary, Renate Zimmermann, whose friendly attitude and organizational skills has made life easier in so many ways.

With my final words, I want to wholeheartedly thank my wife Foteini. Alongside me, she has put up with all kinds of pressure before this thesis was finally complete. Her patience and emotional support have been so valuable; it's at this point tough to properly express my gratitude in words. I thus want to dedicate this work primarily to her and also to my family, who have always been there for me.

Brief CV

Personal Information

Name:	Fillis-Tsirakis, Evangelos
Date of Birth:	22.02.1986
Place of Birth:	Athens, Greece
Marital Status:	Married

Education

09/2000 - 06/2003	High-School Studies, Chania, Greece
09/2003 - 10/2009	Diploma Studies of Applied Physics, School of Applied Mathematical and Physical Science, NTUA, Greece
10/2010 - 10/2012	MSc Studies of Solid State Physics, University of Stuttgart, Germany
01/2013 - 06/2017	Doktoral Studies, Max-Planck-Institute for Solid State Research - University of Stuttgart, Germany

Selected Publications

- M. Thiemann et al., *Single-Gap Superconductivity in Doped $SrTiO_3$*, (submitted 2017)
- E. Fillis-Tsirakis et al., *Evidence for Superconducting Phase Coherence in the Metallic/Insulating Regime of the $LaAlO_3/SrTiO_3$ Interface Electron System*, New J. Phys. **18**, 013046 (2016)
- H. Boschker et al., *Electron-Phonon Coupling and the Superconducting Phase Diagram of the $LaAlO_3/SrTiO_3$ Interface*, Sci. Rep. **5**, 12309 (2015)
- C. Richter et al., *Interface Superconductor with Gap Behaviour like a High-Temperature Superconductor*, Nature **502**, 528 (2013)